

Breakdown of functional networks in mouse models of dementia



Submitted by Maria Francisca Garcia Garrido to the University of Exeter
as a thesis for the degree of
Doctor of Philosophy in Medical Studies
In October 2020

This thesis is available for Library use on the understanding that it is copyright material and that no quotation from the thesis may be published without proper acknowledgement.

I certify that all material in this thesis which is not my own work has been identified and that no material has previously been submitted and approved for the award of a degree by this or any other University.

Signature:

Abstract

Alzheimer's disease (AD) is a progressive neurodegenerative disorder and the major cause of dementia, for which there are no available treatments that can cure or stop its progression. Disorientation in both familiar and unfamiliar places is a symptom often observed in people affected by AD. The entorhinal cortex (EC), which is one of the brain areas earliest affected by this disease, plays a key role in spatial navigation and memory. Despite the important role that the EC may play in the spatial memory deficits observed in AD, the effects of novelty and familiarity on the EC neuronal dynamics of amyloidopathy mouse models is not well understood. This PhD thesis focuses on the study of the medial EC (MEC) neuronal dynamics underlying spatial memory in an amyloidopathy mouse model, the J20 mice, employing *in vivo* electrophysiological techniques.

Chapters 3 and 4 examine local field potential (LFP) signals to study the effects of novelty and familiarity on the MEC neuronal networks of J20 mice. These two chapters highlight deficits in high gamma oscillations in the MEC of these mice related to memory processing.

Chapter 4 further examines the single-unit activity of the neurons involved in these networks in the MEC of J20 mice, during the exploration of novel and familiar environments. This chapter shows that theta modulated cells have a lower frequency of modulation in the MEC of these mice. Furthermore, the results of this chapter suggest that a proportion of functional cell subtypes are affected by the novelty of the environment in the MEC.

Acknowledgements

First of all, I would like to thank my supervisors, Dr Jon Brown and Dr Tom Ridler, for their help, support and advice throughout the years of this PhD. To Jon, thank you for giving me the opportunity to do this fascinating PhD project and giving me the space to grow as a researcher. To Tom, thank you for showing me how to do everything, always with a smile.

I would also like to thank everybody in the Hatherly labs, past and present, for creating such a friendly and open environment, which made me feel very welcome. Additional thanks to Dr Vashti Berry, my pastoral tutor, for her genuine interest in my wellbeing and support through my PhD.

Special thanks to Judith and Marziyeh, I have been incredibly lucky to have shared each step of this roller-coaster of a journey with you both. Thank you for being there in the ups and downs, you have always been there for me to provide support and help. I always looked forward to our lunch and coffee breaks throughout the day, which always provided me with a space to be myself, especially at the beginning, when my English skills were not the sharpest. Meeting up with you both, and the rest of the crew, has always been very fun and filled with lots of laughs.

To Sean, I cannot express how grateful I am for all your love and support. You have always been my pillar of strength. Thank you for taking care of me and always trying your best, I know it has not always been easy, especially when you had your own stresses to deal with as well.

A mis padres y mis hermanos, Cande, Manolo y Rafa, gracias por el apoyo constante a lo largo de estos años y por creer siempre en mí. Sin vosotros, nada de esto habría sido posible.

Table of contents

Abstract.....	3
Acknowledgements.....	5
Abbreviations	16
Chapter 1. Introduction	19
1.1. Alzheimer's disease	19
1.1.1. Dementia overview	19
1.1.2. Pathological features of Alzheimer's disease.....	19
1.1.3. Alzheimer's disease progression	22
1.1.4. Aetiology of Alzheimer's disease	25
1.1.5. Amyloid cascade hypothesis.....	25
1.1.6. Clinical trials.....	28
1.1.7. Rodent models of Alzheimer's disease	29
1.1.8. The J20 mouse model of dementia.....	30
1.1.9. Spatial memory impairments in AD.....	31
1.2. Entorhinal cortex	33
1.2.1. The role of the entorhinal cortex in spatial navigation and memory .	33
1.2.2. Entorhinal cortex anatomy	36
1.2.3. Entorhinal cortex intrinsic connectivity	38
1.2.4. Entorhinal cortex extrinsic connectivity	38
1.2.5. Entorhinal cortex in Alzheimer's disease	40
1.3. Entorhinal cortex neuronal oscillations.....	41
1.3.1. Neuronal oscillations.....	41
1.3.2. Theta oscillations	42
1.3.3. Gamma oscillations.....	44
1.3.4. Cross-frequency coupling	45

1.3.5. Role of neuronal oscillations in novel and familiar contexts	46
1.3.6. Breakdown of neuronal networks in AD	49
1.4. MEC functional cell subtypes	50
1.4.1. Speed sensitive cells	53
1.4.2. Head direction sensitive cells.....	53
1.4.3. Cells with grid periodicity	54
1.4.4. Border sensitive cells	56
1.4.5. Other spatially modulated cells	57
1.4.6. Context effects on MEC functional cell subtypes	57
1.4.7. Alterations of spatial functional cell subtypes in Alzheimer's disease	59
1.5. Hypothesis and aims.....	60
Chapter 2. General methodology	63
2.1. Experimental subjects	63
2.2. Behavioural tests.....	64
2.2.1. Triangular track.....	64
2.2.2. Open arenas	65
2.2.2.1 Open arenas: First experiment	65
2.2.2.2 Open arenas: second experiment.....	67
2.3. <i>In vivo</i> electrophysiology	70
2.3.1. Silicon probes	70
2.3.2. Silicon probe implantation.....	71
2.3.3. Data acquisition	73
2.3.4. Tracking analysis	73
2.3.5. Local field potential signals analysis	74
2.3.6. Spike sorting	78
2.3.7. Theta modulation analysis	80
2.3.7.1 Theta modulation index	80

2.3.7.2 Maximum likelihood estimation method for theta modulation	80
2.3.7.3 Theta firing phase and mean resultant vector length	80
2.3.8. Cell type classification.....	81
2.3.9. Speed sensitive cells	81
2.3.10. Head direction sensitive cells.....	82
2.3.11. Cells with grid periodicity – Langston’s method	83
2.3.12. Cells with grid periodicity – Sargolini’s method	84
2.3.13. Spatial information	85
2.3.14. Border sensitive cells	86
2.3.15. Novelty effects	86
2.4. Perfusions and histology	89
2.5. Statistical analysis	90
Chapter 3. Assessment of novel and familiar environmental stimuli effects in the MEC neuronal networks	91
3.1. Introduction	91
3.2. Methodology.....	93
3.2.1. Animals	93
3.2.2. Behavioural experiments	94
3.2.2.1 Triangular track.....	94
3.2.2.2 Two open arenas	94
3.2.3. Data acquisition and analysis	95
3.2.4. Statistical analysis.....	96
3.3. Results	97
3.3.1. Assessment of novel and familiar environmental stimuli effects in the MEC neuronal networks with a triangular track.....	97
3.3.1.1 J20 mice do not reduce their running speed with familiarity	99
3.3.1.2 Broadband spectral analysis.....	100
3.3.1.3 MEC network oscillations.....	102

3.3.2. Assessment of novel and familiar environmental stimuli effects in the MEC neuronal networks with two open arenas.....	107
3.3.2.1 J20 mice show signs of reduced anxiety	108
3.3.2.2 Spectral analysis shows no differences between genotypes	112
3.3.2.3 Theta frequency oscillations	114
3.3.2.4 High gamma frequency oscillations	118
3.3.2.5 Phase amplitude coupling.....	121
3.4. Discussion.....	123
3.4.1. Summary	123
3.4.2. Limitations of the triangular track experiment	123
3.4.3. J20 mice show signs of reduced anxiety.....	124
3.4.4. Power spectrum analysis	125
3.4.5. No deficits in theta frequency oscillations in the MEC of J20 mice	125
3.4.6. Deficits in high gamma frequency oscillations in the MEC of J20 mice	126
3.4.7. No deficits in phase amplitude coupling in the MEC of J20 mice ...	128
3.5. Conclusions.....	129
Chapter 4. Analysis of MEC network impairments impact at the single unit level	131
4.1. Introduction	131
4.2. Methodology.....	132
4.2.1. Animals	132
4.2.2. Behavioural task	133
4.2.3. Data acquisition	134
4.2.4. Tracking analysis	134
4.2.5. Local field potential signals analysis	134
4.2.6. Single unit classification and analysis.....	135
4.2.6.1 Theta modulation.....	135

4.2.6.2 Cell type classification	136
4.2.6.3 Functional cell subtype metrics.....	136
4.2.6.4 Novelty effects	139
4.2.7. Statistical analysis.....	140
4.3. Results	142
4.3.1. J20 mice and WT mice spend similar time next to the borders of the arena.....	142
4.3.2. Broadband spectral analysis shows no differences between both genotypes	144
4.3.3. MEC network oscillations	148
4.3.4. More cells are classified as theta modulated with the TMI criteria .	155
4.3.5. The analysis with the MLE method for theta modulation shows differences in the frequency of modulation	162
4.3.6. Speed sensitive cells show no deficits in J20 mice	170
4.3.7. HD sensitive cells show no differences between genotypes	181
4.3.8. Cells with grid periodicity analysed with Langston's method.....	189
4.3.9. Cells with grid periodicity analysed with Sargolini's method	196
4.3.10. Border sensitive cells show no differences between genotypes ..	203
4.3.11. Spatial information does not differ between genotypes.....	210
4.3.12. Number of MEC cells passing multiple criteria.....	217
4.4. Discussion.....	219
4.4.1. Summary	219
4.4.2. Layer effects in MEC recordings	219
4.4.3. Anxiety levels and hyperactivity in J20 mice	220
4.4.4. The slope of theta power is modulated by novelty	221
4.4.5. The slope of high gamma power.....	222
4.4.6. Phase amplitude coupling between theta and high gamma frequency oscillations	223

4.4.7. TMI analysis provides less restricted criteria to classify theta modulated cells	224
4.4.8. J20 cells exhibit lower frequency of the cell rhythmicity than WT cells	224
4.4.9. J20 mice cells show normal speed modulation	228
4.4.10. HD sensitive cells show no differences between genotypes	229
4.4.11. The number of cells with grid periodicity is lower than expected..	230
4.4.12. Border sensitive cells and cells conveying significant spatial information show no differences between genotypes	231
4.4.13. A proportion of some MEC cell subtypes is affected by novelty...	232
4.5. Conclusions.....	236
Chapter 5. General discussion.....	237
5.1. Summary of key findings	237
5.2. Deficits in memory processing in J20 mice	238
5.3. Implications of a lower frequency of the modulation in theta modulated cells.....	240
5.4. Limitations and directions for future research	241
5.4.1. Mouse models of Alzheimer's disease	241
5.4.2. Future directions	242
5.5. Conclusions.....	243
References	245

Figures

Figure 1.1 Amyloidogenic and non-amyloidogenic pathways for the processing of APP	21
Figure 1.2 The progression of AD is divided in different stages.	24
Figure 1.3 human APP mutations used in amyloid mouse models.....	30
Figure 1.4 Anatomy of the MEC in the rodent and human brain	37
Figure 1.5 Summary of EC connectivity	40
Figure 1.6 PAC between theta and gamma oscillations	46
Figure 1.7 Spatially modulated functional subtypes.	52
Figure 2.1 Experimental set up of the triangular track experiment	65
Figure 2.2 Experimental design of the first experiment with two open arenas..	67
Figure 2.3 Experimental design of the second experiment with two open arenas.	
.....	69
Figure 2.4 Silicon probes used in all experiments	71
Figure 2.5 Implanted mouse with 32-channel probe (CAMBRIDGE NeuroTech)	
.....	73
Figure 2.6 Analysis of theta and high gamma oscillations	77
Figure 2.7 Clustering of single unit data visualized in KlustaViewa	79
Figure 2.8 Diagram showing the different patterns observed	89
Figure 3.1 MEC recording sites of 6 mo mice.....	98
Figure 3.2 MEC recording sites of 10 – 15 mo mice.....	99
Figure 3.3 J20 mice do not reduce their running speed in trial 2	100
Figure 3.4 Power spectrum shows no deficits in J20 mice	102
Figure 3.5 Theta power slope increaseases in trial 2 in 10 – 15 mo mice	104
Figure 3.6 No deficits are observed in high gamma frequency oscillations in J20 mice.....	105
Figure 3.7 Averaged phase-amplitude comodulograms across animals.	106
Figure 3.8 MI slopes show no differences due to trial nor between genotypes	
.....	107
Figure 3.9 J20 mice show signs of reduced anxiety	110
Figure 3.10 Both WT and J20 mice reduce their running speed in familiar environments.....	111

Figure 3.11 Normalised power in the different frequency bands across all trials	113
Figure 3.12 Power spectrum shows no deficits in J20 mice	114
Figure 3.13 Relationship of theta frequency oscillations with running speed across all trials.....	116
Figure 3.14 Theta power slope is affected by familiarity.....	117
Figure 3.15 Relationship of high gamma frequency oscillations with running speed across all trials.....	119
Figure 3.16 High gamma power and frequency slopes increase with familiarity only in WT mice	120
Figure 3.17 Theta – high gamma MI slopes are affected by context	122
Figure 4.1 J20 mice and WT mice spend a similar amount time next to the borders of the arena	143
Figure 4.2 MEC recording sites	146
Figure 4.3 Power spectrum shows no deficits in J20 mice	147
Figure 4.4 The power slope of theta oscillations is affected by novelty in both WT and J20 mice	150
Figure 4.5 The power slope of high gamma oscillations is affected by novelty only in J20 mice	152
Figure 4.6 MI slopes decrease with novelty in the MEC of both WT and J20 mice	154
Figure 4.7 The proportion of theta modulated cells is lower in layer III of the MEC	157
Figure 4.8 The firing of a higher proportion of layer III cells is locked to the peak of theta oscillations.....	158
Figure 4.9 The frequency of the modulation is lower in cells of layer III of the MEC	159
Figure 4.10 The TMI is lower in putative excitatory cells than in putative interneurons	160
Figure 4.11 The mean vector length is lower in putative excitatory cells than in putative interneurons.....	161
Figure 4.12 The proportion of theta modulated cells is lower in layer III of the MEC	164

Figure 4.13 A similar proportion of cells have their firing locked to the trough of theta oscillations in both genotypes.....	165
Figure 4.14 The frequency of the modulation is lower in J20 cells	166
Figure 4.15 The frequency of modulation does not correlate with distance from MEC border.....	167
Figure 4.16 The TMI is lower in putative excitatory cells than in putative interneurons	168
Figure 4.17 The mean vector length is lower in putative excitatory cells than in putative interneurons.....	169
Figure 4.18 The proportion of speed sensitive cells decreases with novelty ..	172
Figure 4.19 Layer III has a higher proportion of saturating speed sensitive cells than layer II.....	173
Figure 4.20 The proportion of decreasing speed sensitive cells is higher than the level expected by chance	175
Figure 4.21 Speed scores are higher in speed sensitive putative interneurons. A) Pooled speed scores by genotype	177
Figure 4.22 Firing rate is higher in speed sensitive putative interneurons	179
Figure 4.23 No cells pass the rate difference index threshold	180
Figure 4.24 The proportion of HD sensitive cells is the same between both genotypes.....	183
Figure 4.25 The proportions of decreasing and increasing HD sensitive cells are not different to the simulated data	184
Figure 4.26 Head direction sensitive cells with small phase shifts (<60°) show a higher correlation in their polar plots between the two familiar trials	185
Figure 4.27 Mean resultant vector length (HD scores) of HD sensitive cells are similar between WT and J20 mice.....	186
Figure 4.28 The firing rate of HD sensitive cells is similar between WT and J20 mice.....	188
Figure 4.29 The proportion of cells with significant grid periodicity is not above chance levels.....	191
Figure 4.30 The proportion of decreasing and increasing cells with grid periodicity is similar to the simulated data	192
Figure 4.31 Grid scores are similar in J20 mice than in WT mice.....	194

Figure 4.32 There are no changes in the firing rate of cells with grid periodicity between both genotypes	195
Figure 4.33 The proportion of cells with significant grid periodicity is higher in WT mice.....	198
Figure 4.34 The proportion of decreasing and increasing cells with grid periodicity is similar to the simulated data	199
Figure 4.35 Cells with grid periodicity show stability between both familiar exposures.....	200
Figure 4.36 Grid scores are similar in WT mice and J20 mice	201
Figure 4.37 The firing rate of cells with grid periodicity increases during the exploration of the novel environment.....	202
Figure 4.38 The proportion of border sensitive cells is the same between both genotypes.....	204
Figure 4.39 WT and J20 mice show a higher proportion of decreasing border sensitive cells than the simulated data	205
Figure 4.40 Border scores of WT and J20 mice are similar.....	207
Figure 4.41 The firing rate of border sensitive cells is similar in WT and J20 mice.	
A) Pooled firing rate data by genotype	209
Figure 4.42 The proportion of cells conveying significant spatial information is similar in WT and J20 mice	211
Figure 4.43 WT and J20 mice show a higher proportion of decreasing cells conveying significant spatial information than the simulated data	212
Figure 4.44 The spatial information score of cells conveying significant spatial information are similar between WT and J20 mice.....	214
Figure 4.45 The firing rate of cells conveying significant spatial information show no changes between genotypes.....	216
Figure 4.46 The proportion of single class and conjunctive cells is similar in WT mice and J20 mice	218

Abbreviations

Aβ	Amyloid-β
AD	Alzheimer's disease
AIC	Akaike Information Criterion
aLEC	Anterior-lateral entorhinal cortex
AMG	Amygdala
AMPA	α-amino-3-hydroxyl-5-methyl-4-isoxazole-propionate
ApoE	Apolipoprotein E
APP	Amyloid precursor protein
5-HT3AR	5-Hydroxytryptamine (serotonin) Receptor 3 ^a
CSF	Cerebrospinal fluid
CTF	C-terminal fragment
DB	Diagonal band of Broca
DG	Dentate gyrus
EC	Entorhinal cortex
EGG	Electroencephalography
EM	Expectation-maximization
FFT	Fast Fourier transform
FIR	Finite impulse response
fMRI	Functional magnetic resonance imaging
FS	Fast-spiking
GABA	γ-aminobutyric acid
HD	Head direction

HFO	High Frequency Oscillations
iPSC	Induced pluripotent stem cell
LED	Light emitting diode
LEC	Lateral entorhinal cortex
LFP	Local field potential
LTD	Long term depression
LTP	Long term potentiation
LTS	Low threshold-spiking
MAPK	Mitogen-Activated Protein Kinases
MAPT	Microtubule-Associated Protein Tau
MCI	Mild Cognitive Impairment
MEC	Medial entorhinal cortex
MEG	Magnetoencephalography
mGlu	metabotropic glutamate
MI	Modulation index
MLE	Maximum likelihood estimation
mo	Months old
mPFC	Medial prefrontal cortex
MRI	Magnetic resonance imaging
MS	Medial septum
MSDB	Medial septum and diagonal band of Broca
MTL	Medial temporal lobe
MWM	Morris water maze
NMDA	N-methyl-D-aspartate
NAc	Nucleus accumbens

PAC	Phase amplitude coupling
PDGF	Platelet-derived growth factor
PET	Positron emission tomography
PFA	Paraformaldehyde
PING	Pyramidal-interneuron-gamma
pMEC	posterior-medial Entorhinal Cortex
PSEN1	Presenilin 1
PSEN2	Presenilin 2
PV	Parvalbumin
RSC	Retrosplenial cortex
SD	Standard deviation
SE	Standard error
SEM	Standard error on the mean
SI	Spatial information
SOM	Somatostatin
TMI	Theta modulation index
WT	Wild type

Chapter 1. Introduction

1.1. Alzheimer's disease

1.1.1. Dementia overview

Dementia affected an estimate of 885,000 people above the age of 65 in the UK in 2019 and is forecast to increase to around 1.6 million of people by 2040 (Wittenberg *et al.*, 2019). This projected increase in the number of people affected by dementia will likely have a very significant economic impact. The costs associated with dementia care in the UK were £34.7 billion in 2019 and it is expected that these numbers will almost triple by 2040, reaching £94.1 billion (Wittenberg *et al.*, 2019). The impact of dementia is not only economic. Dementia is a syndrome that progressively affects memory, thinking, problem solving, language and behaviour, ultimately leading to difficulties in daily functions (Galvin and Balasubramaniam, 2013; Mayo and Bordelon, 2014; Prince *et al.*, 2014; Gale, Acar and Daffner, 2018). Dementia is a clinical feature of different diseases rather than a disease itself. Some diseases that lead to dementia are Alzheimer's disease (AD), dementia with Lewy bodies, Parkinson's disease, cerebrovascular disease and frontotemporal lobar degeneration (Gale, Acar and Daffner, 2018; Alzheimer's Association, 2019). Amongst them, AD is the most common cause of dementia (Prince *et al.*, 2014; Alzheimer's Association, 2019). However, no currently available treatments can cure or stop its progression (Alzheimer's Association, 2019; Atri, 2019), which highlights the need for further research and for a better understanding of this disease.

1.1.2. Pathological features of Alzheimer's disease

AD was described by Alöis Alzheimer in 1907 (Stelzma, Schnitzlein and Murllagh, 1995). This disease is characterised by a progressive loss of synapses and neurons, which results in cortical atrophy (Serrano-Pozo *et al.*, 2011). Abnormal

protein aggregates are a common factor of different neurodegenerative diseases, known as proteinopathies (Bayer, 2015), of which some examples are AD, Parkinson's disease, dementia with Lewy bodies and Huntington disease. Two different protein aggregates are characteristic of AD: neurofibrillary tangles and amyloid plaques (Serrano-Pozo *et al.*, 2011).

Neurofibrillary tangles are composed of intracellular aggregates of misfolded hyperphosphorylated protein tau, which becomes extracellular when the neuron dies (Grundke-Iqbali *et al.*, 1986; Kosik, Joachim and Selkoe, 1986; Serrano-Pozo *et al.*, 2011). Tau is a microtubule-associated protein, mainly located in the neuronal axons, that stabilises microtubules, promotes their assembly and regulates axonal transport (Wang and Mandelkow, 2016). This protein is encoded by the microtubule-associated protein tau (*MAPT*) gene, located in chromosome 17 (Neve *et al.*, 1986). Protein tau can be found in 6 different isoforms in the human brain, which may contain 3 (3R) or 4 (4R) microtubule binding repeat sequences, and has 85 potential phosphorylation sites (Morris *et al.*, 2011; Wang and Mandelkow, 2016). Both 3R and 4R tau isoforms can be found in the neurofibrillary tangles (Jakes *et al.*, 1991).

On the other hand, amyloid plaques are the result of extracellular accumulations of amyloid- β (A β) peptides (Glenner and Wong, 1984; Serrano-Pozo *et al.*, 2011). A β peptides are produced through the sequential cleavage of the transmembrane amyloid precursor protein (APP) (Xu, 2009; Sun, Chen and Wang, 2015). APP is highly expressed in the brain and its function has been linked to normal brain development, the formation of synapses and neuronal migration (van der Kant and Goldstein, 2015). This protein can be processed through two different pathways (Fig. 1.1) (Xu, 2009; Sun, Chen and Wang, 2015). The non-amyloidogenic pathway involves the cleavage of APP first by a α -secretase, producing a soluble ectodomain (sAPP α), which is released into the extracellular space, and a C-terminal fragment (CTF α). Subsequently, CTF α is cleaved by a γ -secretase producing a short peptide, p3. The amyloidogenic pathway, on the other hand, involves the cleavage of APP first by a β -secretase which generates a soluble ectodomain (sAPP β) and a C-terminal fragment (CTF β), which remains in the membrane. Subsequently, CTF β is cleaved by a γ -secretase producing A β peptides between 38 and 43 amino acids long, which aggregate to form A β

oligomers. The aggregation of A β peptides results in the formation of soluble A β oligomers, which may further aggregate to form insoluble A β fibrils composing amyloid plaques (Serpell, 2000; Breydo and Uversky, 2015).

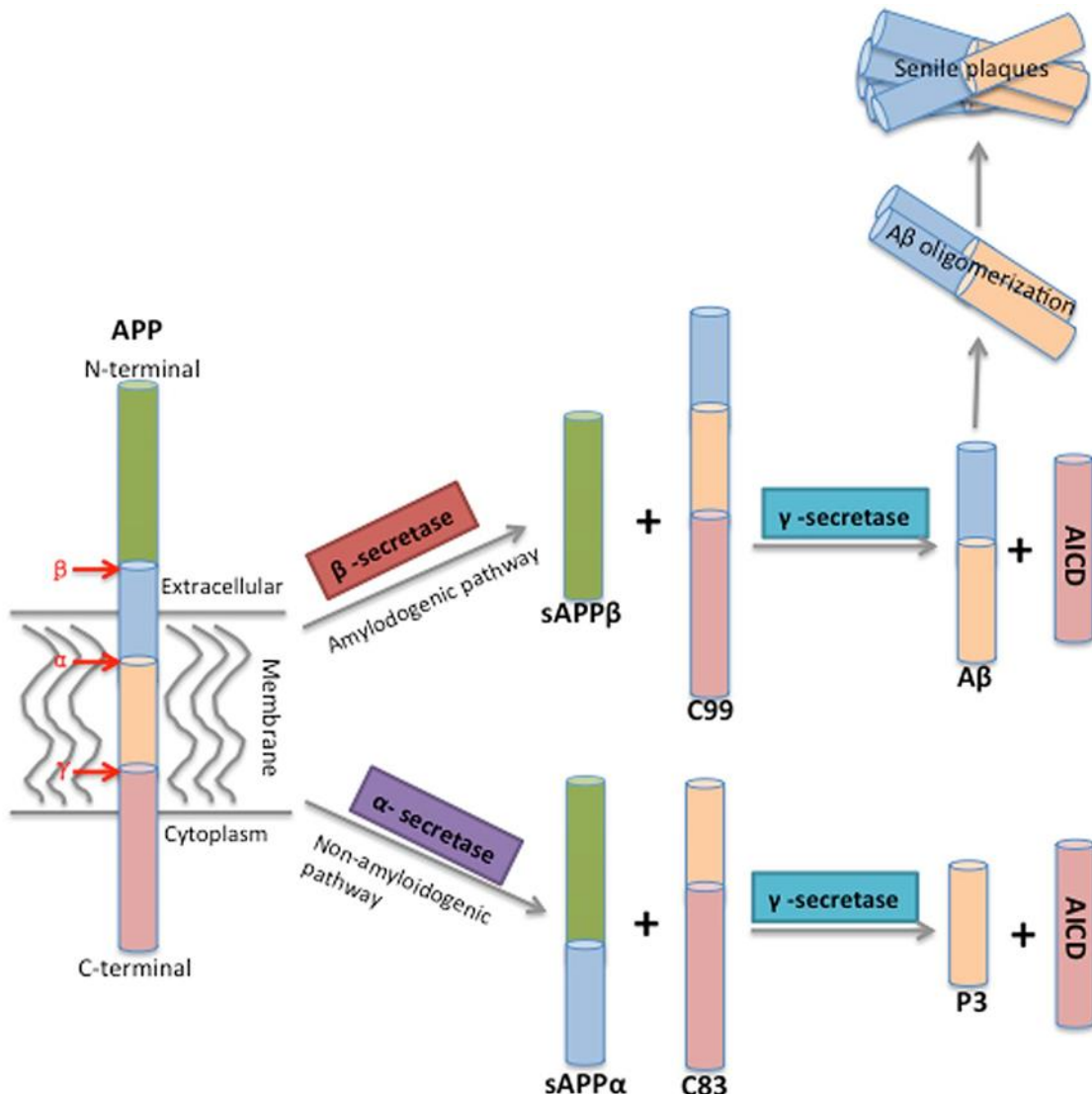


Figure 1.1 Amyloidogenic and non-amyloidogenic pathways for the processing of APP. APP can be processed through two different pathways: the amyloidogenic and the non-amyloidogenic pathways. The amyloidogenic (top) involves the subsequent cleavage of APP by a β -secretase and a γ -secretase, which produces a soluble ectodomain (sAPP β), a A β peptide of variable length (38 to 43 amino acids) and an APP intracellular domain (AICD). The non-amyloidogenic (bottom) involves the subsequent cleavage of APP by a α -secretase and a γ -secretase, which produces a soluble ectodomain (sAPP α), a short peptide (p3) and an AICD. Image reproduced from (Sun, Chen and Wang, 2015).

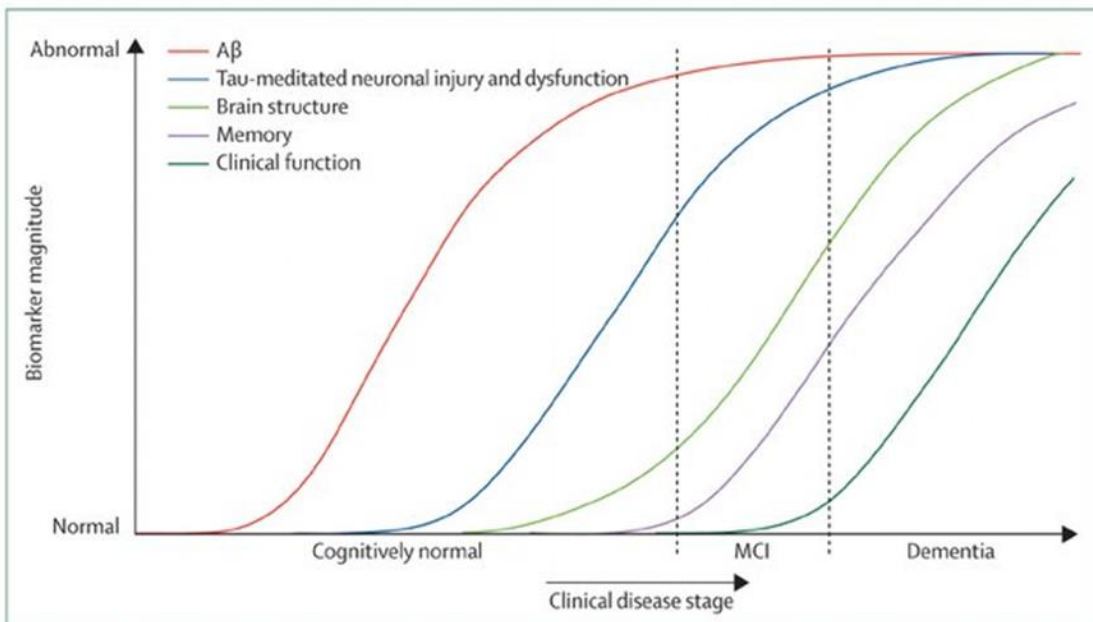
1.1.3. Alzheimer's disease progression

The progression of AD has been divided into three different stages. First, there is a preclinical stage (Dubois *et al.*, 2016) in which the disease is progressing, but clinical symptoms are not apparent. After this stage, the disease progresses to a mild cognitive impairment (MCI) stage, where there is evidence of cognitive decline but it is not severe enough to impact daily functions (Albert *et al.*, 2011). However, not all cases of MCI progress to AD and it has been reported that the annual conversion rate from MCI to AD is ~ 8% (Mitchell and Shiri-Feshki, 2009). Finally, a dementia stage is reached. In this stage, the disease progresses from mild to moderate and patients experience severe cognitive decline, which impairs their ability to function independently (Lyketsos *et al.*, 2006). At this moderate stage, patients need help to perform daily activities, which significantly affects the lives of their caregivers and their own life.

Biomarkers may allow for the monitoring of treatment effects in clinical trials and of the progression of the disease. Reductions in the concentration of A β ₁₋₄₂ in the cerebrospinal fluid (CSF) and the detection of amyloid plaques through amyloid positron emission tomography (PET) imaging are used as biomarkers of A β deposition (Jack *et al.*, 2010; Blennow *et al.*, 2015). On the other hand, increments in the concentration of tau in the CSF and structural magnetic resonance imaging (MRI) detected cerebral atrophy are used as biomarkers of neurodegeneration (Frisoni *et al.*, 2010; Jack *et al.*, 2010). Abnormalities in the A β deposition and neurodegeneration biomarkers begin on the preclinical stage of AD (Fig. 1.2A), with changes in the A β deposition biomarkers preceding those in the neurodegeneration biomarkers (Jack *et al.*, 2010). During the MCI stage progression (Fig. 1.2A), the magnitude of changes in the A β deposition and CSF tau biomarkers decrease, whereas the structural MRI biomarker shows an intermediate rate of change (Jack *et al.*, 2010). Finally, during the dementia stage progression (Fig. 1.2A), the rate of changes in the A β deposition biomarker is not different from zero and is considerably low in the CSF tau biomarker. On the other hand, the structural MRI biomarker shows a high rate of change (Jack *et al.*, 2010).

On the other hand, the neuropathology of AD has been staged in accordance with the spatial distribution of neurofibrillary tangles in the brain of people with AD (Braak and Braak, 1991). The different stages were classified into three different main stages with the following key features (Fig. 1.2B): In stages I and II, which comprise the transentorhinal stages, neurofibrillary tangles primarily develop in the transentorhinal region and there is a mild involvement of the hippocampal CA1 region. In stages III and IV, known as the limbic stages, the accumulation of neurofibrillary tangles increases in these brain regions and extend to the entorhinal cortex (EC), while the hippocampus involvement is mild to moderate. In stages V and VI, known as the isocortical stages, the accumulation of neurofibrillary tangles extends to the isocortex, which becomes highly affected.

A



B

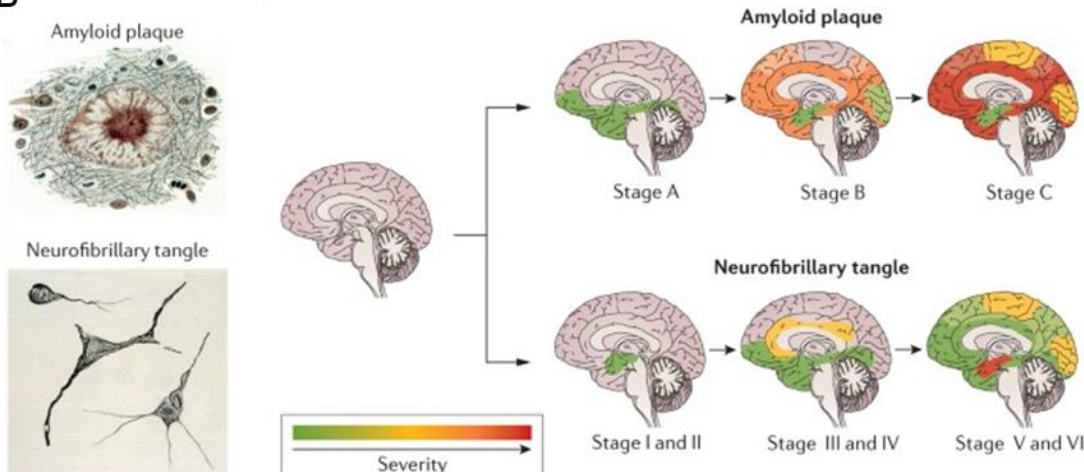


Figure 1.2 The progression of AD is divided in different stages. A) Changes in the magnitude of $\text{A}\beta$ deposition and neurodegeneration biomarkers in the preclinical (cognitively normal), mild cognitive impairment (MCI) and dementia stages. Image reproduced from (Jack *et al.*, 2010). **B)** Progression stages of amyloid and tau pathology as described in (Braak and Braak, 1997). Image reproduced from (Masters *et al.*, 2015).

1.1.4. Aetiology of Alzheimer's disease

AD can be classified into a sporadic and a familial form, with >99% of cases corresponding to the sporadic form (Van Cauwenbergh, Van Broeckhoven and Sleegers, 2016). Although sporadic AD has been associated with different risk factors, such as the ε4 allele of apolipoprotein E (ApoE) (Liu *et al.*, 2013), high systolic blood pressure or high serum cholesterol (Kivipelto *et al.*, 2001), its aetiology is still not well understood (Van Cauwenbergh, Van Broeckhoven and Sleegers, 2016). On the other hand, familial AD is triggered by autosomal dominant mutations in different genes, including the *APP* gene located in chromosome 21, the presenilin 1 gene (*PSEN1*) located in chromosome 14 and the presenilin 2 gene (*PSEN2*) located in chromosome 1 (Castellani, Rolston and Smith, 2010; Van Cauwenbergh, Van Broeckhoven and Sleegers, 2016; Lanoiselée *et al.*, 2017). Multiple pathogenic mutations have been reported in these genes, with most of them being found in the *PSEN1* gene (Van Cauwenbergh, Van Broeckhoven and Sleegers, 2016; Lanoiselée *et al.*, 2017). *PSEN1* and *PSEN2* genes encode for subunits of the γ-secretase complex (Xu, 2009; Lanoiselée *et al.*, 2017). It is believed that mutations in these three genes lead to the aggregation of Aβ peptides by either increasing the levels of Aβ peptides or producing aggregation-prone forms of Aβ peptides, such as Aβ₁₋₄₂ fragments (Van Cauwenbergh, Van Broeckhoven and Sleegers, 2016; Veugelen *et al.*, 2016; Lanoiselée *et al.*, 2017). On the other hand, mutations in the *MAPT* gene have not been linked to familial AD (Jankowsky and Zheng, 2017) but have been linked to some types of frontotemporal dementia, in which neuronal loss and the development of neurofibrillary tangles is also observed (Rademakers, Cruts and Van Broeckhoven, 2004; Seelaar *et al.*, 2008).

1.1.5. Amyloid cascade hypothesis

The amyloid cascade hypothesis (Hardy and Higgins, 1992) proposed Aβ peptides deposition as the cause of AD, and was hypothesised that this deposition triggers the formation of neurofibrillary tangles and cell loss. This idea

was initially supported by the discovery of different mutations in the APP gene of AD patients, the neuronal toxicity of A β peptides and its potential capacity to trigger hyperphosphorylation of protein tau (Hardy and Higgins, 1992). The results of some later studies further supported the amyloid cascade hypothesis, showing that mutations in the *PSEN1* and *PSEN2* genes lead to abnormal APP metabolism (Borchelt *et al.*, 1996; Citron *et al.*, 1997). In addition, mouse models expressing mutated forms of both human APP and tau appear to enhance the formation of neurofibrillary tangles whilst amyloid pathology remains the same, suggesting an effect of altered APP metabolism on tau (Lewis *et al.*, 2001). However, other studies raised concerns, with evidence showing that soluble forms of A β , but not insoluble ones, correlate well with AD severity (Lue *et al.*, 1999; McLean *et al.*, 1999). An update of this hypothesis was proposed based on new evidence supporting and opposing it, and was suggested that A β oligomers play a central role in AD (Hardy and Selkoe, 2002).

In the recent years, multiple studies have further supported a key role of A β oligomers in AD pathogenesis (Hayden and Teplow, 2013; Cline *et al.*, 2018; Fantini, Chahinian and Yahi, 2020). For instance, amyloid mouse models show cognitive deficits without plaque deposition (Meilandt *et al.*, 2009; Wright *et al.*, 2013). Furthermore, it has been shown that expressing a mutated form of the human APP in a rat model leads to the development of neurofibrillary tangles and neuronal loss, supporting the amyloid cascade hypothesis (Cohen *et al.*, 2013). There are multiple studies exploring the effects of A β oligomers. For example, it is thought that they play an important role in the disruption of synaptic plasticity, which is believed to underlie memory (Neves, Cooke and Bliss, 2008). It has been reported that low concentrations of A β oligomers induce long term potentiation (LTP), whereas high concentrations induce long term depression (LTD) (Puzzo *et al.*, 2008). Their role in synaptic plasticity disruption is supported by studies suggesting that A β oligomers inhibit LTP in hippocampal mouse and rat slices (Wang *et al.*, 2002, 2004; Li *et al.*, 2009, 2011, 2018).

Different action mechanisms leading to the inhibition of LTP have been proposed. For instance, this inhibition may be mediated by the increase of the extracellular levels of glutamate induced by A β oligomers (Li *et al.*, 2009, 2011), which has been suggested to lead to the desensitization of synaptic N-methyl-D-aspartate

(NMDA) receptors, internalization of NMDA and α-amino-3-hydroxyl-5-methyl-4-isoxazole-propionate (AMPA) receptors, and activation of extrasynaptic NMDA and metabotropic glutamate (mGlu) receptors (Mucke and Selkoe, 2012). This is supported by studies showing that the inhibition of extrasynaptic NMDA receptors (Li *et al.*, 2011) and mGlu receptor 5 (Wang *et al.*, 2004) prevents the inhibition of LTP induced by Aβ oligomers. In addition, it has been observed that the inhibition of LTP may be mediated through the activation of different kinases, such as p38 mitogen-activated protein kinases (MAPK) (Wang *et al.*, 2004; Li *et al.*, 2011). On the other hand, it has also been shown that intracellular Aβ oligomers, but not extracellular ones, inhibit LTP in hippocampal CA1 pyramidal cells, suggesting that the internalization of extracellular Aβ oligomers is necessary for these effects (Ripoli *et al.*, 2014). Aβ oligomers have also been shown to reduce the length of neurites and the number of branches in human induced pluripotent stem cell (iPSC)-derived neurons (Li *et al.*, 2018).

A cytotoxic role of Aβ oligomers has also been described. For example, exposing mouse brain slices to Aβ oligomers leads to neuronal death in the hippocampal formation, suggesting a selective vulnerability of these cells (Kim *et al.*, 2003). Aβ oligomers have been shown to trigger endoplasmic reticulum Ca²⁺ release, rising cytosolic levels and leading to cell apoptosis, which was suggested to be mediated by the activation of caspases (Resende *et al.*, 2008).

Together, these studies support that Aβ oligomers impair synaptic function and produce neuronal toxicity. Furthermore, it has been suggested that Aβ oligomers alter the normal synaptic excitatory/inhibitory (E/I) balance. For example, it has been reported that Aβ oligomers induce hyperexcitability in principal cells of the cingulate cortex, triggered by depressed inhibitory activity (Ren *et al.*, 2018). Ultimately these changes may lead to the disruption of neuronal networks and cognitive decline. Nonetheless, these only comprise some of the multiple effects that have been described for Aβ oligomers in literature, for which a more complete and detailed review can be found in Cline *et al.*, 2018.

1.1.6. Clinical trials

The cholinergic deficits observed in AD patients, such as disrupted cholinergic transmission and the loss of cholinergic neurons in the basal forebrain, led to a cholinergic hypothesis of memory dysfunction (Bartus *et al.*, 1982). This hypothesis suggested that cognitive decline was associated with decreased cholinergic activity, and the subsequent development of treatments aimed to enhance it with cholinesterase inhibitors (Francis *et al.*, 1999; Hampel *et al.*, 2019). Only 4 drugs have been approved for AD treatment: donepezil (1997), rivastigmine (2000), galantamine (2001) and memantine (2003) (Briggs, Kennelly and Neill, 2016; Mehta *et al.*, 2017). Donepezil, rivastigmine and galantamine are cholinesterase inhibitors, whereas memantine is a NMDA receptor antagonist (Briggs, Kennelly and Neill, 2016). These treatments are considered to act on the symptoms of AD but have been shown to induce relatively modest cognitive improvements (Raina *et al.*, 2008).

Current research is focused on the development of disease-modifying treatments targeting steps of the amyloid pathway, with the aim of delaying or stopping the progression of this disease (Galimberti and Scarpini, 2011). However, multiple promising therapies developed in the last years have failed in clinical trials, such as anti-amyloid monoclonal antibodies aiming to clear amyloid (Mehta *et al.*, 2017; Oxford, Stewart and Rohn, 2020). The high failure of new AD treatments has raised concerns. Some of the possible explanations suggested are that these treatments may be targeting the wrong A β forms or acting too late in the progression of the disease, alongside possible assessment inconsistencies within and between clinical trials (Mehta *et al.*, 2017; Oxford, Stewart and Rohn, 2020). However, it has also been suggested that targeting tau may be more effective than clearing A β forms, and different therapeutical approaches are focusing currently on tau (VandeVrede, Boxer and Polydoro, 2020).

1.1.7. Rodent models of Alzheimer's disease

Although the familial form of AD only encompasses a small percentage of the cases, the identification of autosomal dominant genetic mutations allowed for the development of experimental models. The first amyloid mouse model overexpressed a mutated form of the human *APP* gene carrying the Indiana mutation (Murrell *et al.*, 1991; Games *et al.*, 1995), which has been shown to increase the levels of A β (Citron *et al.*, 1992; Mucke *et al.*, 2000). Since then, multiple models have been developed through the inclusion of known familial AD mutations in the *APP* gene (Fig. 1.3) and the *PSEN1* and *PSEN2* genes (Drummond and Wisniewski, 2017; Götz, Bodea and Goedert, 2018). However, amyloid mouse models do not show all the pathological features observed in AD, such as the development of neurofibrillary tangles nor extensive cell loss, which are hallmarks of AD (Ashe and Zahs, 2010; Elder, Sosa and Gasper, 2010; Serrano-Pozo *et al.*, 2011; Drummond and Wisniewski, 2017). Although mouse models expressing mutant forms of the human *MAPT* gene develop neurofibrillary tangles and display high cell loss, these mutations are associated to frontotemporal dementia and may not be representative of AD (Jankowsky and Zheng, 2017). More recently, knockin mouse models have been developed in which the transgene is introduced in the endogenous gene locus. The advantage of these models is that they exhibit physiological expression levels within the right type of cells and brain regions (Drummond and Wisniewski, 2017).

At present, there are no available models that replicate all aspects of AD. However, rodent models can provide important insights into specific features of AD. Specifically, amyloid mouse models show some relevant AD pathology. For example, different studies have reported impairments in spatial memory (Reiserer *et al.*, 2007; Meilandt *et al.*, 2009; Harris *et al.*, 2010; Walker *et al.*, 2011; Wright *et al.*, 2013; Etter *et al.*, 2019) and object recognition memory (Harris *et al.*, 2010; Francis *et al.*, 2012) in different amyloid models. These cognitive deficits occur without amyloid plaque formation, and are likely linked to high levels of A β oligomers (Meilandt *et al.*, 2009; Tomiyama *et al.*, 2010; Wright *et al.*, 2013; Drummond and Wisniewski, 2017). Neuroinflammation, hippocampal neuronal loss and tau hyperphosphorylation have also been described in amyloid

mouse models (Tomiyama *et al.*, 2010; Wright *et al.*, 2013). Furthermore, synaptic plasticity impairments have also been reported in these models (Spires-jones and Knafo, 2012).

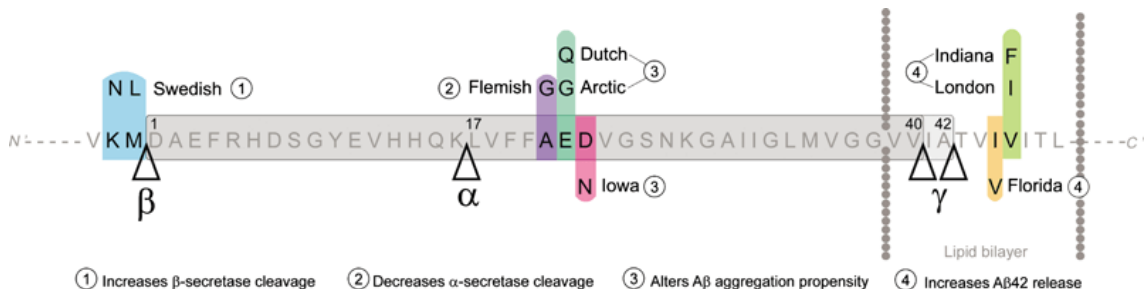


Figure 1.3 human APP mutations used in amyloid mouse models.
Image reproduced from (Philipson *et al.*, 2010).

1.1.8. The J20 mouse model of dementia

This mouse line expresses a mutant form of the human *APP* gene containing both the Swedish (Mullan *et al.*, 1992) and Indiana (Murrell *et al.*, 1991) mutations (Fig. 1.3). The Swedish mutation results in the substitution of lysine and methionine amino acids by leucine and asparagine in the APP (Mullan *et al.*, 1992). It has been shown that this mutation increases the levels of A β (Citron *et al.*, 1992; Mucke *et al.*, 2000). On the other hand, the Indiana mutation results in the substitution of valine by phenylalanine in the APP (Murrell *et al.*, 1991). This mutation leads to an increase of A β_{1-42} levels (Johnson-Wood *et al.*, 1997; Mucke *et al.*, 2000). This mouse line uses the platelet-derived growth factor β -chain (PDGF- β) promoter to express the transgene in neurons (Sasahara *et al.*, 1991).

J20 mice exhibit relevant AD related pathology and symptoms. This model shows high concentrations of A β_{1-42} peptides, with hippocampal and neocortical plaque formation being detected at 5-7 months of age and widespread deposition occurring at 8-10 months of age (Mucke *et al.*, 2000; Castanho *et al.*, 2020). However, synaptic and spatial memory deficits precede amyloid plaque deposition (Wright *et al.*, 2013), and are likely associated to the high levels of A β oligomers (Wright *et al.*, 2013; Mably *et al.*, 2015). For example, hippocampal synaptic deficits occur at an early stage in this mouse model, with 3-6 months old (mo) J20 mice exhibiting synaptic plasticity dysfunction in the CA1 region

(Saganich *et al.*, 2006). In addition, synaptic loss has also been described in the CA1 region of 3-4 mo J20 mice (Hong *et al.*, 2016). Furthermore, neuroinflammation and localised hippocampal progressive cell death has also been observed in 3-9 mo J20 mice (Wright *et al.*, 2013). On the other hand, several studies have reported spatial memory deficits in J20 mice (Harris *et al.*, 2010; Wright *et al.*, 2013; Etter *et al.*, 2019), which can be observed at 4 months of age (Wright *et al.*, 2013).

Taken together, the J20 mouse model shows AD related deficits which are relevant for the study of the spatial memory impairments present in AD, making it a good model to investigate the research questions formulated in this PhD thesis. In addition, the spatial progression of plaque formation in different brain regions provides two age points of interest for this project. 5-7 and 8-10 mo J20 mice, which model an early and an advanced stage of AD disease, respectively (Thal *et al.*, 2002).

1.1.9. Spatial memory impairments in AD

In addition to the characteristic memory deficits, a symptom often observed in AD is disorientation in both familiar and unfamiliar places. This likely results from spatial memory deficits (Henderson, Mack and Williams, 1989; Alzheimer's Association, 2019). Spatial disorientation results in people affected by AD as wandering and getting lost (Henderson, Mack and Williams, 1989), which can be a very distressing and dangerous experience for them and others (Hunt, Brown and Gilman, 2010; Rowe *et al.*, 2011).

Spatial memory is the process of encoding and retrieving different features of the environment that are necessary to recognise where we are and to navigate to a specific place (Brandner, 2009). The encoding of the spatial features of an object needs to occur in the context of a reference frame. In the brain, two different reference frames coexist together to create a spatial representation of our surroundings. In the egocentric reference frame objects are represented relative to the observer, whilst in the allocentric reference frame objects are represented relative to other external landmarks (Klatzky, 1998).

Path integration (Parron and Save, 2004; Gallistel, 2008) is an essential aspect of spatial navigation that relies on idiothetic cues, which are those generated by self-movement information. This process provides an estimate of the current position, relative to a reference location, by integrating information about the distance travelled and heading direction (Savelli and Knierim, 2019). However, in the absence of external spatial landmarks, which are used in allocentric navigation, the accuracy of path integration decreases due to error accumulation (Whishaw and Brooks, 1999; Parron and Save, 2004; Gallistel, 2008).

When we navigate to a specific place, it is often important to remember how to return to the starting location. This becomes possible as we obtain and store spatial information while we navigate through a given environment. The spatial information obtained through both path integration and allocentric navigation is believed to be integrated in order to form an allocentric representation of the environment (Ekstrom, Arnold and Iaria, 2014), which has also been referred to as cognitive map. The first idea about the existence of a cognitive map was proposed by (Tolman, 1948), and was further developed by (O'Keefe and Nadel, 1978). A cognitive map can be defined as an internal neuronal representation of the spatial layout and of where objects are in each environment, which is stored and can be retrieved while navigating.

Spatial navigation and memory deficits in AD have been linked to both path integration and allocentric navigation impairments (Monacelli *et al.*, 2003; Delpolyi *et al.*, 2007; Mokrisova *et al.*, 2016). Importantly, these deficits have also been observed in patients with MCI at risk of AD (Delpolyi *et al.*, 2007; Allison *et al.*, 2016; Mokrisova *et al.*, 2016; Howett *et al.*, 2019) and in preclinical AD cases and AD risk carriers (Allison *et al.*, 2016; Bierbrauer *et al.*, 2020), showing that spatial navigation and memory deficits are present at an early stage of the disease.

1.2. Entorhinal cortex

Several factors make the EC a highly relevant brain region for the study of the spatial memory deficits observed in AD. First, the EC is considered the major input and output area of the hippocampal formation, functioning as an interface between the neocortex and the hippocampal circuits (Canto, Wouterlood and Witter, 2008). In addition to this important function, the EC plays a fundamental role in spatial navigation and memory via a variety of functional cell subtypes (McNaughton *et al.*, 2006; Grieves and Jeffery, 2017). Furthermore, the EC is one of the first brain regions to be affected in AD (Braak and Braak, 1991; Moreno *et al.*, 2007; Khan *et al.*, 2014), with studies showing that its thickness correlates with the cognitive deficits seen in this disease (Burggren *et al.*, 2011; Velayudhan *et al.*, 2013; Mokrisova *et al.*, 2016; Howett *et al.*, 2019) and a high vulnerability of layer II cells (Gómez-Isla *et al.*, 1996; Scheff *et al.*, 2006). A more detailed overview about the EC, its role in spatial navigation and how it is affected in AD will be provided in the following subsections.

1.2.1. The role of the entorhinal cortex in spatial navigation and memory

The existence of a cognitive map of the environment (Tolman, 1948) was supported by the discovery of different functional cell subtypes, which are involved in the depiction of different spatial features of the environment and contribute to produce a changing representation of one's location (McNaughton *et al.*, 2006; Grieves and Jeffery, 2017). Several functional cell subtypes, involved in processing different spatial signals, have been found in the medial EC (MEC) of rodents. The first of these cells to be described were cells with grid periodicity (Fyhn *et al.*, 2004; Hafting *et al.*, 2005), which fire forming a hexagonal pattern that covers the entire environment. The discovery of cells with grid periodicity was followed by the identification of head direction sensitive cells (Sargolini *et al.*, 2006) which fire when the animal is facing a specific direction; border sensitive cells (Solstad *et al.*, 2008) that increase their activity in the borders of the environment; and more recently, speed sensitive cells (Kropff *et al.*, 2015) that

increase their firing rate as the animal is running faster. The combined activity of these functional cell subtypes is believed to underlie the neuronal basis of an allocentric representation of the environment (Moser and Moser, 2008; Giocomo, Moser and Moser, 2011). A more detailed description of these functional cell subtypes is provided in section 1.4.

Experimental evidence supports that the MEC plays an important role in path integration. For instance, smaller EC volumes correlate with larger path integration errors in humans (Howett *et al.*, 2019). In rodents, the estimation of distance travelled based on self-movement information is impaired when MEC lesions are performed (Jacob, Gordillo-Salas, *et al.*, 2017). Furthermore, rodents with MEC lesions show inaccurate returns to the refuge location in homing tasks (Parron and Save, 2004). In specific, both experimental (Gil *et al.*, 2018) and computational (Fuhs and Touretzky, 2006; Burgess, Barry and O'Keefe, 2007) evidence suggest that cells with grid periodicity play a key role in path integration by integrating heading and velocity information. Since cells with grid periodicity were discovered, different computational models have been developed to explain how their spatial firing patterns are produced. Two main classes of models can be distinguished (Giocomo, Moser and Moser, 2011; Bush and Schmidt-hieber, 2018): oscillatory interference models and continuous attractor network models. However, both types of model are not incompatible with each other and seem to represent different characteristics of the grid spatial firing patterns. To account for this, hybrid grid cell models have also been developed (Bush and Burgess, 2014; Bush and Schmidt-hieber, 2018).

On one hand, oscillatory interference models (Burgess, Barry and O'Keefe, 2007; Burgess, 2008; Giocomo, Moser and Moser, 2011; Bush and Schmidt-hieber, 2018) predict that grid spatial firing patterns arise from interference between different oscillatory inputs at the single cell level. This model is constructed with one oscillator that has a baseline frequency in the theta frequency band and several ones whose frequency vary above the baseline frequency with speed signal inputs, named velocity-controlled oscillators. Velocity controlled oscillators are sensitive to the speed input in specific preferred directions. Each velocity-controlled oscillator has a linear interference pattern with the animal's movement in the preferred direction. At least three linear interference patterns, differing by

multiples of 60°, seem to be necessary for the generation of hexagonal grid fields. The maximum cell firing is reached when all oscillators are in the same phase and the minimum cell firing when they are completely out of phase. This type of model predicts that cells with grid periodicity progressively fire at earlier phases of the extracellular theta wave, a process called phase precession, which has also been observed *in vivo* (Hafting *et al.*, 2008).

On the other hand, continuous attractor network models (Fuhs and Touretzky, 2006; Giocomo, Moser and Moser, 2011; Bush and Schmidt-hieber, 2018) predict that grid spatial firing patterns are the result of recurrent local interactions within a network of cells. This network of cells is distributed in a topographical sheet of two dimensions which is characterised a specific synaptic weight profile, with the synaptic strength between cells decreasing with higher distances between their firing fields. The cells located in the edges of the sheet connect to cells located in the opposite edges, generating a torus shape. This results in periodic activity bumps which move based on heading and velocity information. Conjunctive cells with grid periodicity that integrate heading and velocity information, which have been found experimentally within the MEC (Sargolini *et al.*, 2006), are predicted by the model to provide these inputs to the network.

Both computational and experimental evidence situate the MEC as a path integrator. Complementing its role in spatial navigation, both human and rodent studies have highlighted the importance of the EC in spatial memory. Several human studies have shown that the activity of the EC is increased during memory encoding and retrieval (Kirwan and Stark, 2004; Bellgowan *et al.*, 2006; Vanssay-maigne *et al.*, 2011; Okada, Vilberg and Rugg, 2012). Although in disagreement, the role of the EC in memory is also apparent in studies which show that the electrical stimulation of the EC results in memory improvements (Suthana *et al.*, 2012; Titiz *et al.*, 2017) or impairments (Jacobs *et al.*, 2016; Goyal *et al.*, 2018) in epilepsy patients. Further supporting the role of the EC in memory encoding and retrieval, a recent study has shown that the activity of EC neuronal populations code object representations during learning, and the same populations are re-engaged during the memory retrieval of these representations (Staresina *et al.*, 2019). Furthermore, another study has shown the existence of “memory-trace” cells in the human EC, whose spatial firing pattern reflects the

memory retrieval of an object location (Qasim *et al.*, 2019). On the other hand, MEC lesions in rodents result in profound learning deficits and memory retrieval impairments in the Morris water maze (MWM) task (Steffenach *et al.*, 2005; Hales *et al.*, 2014, 2018), suggesting impairments in allothetic navigation and memory.

Together, these studies highlight the central role that the EC plays in spatial navigation and memory.

1.2.2. Entorhinal cortex anatomy

The human EC (Brodmann area 28) is part of the hippocampal formation (Fig. 1.4A), which is situated in the medial temporal lobe (MTL) and also includes the dentate gyrus, hippocampus, parasubiculum, presubiculum and subiculum (Insausti and Amaral, 2012). Some studies have proposed that the human EC can be functionally divided into a posterior-medial (pMEC) and an anterior-lateral (aLEC) region (Maass *et al.*, 2015; Navarro Schroder *et al.*, 2015), homologous to the medial EC (MEC) and lateral EC (LEC) subdivisions observed in rodents (Fig. 1.4B) (Knierim *et al.*, 2014). Functionally, the MEC appears to be involved in the encoding of the allocentric representation of the environment, whereas the LEC seems to encode information about the items contained in that environment (Knierim *et al.*, 2014).

The EC can be divided into six different layers (Fig. 1.4C) (Tahvildari and Alonso, 2005; Canto, Wouterlood and Witter, 2008; Insausti and Amaral, 2012; Witter *et al.*, 2017): Layer I is a plexiform layer relatively free of cells and rich in transversely oriented fibres. Layer II is composed mainly of pyramidal cells and stellate or fan cells, in the MEC and the LEC respectively. Layer III is a wider layer which contains mostly pyramidal cells. Layer IV, also referred to as lamina dissecans, is a sparse cell layer. Layer V contains large pyramidal cells. Finally, layer VI is a diffuse layer showing a diminishing gradient of cell density.

Principal cells in layer II of both the MEC and the LEC express calbindin or reelin, with reelin being expressed by stellate and fan cells, and calbindin being expressed in pyramidal cells (Ray *et al.*, 2014; Kitamura *et al.*, 2015; Armstrong *et al.*, 2016; Leitner *et al.*, 2016). In the MEC, calbindin positive pyramidal cells,

also called ECII island (ECIIi) cells, appear to be grouped forming patches (Fig. 1.4C), which show a hexagonal organization with their dendrites confined to them (Ray *et al.*, 2014). On the other hand, MEC reelin positive stellate cells, also named ECII ocean (ECIIO) cells, are uniformly distributed and have larger dendrites (Ray *et al.*, 2014). In the LEC, reelin positive fan and calbindin positive pyramidal cells cluster in two different sublayers of layer II (Leitner *et al.*, 2016).

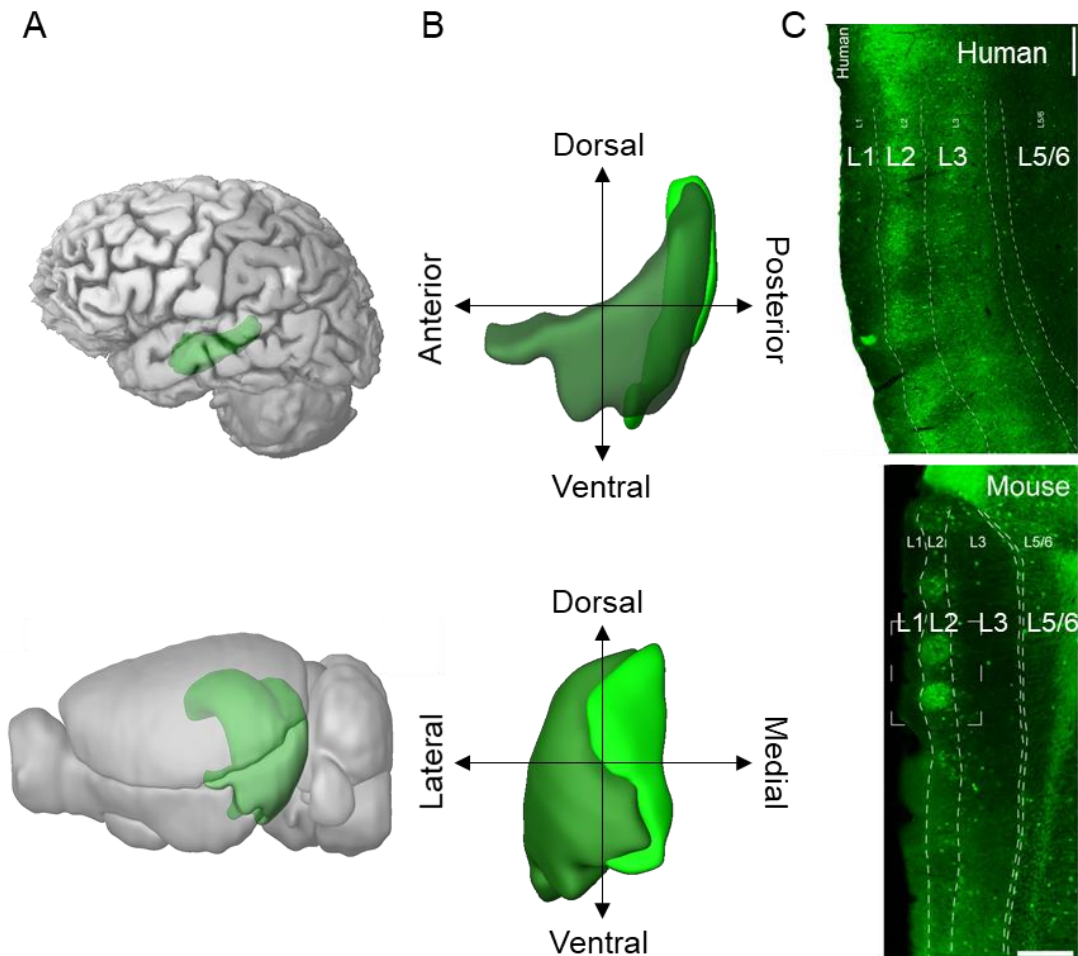


Figure 1.4 Anatomy of the MEC in the rodent and human brain. A) Hippocampal formation (green) in the human (top) and mouse brain (bottom). Images adapted from the Allen human (top) and mouse (bottom) brain atlases. **B)** Lateral (top) and posterior (bottom) view of the mouse MEC (dark green) and LEC (light green). Images adapted from the Allen mouse brain atlas. **C)** Coronal section of a human caudal EC (top) and of a sagittal section of a mouse MEC (bottom) stained for calbindin positive pyramidal cells, which are found forming patches. Images taken from (Naumann *et al.*, 2016).

1.2.3. Entorhinal cortex intrinsic connectivity

In the layer II of the EC, the excitation of reelin positive cells results in an inhibitory response in a large percentage of reelin positive cells mediated through interneurons, however excitatory connections between reelin positive cells or with calbindin positive cells are very sparse (Couey *et al.*, 2013; Pastoll *et al.*, 2013; Nilssen *et al.*, 2018).

All types of EC principal cells are targeted by EC γ -aminobutyric acid (GABA) releasing interneurons, which can be separated into three main different types: parvalbumin expressing (PV), also known as fast-spiking (FS) interneurons; 5-hydroxytryptamine (serotonin) receptor 3A expressing (5-HT3AR) interneurons; and somatostatin interneurons (SOM) also known as low threshold-spiking (LTS) interneurons (Lee *et al.*, 2010; Armstrong and Soltesz, 2012; Armstrong *et al.*, 2016; Fuchs *et al.*, 2016; Leitner *et al.*, 2016; Nilssen *et al.*, 2018).

1.2.4. Entorhinal cortex extrinsic connectivity

The EC receives spatial and non-spatial information through multiple cortical and subcortical structures (Fig. 1.5) (Insausti and Amaral, 2012). However, this section will only highlight some key examples. The EC receives spatial and item related information of a given environment through the postrhinal cortex, homologous to the parahippocampal cortex in humans (Furtak, Ahmed and Burwell, 2012), and perirhinal cortex, respectively (Kravitz *et al.*, 2011, 2013; Knierim *et al.*, 2014; Doan *et al.*, 2019). The LEC appears to receive spatial and non-spatial information from both the postrhinal and perirhinal cortices (Deshmukh, Johnson and Knierim, 2012; Doan *et al.*, 2019), whereas the MEC seems to only receive spatial information from the postrhinal cortex (Koganezawa *et al.*, 2015; Doan *et al.*, 2019). In addition, the MEC receives information about heading direction from the dorsal part of the presubiculum, which originates subcortically in the dorsal tegmental nucleus (Taube, 2007; Winter, Clark and Taube, 2015). Recently, it has been suggested that speed signals originate in the pedunculopontine tegmental nucleus of the mesencephalic locomotor region, and

are received by the MEC through the horizontal limb of the diagonal band of Broca (DB) (Carvalho *et al.*, 2020).

The EC serves as the major source of input to the dentate gyrus and the hippocampus, and at the same time is the major output area, functioning as an interface between the neocortex and the hippocampus. EC reelin positive cells in layer II project through the perforant path (Fig. 1.5), also referred to as the first node of the trisynaptic pathway, to the stratum moleculare of the dentate gyrus which in turn projects to the stratum lacunosum-moleculare of the CA3 region of the hippocampus (Amaral and Witter, 1989; Groen, 2001; Insausti and Amaral, 2012; Ray *et al.*, 2014; Leitner *et al.*, 2016). CA3 pyramidal neurons excite CA1 pyramidal neurons, completing the path (Ishizuka, Weber and Amaral, 1990). The perforant path does not only contain EC excitatory projections but also inhibitory projections (Germroth, Schwerdtfeger and Buhl, 1989; Melzer *et al.*, 2012).

MEC calbindin positive cells in layer II, on the other hand, participate in a feedforward inhibitory circuit in which their projections mainly synapse onto stratum lacunosum interneurons of the CA1 region and rarely onto CA1 pyramidal cells (Kitamura *et al.*, 2014). At the same time, pyramidal cells in layer III of the EC project directly via the temporoammonic pathway (Fig. 1.5), also called the monosynaptic path, to pyramidal cells in the stratum moleculare of the CA1 region and to the subiculum (Amaral and Witter, 1989; Lavenex and Amaral, 2000; Groen, 2001; Fyhn *et al.*, 2004; Kitamura *et al.*, 2014; Ray *et al.*, 2014).

The EC also receives projections back from the CA1 region and the subiculum, which send projections to the deep layers of the EC (Fig. 1.5) (Kloosterman, Witter and Van Haeften, 2003; Canto, Wouterlood and Witter, 2008). Furthermore, long-range projections onto interneurons in layers II and III of the EC from GABAergic, cells located in the stratum lacunosum-moleculare/radiatum of the hippocampus and the stratum moleculare of the dentate gyrus, have also been observed (Melzer *et al.*, 2012).

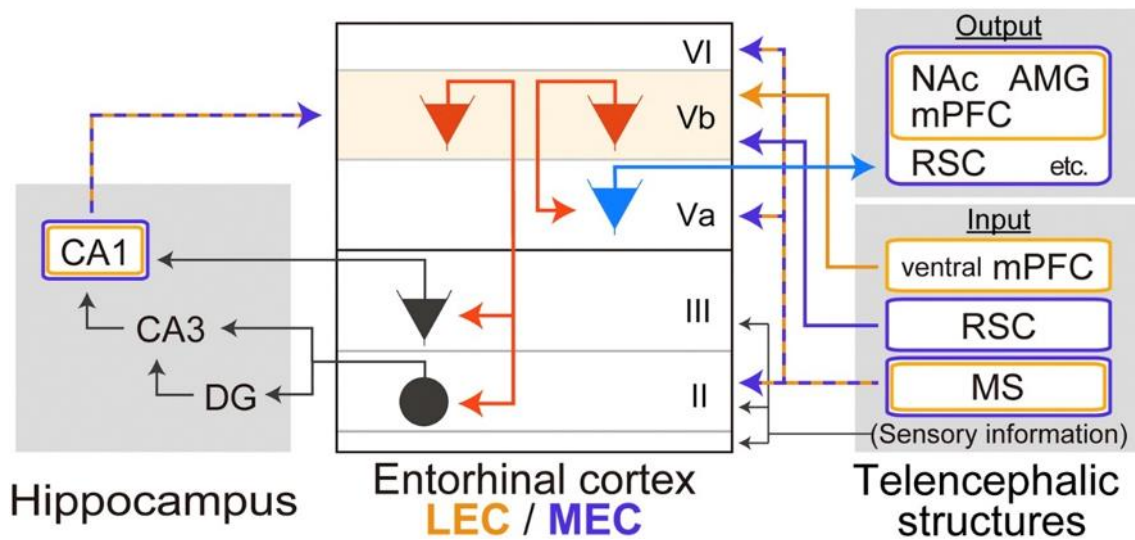


Figure 1.5 Summary of EC connectivity. Diagram showing main inputs and outputs of the LEC and the MEC. DG = dentate gyrus; NAc = nucleus accumbens; AMG = amygdala; mPFC = medial prefrontal cortex; RSC = retrosplenial cortex; MS = medial septum. Adapted from (Ohara *et al.*, 2018).

1.2.5. Entorhinal cortex in Alzheimer's disease

The EC is one of the first areas affected in AD (Braak and Braak, 1991; Moreno *et al.*, 2007; Khan *et al.*, 2014). Cortical thinning has been described in different brain regions, including the EC, in people with MCI at risk of AD and people affected by AD (Lerch *et al.*, 2005; Stoub *et al.*, 2006; Krumm *et al.*, 2016). Furthermore, several studies have shown that the thickness of the EC correlates with the severity of the cognitive deficits observed in MCI and AD cases (Burggren *et al.*, 2011; Velayudhan *et al.*, 2013; Mokrisova *et al.*, 2016; Howett *et al.*, 2019).

Literature points towards a higher vulnerability of cells in layer II of the EC in AD, which project through the perforant path to the dentate gyrus and, ultimately, the hippocampus (Stranahan and Mattson, 2010). A large reduction of layer II cells has been reported in the EC of very mild and severe cases of AD (Gómez-Isla *et al.*, 1996). Furthermore, a decrease in the number of synaptic contacts in the molecular layer of the dentate gyrus, where EC layer II cells synapse, has also been observed (Scheff *et al.*, 2006). Reelin positive cells, in specific, express intracellular A β peptides at very early and late stages of AD in humans and rats,

which may lead to a disruption in the reelin transport, induced by the intracellular A β peptides, and potentially result in synaptic plasticity dysfunction (Kobro-Flatmoen, Nagelhus and Witter, 2016).

1.3. Entorhinal cortex neuronal oscillations

1.3.1. Neuronal oscillations

All active cellular processes generating electrical currents contribute to changes in voltage, which can be measured extracellularly at a given site in the brain. Specifically, the main contributor to these extracellular currents is synaptic activity (Buzsáki, 2006; Buzsáki, Anastassiou and Koch, 2012). Neuronal oscillations emerge from the synchronized and rhythmic patterns of electrical activity of neuronal ensembles (Buzsáki, 2006), thus providing information about the behaviour of these neuronal populations. The synchronous rhythmic activity of neuronal ensembles seems necessary for different cognitive processes such as memory (Varela *et al.*, 2001; Ward, 2003). The synchronization of neuronal oscillations, across different brain regions, has been linked to the transient synchronization of neuronal ensembles, which allows for information processing, transfer and storage (Engel, Fries and Singer, 2001; Buzsáki and Draguhn, 2004).

Electrical signals can be measured through non-invasive techniques such as electroencephalography (EEG) or magnetoencephalography (MEG), measured on the scalp, and invasive techniques such as the local field potential (LFP), which can be measured by implanting an extracellular electrode in a given brain region (Buzsáki, 2006). Since Hans Berger first observed and described neuronal oscillations in the human EEG (Millett, 2001), different oscillatory bands associated with different cognitive functions have been established (Kane *et al.*, 2017): delta (δ , 0.1 – 4 Hz), theta (θ , 4 – 8 Hz), alpha (α , 8 – 13 Hz), beta (β , 14 – 30 Hz), gamma (γ , 30 – 80 Hz) and high frequency oscillations (HFOs), which include ripples (80 – 250 Hz) and fast ripples (250 – 500 Hz). Multiple functions have been associated with these frequency bands. For instance, delta

oscillations are prominent during sleep (Bernardi *et al.*, 2019), alpha oscillations have been linked to attention (Foxe and Snyder, 2011; Klimesch, 2012) and beta oscillations have been linked to processes such as sensory processing, working memory and decision making (Spitzer and Haegens, 2017). It has been shown that HFOs play an important function in memory consolidation (Girardeau *et al.*, 2009). On the other hand, both theta and gamma oscillations have been associated to memory processing (Ward, 2003). This PhD thesis will particularly focus on the roles of theta and gamma frequency oscillations in memory, which will be described in more detail in the following sections.

1.3.2. Theta oscillations

Theta oscillations are the most prominent rhythm in the MEC of rodents (Mitchell and Ranck, 1980). The limits of the theta band appears to not be consistently defined in literature, with definitions such as 4 – 10 Hz (Jacobs, 2014), 5 – 10 Hz (Buzsáki, 2006; Mizuseki *et al.*, 2009) and 6 – 12 Hz (O’Keefe, 2006; Wells *et al.*, 2013). However, it is agreed that these limits in rodents are wider than in humans, encompassing both theta and alpha bands (Buzsáki, 2006). Cognitive processes need the coordination of different brain regions involved in the processing of related information. The synchronization of theta oscillations between brain regions may temporally segregate and link related neuronal ensembles to allow for the transfer of information between them (Salinas and Sejnowski, 2001; Buzsáki, 2002).

The generation of the theta rhythm is likely to require the involvement of different mechanisms. The medial septum (MS) appears to act as a pacemaker of theta oscillations in the hippocampal formation. Lesions performed in the MS, or its inactivation, disrupt the theta rhythm in both the MEC and the hippocampus (Mitchell *et al.*, 1982; Bland and Bland, 1986; Koenig *et al.*, 2011). The MS sends cholinergic, GABAergic, and glutamatergic projections to these brain regions (Manns, Mainville and Jones, 2001; Colom *et al.*, 2005; Justus *et al.*, 2017). Specifically, MS GABAergic projections seem to be necessary to pace theta oscillations (Hangya *et al.*, 2009; Gonzalez-Sulser *et al.*, 2014; Dannenberg *et al.*, 2019), with interneurons being their main target in the MEC and the

hippocampus (Gonzalez-Sulser *et al.*, 2014; Unal *et al.*, 2015; Justus *et al.*, 2017). On the other hand, stellate cells in layer II of the MEC exhibit intrinsic theta resonance (Alonso and Llinás, 1989; Quilichini, Sirota and Buzsáki, 2010), which may help to generate and maintain theta oscillations.

In awake rodents, theta oscillations emerge from two different behaviours, one related to the animal's movement (7-12 Hz) and another related to alert immobility (4-7 Hz), which are also referred to as type 1 and 2 theta, respectively (Kramis, Vanderwolf and Bland, 1975). Both types of hippocampal theta are present during movement (Yoder and Pang, 2005), but show different sensitivity to atropine, a muscarinic receptor antagonist. Movement-related theta oscillations are resistant to atropine, whereas theta related to alert immobility is abolished by it (Kramis, Vanderwolf and Bland, 1975). In addition, only theta related to alert immobility is present during urethane anaesthesia (Kramis, Vanderwolf and Bland, 1975). MS and DB (MSDB) cholinergic and GABAergic inputs, together with glutamatergic EC inputs, contribute to generate hippocampal movement-related theta oscillations (Buzsáki, 2002; Yoder and Pang, 2005; Gu *et al.*, 2017). On the other hand, either MSDB GABAergic or cholinergic lesions abolish theta related to alert immobility during urethane anaesthesia, suggesting that both MSDB GABAergic and cholinergic inputs are necessary for their generation (Yoder and Pang, 2005). Together, these studies suggest that there is potential for both types of theta to be affected by changes in MSDB cholinergic or GABAergic activity. However, these effects may be larger in theta related to alert immobility. In addition, EC dysfunction is likely to affect movement-related theta oscillations (Buzsáki, 2002; Yoder and Pang, 2005; Gu *et al.*, 2017).

Self-movement information is necessary for the generation of movement-related theta oscillations, as they are abolished in rats during passive transport (Winter *et al.*, 2015). Furthermore, theta oscillations related to movement correlate with the running speed of the animal. The increase in power and frequency of theta oscillations with running speed has been well studied in different areas of the brain such as the hippocampus and the MEC (Hinman *et al.*, 2011; Wells *et al.*, 2013; Chen *et al.*, 2016). The majority of MEC cells are modulated by theta oscillations and the strength of this modulation increases with running speed, which is likely linked to the modulation of theta oscillations by running speed

(Hinman *et al.*, 2016). This modulation by running speed could imply that theta oscillations convey a speed signal or could reflect changes in the processing of sensory inputs at faster running speeds (Grieves and Jeffery, 2017; Dannenberg *et al.*, 2019). Interestingly, the slope resulting from this relationship can be affected by different factors, such as the familiarity of the environment in which the animal is introduced or the absence of visual inputs (Wells *et al.*, 2013; Chen *et al.*, 2016).

1.3.3. Gamma oscillations

Gamma oscillations can be subdivided into two different frequency sub-bands, which have been observed in the CA1 region of the hippocampus: a low (~30 – 50 Hz) and a high (~50 – 100 Hz) gamma band (Colgin, Denninger, Fyhn, Hafting, Bonnevie, Jensen, M. B. Moser, *et al.*, 2009; Kemere *et al.*, 2013). Experimental evidence supports that FS interneurons generate gamma oscillations (Fuchs *et al.*, 2007; Cardin *et al.*, 2009; Sohal *et al.*, 2009). Specifically in the MEC, stimulation at theta frequency of both principal cells and FS interneurons generates nested high gamma oscillations (~60 – 100 Hz) (Pastoll *et al.*, 2013). Gamma oscillations can either be generated only by mutually connected interneurons or by reciprocally connected principal cells and interneurons (Buzsáki and Wang, 2012). In the MEC, the excitatory inputs of principal cells onto FS interneurons appears to be necessary for the generation of nested gamma oscillations (Pastoll *et al.*, 2013), which is consistent with a pyramidal-interneuron-gamma model (PING) for gamma generation. In the PING model, cyclic interspersed spikes from inhibitory and principal cells is observed. Principal cells excite inhibitory cells, triggering synchronous discharges of the inhibitory cells with a subsequent brief period of inhibitory inactivity, which allows for spiking from principal cells (Buzsáki and Wang, 2012; Cannon *et al.*, 2014). Principal cells may spike on the majority of the gamma cycles or only sometimes, which describes a strong or a weak PING, respectively (Cannon *et al.*, 2014).

Gamma oscillations may temporally bind neuronal ensembles involved in the processing of related information (Buzsáki and Wang, 2012). The MEC and CA1

region are more coherent at high gamma, whereas the CA3 and CA1 regions are more synchronised at low gamma (Colgin, Denninger, Fyhn, Hafting, Bonnevie, Jensen, M. B. Moser, *et al.*, 2009; Kemere *et al.*, 2013), suggesting that high gamma oscillations mediate the transfer of information from the MEC to the CA1 region. High gamma oscillations increase with the running speed of the animal in both the hippocampus and the MEC (Chen *et al.*, 2011; Ahmed, 2012; Kemere *et al.*, 2013). It has been observed that the slope of high gamma power vs running speed decreases as the environment becomes more familiar in the hippocampus and MEC (Kemere *et al.*, 2013), suggesting an effect of the novelty of the environment.

1.3.4. Cross-frequency coupling

Phase amplitude coupling (PAC) is a well-studied type of cross-frequency coupling, which occurs when the phase of a slower rhythm modulates the amplitude of a faster rhythm (Fig. 1.6) (Canolty and Knight, 2010). Specifically, PAC between theta and gamma oscillations has been observed in several brain areas, including the MEC and the hippocampus (Chen *et al.*, 2011; Newman *et al.*, 2013; Pastoll *et al.*, 2013). The theta rhythm may coordinate the gamma rhythm across different brain regions, by providing a temporal window of activity which could link related neuronal ensembles and facilitate information transfer between them (Buzsáki, 2006; Jensen and Colgin, 2007; Sirota *et al.*, 2008).

Theta-gamma PAC has been previously linked to working memory. It has been hypothesised that in each gamma cycle a single memory item is represented by a neuronal ensemble, limiting the capacity of working memory by the number of gamma cycles within a single theta cycle (Lisman and Idiart, 1995). This hypothesis has been supported by experimental evidence (Axmacher *et al.*, 2010). Other studies have also linked theta-gamma PAC to related cognitive functions, such as memory retrieval (Mormann *et al.*, 2005; Tort *et al.*, 2009) and decision-making (Tort *et al.*, 2008), suggesting the involvement of theta-gamma PAC in memory processing.

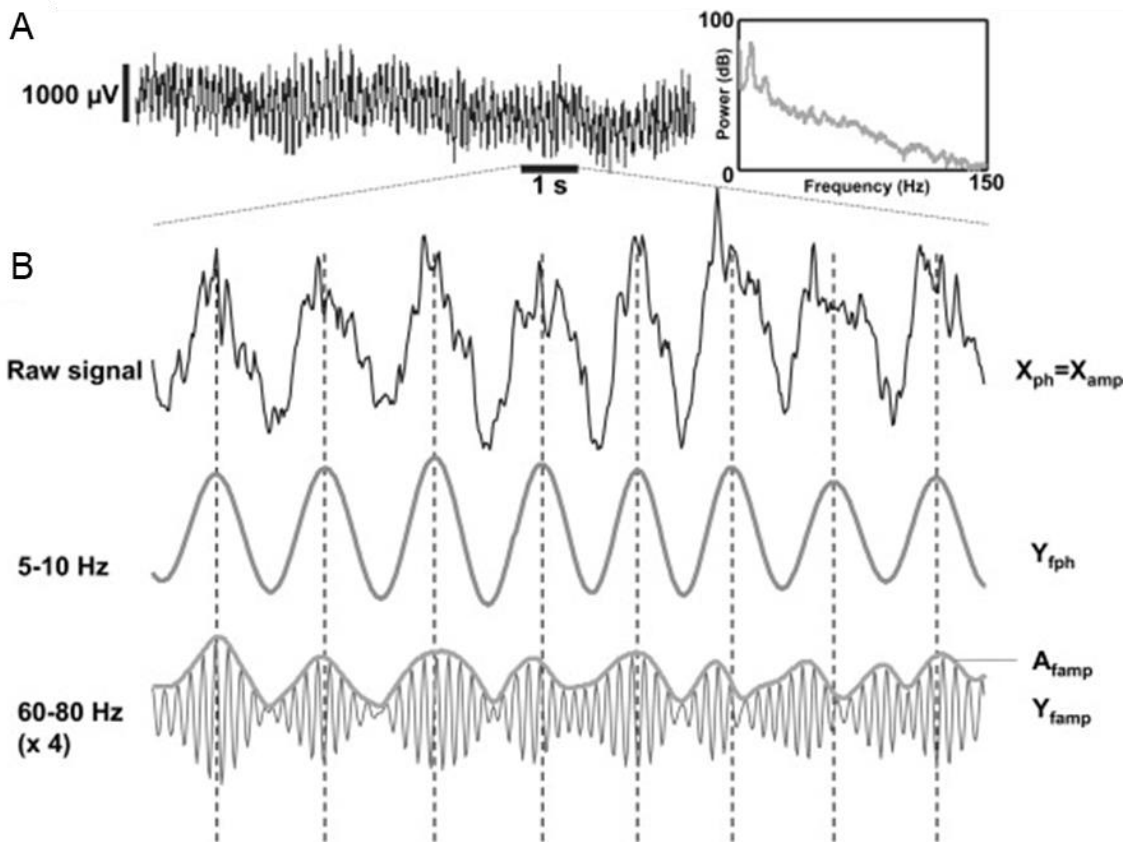


Figure 1.6 PAC between theta and gamma oscillations. **A)** Raw LFP signal. **B)** 1 second long raw LFP signal (top), same LFP signal filtered at theta band (middle) and same LFP signal filtered at gamma band with amplitude envelope (bottom). Figure reproduced from (Onslow, Bogacz and Jones, 2011).

1.3.5. Role of neuronal oscillations in novel and familiar contexts

Theta oscillations have been associated with spatial navigation and memory. Although some studies suggest that theta oscillations are slower in humans than in rodents (Jacobs, 2014), recent studies show that humans also exhibit high theta frequency oscillations (~8 Hz) during navigation (Bohbot *et al.*, 2017; Bush *et al.*, 2017; M. Aghajan *et al.*, 2017; Goyal *et al.*, 2020). The power of low and high theta oscillations has been reported to increase during the initiation of movement (Kaplan *et al.*, 2012; Bush *et al.*, 2017). In addition, it has been shown that the frequency and power of high theta oscillations correlate with running speed in the MTL of humans (M. Aghajan *et al.*, 2017; Goyal *et al.*, 2020), as it has been described in rodents (Hinman *et al.*, 2011; Wells *et al.*, 2013; Chen *et al.*, 2016).

Increases in low and high theta power have also been linked to the planning of longer paths during navigation in humans, a process that likely involves the retrieval of more spatial information than planning shorter paths (Bush *et al.*, 2017). Furthermore, the increment of theta power with the initiation of movement is larger in familiar contexts than in novel ones in humans (Kaplan *et al.*, 2012). In rodents, the slope of the frequency of theta oscillations vs running speed has been observed to increase as animals get familiar with a novel context in the hippocampus and the MEC (Newman *et al.*, 2013; Wells *et al.*, 2013), linking greater gradients to familiar contexts. Overall, theta oscillations appear to play a role in spatial memory processing.

Gamma oscillations may also support memory processing by facilitating both the encoding and retrieval of information. For instance, the slope of high gamma power vs running speed is increased during novelty, both in the hippocampus and the MEC in rodents (Kemere *et al.*, 2013), linking greater gradients to novel environments. Similarly, hippocampal high gamma power is increased during the exploration of a novel object in a new location (Zheng *et al.*, 2016). However, the power of high gamma oscillations also increases while performing spatial working memory tasks in the MEC (Yamamoto *et al.*, 2014). On the other hand, the strength of theta-low gamma PAC positively correlates with learning in the hippocampus, associating it to memory recall (Tort *et al.*, 2009). However, low gamma power also increases during the exploration of novel objects in the hippocampus, linking low gamma also to memory encoding (Trimper, Stefanescu and Manns, 2014). In addition, the modulation of low gamma power by running speed decreases with familiarity in the hippocampus (Kemere *et al.*, 2013).

It has been proposed that the MS cholinergic projections to the EC and the hippocampus may modulate theta frequency oscillations in response to novelty (Barry, Heys and Hasselmo, 2012). In support of this, increases in cholinergic activity have been related to the exploration of novel environments (Giovannini *et al.*, 2001). Furthermore, eliminating cholinergic neurons in the MSDB results in spatial memory deficits in rodents (Okada *et al.*, 2015). Cholinergic activation of stellate cells in the MEC alters the theta resonance properties of these cells, reducing its resonance frequency and strength (Heys, Giocomo and Hasselmo, 2010). In the MEC, cholinergic blockade during the familiarization process

appears to impair the encoding of new information, which was reflected in the lack of a significant increase in the theta frequency slope between the baseline trial and the recovery trial after the blockade (Newman *et al.*, 2013). However, the selective modulation of MS cholinergic activity while rodents explored familiar contexts only decreased the overall theta frequency without affecting its modulation by running speed in the MEC (Carpenter, Burgess and Barry, 2017), which was linked to behaviours related to novelty or anxiety (Wells *et al.*, 2013). Furthermore, the cholinergic inactivation of the MSDB had no effect on theta frequency oscillations in the MEC during the exploration of a familiar environment (Dannenberg *et al.*, 2019). Cholinergic activation also appears to modulate the power of hippocampal gamma oscillations (Betterton *et al.*, 2017), increasing it at lower doses and decreasing at higher ones. Furthermore, cholinergic blockade reduces overall high gamma power without affecting its modulation by running speed in the MEC (Newman *et al.*, 2013).

MS cholinergic and GABAergic inputs are likely to coordinate appropriate balances of excitation and inhibition during the exploration of novel and familiar contexts. GABAergic activity appears to increase during the exploration of familiar environments (Giovannini *et al.*, 2001). In addition, activation of GABA_A receptors has been linked to the impairment of taste memory encoding, whereas their inhibition prevented taste memory retrieval (Rodríguez-García and Miranda, 2016). Furthermore, the inhibition of these receptors leads to increases of acetylcholine (Rodríguez-García and Miranda, 2016). Complementing the idea of a coordination between cholinergic and GABAergic inputs, the frequency slope of theta oscillations vs running speed appears to only be affected when the whole MSDB is inactivated, during the exploration of a familiar context (Dannenberg *et al.*, 2019). Together, these studies may suggest a complementary role of cholinergic and GABAergic inputs in the encoding and retrieval of spatial information, but the precise mechanisms still need to be elucidated.

1.3.6. Breakdown of neuronal networks in AD

Increased activity in theta and delta bands, and decreased activity in alpha and beta bands are characteristic alterations found in the EEG of people affected by AD (Jeong, 2004; Babiloni *et al.*, 2020). The cholinergic deficits observed in AD, such as disrupted cholinergic transmission and the loss of cholinergic neurons in the basal forebrain, led to the development of treatments aiming to enhance cholinergic activity with cholinesterase inhibitors (Francis *et al.*, 1999; Hampel *et al.*, 2019). Furthermore, higher amounts of amyloid deposits correlate with smaller basal forebrain volumes (Kerbler *et al.*, 2015). Although, cholinesterase inhibitors seem to be able to reduce the impairments observed in theta, delta, alpha and beta bands (Balkan *et al.*, 2003; Gianotti *et al.*, 2008), they only improve or stabilise symptoms for a period of time, but cannot prevent cognitive decline (Atri, 2019). Alterations related to gamma oscillations have also been described in AD. For instance, theta-low gamma PAC was found to be reduced in the frontal brain region of people affected by AD, which was linked to working memory performance (Goodman *et al.*, 2018). In a similar manner, amyloid rodent models exhibit reduced theta-gamma PAC in the MEC (Nakazono *et al.*, 2017) and the hippocampus (Etter *et al.*, 2019; Jun *et al.*, 2020). Furthermore, a reduction in coherence of high gamma oscillations between the MEC and the CA1 region has also been described (Jun *et al.*, 2020).

It has been hypothesised that A β accumulation leads to an excitatory/inhibitory imbalance in AD (Busche and Konnerth, 2016), which may cause network hypersynchronization and a loss of functional connectivity (Pusil *et al.*, 2019). Alpha and beta hyposynchronization, and delta hypersynchronization have been observed in AD (Koenig *et al.*, 2005). Delta-theta hypersynchronization between the frontal, parietal and temporal regions has been described in MCI and AD cases, whereas alpha hyposynchronization occurred between the temporal, parietal and occipital regions (Ranasinghe *et al.*, 2020). However, theta hyposynchronization between frontal, occipital and temporal regions has also been observed in AD cases (Pusil *et al.*, 2019). These contrasting results could stem from the bandwidths considered in each study, with delta-theta including 2 to 8 Hz and theta including 4 to 8 Hz (Pusil *et al.*, 2019; Ranasinghe *et al.*,

2020). Furthermore, beta hyposynchronization between the frontal gyrus, parietal and occipital regions has also been observed in AD (Pusil *et al.*, 2019). These results suggest a loss of functional connectivity which may result in a network breakdown as the disease progresses.

1.4. MEC functional cell subtypes

The discovery of place cells in the hippocampus supported the existence of a cognitive map in the hippocampus (O'Keefe and Dostrovsky, 1971; O'Keefe, 1976). The activity of hippocampal place cells forms a spatial firing pattern that usually exhibit a single firing field specific to a given environment, known as the place field (Fig. 1.7A) (O'Keefe, 1976), which remains stable during the exploration of familiar environments (Barry *et al.*, 2012; Alme *et al.*, 2014). When animals explore distinct environments, different subsets of place cells are active and individual place cells unpredictably change both their spatial firing patterns and firing rate, a process which is known as place cell global remapping (Bostock, Muller and Kubie, 1991). Different combinations of place cells appear to be active in distinct environments, producing unique representations of these environments which are stored in memory (Alme *et al.*, 2014). However, a partial remapping, which involves the remapping of only a fraction of the cells, occurs when only part of the features that define a given environment are changed (Latuske *et al.*, 2018). For instance, when rats explored two very similar open arenas, which were connected by a corridor and located in the same room, only a fraction of place cells experienced changes in their spatial firing patterns whereas others remained stable (Skaggs and McNaughton, 1998). On the other hand, when cue changes occur within the same environment, place cells may only experience a rate remap, by exhibiting changes in their firing rate while their spatial firing patterns remain stable (Leutgeb *et al.*, 2005). Global remapping is thought to underlie the representation of distinct environments, whereas rate remapping is believed to represent different sensory experiences within the same environment (Leutgeb *et al.*, 2005). Place cell global remapping also occurs during the exploration of novel environments, which is in addition accompanied by an increase in the scale of their firing fields, decreased stability and a reduction in

the spatial information that these cells convey (Barry *et al.*, 2012). After the discovery of hippocampal place cells, several functional cell subtypes were found in the MEC, which will be described in the following sections.

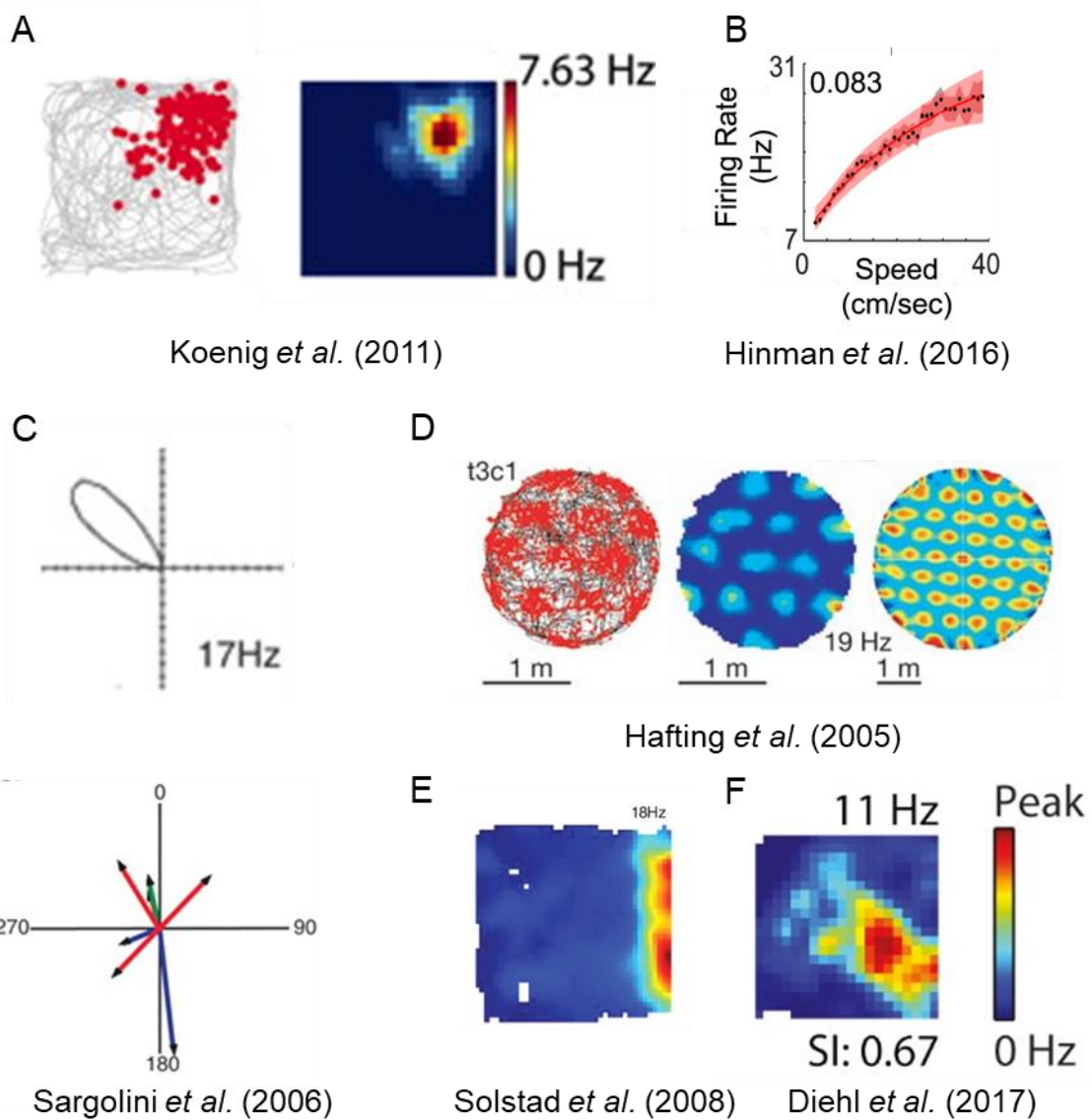


Figure 1.7 Spatially modulated functional subtypes. **A)** Spatial firing pattern of a hippocampal place cell. Plot on the left shows the path followed by the animal (grey) overlapped with the firing of the cell. Plot on the right shows firing rate colour map. Reproduced from (Koenig et al., 2011). **B)** Firing rate of a speed sensitive cell plotted against running speed. Obtained from (Hinman et al., 2016). **C)** Polar plot of a HD sensitive cell (top) and direction and firing rate (length of vector) of several HD sensitive cells (bottom). Obtained from (Sargolini et al., 2006), **D)** Spatial firing pattern of a cell with grid periodicity. Plot on the left shows the path followed by the animal (grey) overlapped with the firing of the cell. Plot in the middle shows firing rate colour map. Plot on the right shows spatial autocorrelation for the rate map. Reproduced from (Hafting et al., 2005), **E)** Plot shows firing rate colour map of a border sensitive cell. Reproduced from (Solstad et al., 2008). **F)** Plot shows firing rate colour map of a non-grid spatial cell. Reproduced from (Diehl et al., 2017).

1.4.1. Speed sensitive cells

Speed information may be used to infer the distance travelled from a reference position, which is essential to performing path integration (Burgess, 2008; Savelli and Knierim, 2019). The spiking activity of different functional cell subtypes is modulated by running speed in the MEC (Fig. 1.7B) (Sargolini *et al.*, 2006; Kropff *et al.*, 2015; Hardcastle *et al.*, 2017), with an estimate of 70 – 80% of MEC cells exhibiting speed sensitivity (Hinman *et al.*, 2016). Speed sensitive cells, apart from theta frequency oscillations, are a candidate to provide this speed signal (Kropff *et al.*, 2015; Ye *et al.*, 2018). Although it has been proposed that MEC cells receive speed information from glutamatergic cells located in the MSDB (Justus *et al.*, 2017), pharmacological inactivation of the MS increased the speed modulation of speed sensitive cells in a different study (Hinman *et al.*, 2016). The role of the MSDB as speed signal providers to MEC speed sensitive cells has been further questioned by a study showing that selective inactivation of glutamatergic cells located in these brain regions, or their whole inactivation, appears to not affect the activity of speed sensitive cells in the MEC (Dannenberg *et al.*, 2019). However, a recent study supports that the horizontal limb of the DB provides speed information to MEC speed sensitive cells, which originates in the pedunculopontine tegmental nucleus of the mesencephalic locomotor region (Carvalho *et al.*, 2020).

1.4.2. Head direction sensitive cells

Heading direction information is also critical to estimate and update the current position through path integration (Burgess, 2008; Savelli and Knierim, 2019). There are cells which increase their activity above their baseline firing rate at preferred head directions (HD) with respect to an allocentric reference frame (Fig. 1.7C), thus signalling the direction of the movement (Taube, 2007). These preferred directions are associated to allothetic cues. For example, the rotation of landmarks in a familiar environment leads to a rotation of the preferred direction

of HD sensitive cells (Taube, Muller and Ranck, 1990b; Taube, 1995; Sargolini *et al.*, 2006).

HD sensitive cells can be found in different brain regions, some of which are the retrosplenial cortex (RSC) (Cho and Sharp, 2001), hippocampus (Leutgeb, Ragazzino and Mizumori, 2000) and MEC (Sargolini *et al.*, 2006). Classic HD cells have been described across the limbic system (Taube, 2007; Winter, Clark and Taube, 2015; Jacob, Casali, *et al.*, 2017). These cells exhibit a single tuning curve, with ensembles of classic HD cells maintaining their preferred firing direction relative to each other (Taube, Muller and Ranck, 1990b; Jacob, Casali, *et al.*, 2017). On the other hand, a fraction of HD sensitive cells located in the RSC, parasubiculum and MEC vary their preferred direction separately from classic HD cells in response to visual cue changes (Jacob, Casali, *et al.*, 2017; Kornienko *et al.*, 2018). In addition, bidirectional HD sensitive cells have also been described in these brain regions (Jacob, Casali, *et al.*, 2017; Kornienko *et al.*, 2018).

In the MEC, both single class and conjunctive HD sensitive cells have been described. While single class cells encode only heading direction information, conjunctive cells encode other additional spatial variables (Sargolini *et al.*, 2006; Hardcastle *et al.*, 2017). Single class and conjunctive cells appear to have a similar directional tuning in the MEC (Sargolini *et al.*, 2006). In addition, both are also modulated by movement, increasing their firing rate at faster running speeds (Sargolini *et al.*, 2006). It is believed that HD sensitive cells in the MEC receive heading direction information from the dorsal part of the presubiculum, which originates in the dorsal tegmental nucleus (Taube, 2007; Winter, Clark and Taube, 2015). The percentage of MEC cells exhibiting HD sensitivity varies between 11 to 40% among different studies (Giocomo *et al.*, 2014; Chen *et al.*, 2018; Ye *et al.*, 2018).

1.4.3. Cells with grid periodicity

Cells with grid periodicity fire at specific positions within a given environment, forming a characteristic hexagonal pattern that covers its entire available surface

(Fig. 1.7D) (Fyhn *et al.*, 2004; Hafting *et al.*, 2005). Experimental and computational evidence supports that cells with grid periodicity play a key role in path integration, by integrating heading direction and speed information (Burgess, Barry and O’Keefe, 2007; Burak and Fiete, 2009; Gil *et al.*, 2018). These cells were first described in the MEC (Fyhn *et al.*, 2004; Hafting *et al.*, 2005) and were subsequently also described in the pre- and parasubiculum (Boccara *et al.*, 2010). Approximately 10-20% of MEC cells show grid periodicity (Giocomo *et al.*, 2011; Perez-Escobar *et al.*, 2016; Diehl *et al.*, 2017; Miao *et al.*, 2017; Munn *et al.*, 2020). The orientation of cells with grid periodicity is anchored to allocentric landmarks in the environment (Hafting *et al.*, 2005). These cells appear to be organised in modules, with cells within the same module sharing a similar orientation and spacing between fields (Hafting *et al.*, 2005; Stensola *et al.*, 2012).

Cells with grid periodicity may provide hippocampal place cells with spatial information, which contributes to the generation of place fields. This is believed to be particularly important for the formation of place fields located far from the borders of the environment (Moser, Kropff and Moser, 2008; Langston *et al.*, 2010; Mallory *et al.*, 2018). The inactivation of the MEC results in the expansion of hippocampal place fields, which is accompanied by a decrease in their intrinsic oscillation frequency and in the spatial information that they convey (Ormond and Mcnaughton, 2015). In addition, increasing the grid field scale also leads to an increase in the place field scale and reduces place cell long term stability, which mainly affects place fields that are far from the borders of the environment (Mallory *et al.*, 2018). However, some studies show that although the inactivation of the MS results in the disruption of the spatial firing pattern of cells with grid periodicity, it does not seem to affect place cells (Brandon *et al.*, 2011; Koenig *et al.*, 2011). Furthermore, hippocampal place fields appear to remain stable in familiar environments and seem able to develop in novel ones during MS inactivation (Brandon *et al.*, 2011, 2014; Koenig *et al.*, 2011). A later study found that MS inactivation results in no hippocampal place fields being formed during the exploration of a novel environment when relevant sensory cues are absent, suggesting that, under these conditions, they can only be generated if proximal cues are available (Wang *et al.*, 2015).

Hippocampal lesions decrease the spatial coherence and the stability between trials of cells with grid periodicity and, in addition, these cells become more modulated by HD (Fyhn *et al.*, 2004). Similarly, cells with grid periodicity progressively become more HD sensitive and lose their firing patterns after inactivation of the dorsal CA1 region in the hippocampus (Bonnevie *et al.*, 2013). Together these studies suggest that reciprocal connections between the MEC and the hippocampus are necessary to maintain stable grid and place fields.

1.4.4. Border sensitive cells

Border sensitive cells increase their firing rate when the animal is next to the proximal geometric borders of a given environment (Fig. 1.7E) (Solstad *et al.*, 2008). Approximately 5 to 10% of cells in the MEC are sensitive to the borders (Solstad *et al.*, 2008; Diehl *et al.*, 2017; Ye *et al.*, 2018; Høydal *et al.*, 2019). Border sensitive cells are associated to allocentric cues, with the rotation of these cues causing a rotation in the firing fields of these cells (Solstad *et al.*, 2008).

It has been hypothesised that MEC border sensitive cells may obtain information from boundary vector cells located in the subiculum (Lever *et al.*, 2009). Subicular boundary vector cells are thought to have receptive fields, which define preferred distances from the boundaries, with the cell's firing increasing when the peak of the field intersects with a boundary (Lever *et al.*, 2009). The firing field of these cells may be offset from the wall when the peak of their receptive field is further away from the head of the animal (Lever *et al.*, 2009). This effect may also occur in border sensitive cells in the MEC (Solstad *et al.*, 2008; Lever *et al.*, 2009). However, although some border sensitive cells meet the characteristics of boundary vector cells, others are not consistent with it as they may only fire in part of the wall or along all walls (Lever *et al.*, 2009). In addition, when the walls of the environment are removed, border sensitive cells seem to experience remapping, which does not occur in subicular boundary vector cells (Solstad *et al.*, 2008; Lever *et al.*, 2009). The activity of boundary vector cells appears to be independent of features of the boundary such as its colour, material or shape (Lever *et al.*, 2009). It has been hypothesised that MEC border sensitive cells

may be a subset of boundary vector cells with small distances between the peak of their receptive field and the head of the animal (Lever *et al.*, 2009).

Hippocampal place cells also receive information from border sensitive cells, with experimental evidence suggesting that these cells mainly influence hippocampal place cells with fields closed to the geometric borders of the environment (Langston *et al.*, 2010; Muessig *et al.*, 2015; Mallory *et al.*, 2018). Place cells with fields closer to the borders of the environment are more stable before weaning, consistent with the later development of grid cells (Langston *et al.*, 2010; Muessig *et al.*, 2015). Furthermore, increasing the grid field scale mainly affects the scale of place fields further away from the borders (Mallory *et al.*, 2018).

1.4.5. Other spatially modulated cells

The majority of MEC cells convey significant spatial information which, including cells with grid periodicity and border sensitive cells, represent approximately 95% of all cells (Diehl *et al.*, 2017). Specifically, the MEC contains spatially modulated cells which do not exhibit grid periodicity nor border sensitivity but show stable spatial firing patterns (Fig. 1.7F), that appear to account for 67.5% (Diehl *et al.*, 2017). These cells have been referred to as non-grid spatial cells or aperiodic spatial cells (Diehl *et al.*, 2017; Miao *et al.*, 2017).

1.4.6. Context effects on MEC functional cell subtypes

There are three main aspects of episodic memory that represent the ‘what, when and where’ of a given experience, which allows to recall its temporal and spatial context (O’Keefe and Nadel, 1978; Nyberg *et al.*, 1996; Hunsaker *et al.*, 2013). In specific, the MEC appears to be mainly involved in processing information related to the spatial context, which can be defined as the circumstances that make up the environment in which an experience takes place (Hunsaker *et al.*, 2013).

Different studies have shown that the context affects the activity of the different functional cell subtypes found in the MEC. A description of these effects is provided in the following paragraphs.

Speed sensitive cells were initially believed to provide a context invariant speed signal (Kropff *et al.*, 2015). However, this view has been challenged by later studies (Perez-Escobar *et al.*, 2016; Campbell *et al.*, 2018; Munn *et al.*, 2020). In the absence of light, speed sensitive cells decrease their firing rate and their speed scores. In addition, their firing rate becomes less modulated by running speed (Perez-Escobar *et al.*, 2016). In a virtual reality exploration task, speed sensitive cells respond asymmetrically to mismatches between real and virtual distance travelled. These cells exhibit larger increases of their firing rate as a function of running speed when the virtual distance travelled is larger than the real distance and show no changes in the opposite scenario, which suggests that speed signals are influenced by allocentric cues (Campbell *et al.*, 2018). Furthermore, speed sensitive cells also respond to environmental perturbation, with their firing rate and its modulation by running speed either increasing when the environment is compressed or decreasing when it is expanded (Munn *et al.*, 2020).

HD sensitive cells also appear to be affected by context changes. These cells exhibit a reduction of their mean vector length in the absence of light (Perez-Escobar *et al.*, 2016). Furthermore, when rodents are taken from one context to a new one, their preferred direction shifts randomly (Yoder *et al.*, 2011). However, when animals move themselves from a familiar context to a novel context, HD sensitive cells only show small shifts in their preferred direction (Taube and Burton, 1995; Yoder *et al.*, 2011). In addition, HD sensitive cells maintain their preferred direction across trials in the same context (Sargolini *et al.*, 2006; Yoder *et al.*, 2011).

Grid patterns remain stable but realign when colour and shape changes are made to the environment (Fyhn *et al.*, 2007; Diehl *et al.*, 2017). In addition, the firing rate across each grid field in a given cell are redistributed with these changes (Diehl *et al.*, 2017). When larger context changes are introduced by recording in two different rooms, the orientation, size and offset of grid fields is modified (Fyhn *et al.*, 2007). Furthermore, when animals are placed in a novel environment, grid

fields expand, reduce their stability and become more irregular (Barry *et al.*, 2012). Although it was initially reported that grid periodicity remains stable in total darkness (Hafting *et al.*, 2005), other studies have shown that darkness disrupts grid patterns (Chen *et al.*, 2016; Perez-Escobar *et al.*, 2016). As seen in speed sensitive cells, cells with grid periodicity also show an asymmetrical response to mismatches between real and virtual distance travelled. Phase shifts occurred when the virtual distance travelled exceeded the real distance travelled, whereas changes in the scale of the grid fields occurred in the opposite scenario (Campbell *et al.*, 2018).

Border sensitive cells elongate their firing fields when the environment is expanded (Solstad *et al.*, 2008). However, the location of their firing fields does not seem to be affected by changes in the shape of the environment within the same room (Solstad *et al.*, 2008). The firing fields of border sensitive cells remain mostly stable during mismatches between real and virtual distance travelled, only showing partial remaps when the real distance travelled is higher than the virtual one (Campbell *et al.*, 2018).

Non-grid spatial cells are affected by shape and colour changes made to the environment, which lead to the reorganization of their firing spatial patterns. They are also affected when recordings take place in different rooms, which yields a similar reorganization (Diehl *et al.*, 2017).

1.4.7. Alterations of spatial functional cell subtypes in Alzheimer's disease

Grid-like activity has been detected in humans with functional MRI (fMRI) (Doeller, Barry and Burgess, 2010) and directly recorded from neuronal activity in different brain regions, including the EC and the hippocampus (Jacobs *et al.*, 2013). Importantly, it has been shown that grid-like activity is reduced in AD genetic risk carriers (Kunz *et al.*, 2015).

In a similar manner, a disruption of grid patterns has also been observed in the MEC of an amyloid mouse model (Jun *et al.*, 2020). In addition, this disruption precedes the deterioration of place cells in the hippocampus (Cacucci *et al.*, 2008; Jun *et al.*, 2020). Furthermore, a decrease in the spatial information

conveyed by both MEC and hippocampal cells has been observed, also suggesting the impairment of non-grid spatial cells in the MEC (Cacucci *et al.*, 2008; Jun *et al.*, 2020). The impairments observed in cells with grid periodicity and place cells correlate with spatial memory deficits (Cacucci *et al.*, 2008; Jun *et al.*, 2020).

1.5. Hypothesis and aims

Compelling evidence highlights that EC impairments contribute to the spatial memory deficits observed in AD. Despite the important role that the MEC plays in spatial navigation and memory, the effects of novel and familiar environmental stimuli on the MEC neuronal dynamics in amyloid mouse models remain unexplored. J20 mice show spatial memory deficits whose underlying mechanisms may be based on abnormalities in the MEC neuronal substrates. The general hypothesis of this PhD project was that:

The MEC neuronal dynamics underlying spatial contextual memory will be disrupted in J20 mice.

To test this hypothesis two different aims were defined:

Aim 1: To assess the effects of novel and familiar environmental stimuli in the MEC neuronal networks of J20 mice.

The frequency of theta oscillations increases with the running speed of the animal, with the slopes resulting from this relationship becoming steeper in familiar environments (Newman *et al.*, 2013; Wells *et al.*, 2013). Thus, the theta frequency slope may be used as a metric of familiarity to a given environment and of spatial memory deficits. J20 mice exhibit synaptic plasticity dysfunction (Saganich *et al.*, 2006). Furthermore, it has been reported that these mice show spatial memory impairments at 4 months of age (Wright *et al.*, 2013). It was hypothesised that these deficits would be reflected in a lack of theta frequency slope increase in J20 mice during the exploration of a familiar context. On the other hand, the power of high gamma oscillations also increases with running speed (Chen *et al.*, 2011; Ahmed, 2012; Kemere *et al.*, 2013). However, an

opposite effect has been observed, with high gamma power slope decreasing as the environment becomes more familiar in both the MEC and the hippocampus (Kemere *et al.*, 2013). It was further hypothesised that the high gamma power slope would remain increased in J20 mice during the exploration of a familiar context.

Aim 2: To study the neuronal cells involved in these networks through single-unit *in vivo* recordings in novel and familiar environments in J20 mice.

Based on evidence in literature and in this thesis, showing that the MEC responds to environmental novelty (Barry *et al.*, 2012; Kemere *et al.*, 2013; Newman *et al.*, 2013), it was hypothesised that the MEC functional cell subtypes may mirror these effects. Based on the deficits observed in MEC high gamma oscillations related to memory processing in J20 mice in this thesis, it was hypothesised that these functional cell subtypes may also be impaired. Specifically, cells with grid periodicity have been reported to respond to the novelty of the environment by expanding their grid fields, reducing their stability and becoming more irregular (Barry *et al.*, 2012). It is possible that the spatial memory deficits together with synaptic plasticity dysfunction and MEC high gamma power impairments observed in J20 mice lead to an alteration in the activity of cells with grid periodicity, which may display expanded, irregular and unstable grid fields.

Chapter 2. General methodology

2.1. Experimental subjects

The J20 mouse model (Mucke *et al.*, 2000) was used for all experiments. All mice were obtained from Eli Lilly (UK) or bred in house at the University of Exeter. Animals obtained from Eli Lilly were habituated after arrival for at least 7 days. All mice were kept on a 12:12h light/dark cycle with food and water being available *ad libitum*. All work complied with the UK Animals (Scientific Procedures) Act 1986.

The triangular track experiment, described in section 2.2.1, was the only one that included two different age ranges, 6 mo and 10-15 mo mice. 10-15 mo mice were not used for the subsequent experiments as it was deemed that this age range could have potentially had an impact on the results obtained. Although after 8-10 months of age J20 mice appear to exhibit a more advanced AD pathology (Mucke *et al.*, 2000; Castanho *et al.*, 2020), which may model later phases of AD (Thal *et al.*, 2002), WT mice older than this age range also show relevant age-related deficits. For example, it has been found that 12 mo WT mice show long-term object recognition memory deficits which are similar to those observed in 12 mo J20 mice (Ameen-Ali *et al.*, 2019). Furthermore, WT mice show an age-related reduction of MS GABAergic contacts onto hippocampal interneurons and of the number of synaptic boutons at 18 months of age (Rubio *et al.*, 2012). It is therefore possible that the 10-15 mo WT mice could exhibit deficits which could prevent the accurate study of spatial memory impairments. Considering this, only 6 mo mice were used for the rest of the studies.

2.2. Behavioural tests

2.2.1. Triangular track

A pilot study to explore the effects of environmental familiarity was carried out with a modified T-maze where animals were only allowed to explore one of the arms (either right or left), thus acting as a triangular track (Fig. 2.1A). This modified T-maze had 5 different doors, which prevented the animals from exploring the opposite arm and from going backwards. Sugar pellets were released on the top left and right corners of the maze to encourage mice to continuously move forward (Fig. 2.1A). During the experiment, lights were turned off to ensure good position tracking. As a result, the only sources of light were the LEDs attached to the animal's headstage and the light coming from the adjoining room. Although it has been shown that the absence of light diminishes the relationship between theta frequency and running speed in mice (Chen *et al.*, 2016), this study was published within the same time period that this experiment was designed and performed.

Prior to the start of this experiment all animals were food restricted to encourage exploration of the triangular track. Food access was restricted once animals were fully recovered from the surgery. All mice initially received a 2 g daily food pellet, which was subsequently adjusted to keep the body weight at 90% of the initial weight. For the experiment, 10-15 mo and 6 mo mice were placed in the triangular track and encouraged to explore it for 30-40 minutes each day for 2 consecutive days (Fig. 2.1B). Animals could explore either the left or right arm of the triangular track across for both days. The number of animals that explored the left or right arm was counterbalanced between groups, as much as reasonably possible, to ensure no effects due to the arm explored.

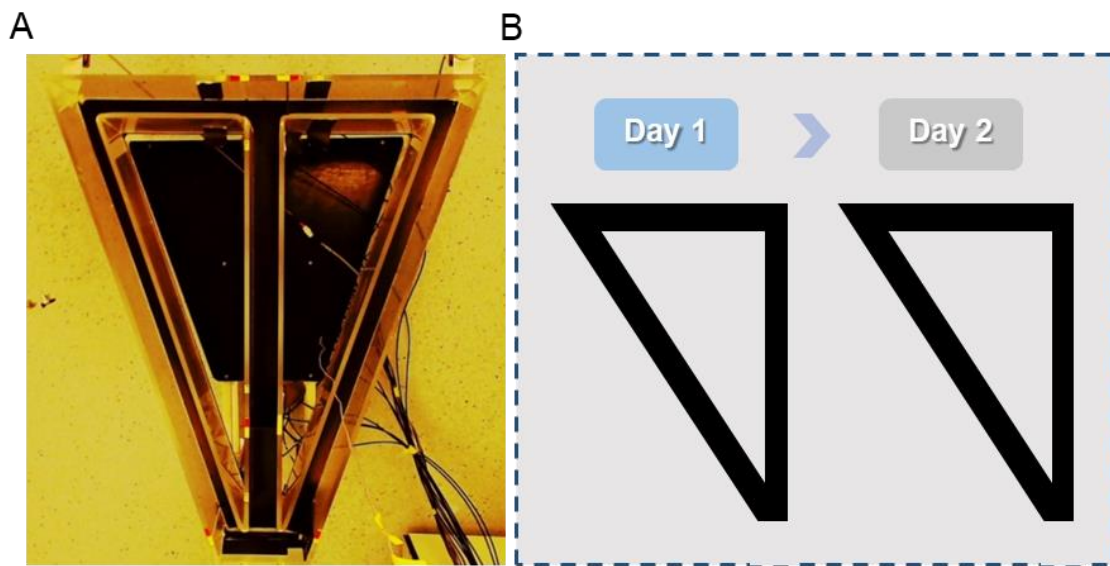


Figure 2.1 Experimental set up of the triangular track experiment. **A)** Modified T-Maze used in this experiment. Animals could either explore the right or left arm. **B)** Experiment procedure showing the two different recording days in the triangular track.

2.2.2. Open arenas

2.2.2.1 Open arenas: First experiment

The triangular track experiment did not achieve the required levels of familiarity to observe significant changes in the frequency of theta oscillations and the power of high gamma oscillations between trials, as it has been reported in literature (Kemere *et al.*, 2013; Wells *et al.*, 2013). This could have been caused by the short duration of this experiment, potentially requiring a longer experimental set up. A second experiment was therefore designed to integrate changes aiming to enhance familiarity to the environment. This was achieved by allowing a longer total exploration time along with more exposure events, together with greater access to visual landmarks. For these recordings two different open arenas of similar area were used, one square arena (Fig. 2.2A) of 56x56 cm and one circular arena (Fig. 2.2B) of 62 cm of diameter. In both arenas the height of the walls was 65 cm. The square arena was painted in white with black stripes on the bottom and on two opposing walls. On the remaining walls different black cues were placed. The circular arena surface and walls had a light brown colour. Two different black cues were placed opposite to each other on the walls.

It has been observed that the absence of light diminishes the relationship between theta frequency and running speed in mice (Chen *et al.*, 2016), a relationship which has been reported to increase with environmental familiarity (Wells *et al.*, 2013). To avoid diminishing effects on the slope of theta frequency oscillations with running speed, an overhead dim source of light was provided. Animals were not food restricted for this experiment. Each mouse was placed in one of the two arenas for 4 consecutive days, for 15 minutes twice a day with an interval of 15 minutes (Fig. 2.2C). Therefore, each animal was exposed a total of 8 times to the familiar environment. On the 5th day, all animals were placed in the opposite arena (circular or square) twice for 15 minutes with an interval of 15 minutes. Animals were familiarised to either the circular or the square arena. In addition, due to time constraints, some mice performed this experiment in the morning, while others in the afternoon. These two factors were kept in balance between both groups as much as reasonably possible.

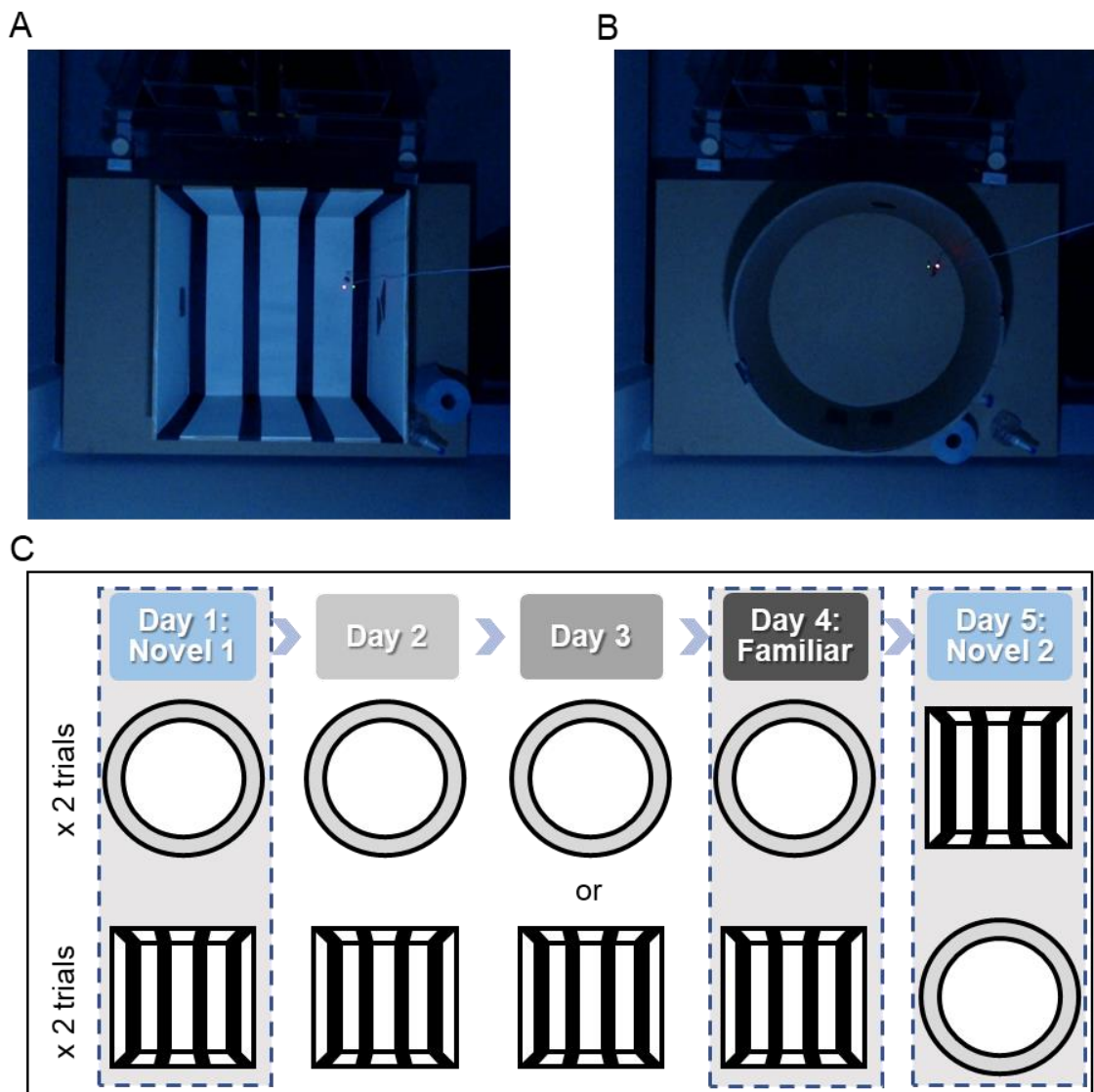


Figure 2.2 Experimental design of the first experiment with two open arenas. **A)** Square arena (56cm x 56cm x 65cm). **B)** Circular arena (62cm of diameter and 65cm of height. **C)** Experiment procedure showing both experimental options (top and bottom). Mice were familiarized either to the circular arena (top) or the square arena (bottom) for four consecutive days twice a day and exposed to the opposite arena on the fifth day. Dash shaded boxes highlight the days analysed in this experiment, with day 1 corresponding to the first novel day, day 4 with the familiar day and day 5 to a second novel day.

2.2.2.2 Open arenas: second experiment

Adaptations to the experiment described above had to be made for the recording of single units. Considering grid spacing (Fyhn *et al.*, 2008), the previous arenas were deemed too small and larger arenas were used instead. However, it was not possible to obtain a circular arena of these dimensions and so all arenas used

were square. All recording sessions took place in the same day to ensure that the same cell was recorded across trials. In addition, animals were food restricted, as described in section 2.2.1, to ensure they covered the surface of the open arenas well.

Three square open arenas of equal area were used. All arenas had a dimension of 86.5 cm x 86.5 cm x 24.5 cm. Arena 1 had brown walls and a white floor, with a black circle, two black rectangles and a black line on the walls (Fig. 2.3A). Arena 2 was painted in grey and had a black cross and a yellow rectangle on the walls (Fig. 2.3B). Arena 3 had a white floor with black strips and brown walls with a black triangle and a black parallelogram (Fig. 2.3C). It is important to acknowledge that white floor open arenas may have an anxiogenic confound (Costall *et al.*, 1989). Although all mice included in this experiment were exposed to the grey arena (arena 2) and the two white-floored arenas (arenas 1 and 3), arena 3 was only used as a novel arena. An overhead dim source of light was provided during the whole experiment. The novel and familiar trials were performed in different rooms with the aim of increasing novelty.

Only arenas 1 and 2 were used as a possible familiar arena, and arena 3 was only used as a novel arena (Fig. 2.3D). Each mouse was repeatedly exposed to either arena 1 (option 1) or 2 (option 2) for a minimum of 7 exposures, with each of these exposures lasting normally between 15-30 minutes. This arena, to which the animal would be repeatedly exposed, was the familiar arena and the remaining two arenas acted as novel environments. The probes (see section 2.3.1 for more details) would be regularly moved down during this period with the aim of reaching the dorsal MEC and recording from a number of cells. Once the probes were estimated to be in the desired area and a good number of cells were detected, all animals were exposed to the familiar arena, the novel arena and again to the familiar arena (Fig. 2.3D). Each recording session did not exceed 1 hour. In between sessions all mice rested for at least 30 minutes in their home cage in their holding room. After this first trial, the probes were moved down until there was no overlap with the previous recording location. A second trial with arena 3 as the novel environment in the novel room was then performed.

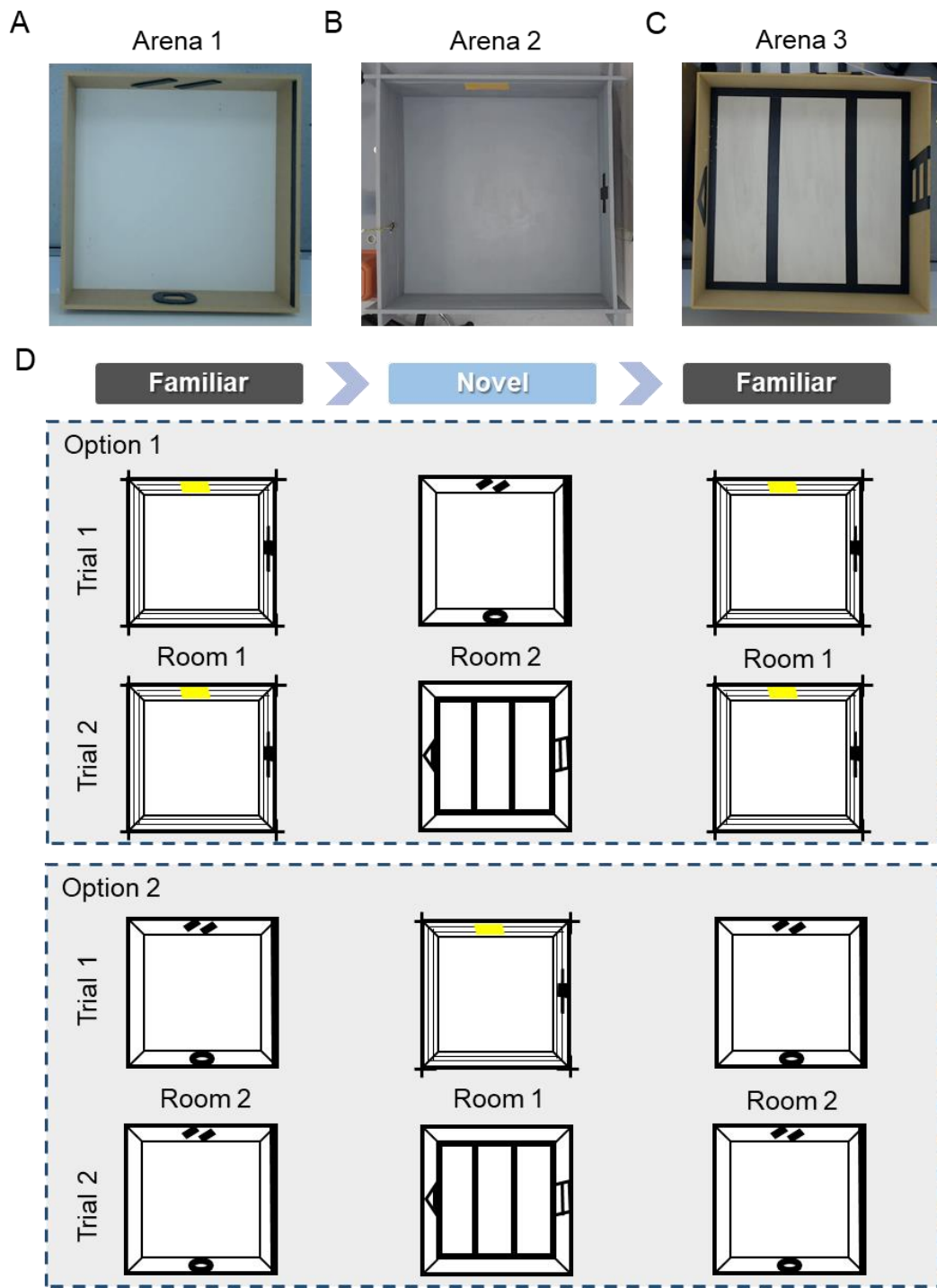


Figure 2.3 Experimental design of the second experiment with two open arenas. A) Square arena 1 (86.5cm x 86.5cm x 24.5cm). B) Square arena 2 (86.5cm x 86.5cm x 24.5cm). C) Square arena 3 (86.5cm x 86.5cm x 24.5cm). D) Experiment procedure showing options 1 and 2, each of them composed of two trials which used arena 1 or 2 as the familiar arena. In trial 1, the opposite open arena (either arena 1 or 2) was used as the novel arena. In trial 2, arena 3 was used as the novel arena for both options.

2.3. *In vivo* electrophysiology

2.3.1. Silicon probes

Two different types of silicon probes were employed in the experiments described in the following chapters.

Qtrodes (*NeuroNexus*, Q1x4-5mm-200-177-CQ4, Fig. 2.4A) were used to record LFP signals in the experiments performed in chapter 3. These are 4-channel linear probes with an interspacing of 200 μm between each recording site. Electrode diameter was 15 μm with an impedance of $\sim 1 \text{ M}\Omega$.

32-channel probes (*CAMBRIDGE NeuroTech*, ASSY-116 – P-1, Fig. 2.4B) were used for the recording of LFP signals and single unit activity in the experiments performed in chapter 4. These probes consist of two shanks, each of them comprising 16 channels arranged in two parallel columns, with a vertical interspacing of 25 μm between each recording site. Each electrode size was 11 by 15 μm with an impedance of $\sim 0.05 \text{ M}\Omega$. The total space between the highest and lowest recording sites is 200 μm with both shanks being 250 μm apart. Probes were attached to a miniature Microdrive which could be moved down 205 μm per turn, thus increasing the total cell number as it allowed recordings from multiple sites.

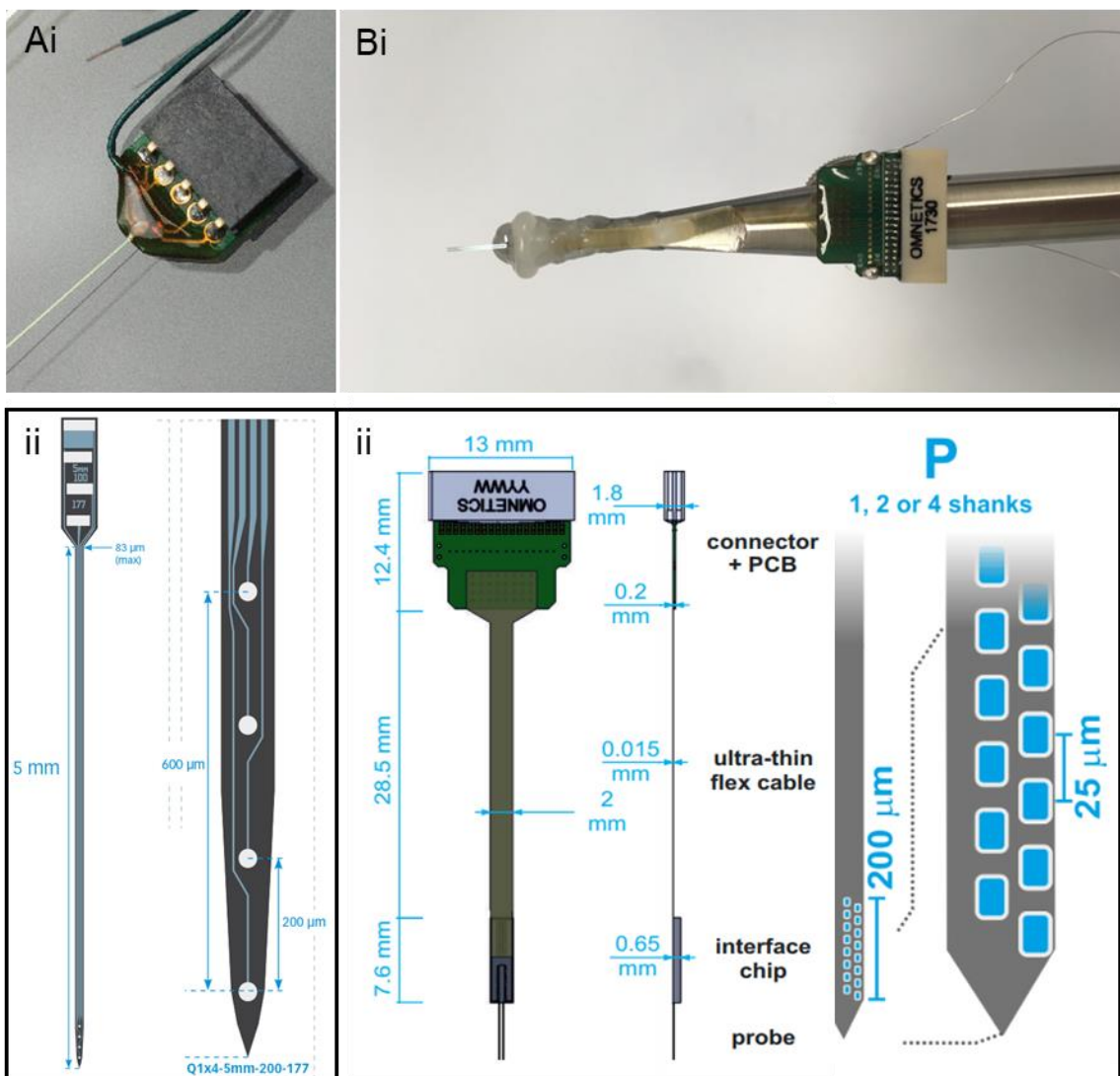


Figure 2.4 Silicon probes used in all experiments. A) Photo (i) and Schematic (ii) of qtrodes (NeuroNexus, Q1x4-5mm-200-177-CQ4, images taken from: www.neuronexus.com). **B)** Photo (i) and Schematic (ii) of 32-channels probes (CAMBRIDGE NeuroTech, ASSY-116-P-1, Schematic taken from: www.cambridgenurotech.com).

2.3.2. Silicon probe implantation

Mice were initially anaesthetised in an induction chamber with 4% isoflurane and subsequently transferred and fixed to a stereotaxic frame (ASI instruments) with 1-2% isoflurane. During the surgery, the body temperature was continuously monitored with a feedback loop homoeothermic blanket system (Harvard instruments) which self-adjusted to maintain a body temperature of approximately 36.5°C. and Hartmann's solution was subcutaneously administered before the surgery and every hour and a half. Carprofen (5mg/kg) was used as a pre- and

post-surgery analgesic before the start of the procedure and afterwards every 12/24 hours.

After the skin incision, the skull surface was cleaned and scraped with a scalpel to assure good implant adhesion. Bregma and Lambda positions were measured, and the head of the animal adjusted to ensure a flat skull position. Five small holes were drilled into each of the bone plates and 5 screws were inserted with the aim of securing the implant. The screw placed on the cerebellum was connected to a silver wire (World Precision Instruments) and served as ground reference. This screw was connected to the reference wire of the probe. All probes were implanted in the dorsal MEC at 3.12 mm mediolateral and 5.25 mm anteroposterior. Qtrodes were implanted at 1.25 mm and 1.65 mm dorsoventrally in 10-15 mo and 6 mo mice respectively; with an angle of 5-10 degrees with the tip of the probe pointing anteriorly. The 32-channel probes were implanted at 0.6-0.8 mm dorsoventrally with an angle of 0-5 degrees with the tip of the probe pointing anteriorly. The movable parts of the 32-channel probes, which were attached to a miniature Microdrive, were covered with Vaseline to ensure probes could be moved down after mice were recovered. RelyX Unicem 2 dental cement (Henry Schein) was used to protect and, together with the screws, fix the probes to the skull (Fig. 2.5A). The total weight of the implant did not exceed 10% of the pre-surgery body weight of each animal, typically weighing around 2g for the 32-channel probes and around 1g for the Qtrodes.

After surgery mice were removed from the frame and carefully monitored on the heat mat until fully awake. Finally, they were transferred to a recovery tank for 3-4 hours. Animals recovered for at least one week with post-surgery checks before the commencement of the experiments.

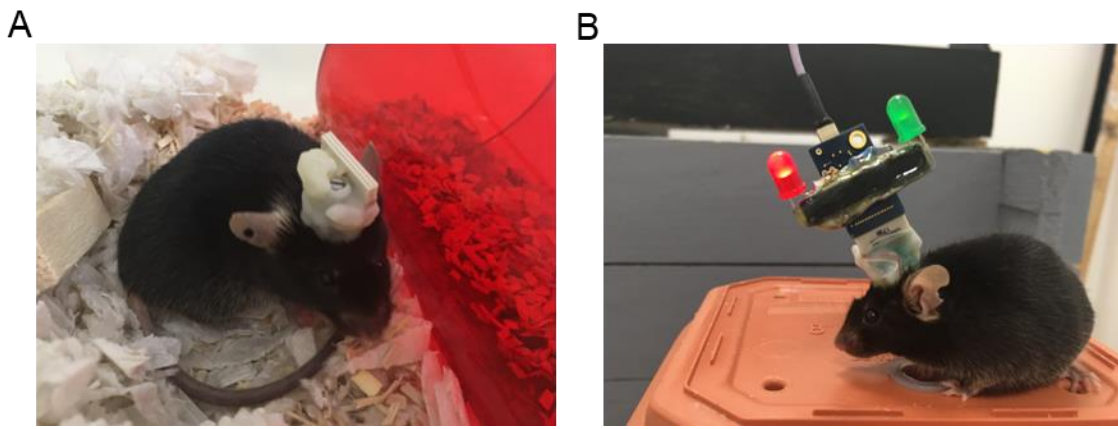


Figure 2.5 Implanted mouse with 32-channel probe (CAMBRIDGE NeuroTech). A) Implanted mouse in its home cage. B) Implanted mouse with RHD2132 amplifier board (Intan Technologies) and LEDs attached.

2.3.3. Data acquisition

For all the experiments described in chapters 3 and 4, real time *in vivo* MEC electrical activity and tracking data were continuously sampled at 30 kHz and recorded with an open-source electrophysiology recording system, OpenEphys (open-ephys.org) acquisition board. This system received position information from tracking software, Bonsai (bonsai-rx.org), which used a webcam (Logitech HD Pro Webcam C920) for this purpose. Tracking data was fed into the OpenEphys acquisition board and simultaneously acquired with the electrical activity. This resulted in an oversampling of the tracking data as the camera frame rate was 30 Hz. The position information was extracted from the tracking of two light emitting diodes (LEDs) attached to the headstage (Fig. 2.5B). All recorded data was stored in a computer for offline processing.

2.3.4. Tracking analysis

The time spent in the borders of the open arena can be used to measure anxiety (Simon, Dupuis and Costentin, 1994; Seibenhener and Wooten, 2015). The open arenas were divided into a border and a central area, with the borders consisting in 15cm from the wall. The time spent in the border area was expressed as a percentage of the total recording time and used for comparisons.

Running speed was obtained from the position information. Periods in which the position of the two LEDs were too far apart were removed and linear interpolation used to fill missing values. Position information was smoothed with a Savitzky-Golay finite impulse response (FIR) smoothing filter of order 3. Running speed was averaged for each animal and trial and used for comparisons.

2.3.5. Local field potential signals analysis

LFP signals were analysed in the same way for all experiments described in chapters 3 and 4. Firstly, LFP signals were bandpass filtered between 1 to 200 Hz, and subsequently down sampled to 3 kHz for further analysis (Fig. 2.6A). LFP multitaper spectral analysis was performed with the Chronux toolbox for MATLAB (available at <http://chronux.org/>) and data analysis was performed with custom made MATLAB scripts. This multitaper spectral analysis is based on a Fast Fourier Transform (FFT), which decomposes a complex signal into individual sine waves (Bergland, 1969). The following frequency bands were used for analysis (Fig. 2.6A): Theta (5-12 Hz) and high gamma (60-120 Hz). High gamma frequency oscillations were analysed with a 200 ms time window, as done in a previous study (Ahmed, 2012). Theta frequency oscillations were analysed with a 1 second time window to account for the lower frequency of these oscillations. Power spectrums of the LFP were generated at each frequency band for each time bin. In addition, the time-bandwidth product (TW) and the number of tapers (K) to use were provided to the Chronux toolbox. These were set to TW = 3 and K = 5 for the high gamma band and TW = 0.1 and K = 2 for the theta band.

Only one channel of the probe was used for LFP analysis. To select the optimum channel for further analysis, the power recorded by each channel, in the first recording session, in both theta and high gamma frequency bands was obtained. Separately for each band, the channel with the minimum power was found, and used to normalise the power in all channels within the band. There were two normalised values for each channel, one corresponding to the normalised theta power and another to the normalised high gamma power. These two values were added together and the channel with the highest total was selected for further analysis.

The relationship of gamma and theta frequency oscillations with running speed was analysed by computing the peak frequency and the power of these oscillations at each time bin (Fig. 2.6B and C). For each time bin, the peak frequency corresponded to the frequency with the highest power value. On the other hand, the power at each time bin was obtained by dividing the power curve into rectangles, with a side corresponding to the frequency bin size and the other to the power in that specific bin. The area of these rectangles was then summated to obtain an approximation of the area under the curve for each time bin. The peak frequency and the power were further computed for each running speed bin (bin size = 3 cm/s) and a linear fit was performed on the pooled data. The slopes resulting from the linear fit for each animal and trial were used for comparisons. In addition, the frequency intercepts resulting from the linear fit for each animal and trial were also used for comparisons. The power of theta and gamma oscillations was normalised to the power corresponding to the first speed bin, as variations in theta power have been observed depending on the recording location within the MEC (Deshmukh *et al.*, 2010). Because of this, the power intercept resulting from the linear fit was not studied.

PAC between theta and high gamma oscillations was obtained using the modulation index (MI) (Canolty *et al.*, 2006), which was calculated using a toolbox available at: <https://data.mrc.ox.ac.uk/data-set/matlab-toolbox-estimating-phase-amplitude-coupling> (Onslow, Bogacz and Jones, 2011). To obtain the MI, the LFP signal was filtered in the theta and the high gamma band for the phase signal and the amplitude signal, respectively. The instantaneous amplitude envelope ($A_{famp}(t)$) of the amplitude signal and the instantaneous phase ($\theta_{fph}(t)$) of the phase signal were both obtained through a complex Morlet wavelet. $A_{famp}(t)$ and $\theta_{fph}(t)$ were combined into a composite signal of complex values ($Z_{fph,famp}(t)$) with the following equation:

$$Z_{fph,famp}(t) = A_{famp}(t) * e^{i\theta_{fph}(t)}$$

Finally, a MI value was obtained for each combination of $A_{famp}(t)$ and $\theta_{fph}(t)$ as the absolute value of the average of $Z_{fph,famp}(t)$, resulting in a matrix of PAC values, as described in the following equation:

$$Z_{fph,famp}(t) = |\text{average}(Z_{fph,famp}(t))|$$

To determine significant PAC, the amplitude signal was divided into 1000 sections of random lengths which were reordered to shuffle it. The signal was shuffled 50 times. After shuffling, the MI values were again obtained for each combination of the shuffled $A_{famp}(t)$ and $\theta_{fph}(t)$, as described above. An observed MI, for a given $A_{famp}(t)$ and $\theta_{fph}(t)$ combination, was considered significant if less than 5% of the shuffled MI values exceeded its value. Non-significant MI values were set to zero.

The MI was calculated for each running speed bin (bin size = 3 cm/s) and trial. Each of the matrices of PAC values obtained were normalised by the mean value of the non-zero elements of the PAC matrix obtained at 3-6cm/s for each animal and trial. MI final values were obtained by summing all the PAC values of each matrix contain within the theta frequency limits and either the low or high gamma limits. Linear fits were performed on the MI final values against the running speed data for each animal and trial. The resulting slopes were used for comparisons.

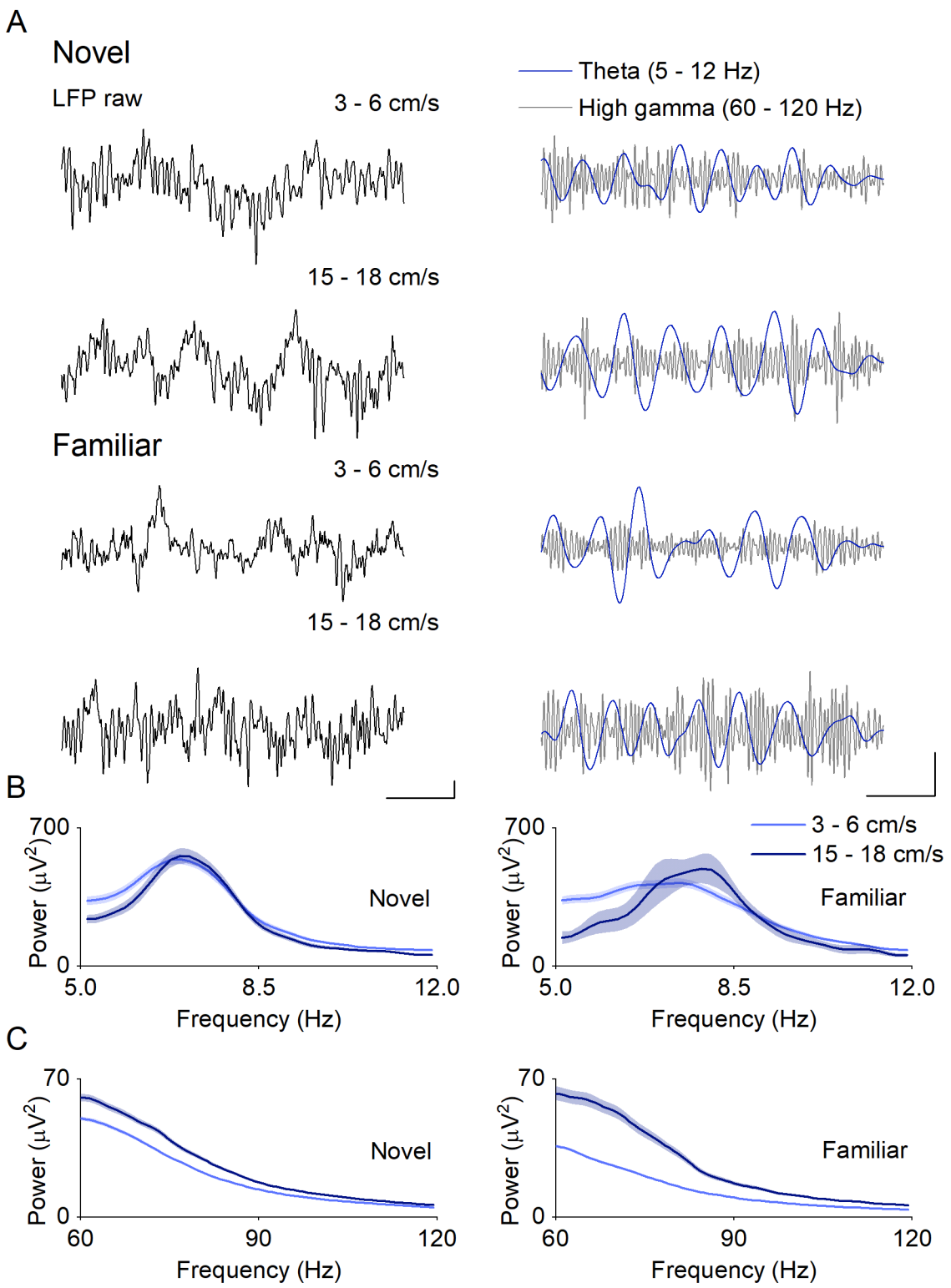


Figure 2.6 Analysis of theta and high gamma oscillations. **A)** Example of recorded LFP raw signals on the left and filtered at theta and high gamma frequency on the right in one example animal. This is shown for the first (novel) and fourth day (familiar) at two different running speeds in the first experiment with two open arenas. Scale bar is 200 ms by 200 μV . **B)** Power spectrum of the recorded data showing theta power and frequency in day 1 (novel) and day 4 (familiar) at two different running speeds for the same animal. **C)** Power spectrum of the recorded data showing high gamma

power and frequency in day 1 (novel) and day 4 (familiar) at two different running speeds for the same animal.

2.3.6. Spike sorting

Single unit data was bandpass filtered (1–10000 Hz) and continuously sampled at 30 kHz. Recordings were saved in Open Ephys format ('.continuous') which stores each channel's data in an individual binary file. For pre-processing, Open Ephys data was reformatted to a flat binary file ('.dat'). All channels were referenced to a common average made with the channels of the opposite shank.

Spike detection and automatic clustering was done using an open source software, Klusta (Rossant *et al.*, 2016) (<https://klusta.readthedocs.io/en/latest/>). Spike detection was carried out by the SpikeDetekt program which firstly band-pass filtered the raw data between 500 Hz to 0.95*Nyquist (half of the sampling rate), to remove LFP signals, and detected spikes through a double-threshold flood fill algorithm. Detected spikes consisted of spatiotemporally connected nodes in which all points passed a weak threshold and at least one point passed a strong threshold, each threshold corresponding to 2 and 4 times the signal's standard deviation, respectively.

Subsequently, automatic clustering was achieved with Klustakwik. This program uses a masked expectation-maximization (EM) algorithm which fits the data with a number of Gaussians. Finally, resulting clusters were visualised with KlustaViewa for manual refinement (Fig. 2.7).

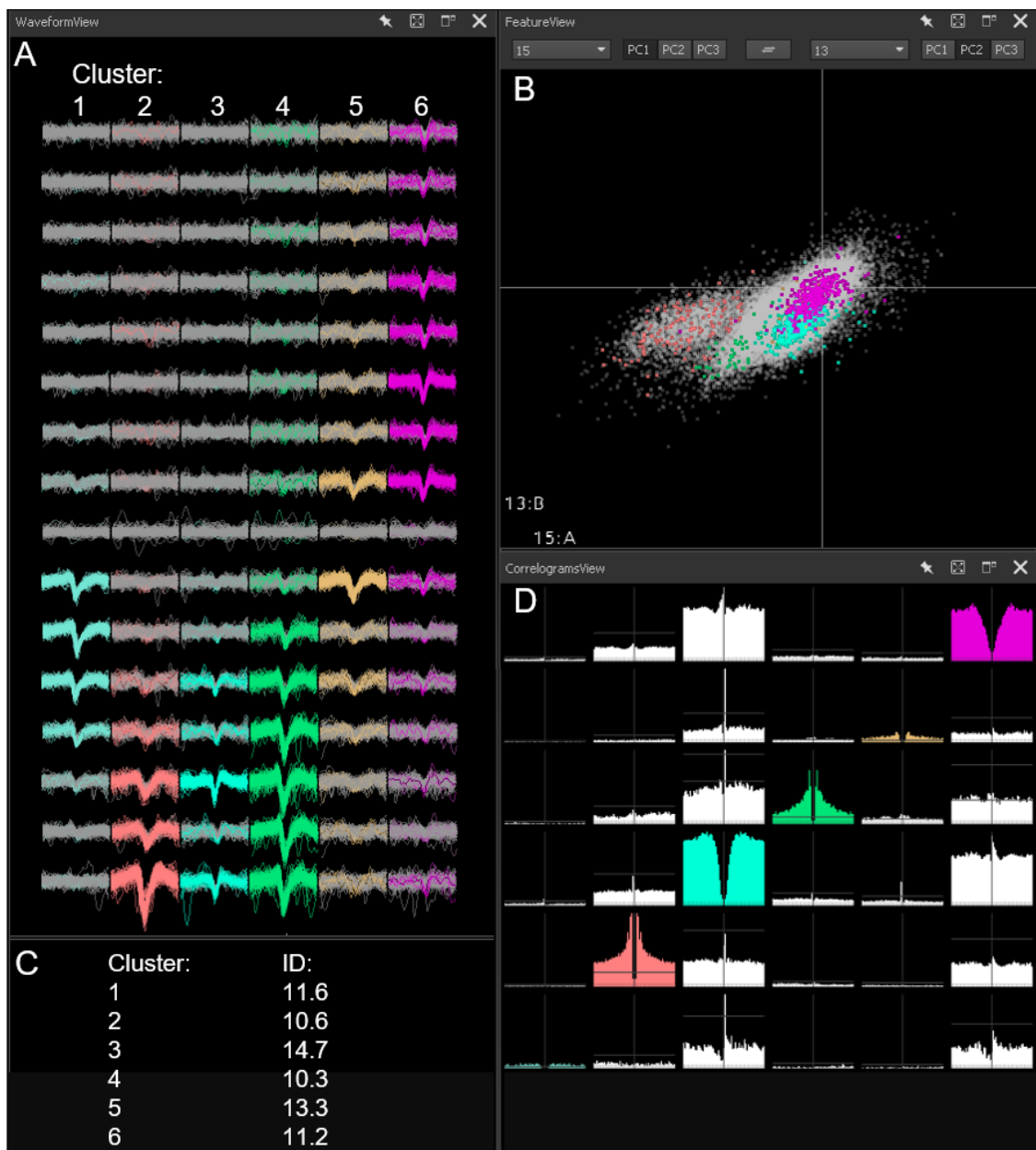


Figure 2.7 Clustering of single unit data visualized in KlustaViewa. **A)** Spike waveforms of 6 example clusters, recorded from the MEC, for which the 16 channels of a shank are shown. **B)** Feature view showing the comparison of principal components in two different channels for the same example clusters. **C)** Isolation distance of each cluster. **D)** Autocorrelations (coloured) and crosscorrelations (white) of the example clusters.

2.3.7. Theta modulation analysis

2.3.7.1 Theta modulation index

The theta modulation index (TMI) (Langston *et al.*, 2010) was calculated through a Fast Fourier Transform (FFT) of the spike timestamps auto-correlogram of each cell with lags up to 500ms. The maximum power in the theta band (5-12 Hz), and its corresponding frequency value, was found and used to calculate an average power. This was achieved by taking the mean power of a frequency range of ± 1 Hz of the frequency value. TMI was obtained by dividing this mean power by the mean broadband power (0-125 Hz). A cell was considered theta modulated for values of TMI above the arbitrary threshold of 5 (Langston *et al.*, 2010). The modulation frequency corresponded to the frequency with the maximum power in the theta range for theta modulated cells.

2.3.7.2 Maximum likelihood estimation method for theta modulation

Characteristics of theta rhythmic firing such as the modulation frequency were determined using a maximum likelihood estimation (MLE) as described in literature (Climer *et al.*, 2015; Hinman *et al.*, 2016). The open source MATLAB scripts used in this analysis are available at: https://github.com/jrclimer/mle_rhythmicity. Time windows of 0.6s were produced after every recorded spike. The lags at which the spikes within these windows occurred, with respect to the first spike, were obtained. These lags were used to fit a flat and a rhythmic model through an MLE method. To assess significant cell rhythmicity, a likelihood-ratio test between the two fits was used. Only cells with significant cell rhythmicity and with a frequency of rhythmic modulation in the theta band were classified as theta modulated.

2.3.7.3 Theta firing phase and mean resultant vector length

To obtain the theta firing phase and the mean resultant vector length, LFP signals were first bandpass filtered at the theta frequency (5-12Hz) and the instantaneous

phase was obtained with the Hilbert transform. The theta firing phase for each cell was obtained by linearly interpolating the theta phase to generate values at the cell firing timestamps. The mean firing phase and the mean resultant vector length were obtained through an open/source Circular Statistics Toolbox for Matlab (Berens, 2009):

<https://uk.mathworks.com/matlabcentral/fileexchange/10676-circular-statistics-toolbox-directional-statistics>. Cells with mean firing phases between 90 to 270° were classified as locked to the peak and between 270 to 90° as locked to the trough, with 180° corresponding to the highest point of the peak and 0/360° to the lowest point of the trough.

2.3.8. Cell type classification

Cells were classified as putative excitatory cells or putative interneurons depending on the average spike width, defined as the time from the peak to the trough. These parameters were as specified in (Frank *et al.*, 2001), with putative excitatory cells defined as having a spike width >0.4ms, and putative interneurons defined as the opposite.

2.3.9. Speed sensitive cells

Speed modulation analysis was performed as described in (Kropff *et al.*, 2015). A time window of 0.04s was used for analysis. The speed bin size was set to 1cm/s, with lower and upper speed limits of 2 cm/s and 30 cm/s, respectively. The average firing rate was calculated for each running speed bin and smoothed with a Gaussian function ($\sigma = 3.75$). The speed score was defined as the Fisher transformation of the Pearson's linear correlation coefficient. This was computed for both the firing rate versus running speed, and the logarithmic of the firing rate versus running speed for linearly modulated and saturating speed sensitive cells, respectively.

Spike time stamps were shuffled 250 times and reanalysed as described above. Spike shuffling was performed by forward shifting the spike time stamps by a

random amount, with the minimum shuffled duration being set to 30 s and the maximum to the total length of the trial minus 30s. The end of the trial was wrapped to the beginning. A cell was classified as speed sensitive if its speed score was above the 95th percentile or below the 5th percentile of the shuffled speed score distribution, resulting in a 10% acceptance rate. In addition, this analysis was performed twice for linear and saturating speed modulation. Together, these factors are likely to yield a false positive rate above 5%.

All cells were analysed for linear and saturating speed modulation, which resulted in the speed analysis being performed twice.

Context-specific speed sensitive cells were determined by obtaining a rate difference index (*RD_I*) with the following equation (Kitamura *et al.*, 2015):

$$RD_I = (FR_{Fam1} - FR_{Fam2}) / (FR_{Fam1} + FR_{Fam2})$$

with *FR_{Fam1}* and *FR_{Fam2}* corresponding to the firing rate of the first and the second exposure of the animal to the familiar arena, respectively. The 99th percentile of these rate difference indexes was used as a threshold, in the following calculation, to determine if a cell was considered context specific. This threshold was applied to a second rate difference index, which was calculated for each cell using the average firing rate between the two exposures to the familiar arena and the firing rate in the novel arena. Cells were considered context specific if this second rate index exceeded the 99th percentile threshold. In this case, the 99th percentile was used instead of the 95th percentile to keep consistency with the methods followed in (Kitamura *et al.*, 2015).

2.3.10. Head direction sensitive cells

For the analysis of cell sensitivity to head direction a time window of 0.04s was used. The direction was extracted from two LEDs attached to the headstage, and both running speed and angles were smoothed with a Gaussian filter ($\sigma = 3.75$). The firing rate was calculated for each angle bin, between 1 and 360°, and smoothed with a Gaussian filter. The angle bin size was set to 3°. The head direction score was calculated as the mean resultant vector length. Spike time stamps were shuffled 250 times and a 95th percentile of the shuffled distribution

was chosen to determine significance. Spike shuffling was performed by forward shifting the spike time stamps by a random amount, with the minimum shuffled duration being set to 30 s and the maximum to the total length of the trial minus 30s. The end of the trial was wrapped to the beginning.

Phase shifts (Taube, Muller and Ranck, 1990a) between the two exposures to the familiar arena were also computed for head direction sensitive cells. The firing rate of each angle bin in the first exposure was circularly correlated to the one of the second exposure. The head direction data for the second exposure was shifted in steps of 6° for a full circular cycle and circularly correlated at each step. The shift step with the highest circular correlation was taken as the phase shift that a head direction sensitive cell experienced between both trials.

2.3.11. Cells with grid periodicity – Langston’s method

The calculation of the grid score was as described in (Langston *et al.*, 2010). A time window of 0.04s was used. Bins containing spikes were first identified and only those in which the running speed was > 5 cm/s were considered. The arena was divided into 58 x 58 equal size bins and a firing rate map was produced. The rate map was smoothed with a 2-D convolution with a Gaussian filter ($\sigma = 1.5$).

Firstly, the firing rate map was autocorrelated, subsequently the centre of this resulting matrix was cropped. The cropped size radius increased in each step, starting at 10% of the total length up to the 50%, in steps 1%. For each size, the cropped original autocorrelation was rotated with the following angles: 0°, 30°, 60°, 90°, 120°, 150°, and correlated with the original autocorrelation. Grid scores were calculated as the difference between values at 30°, 90° and 150° and values at 60° and 120°, which correspond to rotation angles with low and high correlations, respectively.

Spike time stamps were shuffled 250 times and grid scores were again calculated as explained above. Only scores above the 95th percentile, computed from the distribution of the shuffled data, were considered significant. Spike shuffling was performed by forward shifting the spike time stamps by a random amount, with

the minimum shuffled duration being set to 30 s and the maximum to the total length of the trial minus 30s. The end of the trial was wrapped to the beginning.

2.3.12. Cells with grid periodicity – Sargolini’s method

A second method was used to analyse cells with grid periodicity as described in (Sargolini *et al.*, 2006). To perform this analysis, the CMBHOME MATLAB toolbox was used (<https://github.com/hasselmonians/CMBHOME/wiki>). A time window of 0.04s was used. Bins containing spikes were first identified and only those in which the running speed was > 5 cm/s were considered. The arena was divided into 50 x 50 equal size bins and both spike and occupancy maps were produced. Both the spike and occupancy maps were smoothed with a 2-D convolution with a Gaussian filter ($\sigma = 1.73$). Firstly, a firing rate map was obtained by dividing the smoothed spike map by the smoothed occupancy map.

Secondly, the autocorrelation of the smoothed firing rate map was obtained. This autocorrelation, which was based on Pearson’s product moment correlation coefficient, is described by the following formula:

$$r(\tau_x, \tau_y) = \frac{n\sum\lambda(x, y)\lambda(x - \tau_x, y - \tau_y) - \sum\lambda(x, y)\lambda(x - \tau_x, y - \tau_y)}{\sqrt{n\sum\lambda(x, y)^2 - (\sum\lambda(x, y))^2} \sqrt{n\sum\lambda(x - \tau_x, y - \tau_y)^2 - (\sum\lambda(x - \tau_x, y - \tau_y))^2}}$$

With $\lambda(x, y)$ referring to the average firing rate of a cell in the coordinates (x, y) , τ_x and τ_y to the spatial lags and n to the number of overlapping spatial bins.

Subsequently, the centre peak of the autocorrelation was removed and the surrounding 6 or less peaks were identified to produce a donut. The donut was rotated in steps of 3° at a time, up to 360°. A correlation was obtained between the original donut and the rotated one at each of these steps. The highest correlation values are expected at 60° and 120°, whereas the lowest are expected at 30°, 90°, 150°. The grid score was obtained by subtracting the highest correlation value within the values at 30°, 90° and 150°, from the lowest correlation value within the values at 60° and 120°.

Elliptical correction, which was first described in (Brandon *et al.*, 2011), was also performed with the CMBHOME MATLAB toolbox (<https://github.com/hasselmonians/CMBHOME/wiki>). The correction was only attempted if 6 surrounding peaks were detected in the autocorrelation. These peaks were used to fit an ellipse and its major and minor axis were obtained. An eccentricity factor was obtained by dividing the minor axis by the major axis. Elliptical correction was only applied for eccentricity values below 0.5 and if the resulting corrected grid score was higher than the uncorrected one. Elliptical correction was performed by resizing the major axis with the eccentricity factor.

Spike time stamps were shuffled 250 times and grid scores were again calculated as explained above. Spike shuffling was performed by forward shifting the spike time stamps by a random amount, with the minimum shuffled duration being set to 30 s and the maximum to the total length of the trial minus 30s. The end of the trial was wrapped to the beginning. Only scores above the 95th percentile, computed from the distribution of the shuffled data, were considered significant.

2.3.13. Spatial information

The spatial information (Skaggs, McNaughton and Gothard, 1993) was calculated using the following equation:

$$SI = \sum(P_i(R_i/R)\log_2(R_i/R))$$

With SI corresponding to the spatial information, R to the mean firing rate, R_i to the firing rate in bin i and P_i to the occupancy probability of a spatial bin.

Spike time stamps were shuffled 250 times and spatial information scores were again calculated as explained above. Only scores above the 95th percentile, computed from the distribution of the shuffled data, were considered significant. Spike shuffling was performed by forward shifting the spike time stamps by a random amount, with the minimum shuffled duration being set to 30 s and the maximum to the total length of the trial minus 30s. The end of the trial was wrapped to the beginning.

2.3.14. Border sensitive cells

The calculation of border scores was based on the analysis described in (Solstad *et al.*, 2008), and followed this equation:

$$\text{Border scores} = (\text{Max}_C - \text{Mean}_{FD}) / (\text{Max}_C + \text{Mean}_{FD})$$

with Max_C corresponding to the maximum coverage and Mean_{FD} to the mean firing distance. A threshold of 30% of the maximum firing rate was obtained and only firing rates above this threshold were considered. The borders of the arena were defined as 10% of the distance from the wall. The arena was split into 58 by 58 bins of equal size and a firing rate map was generated. The occupied bins within 10% of the distance from each of the walls were divided by the total number of bins within each of these areas. This produced the coverage in each of the walls. The most occupied wall of the arena was set equal to the maximum coverage. The firing rate map was normalised to the summation of all firing rates above the threshold. The distance of each bin from the wall was represented with a pyramid shaped matrix of equal size to the firing rate map. The bins within the pyramid shaped matrix with an equivalent firing rate above 0 were averaged to obtain the mean firing distance.

Spike time stamps were shuffled 250 times and border scores were again calculated as explained above. Only scores above the 95th percentile, computed from the distribution of the shuffled data, were considered significant. Spike shuffling was performed by forward shifting the spike time stamps by a random amount, with the minimum shuffled duration being set to 30 s and the maximum to the total length of the trial minus 30s. The end of the trial was wrapped to the beginning.

2.3.15. Novelty effects

It was apparent that not all cells behaved in the same way when the different scores for each functional cell subtype were compared between the two familiar and the novel trials. The scores of some cells decreased with novelty, others increased, and some did not show any changes related to novelty. Four main

different patterns were observed (Fig. 2.8) and cells were classified according to them. Cells were classified as “decreasing” if their score was lower in the novel trial than in both familiar trials, as “increasing” if their score was higher in the novel trial than in both familiar trials and as “no changes” if their scores did not follow either of these patterns. “No changes” cells encompassed mainly two patterns: (1) cells whose score increased in the novel trial and further increased in the second exposure to the familiar trial and (2) cells whose score decreased in the novel trial and further decreased in the second exposure to the familiar trial.

Spatially modulated cells are usually identified during the exploration of familiar environments. However, limiting the identification of spatially modulated cells to the familiar exposures may mask effects of cells becoming more spatially modulated during the exploration of novel environments. Nevertheless, there is a potential that “increasing” cells are the result of an artefact of the recording procedures. In this experiment, all the recording equipment between both recording rooms was the same. In addition, the number of animals which experienced either recording room 1 or 2 as their novel room was counterbalanced in both groups. Taken together, it was deemed appropriate to identify spatially modulated cells also during the exploration of the novel environment.

There is also a potential that the variations in the different scores described above are the result of chance, and therefore not related to novelty. Thus, it was necessary to assess if the observed proportions of “decreasing” and “increasing” cells were significantly different to those that could be expected if these changes were purely occurring by chance. The approach taken in this study was to simulate randomly changing scores for the novel trial and the second familiar trial, based upon the scores obtained in the first familiar trial.

The first step to generating the simulated data was to subtract the scores observed in the first and second familiar trials from the scores observed in the novel trial, thus obtaining two sets of differences, $diff_1$ and $diff_2$. To achieve this, the following equations were used:

$$diff_1 = S_{nov} - S_{fam1}$$

$$diff_2 = S_{nov} - S_{fam2}$$

with S_{nov} corresponding to the scores in the novel trial, S_{fam1} corresponding to the scores in the first familiar trial and S_{fam2} corresponding to the scores in the second familiar trial. The standard deviation of both sets of differences, $diff_1$ and $diff_2$, were calculated and used to generate two random new sets of differences, $diff'_1$ and $diff'_2$, with zero mean and with each respective standard deviation. One hundred iterations of this process were performed.

The scores corresponding to the first familiar trial were used as a base to calculate simulated values for the novel and the second familiar trials. The simulated scores for the novel trial (S'_{nov}) were obtained by adding the first set of simulated differences ($diff'_1$) to the scores of the first familiar trial (S_{fam1}). The simulated scores for the second familiar trial (S'_{fam2}) were obtained by subtracting the second set of simulated differences ($diff'_2$) from the simulated scores for the novel trial (S'_{nov}). This process is described with the following equations:

$$S'_{nov} = S_{fam1} + diff'_1$$

$$S'_{fam2} = S'_{nov} - diff'_2$$

As performed with the observed data, simulated data was classified into “decreasing”, “increasing” and “no changes” cells using the scores observed in the first familiar trial, S_{fam1} , and the simulated scores for the novel and second familiar trial, S'_{nov} and S'_{fam2} . Although no limitations were imposed on this simulation, 4 outcomes were statistically equally probable: (1) the score was lower in the novel trial than in both familiar trials, (2) the score was higher in the novel trial than in both familiar trials, (3) the score increased in the novel trial and further increased in the second familiar trial, and (4) the score decreased in the novel trial and further decreased in the second familiar trial. Therefore, options 1 and 2, which correspond to “decreasing” and “increasing” cells respectively, should match the statistically expected proportions of approximately 25% each.

To study if the proportion of decreasing cells was higher than chance levels, the proportions of “decreasing” cells observed in wild type (WT) and J20 mice were compared to the simulated proportions. The same process was used to study if the proportions of “increasing” cells were higher than chance levels in WT and J20 mice.

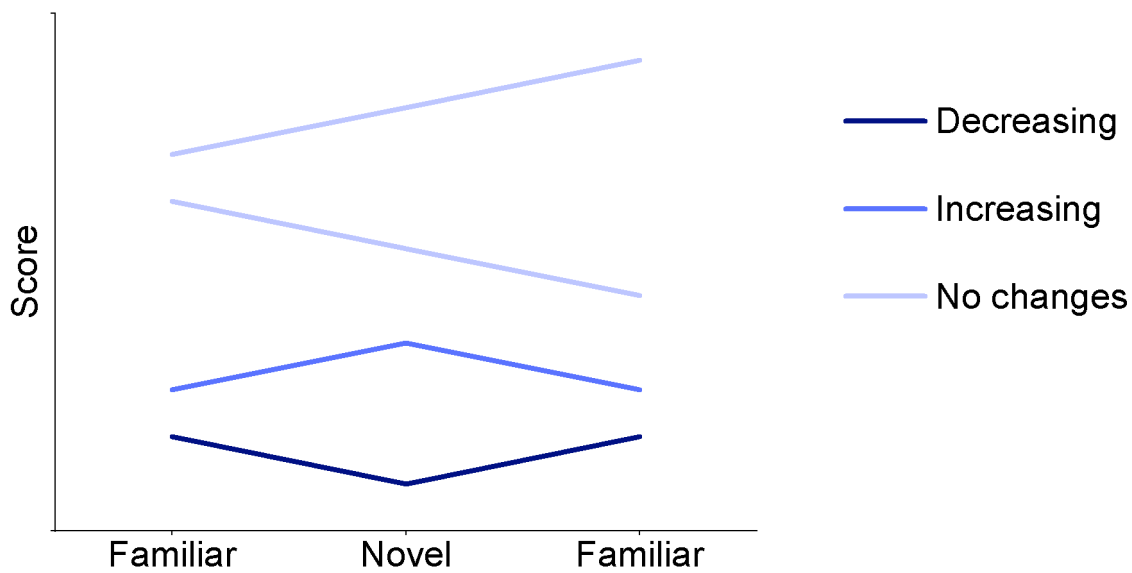


Figure 2.8 Diagram showing the different patterns observed. This diagram shows the pattern followed by “decreasing”, “increasing” and “no changes” cells.

2.4. Perfusions and histology

At the end of the experiments, all animals were injected with 0.1 ml of sodium pentobarbital. Electrolytic lesions were performed using a constant current isolated stimulator (Digitimer DS3). 5 pulses with an amplitude of 100 µA and a duration of 1 s were performed in all channels in 10-15 mo mice and in the top and bottom channels in 6 mo mice. Subsequently, all mice were perfused with 4% paraformaldehyde (PFA) and the brains stored in the same solution. For determining the electrode positions, the brains were cut into 50 µm sagittal sections with a vibratome (Leica), mounted on frosted microscope slides and allowed to dry at room temperature for 1 day. The next day, slices were stained by immersing them in a 1% cresyl violet solution, dehydrated in alcohol and cleared in xylene before being mounted. Afterwards, brain slices were visualised with a 4x objective on a light microscope. Images of the slices containing the electrolytic lesions were taken using the QCapture pro 7 software (Qimaging). The layer and depth in which the probe was located was estimated using the Paxinos and Franklin brain atlas (Paxinos and Franklin, 2001).

2.5. Statistical analysis

All statistical analysis for repeated measured data was performed with linear mixed-effects models when the inclusion of mixed effects improved the model. For this analysis, the ‘lme4’ package in R studio was used (<https://cran.r-project.org/web/packages/lme4/lme4.pdf>). Depending on the distribution of the residuals of the response variable, the functions ‘lmer’ or ‘glmer’ were used. The function ‘lmer’ was used for Gaussian distributions and ‘glmer’ for other distributions with the appropriate distribution family to ensure the best model fit. If including mixed effects did not improve the model, the ‘lm’ or ‘glm’ functions in R studio were used instead, depending on if the residuals of the response variable followed a Gaussian distribution or not. Models were specified from simplistic to complex and compared with a likelihood-ratio test. If no significant differences between the models were detected, the simplest model was selected. If there were significant differences, the model with the lowest Akaike Information Criterion (AIC) (Akaike, 1974) was selected. Lower values of the AIC, which is expressed with the following equation, represent a better fit of the model:

$$AIC = -2 \log(L) + 2K$$

Where L corresponds to the maximum likelihood of the model and K to the number of parameters within the model. The functions ‘joint_tests’ and ‘emmeans’ from the package ‘emmeans’ were used for main effects and post-hoc pairwise comparisons with Tukey corrections, respectively. Linear mixed-effects models allowed the specification of the hierarchical structure of the data and of repeated measures. Infinite degrees of freedom are obtained with the functions ‘joint_tests’ and ‘emmeans’ when estimates are tested against the standard normal (z) distribution instead of the t-distribution. This is always the case for generalised linear mixed-effects models (‘glmer’). It is important to note that the t-distribution with infinite degrees of freedom is equivalent to the z distribution (Brereton, 2015). The proportions of different cell types were compared through a Fisher's exact test, when the n numbers were low (Kim, 2017), and through a linear mixed-effect model with a binomial distribution when the numbers were sufficiently high.

Chapter 3. Assessment of novel and familiar environmental stimuli effects in the MEC neuronal networks

3.1. Introduction

Impairments in spatial navigation and memory are present at an early stage in AD patients, which manifests as wandering and getting lost in familiar and unfamiliar places (Henderson, Mack and Williams, 1989; Allison *et al.*, 2016). Relevantly, these impairments have also been described in amyloid mouse models (Reiserer *et al.*, 2007; Walker *et al.*, 2011), in both mice and rats after hippocampal chronic infusion of A β peptides (Morzelle *et al.*, 2016; Macêdo *et al.*, 2018) and in an amyloid rat model which develops tau pathology (Cohen *et al.*, 2013). In specific, J20 mice have also been reported to exhibit spatial memory impairments (Harris *et al.*, 2010; Wright *et al.*, 2013; Etter *et al.*, 2019), with these deficits being present at 4 months of age (Wright *et al.*, 2013).

Cognitive processes, such as memory, are likely to require the synchronous activity of neuronal ensembles (Varela *et al.*, 2001; Ward, 2003), which is reflected in the neuronal oscillations (Buzsáki, 2006). The synchronization of these neuronal oscillations across different brain regions is believed to allow for the processing, transfer and storage of information (Engel, Fries and Singer, 2001; Buzsáki and Draguhn, 2004). Theta oscillations are the most prominent rhythm in the MEC of rodents (Mitchell and Ranck, 1980) and are hypothesised to provide a temporal window of activity, which may link related neuronal ensembles (Buzsáki, 2006; Jensen and Colgin, 2007; Sirota *et al.*, 2008). Theta oscillations have been widely linked to spatial navigation and memory in rodents (Winson, 1978; Buzsáki, 2005; Wells *et al.*, 2013). The MEC plays a key role in path integration (Parron and Save, 2004; Jacob, Gordillo-Salas, *et al.*, 2017), a process which requires the integration of speed and heading direction information to estimate the current position (Savelli and Knierim, 2019). Theta frequency oscillations are hypothesised to be one of the candidates which may provide the speed signal necessary for path integration (Hinman *et al.*, 2016; Dannenberg *et*

al., 2019). It has been shown that both the frequency and power of these oscillations increase in relation to running speed in different areas of the brain such as the MS, the hippocampus and the MEC (Hinman *et al.*, 2011; Wells *et al.*, 2013; Chen *et al.*, 2016). In the same manner, high gamma frequency oscillations also increase their power with running speed during exploratory behaviours in the MEC (Chen *et al.*, 2011; Newman *et al.*, 2013). However, these increases could also reflect changes in the processing of sensory inputs at faster running speeds (Grieves and Jeffery, 2017; Dannenberg *et al.*, 2019).

The relationship of theta oscillations with running speed is not fixed and seems to be affected by different factors, such as the absence of visual inputs and the novelty of the environment (Wells *et al.*, 2013; Chen *et al.*, 2016). The exposure to novel and familiar environments appears to affect the running speed-frequency slope of theta oscillations in the hippocampus and the MEC, decreasing or increasing it, respectively (Newman *et al.*, 2013; Wells *et al.*, 2013). In an opposite manner, the power slope of high gamma oscillations has been observed to decrease with familiarity in both brain regions (Kemere *et al.*, 2013). These changes are especially relevant as they may be used as a metric to study memory deficits and provide an insight into the mechanisms behind the spatial navigation and memory impairments observed in J20 mice.

MS GABAergic projections onto GABAergic interneurons appears necessary to drive theta oscillations in the hippocampus and the MEC (Hangya *et al.*, 2009; Gonzalez-Sulser *et al.*, 2014; Bender *et al.*, 2015). Furthermore, evidence suggests that networks of FS interneurons generate gamma oscillations (Cardin *et al.*, 2009; Sohal *et al.*, 2009; Pastoll *et al.*, 2013). It has been observed that J20 mice exhibit a progressive loss of MS GABAergic synaptic complexity and innervations onto FS hippocampal interneurons (Rubio *et al.*, 2012), which may also occur in the MEC. In addition, FS interneurons show a more depolarized resting membrane potential and reduced amplitude in the action potentials in the parietal cortex of J20 mice (Verret *et al.*, 2012). Taken together, these deficiencies in the GABAergic system could have an impact on theta and gamma oscillations in these mice, which may be linked to the spatial navigation and memory impairments observed. In this regard, reductions in gamma power have been previously observed in J20 mice (Verret *et al.*, 2012; Etter *et al.*, 2019).

Furthermore, synaptic plasticity dysfunction has been described in the hippocampus of these mice (Saganich *et al.*, 2006), which may be associated to memory deficits (Neves, Cooke and Bliss, 2008).

Despite the important role that the MEC plays in spatial navigation and memory, the effects of contextual novelty and familiarity on the network oscillations of amyloidopathy models remain unexplored. It is therefore the main aim of this chapter to study how the relationship with running speed of theta and gamma frequency oscillations change with novelty and familiarity in the MEC of WT and J20 mice.

3.2. Methodology

3.2.1. Animals

Two different age points were used in the experiments described below. 6 mo WT ($n = 7$) and J20 ($n = 8$) mice which represent the middle stage of the disease. At this age point, these mice show spatial navigation and memory impairments (Wright *et al.*, 2013) but no widespread plaques (Hong *et al.*, 2016). The second age point corresponded to 10 – 15 mo WT ($n = 6$) and J20 ($n = 5$) mice which exhibit widespread plaques (Hong *et al.*, 2016).

All mice underwent stereotaxic surgeries to implant 4-channel silicon probes (Q1x4-5mm-200-177-CQ4, NeuroNexus Technologies, see section 2.3.1 in the general methodology for more details) in the dorsal MEC. All probes were implanted at 3.11 mm mediolateral and 5.25 mm anteroposterior, with angles ranging from 5-10 degrees, with the tip of the probe pointing anteriorly. Initially, probes were implanted in 10 – 15 mo mice at 1.25 mm dorsoventrally. However, subsequent histology highlighted that some of the top channels of the probe were placed above the dorsal border of the MEC. Because of this, probes were implanted 0.4 mm deeper in 6 mo mice, at 1.65 mm, to place all channels within the dorsal MEC. Thus, probes were implanted at 1.65 mm and 1.25 mm dorsoventrally in 6 mo and 10 – 15 mo mice, respectively.

Part of the stereotaxic surgeries and the behavioural experiments done in the 10 – 15 mo mice group were performed by Dr Thomas Ridler, who also assisted with the design of the behavioural task.

3.2.2. Behavioural experiments

3.2.2.1 Triangular track

Prior to the start of this experiment all animals were food restricted, as described in section 2.2.1, to encourage mice to perform this task. 10-15 mo and 6 mo mice were used in this experiment. All mice were placed in the triangular track and encouraged to explore it for 30 – 40 minutes each day for 2 consecutive days (Fig. 2.1B). Mice could either explore the right or left arm of the modified T-maze and it was counterbalanced between groups. During every recording session the LFP signals were recorded and the mouse's location tracked using an overhead camera and two LEDs attached to the headstage. See section 2.2.1 in the general methodology for more details.

3.2.2.2 Two open arenas

For the duration of this experiment, mice were not food restricted. This experiment used two different open arenas of equal surface, circular and square, which were annotated with different cues (Fig. 2.2A and B). An overhead dim source of light was provided for the duration of the recording session.

Only 6 mo WT and J20 mice were used in this experiment. All mice were placed in one of these two open arenas, either circular or square, for 4 consecutive days (Fig. 2.2C). Mice were placed in the open arena for 15 minutes twice a day, with an interval of 15 minutes in between. Each animal was exposed to the familiar environment for a total of 8 times. On the 5th day, mice were placed on the opposite arena (Fig. 2.2C), which acted as a second novel arena, and left to explore it twice for 15 minutes with an interval of 15 minutes. During every recording session the LFP signals were recorded and the mouse's location

tracked using an overhead camera and two LEDs attached to the headstage. See section 2.2.2.1 in the general methodology for more details.

3.2.3. Data acquisition and analysis

Electrophysiological and tracking data was continuously sampled at 30 kHz and recorded through the duration of each recording session. However, this was an oversampling of the tracking data as the camera frame rate was 30 Hz.

The average running speed and the time spent at the border of the arena was computed for each animal in each trial and used for comparisons. The border area was specified as 15 cm from the walls of the open arenas.

Custom made MATLAB scripts were used for data analysis and the Chronux toolbox for MATLAB (available at <http://chronux.org/>) was used to perform LFP spectral analysis. LFP frequencies were divided in the following bands: Theta (5-12 Hz) and high gamma (60-120 Hz). Channel selection was performed as described in section 2.3.5 of the general methodology. Only the first two and the last two channels were considered for channel selection in 6 mo and 10-15 mo mice, respectively. This was due to the differences in the implantation depth of probes, which were implanted dorsoventrally at 1.65 mm in 6 mo mice and at 1.25 mm in 10-15 mo J20 mice. The relationship between high gamma and theta oscillations with running speed was studied obtaining the mean peak frequency and power of these frequency bands at each running speed bin (bin size = 3 cm/s; 4 speed bins in total from 3 cm/s to 15 cm/s for the triangular track experiment and 5 speed bins in total from 3 cm/s to 18 cm/s for the two open arenas experiment). The mean power at each running speed bin was normalised relative to the mean power in the first speed bin. Both the normalised power and the frequency vs running speed were fitted using a linear fit, with the resulting slopes and intercepts used for comparisons.

To measure theta-high gamma PAC the MI (Canolty *et al.*, 2006) was calculated using an MATLAB toolbox which is available upon request at: <https://data.mrc.ox.ac.uk/data-set/matlab-toolbox-estimating-phase-amplitude-coupling> (Onslow, Bogacz and Jones, 2011). PAC matrices were obtained for

each running speed bin (bin size = 3 cm/s; 4 speed bins in total from 3 cm/s to 15 cm/s for the triangular track experiment and 5 speed bins in total from 3 cm/s to 18 cm/s for the two open arenas experiment) and normalised. MI values at each running speed bin were calculated as the summation of all the PAC values within the frequency limits high gamma oscillations. The slopes resulting from the linear fit between MI values and running speed were used for comparisons. See sections 2.3.3 to 2.3.5 in the general methodology for further details.

3.2.4. Statistical analysis

Linear mixed effects models were used to analyse all the data presented in this chapter, using the package ‘lme4’ in R studio. When the residuals of the response variable followed a Gaussian distribution, the function ‘lmer’ of this package was used. When they followed a non-Gaussian distribution, the function ‘glmer’ was used instead with the appropriate family of distribution. Increasingly complex models were built for each response variable and the AIC values of each model compared to assess the best fit when significant differences between models were present. These models accounted for repeated measures belonging to the same animal. The possible effects of layer variability, of using different open arenas and if recordings were performed in the morning or afternoon were also considered when relevant for each model. See section 2.5 in the general methodology for further details.

The main effects obtained by the liner mixed effects models are reported with the F-statistic (F), with its associated degrees of freedom within brackets, and the p value (p). The results obtained with pairwise comparisons by the linear mixed effects models are reported with the fixed-effects estimate (β), the standard error (SE), the t-statistic (t) and the p value (p). The z-statistic (z) is reported, instead of the t-statistic, when the function ‘glmer’ for generalised mixed effects models is used.

3.3. Results

3.3.1. Assessment of novel and familiar environmental stimuli effects in the MEC neuronal networks with a triangular track

Initially, the effects of environmental familiarity were assessed with a pilot study, in which J20 and WT mice were placed in a triangular track and encouraged to explore it in two different trials carried out in consecutive days. Trial 1 was a novel trial as it was the first time these animals were exposed to the environment, with trial 2 as a more familiar trial as it was the second time (Fig. 2.1B). This study was performed in two different age groups, 6 mo and 10-15 mo, aiming to model the middle and late stage of the disease, respectively. Recordings were performed mainly in the superficial layers of the dorsal MEC in both 6 mo (Fig. 3.1) and 10-15 mo (Fig. 3.2) mice. In both of these age groups spatial memory and learning impairments are present (Wright *et al.*, 2013). However, although amyloid plaques are present at between 5-7 mo in the dentate gyrus and neocortex, widespread plaques only occurs at between 8-10 mo (Hong *et al.*, 2016).

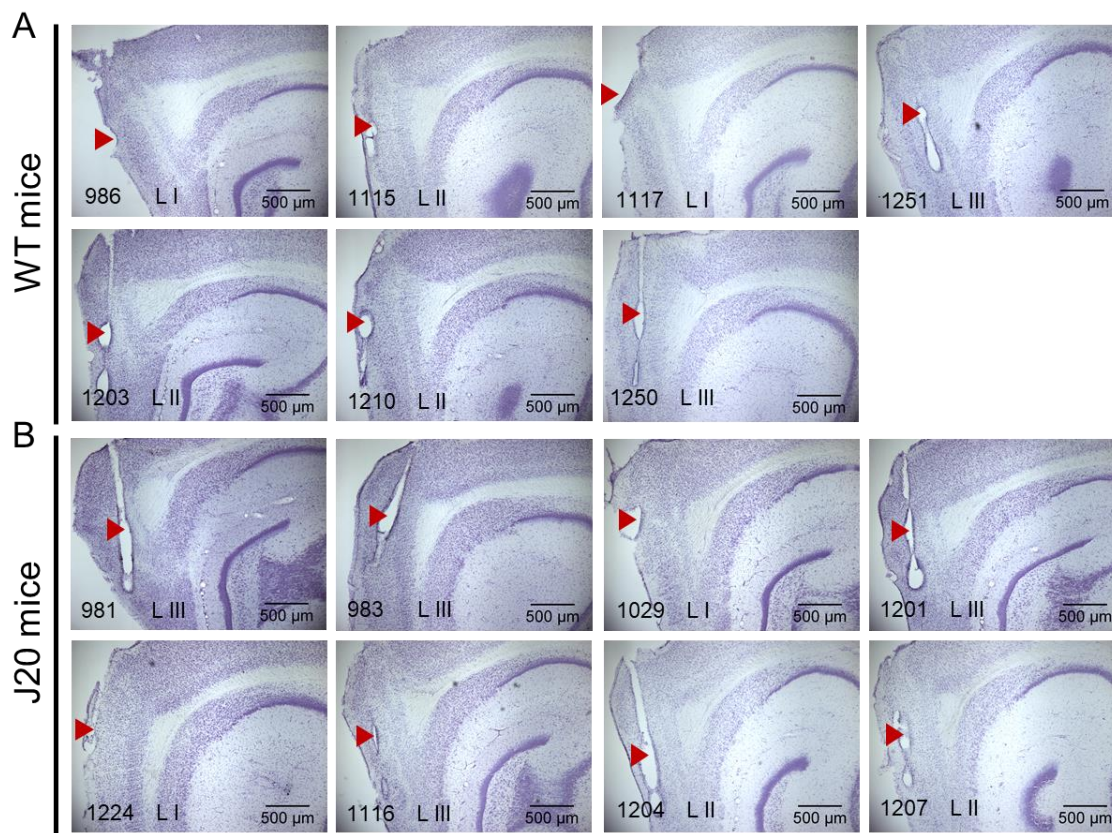


Figure 3.1 MEC recording sites of 6 mo mice. A) Recording sites for WT mice. **B)** Recording sites for J20 mice. Numbers show the animal ID, with the estimated layer on the right. Red arrows show the probable location of the first recording channel.

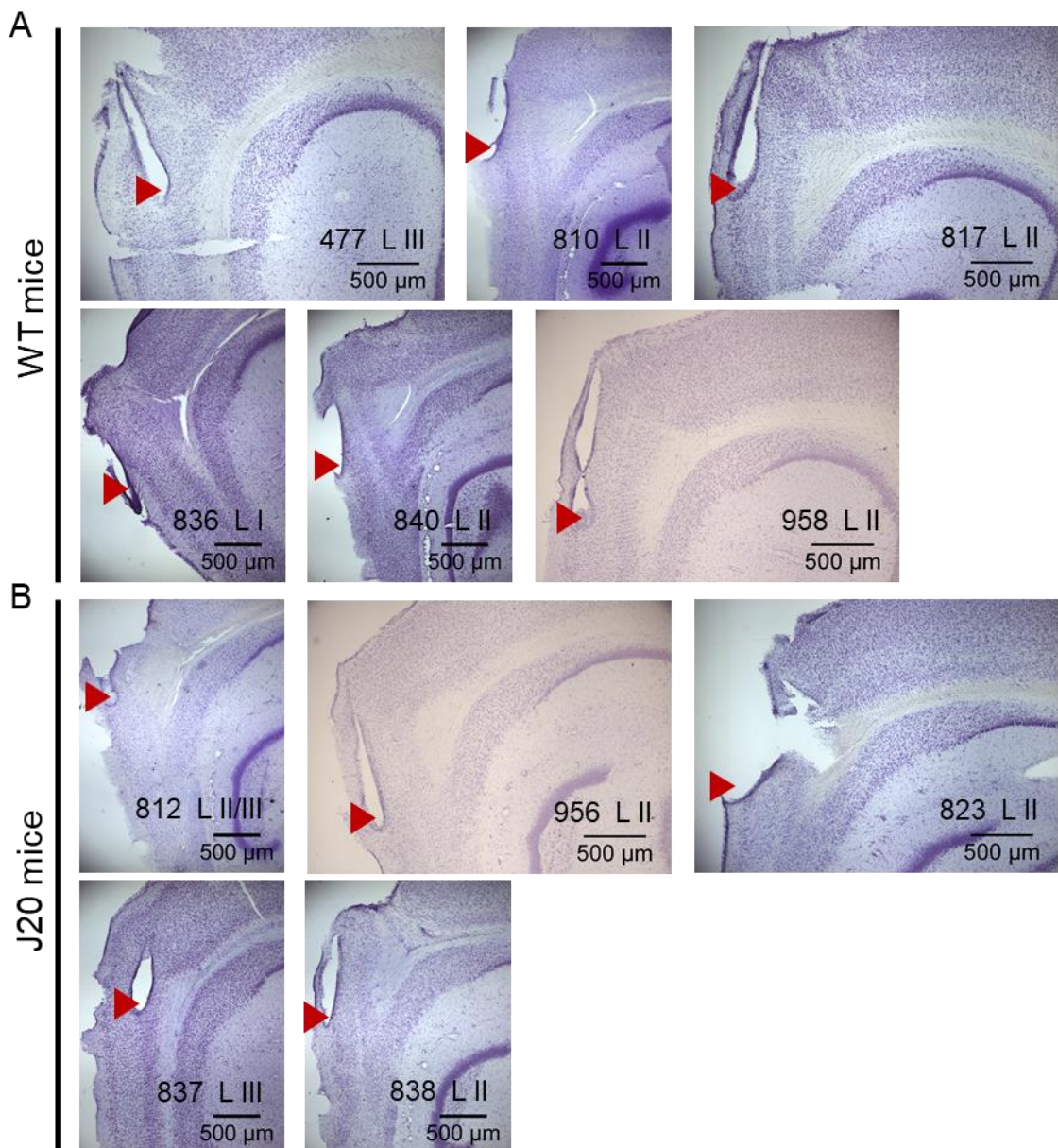


Figure 3.2 MEC recording sites of 10 – 15 mo mice. A) Recording sites for WT mice. **B)** Recording sites for J20 mice. Numbers show the animal ID, with the estimated layer on the right. Red arrows show the probable location of the last recording channel.

3.3.1.1 J20 mice do not reduce their running speed with familiarity

The time that animals in each group spent at each running speed bin is represented in figure 3.3A. The average running speed of the animals in each group was further analysed. As a result of an increased familiarity to the environment, a significant interaction between genotype and trial was observed ($F(1, \text{Inf}) = 16.48, p < 0.0001$, Fig. 3.3B). Further pairwise comparisons showed

that WT mice of both age groups experienced a significant decrease in their average running speed ($\beta = 0.27$, $SE = 0.06$, $z(52) = 4.55$, $p < 0.0001$, Fig. 3.3B), which was not observed in J20 mice ($\beta = -0.07$, $SE = 0.06$, $z(52) = -1.23$, $p = 0.61$, Fig. 3.3B).

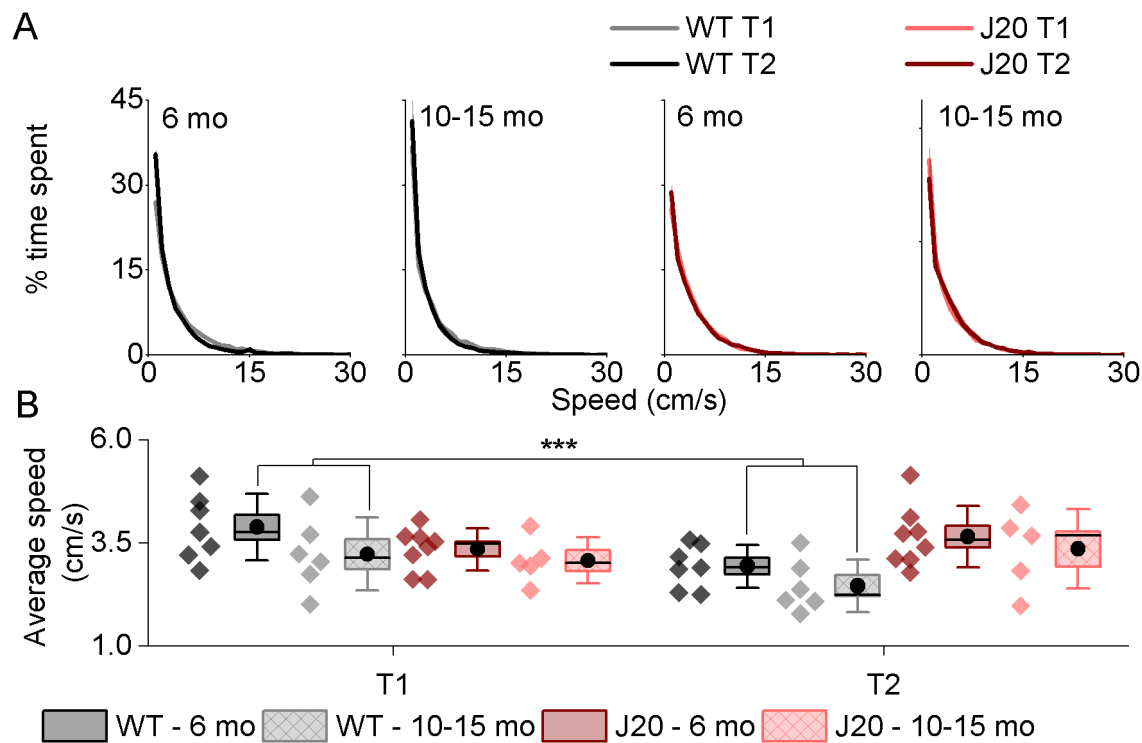


Figure 3.3 J20 mice do not reduce their running speed in trial 2. A) Average time spent in each running speed bin, from 0 to 30 cm/s, expressed as a percentage. This is shown for the first and second exposure to the triangular track for both age groups of WT and J20 mice. **B)** Average speed decreases in trial 2 for WT mice but not for J20 mice. Line plots: line corresponds to the mean and error bars represent the \pm SEM. Box plots: box corresponds to the mean \pm SEM, the circle to the mean, the line to the median and the whiskers to the SD. (* $p \leq 0.05$, ** $p \leq 0.01$, *** $p \leq 0.001$)

3.3.1.2 Broadband spectral analysis

Spectral analysis was performed for theta and high gamma frequency bands, and the power in these bands normalised with the total broadband power. Total broadband power in each trial can be observed in figure 3.4A for each of the groups analysed here. The normalised theta power was not different between both genotypes ($F(1, 22) = 2.08$, $p = 0.16$, Fig. 3.4B). In addition, no effects of

trial were seen ($F(1, 22) = 0.01$, $p = 0.92$, Fig. 3.4B). Normalised high gamma power was not affected by genotype ($F(1, Inf) = 0.28$, $p = 0.60$, Fig. 3.4C). However, a significant interaction between trial and age was seen ($F(1, Inf) = 10.27$, $p = 0.001$, Fig. 3.4C), with pairwise comparisons showing a significant difference in power between trials 1 and 2 in 6 mo mice ($\beta = 0.18$, $SE = 0.05$, $z(52) = 3.69$, $p = 0.001$, Fig. 3.4C) but not in 15 mo mice ($\beta = -0.06$, $SE = 0.06$, $z(52) = -1.06$, $p = 0.71$, Fig. 3.4C).

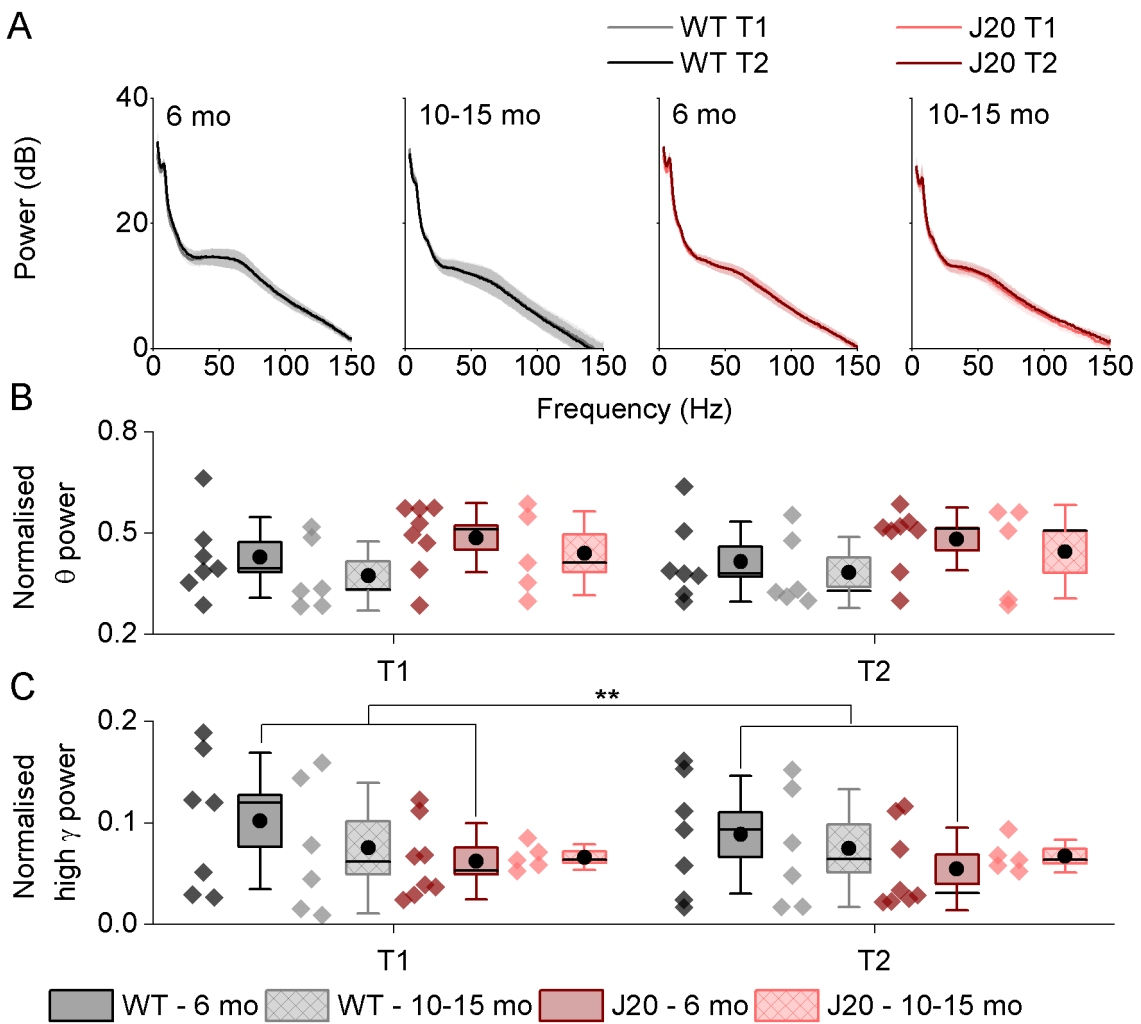


Figure 3.4 Power spectrum shows no deficits in J20 mice. A) Pooled power spectrum averaged across animals in each group for each trial. **B)** Pooled data showing power in theta band, normalised using the broadband power, in the different groups and trials. **C)** Pooled data showing power in high gamma band, normalised using the broadband power, in the different groups and trials. Line plots: line corresponds to the mean and error bars represent the \pm SEM. Box plots: box corresponds to the mean \pm SEM, the circle to the mean, the line to the median and the whiskers to the SD. (* $p \leq 0.05$, ** $p \leq 0.01$, *** $p \leq 0.001$)

3.3.1.3 MEC network oscillations

The changes in power and frequency with running speed of the different frequency bands were quantified through the slopes resulting from linear fits and compared between groups and trials. The relationship of theta power and frequency with running speed, averaged across animals in each group, can be seen in figure 3.5Ai and ii. Theta power slopes were not affected by genotype

($F(1, 22) = 0.61$, $p = 0.44$, Fig. 3.5B). However, a significant interaction between age and trial was observed ($F(1, 22) = 5.10$, $p = 0.03$, Fig. 3.5B), with pairwise comparisons showing a slope increase in trial 2 in 10-15 mo mice ($\beta = -0.02$, SE = 0.006, $t(52) = -2.85$, $p = 0.04$, Fig. 3.5B) but not in 6 mo mice ($\beta = 0.001$, SE = 0.005, $t(52) = 0.14$, $p = 0.999$, Fig. 3.5B). Theta frequency slopes were also not affected by genotype ($F(1, 22) = 1.54$, $p = 0.23$, Fig. 3.5C) or trial ($F(1, 22) = 0.71$, $p = 0.41$, Fig. 3.5C). A significant interaction between genotype, trial and age was observed in the intercept of theta frequency oscillations ($F(1, \text{Inf}) = 6.21$, $p = 0.01$, Fig. 3.5D), with pairwise comparisons showing a significant intercept increase in trial 2 in 10-15 mo J20 mice ($\beta = -0.06$, SE = 0.02, $z(52) = -3.13$, $p = 0.036$, Fig. 3.5D).

Changes in high gamma power and frequency with running speed, averaged across animals in each group, can be seen in figure 3.6Ai and ii. The effect of genotype on high gamma power slope showed only a trend ($F(1, 22) = 4.04$, $p = 0.057$, Fig. 3.6B) and no effects of trial were observed ($F(1, 22) = 0.27$, $p = 0.60$, Fig. 3.6B). In a similar manner, no effects of genotype (slope: $F(1, 21) = 1.02$, $p = 0.32$, Fig. 3.6C; intercept: $F(1, 22) = 2.42$, $p = 0.13$, Fig. 3.6D) or trial (slope: $F(1, 22) = 2.50$, $p = 0.13$, Fig. 3.6C; intercept: $F(1, 22) = 2.18$, $p = 0.15$, Fig. 3.6D) were observed in the frequency slope and intercept of high gamma oscillations.

To assess the PAC of theta with high gamma oscillations, the MI was calculated and the slopes, resulting from its relationship with running speed, were compared. Averaged phase-amplitude comodulograms at representative running speeds can be seen in figure 3.7, for 6 mo (Fig. 3.7A) and 10 – 15 mo mice (Fig. 3.7B). Changes in theta – high gamma MI with running speed, averaged across animals in each group, can be seen in figure 3.8A. Theta – high gamma MI slopes were not affected by genotype ($F(1, 20) = 0.17$, $p = 0.68$, Fig. 3.8B) or trial ($F(1, 22) = 0.32$, $p = 0.57$, Fig. 3.8B).

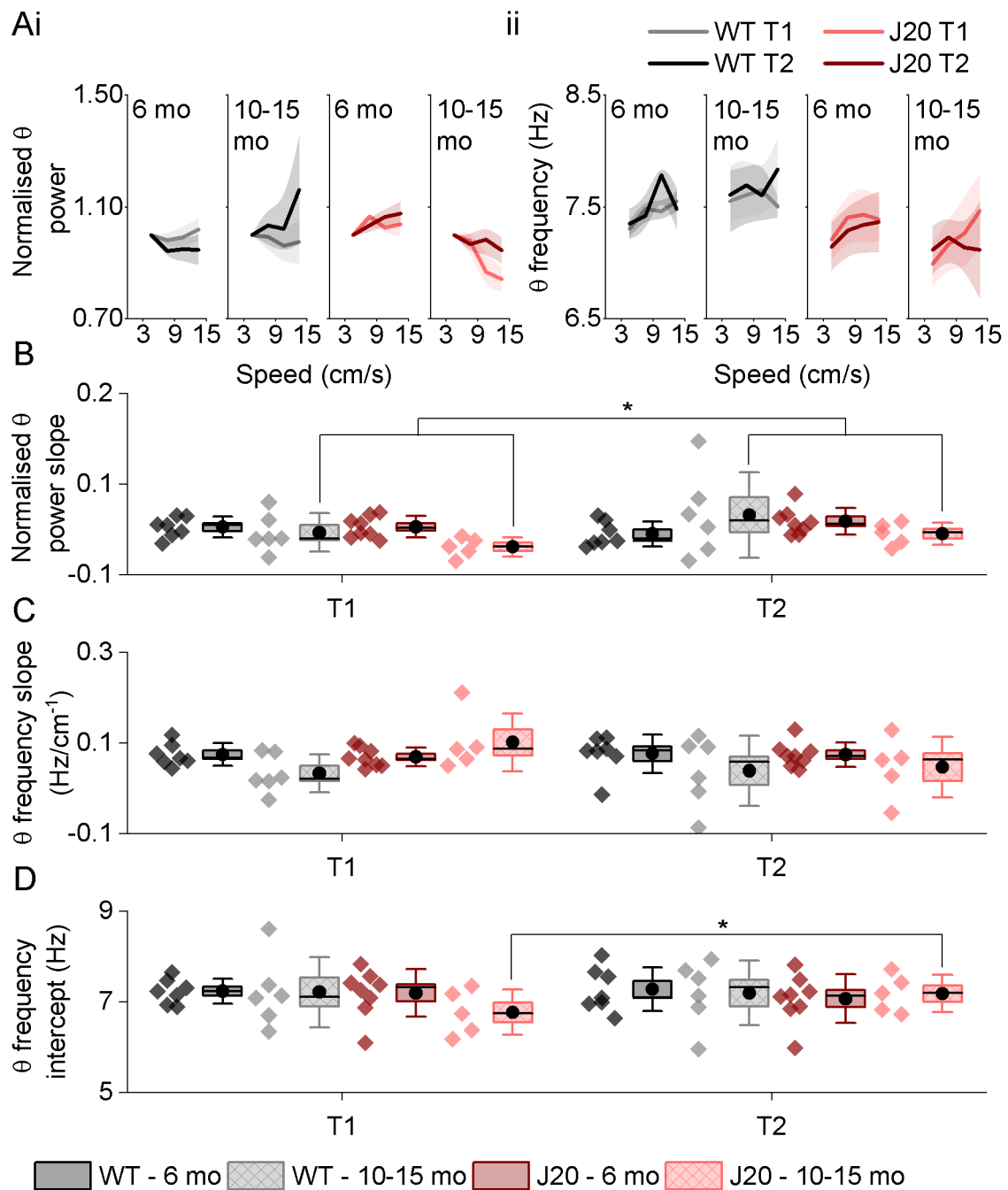


Figure 3.5 Theta power slope increaseases in trial 2 in 10 – 15 mo mice.
A) Pooled theta power (normalised using the first value) **(i)** and frequency **(ii)** versus running speed, averaged across animals in each group for each trial. **B)** Comparison of theta power – running speed slopes between each group and trial. **C)** Comparison of theta frequency – running speed slopes between each group and trial. **D)** Comparison of theta frequency – running speed intercepts between each group and trial. Line plots: line corresponds to the mean and error bars represent the \pm SEM. Box plots: box corresponds to the mean \pm SEM, the circle to the mean, the line to the median and the whiskers to the SD. (* $p \leq 0.05$, ** $p \leq 0.01$, *** $p \leq 0.001$)

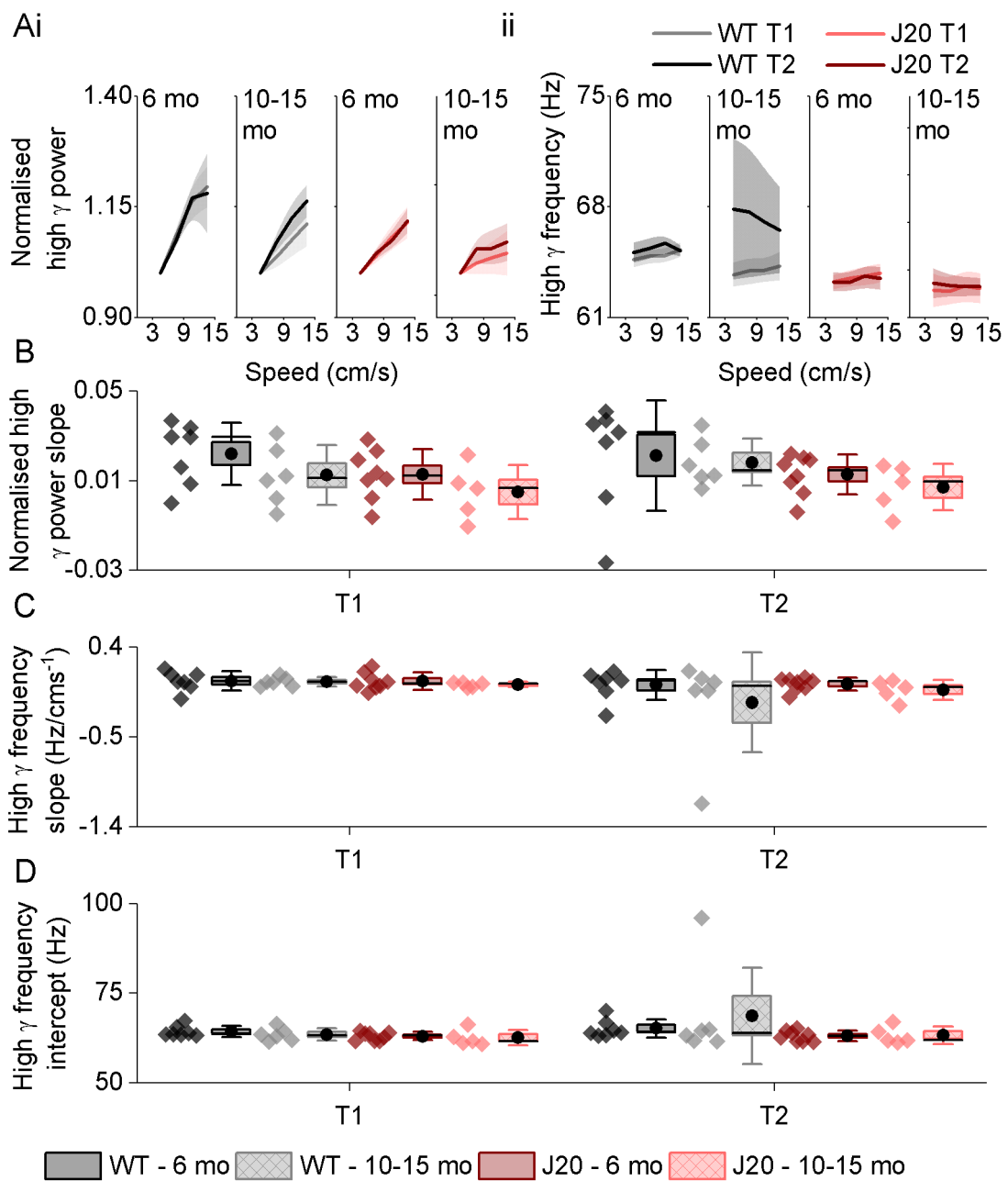


Figure 3.6 No deficits are observed in high gamma frequency oscillations in J20 mice. **A)** Pooled high gamma power (normalised using the first value) **(i)** and frequency **(ii)** versus running speed, averaged across animals in each group for each trial. **B)** Comparison of high gamma power – running speed slopes between each group and trial. **C)** Comparison of high gamma frequency – running speed slopes between each group and trial. **D)** Comparison of high gamma frequency – running speed intercepts between each group and trial. Line plots: line corresponds to the mean and error bars represent the $\pm \text{SEM}$. Box plots: box corresponds to the mean $\pm \text{SEM}$, the circle to the mean, the line to the median and the whiskers to the SD. (* $p \leq 0.05$, ** $p \leq 0.01$, *** $p \leq 0.001$)

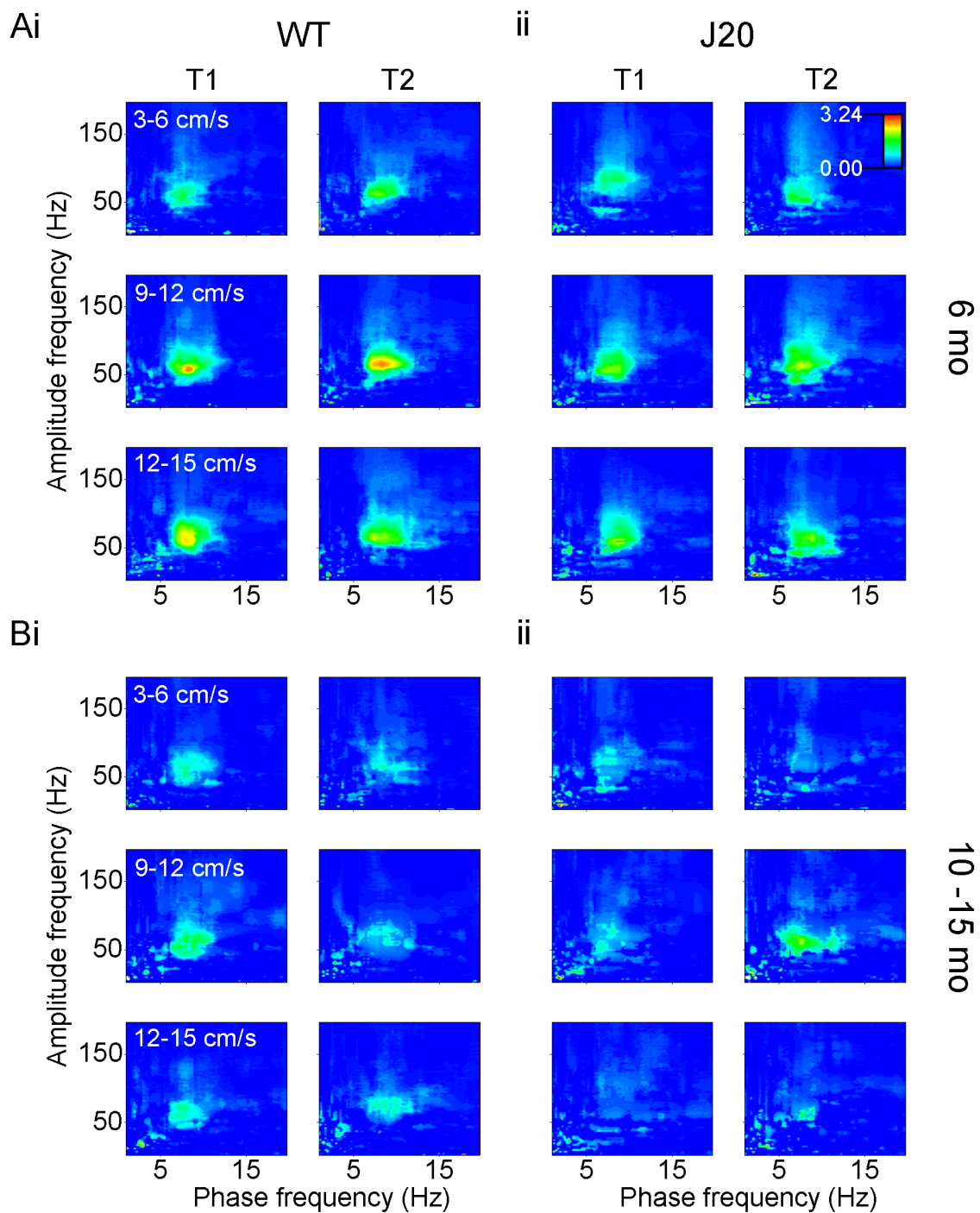


Figure 3.7 Averaged phase-amplitude comodulograms across animals. **A)** Averaged phase-amplitude comodulograms across animals in the 6 mo WT (**i**) and J20 (**ii**) mice groups for certain speed examples. **B)** Averaged phase- amplitude comodulograms across animals in the 10 – 15 mo WT (**i**) and J20 (**ii**) mice groups for certain speed examples.

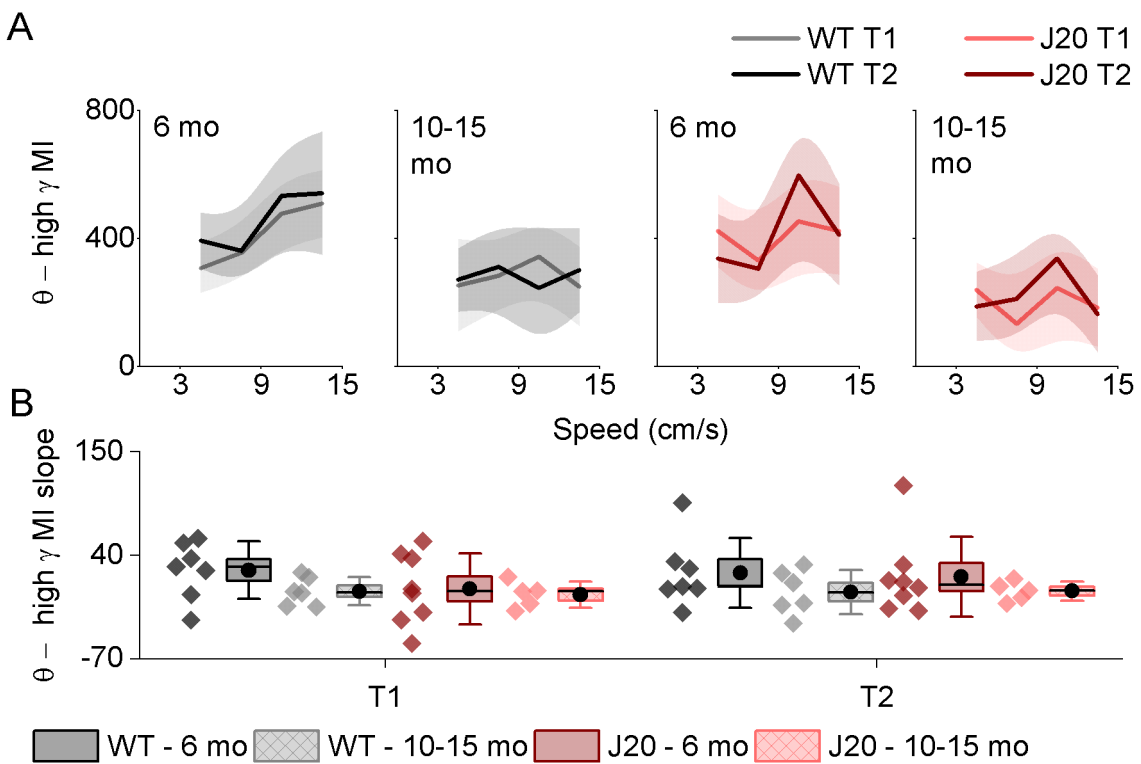


Figure 3.8 MI slopes show no differences due to trial nor between genotypes. **A)** Pooled MI values for high gamma versus running speed, averaged across animals in each group for each trial. **B)** Comparison of theta – high gamma MI – running speed slopes between each group and trial. Line plots: line corresponds to the mean and error bars represent the \pm SEM. Box plots: box corresponds to the mean \pm SEM, the circle to the mean, the line to the median and the whiskers to the SD. (* $p \leq 0.05$, ** $p \leq 0.01$, *** $p \leq 0.001$)

3.3.2. Assessment of novel and familiar environmental stimuli effects in the MEC neuronal networks with two open arenas

The experimental design of the triangular track had a few limitations. All recordings were performed in darkness with the only sources of light being the LEDs attached to the animal's headstage and the light coming from the adjoining room. However, it has been shown that total darkness reduces the relationship between the frequency of theta oscillations and running speed (Chen *et al.*, 2016). In addition, the transparent material of the triangular track walls was highly reflective, which caused tracking interference. Furthermore, two exposures to the triangular track may have not been enough to boost familiarity, as no increases in the theta frequency slope were observed in the second trial. However, this

effect has been described in literature (Newman *et al.*, 2013; Wells *et al.*, 2013). To improve these limitations, a two open arenas experiment was designed. This experiment aimed to boost environmental familiarity, by allowing a longer total exploration time along with more exposure events. Furthermore, a dim source of light was provided to allow greater access to visual landmarks. Finally, the walls of the arenas did not reflect the LED lights, decreasing tracking interferences. Only the first trial of days 1, 4 and 5 were statistically analysed, with days 1 and 5 being considered two different novel days and day 4 being considered the most familiar day (Fig. 2.2C).

3.3.2.1 J20 mice show signs of reduced anxiety

Tracking information was divided into a border and a middle area for both the circular (Fig. 3.9Ai) and the square (Fig. 3.9Aii) open arenas for each recorded session. Figure 3.9B shows time spent in the borders for both genotypes across all the recording sessions. An overall effect of genotype was observed, with J20 mice spending significantly less time in the borders of the open arena than WT mice ($F(1, \text{Inf}) = 7.43, p = 0.006$, Fig. 3.9C). No overall effects of context were observed in the time mice spent at the borders ($F(2, \text{Inf}) = 1.79, p = 0.17$, Fig. 3.9C) nor interactions between context and genotype ($F(2, \text{Inf}) = 0.24, p = 0.79$, Fig. 3.9C). A higher variability within the J20 mice group can be observed in figure 3.9C. This effect is also observed in other figures and could potentially be due to age related variations. Here, the mean age in the J20 mice group was 186.6 days with a standard deviation of 5.8 days, which was considered small. In a related manner, it is also possible that this increased variability reflects the disease progression in each of these mice. Plaque burden was considered to not be a good indicator of disease progression at this age point, as only low hippocampal and neocortical plaque formation is detected at 5-7 months of age (Castanho *et al.*, 2020). On the other hand, synaptic and spatial memory deficits, which precede amyloid plaque deposition (Wright *et al.*, 2013), are likely associated to high levels of A β oligomers (Wright *et al.*, 2013; Mably *et al.*, 2015). However, the levels of A β oligomers were not measured in this study and were not taken into consideration.

Figure 3.10A shows average running speed for both genotypes across all the recording sessions. The time mice spent at each running speed is shown in figure 3.10B. The running speed of WT and J20 mice was similar ($F(1, 13) = 0.22, p = 0.64$, Fig. 3.10Ci) and both genotypes were equally affected by context ($F(2, 26) = 20.55, p < 0.0001$, Fig. 3.10Cii). Further pairwise comparisons showed that the average running speed in the familiar context was significantly reduced when compared with both novel contexts (Fam vs Nov 1: $\beta = -1.86, SE = 0.38, t(45) = -4.83, p = 0.0001$, Fam vs Nov 2: $\beta = -2.33, SE = 0.38, t(45) = -6.06, p < 0.0001$, Fig. 3.10Cii).

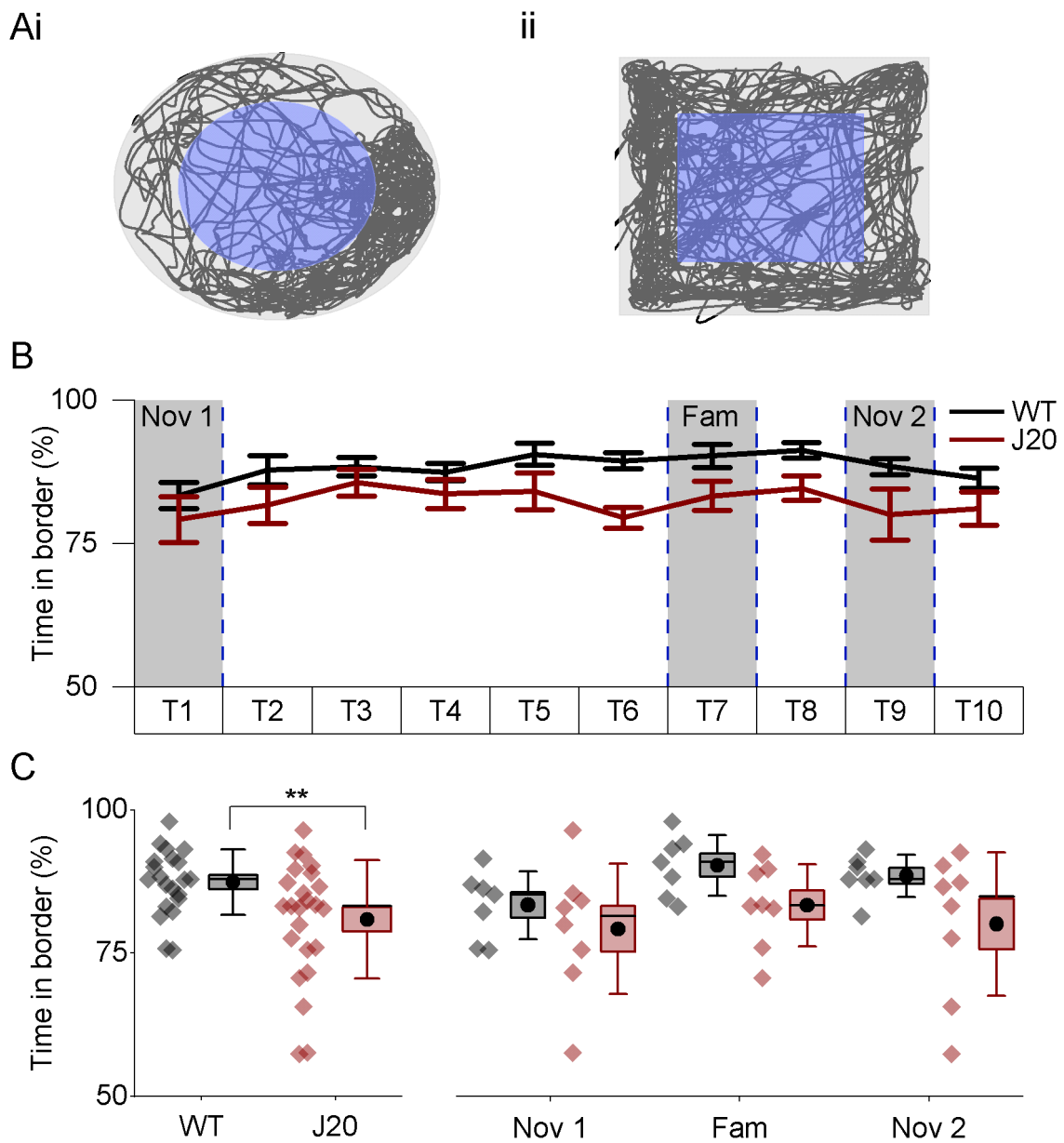


Figure 3.9 J20 mice show signs of reduced anxiety. A) Example of tracking data separated the central (blue shade) and the border (grey shade) areas of the circular (arena diameter = 62 cm) (i) and the square (arena size = 56x56 cm) (ii) arenas. Borders are defined as 15 cm from the wall. **B)** Time spent at the border of the arena across all trials. Shaded areas correspond to the first trial in the first novel arena, the familiar arena and the second novel arena. **C)** Time spent at the border of the open arenas for WT and J20 mice in the two novel trials and the familiar trial. Line plots: line corresponds to the mean and error bars represent the \pm SEM. Box plots: box corresponds to the mean \pm SEM, the circle to the mean, the line to the median and the whiskers to the SD. (* $p \leq 0.05$, ** $p \leq 0.01$, *** $p \leq 0.001$)

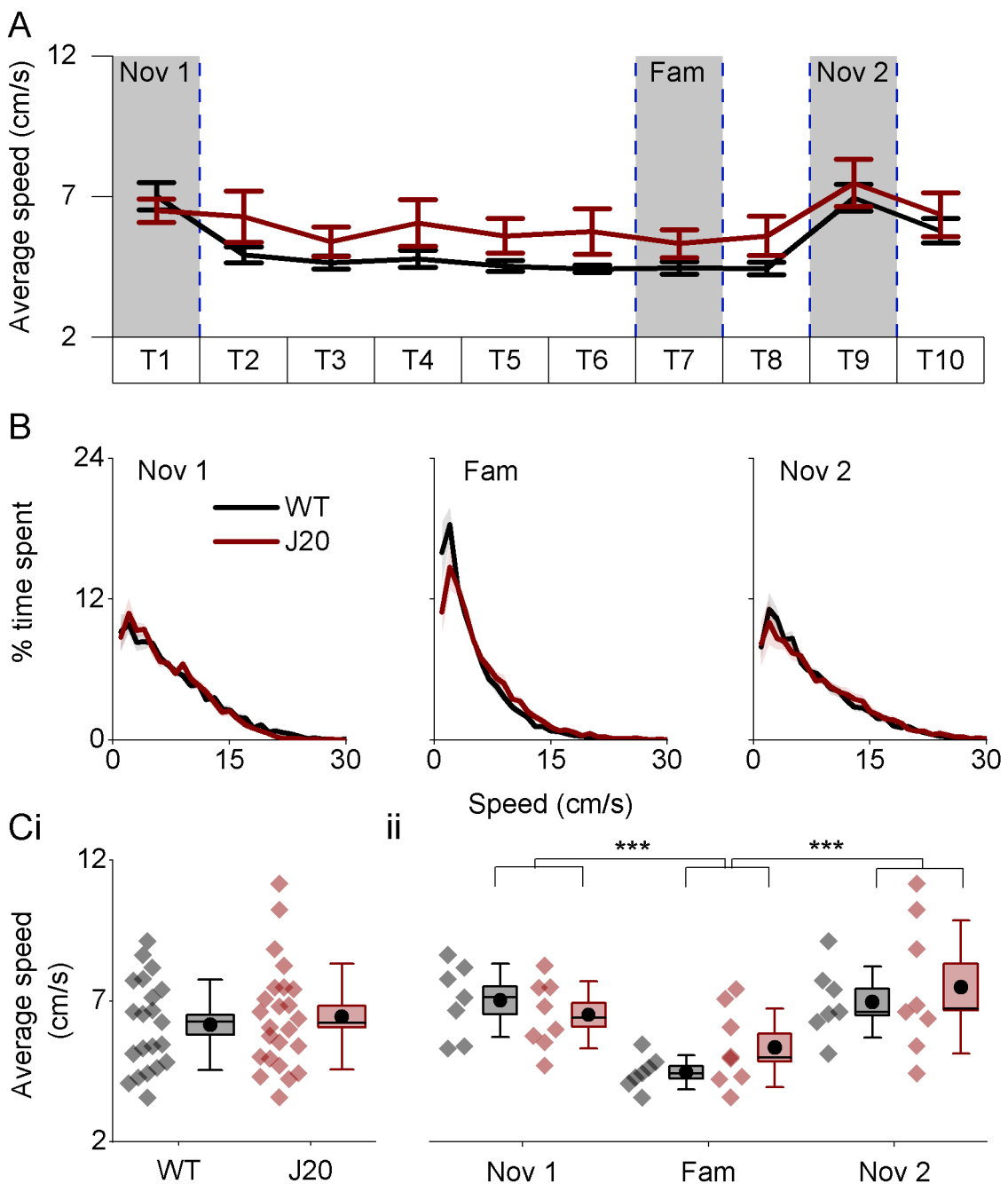


Figure 3.10 Both WT and J20 mice reduce their running speed in familiar environments. **A)** Average running speed of WT and J20 mice across all trials. Shaded areas correspond to the first trial in the first novel arena, the familiar arena and the second novel arena. **B)** Average time spent at each running speed bin expressed as a percentage for the two novel trials and the familiar trial. **C)** Average speed of WT and J20 mice compared between genotypes (**i**) and between genotypes and trial (**ii**). Line plots: line corresponds to the mean and error bars represent the \pm SEM. Box plots: box corresponds to the mean \pm SEM, the circle to the mean, the line to the median and the whiskers to the SD. (* $p \leq 0.05$, ** $p \leq 0.01$, *** $p \leq 0.001$)

3.3.2.2 Spectral analysis shows no differences between genotypes

Spectral analysis was performed for each recording session. An example is represented in figure 3.11Ai and ii, which is averaged across animals on the familiar trial (trial 7). Total broadband power was obtained and used to normalise the power of the frequency bands studied here. Figure 3.11 shows normalised power in the theta (Fig. 3.11B) and high gamma (Fig. 3.11C) frequency bands for each recording session. Further analysis was performed with the two novel sessions and the most familiar session. Figure 3.12A shows the power spectrograms of these three sessions, for each genotype, averaged across animals. The normalised theta power did not differ between both genotypes ($F(1, 13) = 0.06, p = 0.81$, Fig. 3.12Bi) nor contexts ($F(2, 26) = 2.51, p = 0.10$, Fig. 3.12Bii). Similarly, the overall effects of genotype ($F(1, Inf) = 1.97, p = 0.16$, Fig. 3.12Ci) and context ($F(2, Inf) = 1.26, p = 0.28$, Fig. 3.12Cii) were not significant when comparing the normalised high gamma power.

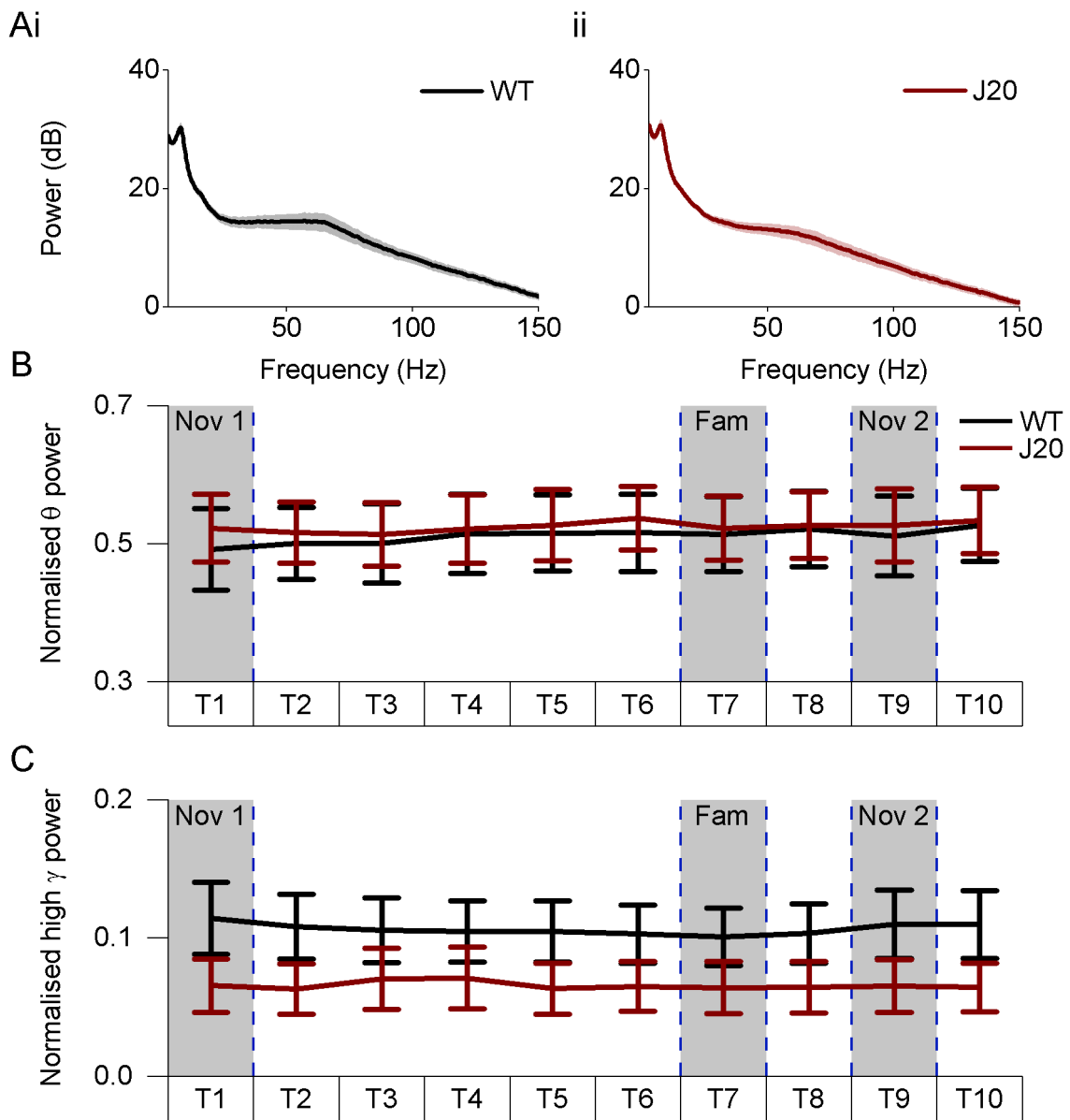


Figure 3.11 Normalised power in the different frequency bands across all trials. **A)** Example of power spectrum averaged across animals in WT (**i**) and J20 (**ii**) in trial 7. **B)** Pooled data showing power in the theta band, normalised using the broadband power, for both WT and J20 mice across all trials. **C)** Pooled data showing power in the high gamma band, normalised using the broadband power, for both WT and J20 mice across all trials. Shaded areas correspond to the first trial in the first novel arena, the familiar arena and the second novel arena. Line plots: line corresponds to the mean and error bars represent the \pm SEM.

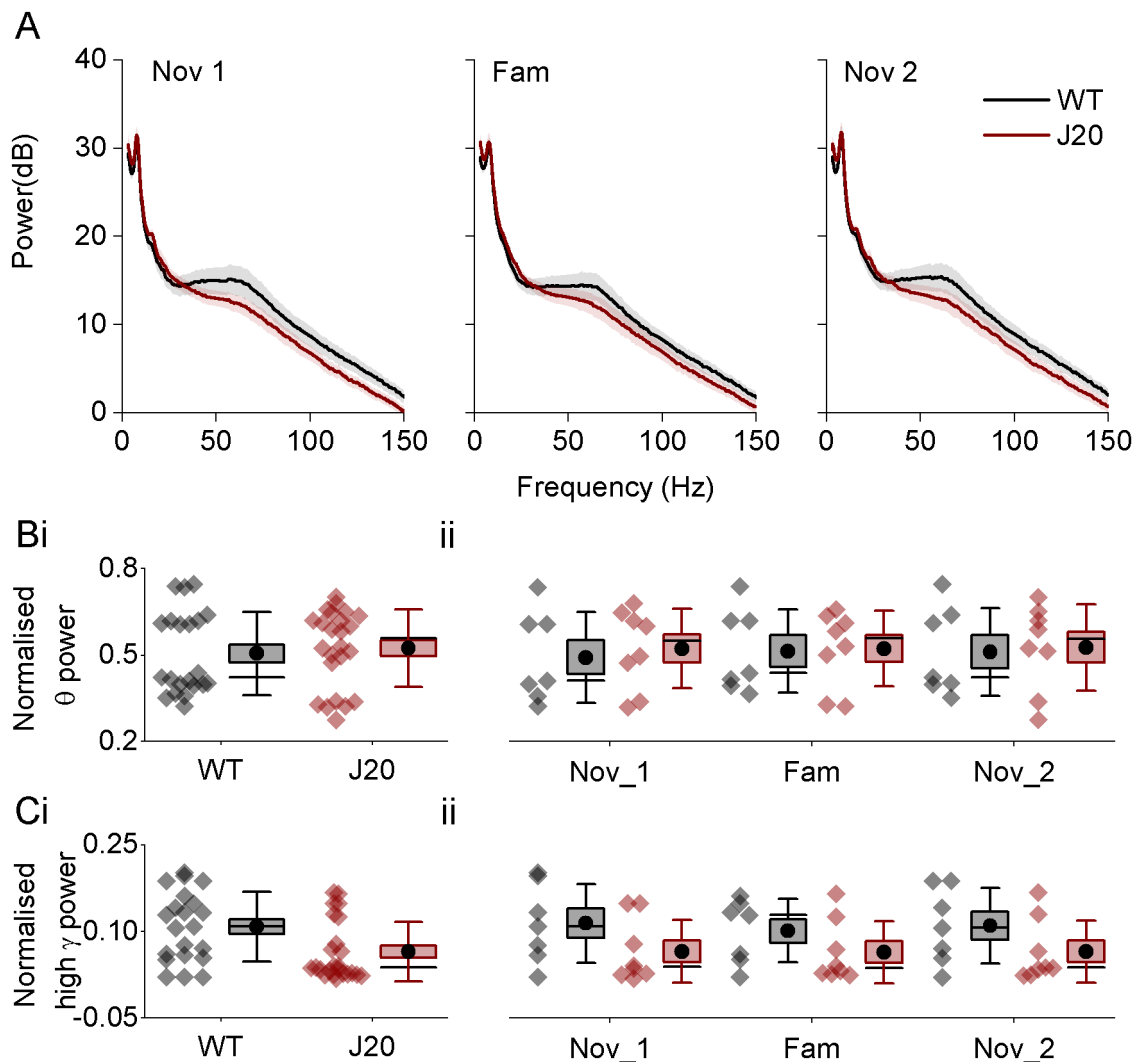


Figure 3.12 Power spectrum shows no deficits in J20 mice. **A)** Pooled power spectrum averaged across animals in each group for each trial. **B)** Pooled data showing power in the theta band, normalised using the broadband power, compared by genotype (**i**) and by genotype and trial (**ii**). **C)** Pooled data showing power in the high gamma band, normalised using the broadband power, compared by genotype (**i**) and by genotype and trial (**ii**). Line plots: line corresponds to the mean and error bars represent the \pm SEM. Box plots: box corresponds to the mean \pm SEM, the circle to the mean, the line to the median and the whiskers to the SD. (* $p \leq 0.05$, ** $p \leq 0.01$, *** $p \leq 0.001$)

3.3.2.3 Theta frequency oscillations

Example spectrograms showing changes in power and frequency on the familiar trial (trial 7), overlapped with the running speed, are presented in figures 3.13Ai and ii for a WT and a J20 mouse, respectively. Figure 3.13 shows changes in the running speed-power (Fig. 3.13B) and -frequency (Fig. 3.13C) slopes, as well as

in the frequency intercept (Fig. 3.13D), of theta frequency oscillations. Changes in theta power and frequency with running speed, averaged across animals in each group, can be seen in figure 3.14Ai and ii for the two novel trials and the most familiar trial. When analysing theta frequency oscillations, no overall changes were observed in the slope of theta power-running speed relationship with respect to genotype ($F(1, 11) = 1.86$, $p = 0.20$, Fig. 3.14Bi). Furthermore, there was no significant interaction between genotype and context ($F(2, 26) = 0.68$, $p = 0.51$, Fig. 3.14Bii). However, context had an overall effect on both genotypes ($F(2, 26) = 6.34$, $p = 0.006$, Fig. 3.14Bii), with post-hoc pairwise comparisons showing a significant difference between the familiar context and the second novel context ($\beta = 0.01$, $SE = 0.004$, $t(45) = 3.54$, $p = 0.004$, Fig. 3.14Bii) but not with the first novel context ($\beta = 0.006$, $SE = 0.004$, $t(45) = 1.45$, $p = 0.33$, Fig. 3.14Bii). Genotype did not have an overall effect on the slope of theta frequency versus running speed ($F(1, 13) = 0.32$, $p = 0.58$, Fig. 3.14Ci). However, an overall effect of context was observed ($F(2, 26) = 3.97$, $p = 0.03$, Fig. 3.14Cii), with further pairwise comparisons showing a significant difference between both novel contexts ($\beta = 0.01$, $SE = 0.006$, $t(45) = 2.57$, $p = 0.04$, Fig. 3.14Cii). Furthermore, there was no significant interaction between genotype and context ($F(2, 26) = 1.22$, $p = 0.31$, Fig. 3.14Cii). In a similar manner, theta frequency intercept did not show significant overall effects of genotype ($F(1, 13) = 1.60$, $p = 0.23$, Fig. 3.14Di), but showed an overall effect of context ($F(2, 26) = 3.52$, $p = 0.04$, Fig. 3.14Dii). Further pairwise comparisons showed differences between the first and second novel contexts ($\beta = -0.16$, $SE = 0.06$, $t(45) = -2.51$, $p = 0.048$, Fig. 3.14Dii). There was not a significant interaction between genotype and context ($F(2, 26) = 1.44$, $p = 0.25$, Fig. 3.14ii).

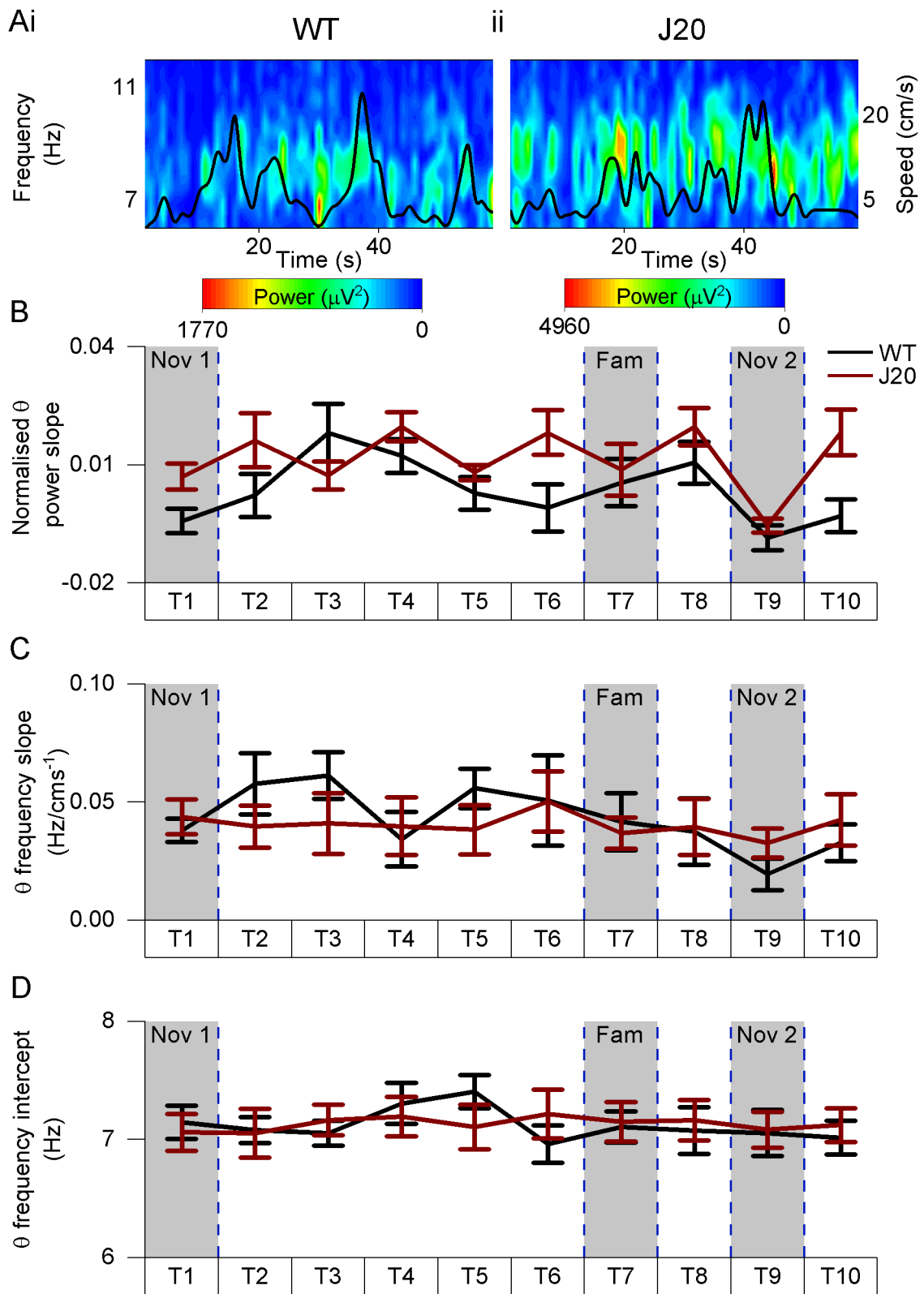


Figure 3.13 Relationship of theta frequency oscillations with running speed across all trials. **A)** Example spectrograms showing changes in the frequency and power of theta oscillations with running speed for a WT (i) and a J20 (ii) mouse over a minute in trial 7. **B)** Comparison of theta power – running speed slopes between WT and J20 mice across all trials. **C)** Comparison of theta frequency – running speed slopes between WT and J20 mice across all trials. **D)** Comparison of theta frequency – running

speed intercepts between WT and J20 mice across all trials. Shaded areas correspond to the first trial in the first novel arena, the familiar arena and the second novel arena. Line plots: line corresponds to the mean and error bars represent the \pm SEM.

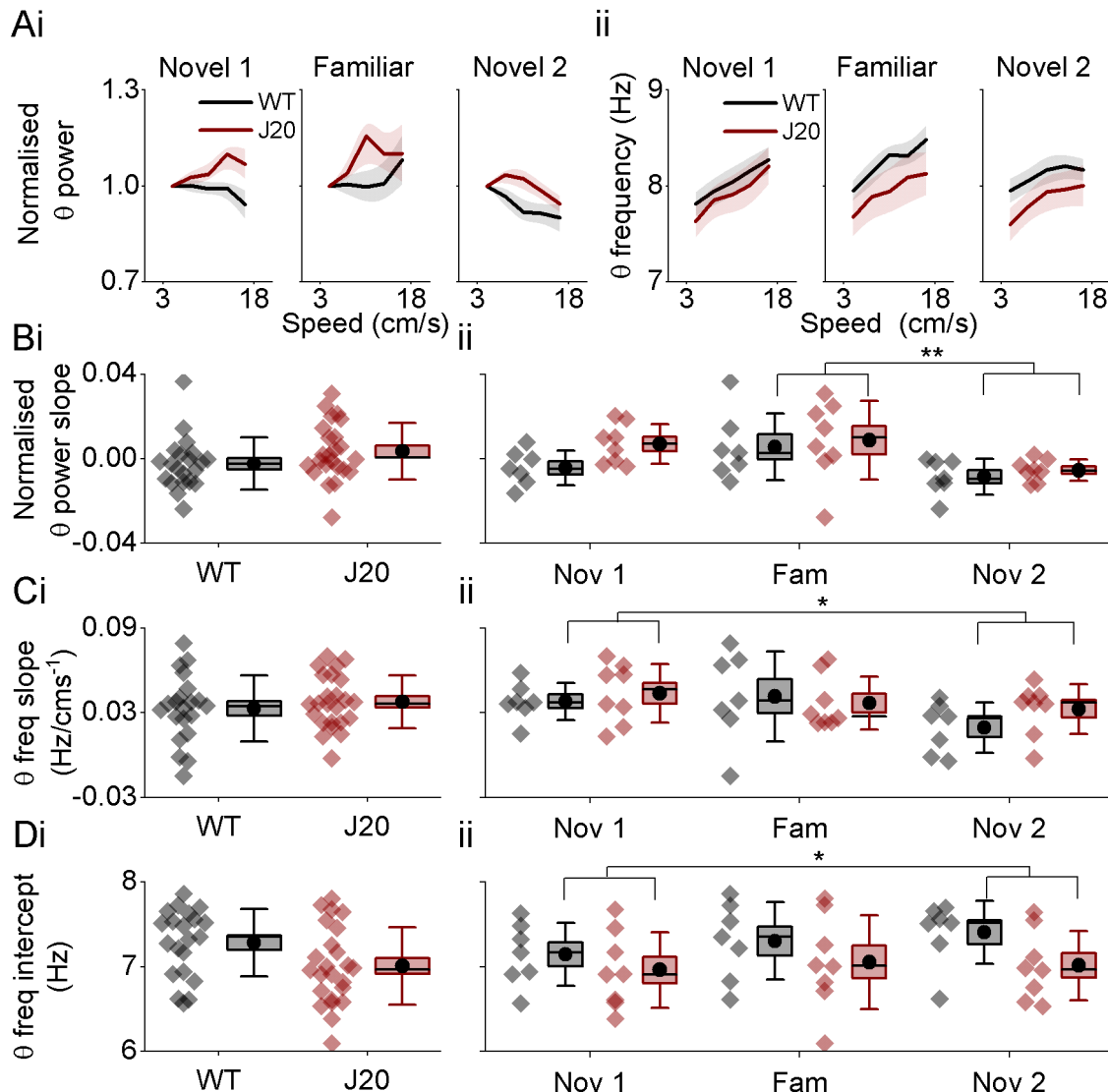


Figure 3.14 Theta power slope is affected by familiarity. A) Pooled theta power (normalised using the first value) (i) and frequency (ii) versus running speed, averaged across animals in each group for each trial. **B)** Comparison of theta power – running speed slopes by genotype (i) and by genotype and trial (ii). **C)** Comparison of theta frequency – running speed slopes by genotype (i) and by genotype and trial (ii). **D)** Comparison of theta frequency – running speed intercepts by genotype (i) and by genotype and trial (ii). Line plots: line corresponds to the mean and error bars represent the \pm SEM. Box plots: box corresponds to the mean \pm SEM, the circle to the mean, the line to the median and the whiskers to the SD. (* p \leq 0.05, ** p \leq 0.01, *** p \leq 0.001)

3.3.2.4 High gamma frequency oscillations

Spectrograms showing changes in high gamma power and frequency on the familiar trial (trial 7), overlapped with the running speed, are presented in figures 3.15Ai and ii for a WT and a J20 mouse, respectively. Figure 3.15 show changes in the power (Fig. 3.15B) and frequency (Fig. 3.15C) slopes, as well as in the frequency intercept (Fig. 3.15D), of high gamma frequency oscillations. Changes in high gamma power and frequency with running speed, averaged across animals in each group, can be seen in figure 3.16Ai and ii for the two novel trials and the most familiar trial.

Contrasting with the results observed in the theta frequency band, the slopes resulting from the relation between high gamma power and running speed showed a significant interaction between context and genotype ($F(2, 26) = 6.01$, $p = 0.007$, Fig. 3.16Bii). Further pairwise comparisons highlighted significant differences between the familiar context and both novel contexts in WT mice (Fam vs Nov 1: $\beta = 0.02$, SE = 0.005, $t(45) = 5.24$, $p = 0.0002$, Fam vs Nov 2: $\beta = 0.02$, SE = 0.005, $t(45) = 3.94$, $p = 0.006$, Fig. 3.16Bii) but not in J20 mice (Fam vs Nov 1: $\beta = 0.002$, SE = 0.004, $t(45) = 0.57$, $p = 0.99$, Fam vs Nov 2: $\beta = 0.005$, SE = 0.004, $t(45) = 1.14$, $p = 0.86$, Fig. 3.16Bii). A significant interaction between genotype and context was also observed in the slope of high gamma frequency ($F(2, 26) = 4.08$, $p = 0.03$, Fig. 3.16Cii). Pairwise comparisons showed significant differences between the familiar context and both novel contexts in WT animals (Fam vs Nov 1: $\beta = 0.11$, SE = 0.02, $t(45) = 4.34$, $p = 0.002$, Fam vs Nov 2: $\beta = 0.10$, SE = 0.02, $t(45) = 4.16$, $p = 0.004$, Fig. 3.16Cii). However, high gamma frequency slopes were not different between the familiar context and both novel contexts in J20 mice (Fam vs Nov 1: $\beta = 0.01$, SE = 0.02, $t(45) = 0.65$, $p = 0.99$, Fam vs Nov 2: $\beta = 0.03$, SE = 0.02, $t(45) = 1.37$, $p = 0.75$, Fig. 3.16Cii). High gamma frequency intercept showed no overall effects of genotype ($F(1, Inf) = 0.46$, $p = 0.50$, Fig. 3.16Di) or significant interactions between genotype and context ($F(2, Inf) = 1.76$, $p = 0.17$, Fig. 3.16Dii). However, context showed a significant overall effect ($F(2, Inf) = 7.73$, $p = 0.0004$, Fig. 3.16Dii). Pairwise comparisons showed differences between the familiar context and both novel contexts (Fam vs Nov 1: $\beta = -0.01$, SE = 0.003, $z(45) = -3.63$, $p = 0.0008$, Fam vs Nov 2: $\beta = -0.008$, SE = 0.03, $z(45) = -3.11$, $p = 0.005$, Fig. 3.16Dii).

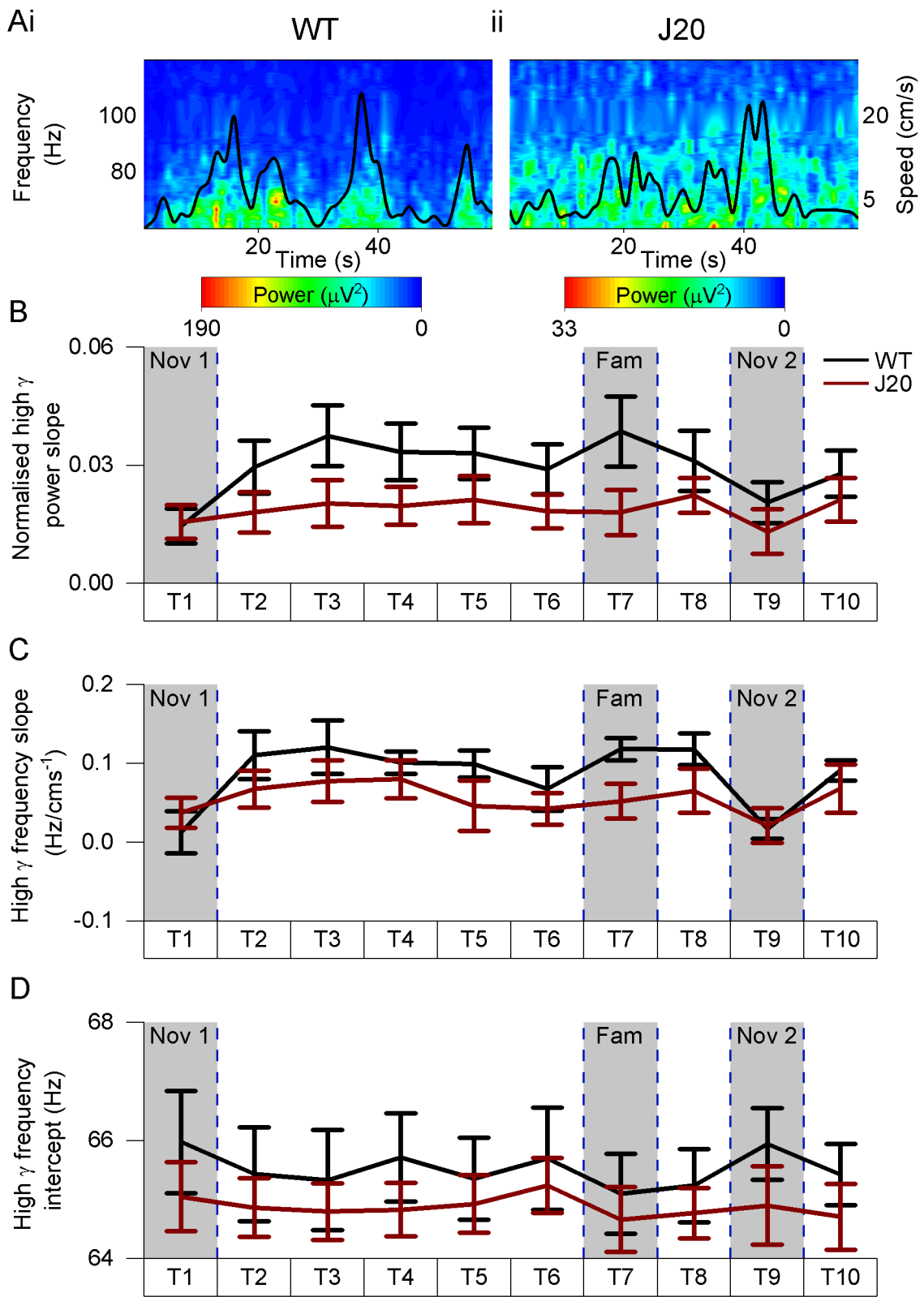


Figure 3.15 Relationship of high gamma frequency oscillations with running speed across all trials. **A)** Example heat plots showing changes in the frequency and power of high gamma oscillations with running speed for a WT (i) and a J20 (ii) mouse over a minute in trial 7. **B)** Comparison of high gamma power – running speed slopes between WT and J20 mice across all trials. **C)** Comparison of high gamma frequency – running speed slopes between WT and J20 mice across all trials. **D)** Comparison of high

frequency – running speed intercepts between WT and J20 mice across all trials. Shaded areas correspond to the first trial in the first novel arena, the familiar arena and the second novel arena. Line plots: line corresponds to the mean and error bars represent the \pm SEM.

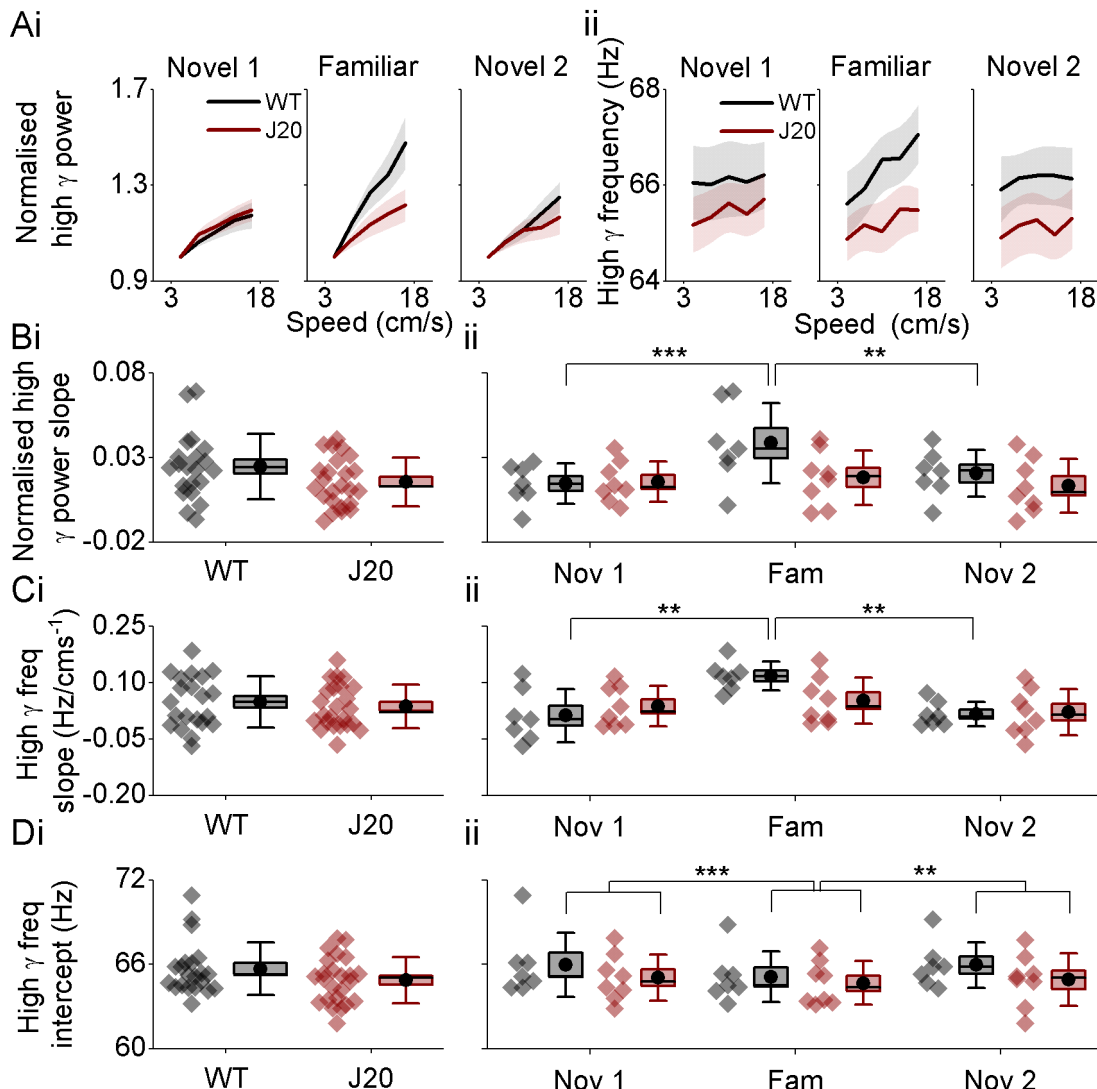


Figure 3.16 High gamma power and frequency slopes increase with familiarity only in WT mice. A) Pooled high gamma power (normalised using the first value) (i) and frequency (ii) versus running speed, averaged across animals in each group for each trial. **B)** Comparison of high gamma power – running speed slopes by genotype (i) and by genotype and trial (ii). **C)** Comparison of high gamma frequency – running speed slopes by genotype (i) and by genotype and trial (ii). **D)** Comparison of high gamma frequency – running speed intercepts by genotype (i) and by genotype and trial (ii). Line plots: line corresponds to the mean and error bars represent the \pm SEM. Box plots: box corresponds to the mean \pm SEM, the circle to the mean, the line to the median and the whiskers to the SD. (* $p \leq 0.05$, ** $p \leq 0.01$, *** $p \leq 0.001$)

3.3.2.5 Phase amplitude coupling

Changes in the theta – high gamma MI slopes over the different trials can be seen in figure 3.17A. Both novel trials and the most familiar trial were considered for further analysis. Figure 3.17B shows PAC comodulograms averaged across animals in each group for representative speed bins in each trial. Figure 3.17C shows changes in the MI of theta – high gamma versus running speed for each trial and genotype.

Theta – high gamma MI slopes were not affected by genotype ($F(1, 11) = 0.70, p = 0.42$, Fig. 3.17Di) and there was no interaction between context and genotype ($F(2, 26) = 0.60, p = 0.55$, Fig. 3.17Dii). However, an overall effect of context was observed ($F(2, 26) = 5.46, p = 0.01$, Fig. 3.17Dii). Pairwise comparisons showed a significant difference between the familiar context and the second novel context ($\beta = 23.82, SE = 7.28, t(45) = 3.27, p = 0.008$, Fig. 3.17Dii) but not with the first novel context ($\beta = 9.02, SE = 7.28, t(45) = 1.24, p = 0.44$, Fig. 3.17Dii).

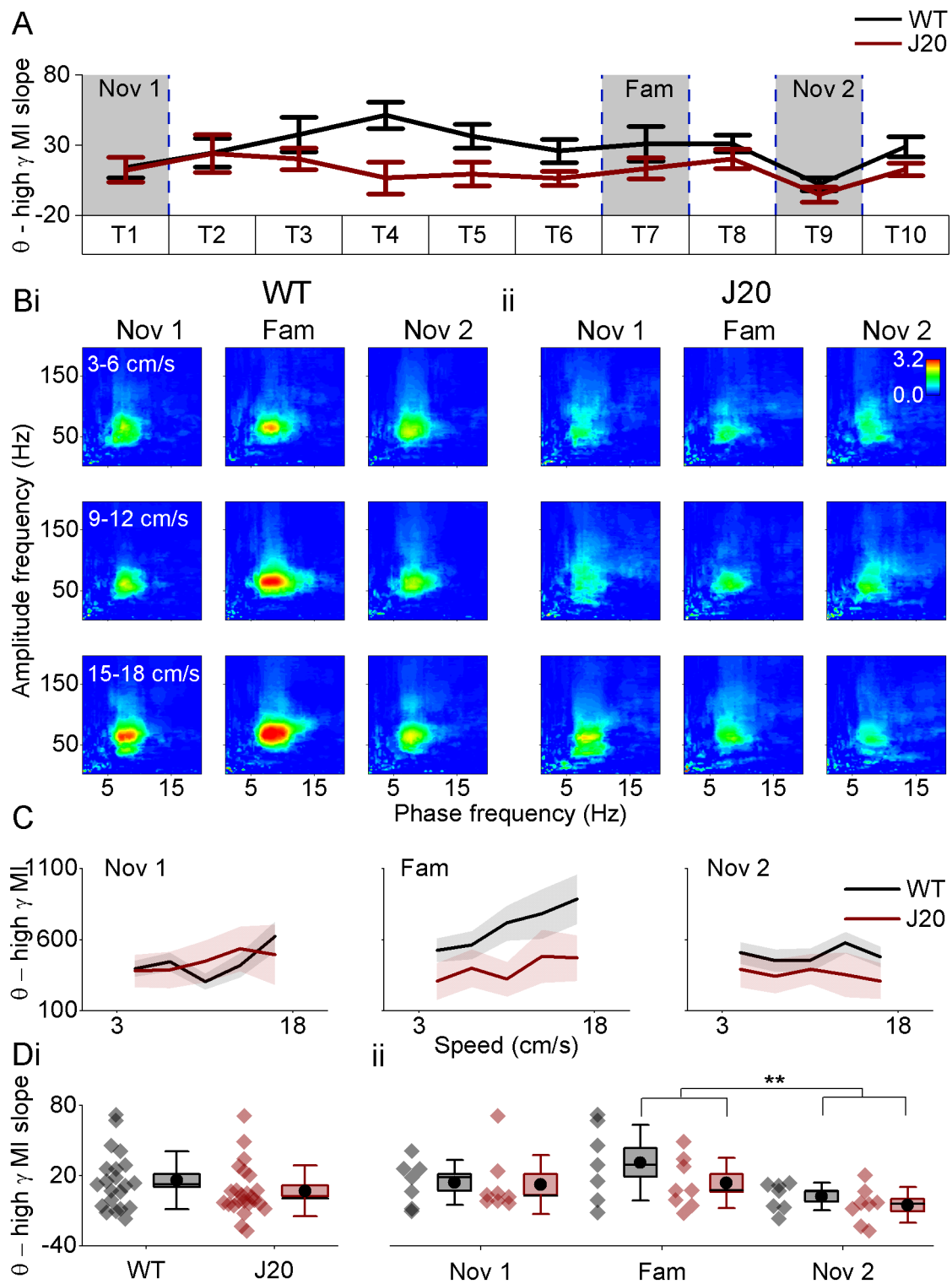


Figure 3.17 Theta – high gamma MI slopes are affected by context. **A)** Comparison of theta – high gamma MI values – running speed slopes between WT and J20 mice across all trials. Shaded areas correspond to the first trial in the first novel arena, the familiar arena and the second novel arena. **B)** Averaged phase-amplitude comodulograms across animals for certain running speed examples in WT (**i**) and J20 (**ii**) mice, for each trial. **C)** Pooled MI values for high gamma versus running speed, averaged across animals in each group for each trial. **D)** Comparison of theta – high gamma MI – running speed slopes by genotype (**i**) and by genotype and

trial (ii). Line plots: line corresponds to the mean and error bars represent the \pm SEM. Box plots: box corresponds to the mean \pm SEM, the circle to the mean, the line to the median and the whiskers to the SD. (* $p \leq 0.05$, ** $p \leq 0.01$, *** $p \leq 0.001$)

3.4. Discussion

3.4.1. Summary

The purpose of these studies was to identify potential deficits in the mechanisms underlying spatial memory in J20 mice, which could explain the impairments observed in the behavioural tasks in these mice.

This study shows, for the first time, that J20 experience significant disruptions in the mechanisms involved in memory processing of spatial information due to impairments in the relationship of high gamma frequency oscillations with running speed.

3.4.2. Limitations of the triangular track experiment

The two open arenas experiment was designed to address the limitations of the experimental design of the triangular track. In contrast to the triangular track, the two open arenas experiment included a dim source of light to reduce the potential effects of darkness in the theta frequency – running speed slope, which has been observed in literature (Chen *et al.*, 2016). In addition, the tracking quality was improved as the walls of the two open arenas were made of medium-density fibreboard, which greatly reduced the reflection of the two LEDs observed in the triangular track. The main change introduced aimed to boost familiarity to the context, which was achieved by allowing a longer total exploration time together with a higher number of exposures. Together, these changes accomplished a greater level of familiarity and allowed to study the effects of context familiarity and novelty more accurately.

3.4.3. J20 mice show signs of reduced anxiety

Rodents have a natural tendency to explore novelty, which has been exploited especially in the novel-object recognition task (Berlyne, 1950; Leger *et al.*, 2013). In the triangular track experiment, both WT age groups reduced their average running speed on the second trial. However, the same effect was not observed in J20 mice, for which their average running speed remained unchanged. It is possible that this reduction was triggered because of the increased familiarity in the second trial, which would highlight that J20 mice did not get as familiarised to the triangular track as WT mice.

However, the average running speed of 6 mo WT and J20 mice equally decreased when exploring the most familiar environment in the two open arenas experiment. A key difference between both experiments is that animals were only food restricted in the triangular track, which could affect the running speed of these animals. Alternatively, the two open arenas experiment allowed animals to explore the environment for a greater number of trials and days, making it likely to reach a higher level of familiarity when compared to the triangular track experiment. If this decrease in average running speed is related to the familiarity of the environment, it is then possible that the J20 mice familiarisation deficiencies are mild at this stage and can reach a similar level when more exploration time is allowed. This has been previously reported in the MWM task, with no differences in the time spent in the target quadrant being observed between WT and J20 mice when the test was performed in a late trial, but differences were observed in an earlier trial (Harris *et al.*, 2010).

Some studies have reported reduced anxiety levels in J20 mice (Chin *et al.*, 2005; Fujikawa *et al.*, 2017). However, normal anxiety levels have also been reported (Wright *et al.*, 2013; Etter *et al.*, 2019). Although, the experiments described in this chapter were not specifically designed to study anxiety, the time rodents spend next to the border and in the middle of the open arena can be used as a measurement of anxiety (Simon, Dupuis and Costentin, 1994; Seibenhener and Wooten, 2015). This was therefore only studied in the two open arenas experiment with 6 mo WT and J20 mice. It was observed that WT mice spent more time next to the borders of the open arenas than J20 mice. These results

suggest that the J20 mice included in this study show lower levels of anxiety than WT mice.

3.4.4. Power spectrum analysis

A study reported that theta power increases during the exploration of novel environments in the hippocampus (Penley *et al.*, 2013). However, a different study showed that this increase is not reliable (Wells *et al.*, 2013). Here, the power in theta and high gamma bands were normalised by the broadband power and compared. Both the triangular track and the two open arenas experiments were consistent in showing no changes in theta power between the different trials, which suggests that theta power does not change during the exploration of novel and familiar environments. In addition, these results suggest that theta power is not reduced or increased in the MEC of J20 mice, consistently with what has been previously observed in the hippocampus of these mice (Etter *et al.*, 2019).

However, a decrease in high gamma power in the MEC of 6 mo mice was observed in the second trial of the triangular track experiment. However, high gamma power remained constant during the different trials in the two open arenas experiment. As the two open arenas experiment reached a higher level of familiarity, it is more likely that no changes occur in high gamma power during the exploration of novel and familiar environments. These results contradict what has been observed in other studies, in which reduced levels of gamma power have been reported in J20 mice (Martinez-Losa *et al.*, 2018; Etter *et al.*, 2019). However, these results are in agreement with what has been reported in the MEC of an APP knock-in mouse model (Nakazono *et al.*, 2017).

3.4.5. No deficits in theta frequency oscillations in the MEC of J20 mice

In the triangular track experiment, theta power slopes, resulting from the relationship of theta power with running speed, showed a significant increase in trial 2. However, this was only observed in 10-15 mo mice and remained constant

in 6 mo mice. On the other hand, 6 mo mice showed an increase of theta power slopes in the most familiar day when compared to the second novel environment in the two open arenas experiment. Together, these results may suggest that the slope of theta power increases with familiarity in both WT and J20 mice. However, it is not clear why such increase was only observed in 10-15 mo mice in the triangular track experiment.

Opposite to what has been reported in the hippocampus and the MEC of rats (Newman *et al.*, 2013; Wells *et al.*, 2013), no changes related to novelty and familiarity were observed in the slope of theta frequency in these two experiments. It is a possibility that different mechanisms occur in different species.

This was also the case in the theta frequency intercept in the two open arenas experiment, which was not different between trials or genotypes. However, 10-15 mo J20 mice showed an increase in their theta frequency intercept during the second trial of the triangular track experiment. Theta frequency intercept has been shown to decrease with anxiolytic drugs and has been linked to anxiety (Wells *et al.*, 2013). It is possible that the anxiety levels of 10-15 mo J20 mice increased during the second trial, increasing in turn the theta frequency intercept. However, this has been described in the hippocampus and the mechanisms leading to this theta frequency intercept increase could be different in the MEC.

3.4.6. Deficits in high gamma frequency oscillations in the MEC of J20 mice

High gamma frequency oscillations have been linked to memory processing in both rodents (Kemere *et al.*, 2013; Yamamoto *et al.*, 2014; Zheng *et al.*, 2016) and humans (Kucewicz *et al.*, 2014). It is possible that the deficits in spatial memory observed in J20 mice could be linked to disruptions in these oscillations. When comparing high gamma power slopes, a trend towards higher slopes in WT mice than in J20 mice was observed in the triangular track experiment. Interestingly, both high gamma power and frequency slopes significantly increased in WT mice when comparing the most familiar trial with both novel trials

in the two open arenas experiment. In contrast, J20 mice showed no differences between trials.

However, a decrease with familiarity in high gamma power-running speed slopes, and not an increase, has been reported in a previous study (Kemere *et al.*, 2013) in both the hippocampus and the MEC of rats. Importantly, hippocampal high gamma frequency oscillations are hypothesised to be driven by the MEC (Colgin, Denninger, Fyhn, Hafting, Bonnevie, Jensen, M.-B. Moser, *et al.*, 2009; Kemere *et al.*, 2013). The results in this chapter show, nevertheless, that high gamma power slopes were lower in both novel trials than in the familiar trial in WT mice. Two main hypotheses arise from this. First, high gamma power slopes could be increasing with familiarity in the MEC of mice instead of decreasing. Second, the two open arenas experiment may have not been long enough to detect a reduction in the slopes of high gamma power with familiarity. If the latter proved true, it would imply that the increase of high gamma power slopes experiences an initial delay in mice, which has not been observed previously in rats (Kemere *et al.*, 2013).

In humans, high gamma frequency oscillations have been related to both memory encoding and retrieval (Sederberg *et al.*, 2007; Kucewicz *et al.*, 2014). In rodents, a role in memory encoding has been primarily suggested (Kemere *et al.*, 2013; Zheng *et al.*, 2016). They have also been linked to working memory in both humans (Vugt *et al.*, 2010) and rodents (Yamamoto *et al.*, 2014). The results presented in this chapter suggest significant impairments in memory processing in J20 mice, but do not allow for distinguishing if these impairments are related to memory encoding or retrieval with certainty. However, the observation of an increase in the slopes of high gamma power in the familiar trial, in respect to both novel trials, may suggest impairments in memory retrieval.

The deficits observed in high gamma oscillations may be the result of abnormalities in the GABAergic system of J20 mice, as evidence suggests that FS interneurons are necessary to generate gamma frequency oscillations (Cardin *et al.*, 2009; Sohal *et al.*, 2009; Pastoll *et al.*, 2013). Reductions in the number of FS interneurons have been observed in the dentate gyrus (DG) and the hippocampus of amyloid models (Popovi *et al.*, 2008; Zallo *et al.*, 2018; Giesers and Wirths, 2020). In particular, J20 mice show a loss in MS GABAergic synaptic

complexity together with reduced innervations onto FS hippocampal interneurons (Rubio *et al.*, 2012). Furthermore, FS interneurons exhibit a more depolarised resting membrane potential along with reduced action potential amplitudes in the parietal cortex of J20 mice (Verret *et al.*, 2012).

Importantly, treatments targeting FS interneurons have been able to rescue spatial memory deficits in amyloid models (Hijazi *et al.*, 2019). Specifically in J20 mice, the observed spatial memory deficits, which were linked to reduced gamma power, were rescued by stimulating MS FS interneurons at low gamma frequency (Etter *et al.*, 2019). Furthermore, increasing Nav1.1 levels in FS interneurons enhanced gamma oscillations and recued spatial memory deficits in these mice (Verret *et al.*, 2012; Magdalena Martinez-Losa *et al.*, 2018).

Taken together, these results suggest that J20 mice experience significant deficits in the network mechanisms underlying spatial contextual memory caused by impairments in MEC high gamma frequency oscillations. These deficits are likely linked to abnormalities in the GABAergic circuits and may contribute to the spatial memory impairments observed in these mice.

3.4.7. No deficits in phase amplitude coupling in the MEC of J20 mice

Theta – gamma PAC has been related to memory processing (Tort *et al.*, 2008, 2009; Canolty and Knight, 2010). In addition, theta – gamma PAC has been reported to increase with running speed in the hippocampus (Chen *et al.*, 2011). The analysis presented in this chapter studied if the relationship of running speed with theta – high gamma PAC changed with novelty and familiarity. No changes in the slopes resulting from these relationships were observed in the triangular track experiment. However, theta – high gamma PAC slopes were affected by context and significantly increased in the familiar trial when compared to the second novel trial in the two open arenas experiment. Both WT and J20 mice equally exhibited the increase of theta – high gamma PAC slopes, which suggests no impairments in the modulation by context of theta – high gamma PAC slopes in J20 mice. However, it has been shown that the strength of theta – gamma PAC depends on theta power, but not on gamma power, with higher

magnitudes of theta power correlating with greater MI values (Canolty *et al.*, 2006; Tort *et al.*, 2009). In the results presented in this chapter, theta power slope was also greater in the familiar context than in the second novel context in the two open arenas experiments, which may explain the changes observed in the theta – high gamma PAC slopes.

3.5. Conclusions

The main conclusion of this chapter is that the MEC of J20 mice show significant deficits in the modulation by context of the relationship of high gamma frequency oscillations with running speed. These deficits suggest impairments in memory processing and shows evidence of a potential mechanism which could contribute to the spatial memory impairments observed in AD.

Chapter 4. Analysis of MEC network impairments impact at the single unit level

4.1. Introduction

The results presented in the previous chapter provided valuable information by showing significant deficits in high gamma frequency oscillations in J20 mice, linked to the encoding and retrieval of spatial information.

In the MEC, a variety of functional subclasses of neurons are involved in the depiction of different spatial features of the environment and contribute to an ever changing representation of the animal's location (Jacob, Gordillo-Salas, *et al.*, 2017). Several studies have shown that J20 mice display spatial navigation and memory deficits in the MWM (Harris *et al.*, 2010; Wright *et al.*, 2013) and the Barnes maze (Etter *et al.*, 2019). These tasks are likely to require both idiothetic and allothetic navigation, which uses self-movement clues and external clues, respectively, to be successfully performed. This supports the hypothesis of possible impairments in the activity of MEC cells with grid periodicity in J20 mice, which play a key role in idiothetic navigation (Gil *et al.*, 2018) but also require the integration of allothetic cues to avoid error accumulation and form stable periodic grid patterns (Perez-Escobar *et al.*, 2016). In fact, studies have shown that human adults at genetic risk of AD display reduced grid pattern activity (Kunz *et al.*, 2015) and spatial memory impairments (Henderson, Mack and Williams, 1989; Allison *et al.*, 2016). Furthermore, a reduction in the number of cells with grid periodicity and in the spatial information conveyed has been recently observed in an APP knockin mouse model (Jun *et al.*, 2020). However, it is not clear how these impairments are reflected in the activity of cells with grid periodicity during the exploration of novel and familiar environments in amyloid models.

Previous studies found that these cells are affected by metric changes, those that can be quantified such as environmental deformation (Barry *et al.*, 2007; Munn *et al.*, 2020), and non-metric changes, such as in olfactory clues (Marozzi *et al.*, 2015). Of specific interest for this chapter, they also respond to the exposure of

a novel environment by increasing their field scale and becoming more irregular (Barry *et al.*, 2012).

However, it is not entirely clear whether and how novelty affects other spatially modulated cell subtypes present in the MEC. In humans, neuronal firing related to the retrieval of information has been shown in EC neurons (Qasim *et al.*, 2019). A recent study (Munn *et al.*, 2020) has shown that environmental perturbations also affect the activity of speed cells, contradicting what was stated in a previous study (Kropff *et al.*, 2015). Environmental perturbations also appear to affect the activity of HD sensitive cells (Munn *et al.*, 2020). This raises the question whether, in addition to cells with grid periodicity, other cell subtypes may also be affected by the novelty of the environment. Furthermore, experimental and computational evidence suggests that cells with grid periodicity integrate both heading and velocity information, which is possibly provided by HD and speed sensitive cells, respectively (Fuhs and Touretzky, 2006; Burgess, Barry and O'Keefe, 2007; Winter, Clark and Taube, 2015). It is possible that these cell subtypes communicate changes in the novelty of the environment through their activity. It is the main aim of this chapter to determine how the different subtypes of MEC cells behave in familiar and novel environments and if J20 cells display any deficits that could lead to the spatial memory impairments observed in different studies.

4.2. Methodology

4.2.1. Animals

5-6 mo J20 mice (WT: n = 5; J20: n = 4) (Mucke *et al.*, 2000) underwent stereotaxic surgery to implant 32-channels silicon probes (*CAMBRIDGE NeuroTech, ASSY-116 – P-1*, Fig. 2.4B, see section 2.3.1 in the general methodology for more details) in the dorsal part of the MEC. Probes were glued to a miniature Microdrive which could be moved down 205 µm per turn. All probes were implanted at 3.12 mm mediolateral, 5.25 mm anteroposterior and 0.6-0.8

mm dorsoventrally with angles ranging from 0-5 degrees, with the tip of the probe pointing anteriorly.

4.2.2. Behavioural task

Prior to the start of this experiment all animals were food restricted to encourage full coverage of the arena surface. Each mouse was repeatedly exposed to only one of two possible initial open arenas (arenas 1 and 2) (Fig. 2.3) for a minimum of 7 exposures, with each of these exposures lasting normally between 15-30 minutes. However, a typical session would last 20 minutes. Longer exposures were mainly done to identify which functional cell subtypes were present during the recording, in specific for cells with grid periodicity, as it is necessary that the animal covers the entire surface of the environment to observe them. A higher number of exposures were carried out when probes needed to keep being driven down in order to increase the number of cells recorded or when animals needed further training to cover the whole surface of the open arena. Different studies have observed that rats get familiar to a given open arena in a time ranging from 60 minutes to 1 hour and 40 minutes (Barry *et al.*, 2007, 2012; Wells *et al.*, 2013). Despite the variations in the number of exposures and their length, all animals included in this study were exposed to the familiar arena for a minimum of 2 hours and 40 minutes before performing the experiment for the first time. This minimum duration was deemed sufficient to ensure that all mice were familiar to the open arena.

The initial arena, to which the animal would be repeatedly exposed, was the familiar arena and the remaining two arenas acted as novel environments. The behavioural experiment consisted of three recording sessions in which the animal was sequentially exposed to the familiar arena, the novel arena and finally again to the familiar arena. The familiar and novel sessions took place in different rooms to increase the level of novelty. Each recording session lasted between 30 to 60 minutes with an interval of at least 30 minutes between each of them. The experiment was repeated (trial 2) with each animal using a second novel arena (arena 3) in the novel room. Further details can be found in section 2.2.2.2 of the

general methodology. Because this experiment was performed twice, and all animals were habituated for longer to the familiar arena the second time that they performed it, a factor corresponding to the trial was included in the statistical analysis.

4.2.3. Data acquisition

Electrophysiological and tracking data was continuously sampled at 30 kHz and recorded through the whole behavioural experiment, with the mouse's location tracked using two LEDs attached to the headstage. Tracking data was oversampled as the camera frame rate was 30 Hz.

4.2.4. Tracking analysis

The time animals spent in the borders of the open arenas were expressed as a percentage of the total recording time. These percentages were used for comparisons. The border area was defined as 15 cm from the wall.

Running speed was obtained from the tracking information and averaged over the total length of the recording for each animal and trial for comparisons.

4.2.5. Local field potential signals analysis

Data analysis was performed with custom made MATLAB scripts and the Chronux toolbox for MATLAB (available at <http://chronux.org/>) was used to perform LFP spectral analysis. LFP frequencies were divided into the following bands: Theta (5-12 Hz) and High Gamma (60-120 Hz).

To assess the relationship of high gamma and theta frequency oscillations with running speed, the peak frequency and the power of these oscillations were computed for each running speed bin (bin size = 3 cm/s; 6 speed bins in total from 3 cm/s to 21 cm/s) with a linear fit performed on the pooled data. The slopes

and intercepts resulting from the linear fit were used for comparisons. The power of both theta and high gamma oscillations was normalised to the power corresponding to the first speed bin.

To measure PAC between theta and gamma, the MI (Onslow, Bogacz and Jones, 2011) was calculated using a toolbox available at: <https://data.mrc.ox.ac.uk/dataset/matlab-toolbox-estimating-phase-amplitude-coupling>. The resulting matrix of PAC values for each recording were obtained for each running speed bin (bin size = 3 cm/s; 6 speed bins in total from 3 cm/s to 21 cm/s), and normalised. The MI values were calculated as the summation of all the PAC values within the frequency limits of high gamma oscillations. MI values at each running speed bin were fitted with a linear fit, and the slopes resulting from the linear fit were used for comparisons. Further details can be found in section 2.3.5 of the general methodology.

4.2.6. Single unit classification and analysis

Spike detection and automatic clustering was done using an open source software, Klusta (Rossant *et al.*, 2016) (<https://klusta.readthedocs.io/en/latest/>). Spike detection was carried out using the SpikeDetekt program which firstly band-pass filtered the raw data to remove LFP signals and detected spikes through a double-threshold flood fill algorithm. Resulting clusters were visualised with KlustaViewa for manual refinement. More details can be found in section 2.3.6 of the general methodology.

4.2.6.1 Theta modulation

Cells were classified as theta modulated through two different methods, which were analysed separately. The first method, the TMI (Langston *et al.*, 2010), was calculated from the spectral analysis of the spike train's autocorrelation as described in section 2.3.7.1 of the general methodology.

The second method employed a MLE (Climer *et al.*, 2015) to detect rhythmic cell firing and the frequency of this rhythmicity, as described in section 2.3.7.2 of the general methodology. The TMI values obtained with the first method were also used as a measure of strength for theta modulation in the cells passing the criteria of the MLE method. For this method, open source MATLAB scripts (https://github.com/jrclimer/mle_rhythmicity) were used.

For both methods, the proportion of theta modulated cells was determined by considering if a cell is theta modulated in any of the three trials, increasing the n number by a factor of three. The TMI and the frequency of the modulation were only studied for cells considered theta modulated in all three trials. In addition to these two variables, the preferred theta firing phase, mean direction and mean resultant vector length were obtained as described in section 2.3.7.3 of the general methodology and were also analysed. These variables were only analysed for cells classified as theta modulated in all three trials were analysed. Cells locked to the trough were defined as cells with mean direction values equal or larger than 270° and equal or smaller than 90° (passing through 0°), and locked to the peak for mean directions larger than 90° and smaller than 270° . The proportion of cells locked to the trough or the peak of the theta oscillation was obtained by only considering cells that were theta modulated in all three trials.

4.2.6.2 Cell type classification

Cells were classified as putative interneurons or putative excitatory cells if their average spike width was smaller or greater than 0.4 ms, respectively (Frank *et al.*, 2001).

4.2.6.3 Functional cell subtype metrics

The speed score of the cells (Kropff *et al.*, 2015) were calculated as the Fisher transformation of the Pearson's linear correlation coefficient. This was obtained for both the firing rate versus running speed, for linearly modulated cells, and the logarithmic of the firing rate versus running speed, for saturating cells. Speed

sensitive cells were classified as linearly modulated if their firing rate increased linearly in response to running speed or saturating if the increase was exponential in the first recorded trial. In addition, speed sensitive cells could show either an increase or a decrease in their firing rate with running speed. Some cells could have a significant positive speed score in one trial and a significant negative speed score in a different trial. Cells were classified as positively modulated if their positive speed score was larger than the absolute negative speed score, and as negatively modulated in the opposite scenario. To compare speed scores of positive and negative modulated cells between the three different trials, the speed score sign of negatively modulated cells for each of trial was inverted, as more negative values show a greater modulation by running speed. More details can be found in section 2.3.9 of the general methodology.

To determine context specificity in speed sensitive cells, the following equation was used to calculate a rate difference index (Kitamura *et al.*, 2015): $(FR_{Fam1} - FR_{Fam2})/(FR_{Fam1} + FR_{Fam2})$; with FR_{Fam1} corresponding to the firing rate of the first exposure of the animal to the familiar arena and FR_{Fam2} corresponding to firing rate in the second exposure. A threshold was calculated with the 99th percentile of these rate difference indexes and applied to a second set of rate difference indexes, which was obtained with the average firing rate between the two exposures to the familiar arena and the firing rate in the novel arena. Cells passing this threshold were classified as context specific. Further details can be found in section 2.3.9 of the general methodology.

The cell sensitivity to HD was calculated using the angles extracted from the two LEDs attached to the headstage, with the firing rate obtained for each angle bin, of 3° width, from 1 to 360°. The resultant mean vector length, considered to be the HD score, and mean direction were obtained from the binned firing rate. See section 2.3.10 of the general methodology for further details.

HD phase shifts (Taube, Muller and Ranck, 1990a) between the two familiar trials were calculated by shifting the firing rate obtained for each angle bin of the second familiar session, in steps of 6°, and performing a circular correlation between the data from both sessions at each step. The phase shift was determined as the angle shift with the maximum circular correlation. Phase shifts

below 60° were defined as small and phase shifts above 60° were defined as large.

Two different methods were used to obtain a grid score. Firstly, single units were analysed with the Langston method (Langston *et al.*, 2010), for which the open arena was divided into 58 x 58 equal size bins of ~1.5 by 1.5 cm and a spatial firing rate map was produced. The firing rate map was autocorrelated and rotated with the following angles: 0°, 30°, 60°, 90°, 120°, 150°, and correlated to the original autocorrelation. Grid scores were calculated as the difference between values at 30°, 90° and 150° and values at 60° and 120°, which correspond to rotation angles with low and high correlations, respectively. More details can be found in section 2.3.11 of the general methodology. Secondly, single units were analysed with the Sargolini's method (Sargolini *et al.*, 2006), for which the open arena was divided into 50 x 50 equal size bins of ~1.7 by 1.7 cm and a spatial firing rate map was produced. The firing rate map was autocorrelated and rotated in steps of 3° at a time, up to 360°, and correlated to the original autocorrelation. The grid score was obtained by subtracting the highest correlation value within the values at 30°, 90° and 150°, from the lowest correlation value within the values at 60° and 120°. Elliptical correction (Brandon *et al.*, 2011) was only attempted if 6 surrounding peaks were detected in the autocorrelation and for eccentricity values below 0.5. Finally, elliptical correction was only applied if the resulting corrected grid score was higher than the uncorrected one. More details can be found in section 2.3.12 of the general methodology.

The spatial information (Skaggs, McNaughton and Gothard, 1993) that a cell conveyed was calculated using $\sum(P_i(R_i/R)\log_2(R_i/R))$; with R corresponding to the mean firing rate, R_i to the firing rate in bin i and P_i to the time spent in a spatial bin.

Border scores (Solstad *et al.*, 2008) were calculated using the following equation: $(Max_C - Mean_{FD})/(Max_C + Mean_{FD})$; with Max_C corresponding to the maximum coverage and $Mean_{FD}$ to the mean firing distance. Further details can be found in section 2.3.14 of the general methodology.

To determine significant spatial information, speed, HD, grid, and border scores, 250 shuffles of the spike time stamps were performed, and the various scores

recalculated. A threshold was calculated by obtaining the 95th percentile of the combined shuffled distributions of all cells. For speed negative modulated sensitive cells, the 5th percentile was also obtained. The proportion of cells classified as a specific functional subtype was determined by considering the scores obtained in each of the three trials for all cells. Thus, there were a total of three scores per cell, which could pass or fail the set threshold.

4.2.6.4 Novelty effects

Three different patterns were seen in the different scores described above when animals were exposed to the familiar and novel arenas (Fig. 2.8). “Decreasing” cells were defined as those that decreased their score in the novel trial with respect to both familiar trials. “Increasing” cells were defined as those that increased their score in the novel trial with respect to both familiar trials. “No changes” cells were defined as those that did not follow either of the previous patterns. To account for the possibility of these patterns being a product of random chance, the scores of each cell in the novel and second familiar trial were simulated at random, using the scores in the first familiar trial as a base. This was achieved by subtracting the scores in the first and second familiar trials from the scores of the novel trial, for each cell. This is expressed in the following equations:

$$diff_1 = S_{nov} - S_{fam1}$$

$$diff_2 = S_{nov} - S_{fam2}$$

with S_{nov} corresponding to the scores in the novel trial, S_{fam1} corresponding to the scores in the first familiar trial and S_{fam2} corresponding to the scores in the second familiar trial. Two populations of differences were generated: $diff_1$ and $diff_2$.

The standard deviation of $diff_1$ and $diff_2$ was used to obtain two randomly generated populations, $diff'_1$ and $diff'_2$, of equal size to the original populations and with a normal distribution. To obtain the simulated scores in the novel trial, $diff'_1$ was added to S_{fam1} . To obtain the simulated scores in the second familiar trial, $diff'_2$ was subtracted from the simulated scores in the novel trial. This

process was repeated 100 times. Simulated data was classified in the same manner as mentioned previously for the observed data, and the proportions of the different cell types compared to the observed proportions. To determine if the proportion of observed “decreasing” cells was higher than what could be expected by chance, it was compared to the proportion of simulated “decreasing” cells. The same process was followed to determine if the proportion of increasing cells was higher than chance levels. Further details can be found in section 2.3.15 of the general methodology.

4.2.7. Statistical analysis

All repeatedly measured data was analysed by using linear mixed effects models with the package ‘lme4’ in R studio. The function ‘lmer’ was used when the residuals of the response variable fit well with a Gaussian distribution. In cases in which another family of distribution better fit the residuals, the function ‘glmer’ was used instead. Models were built up, from simplistic to complex, for each response variable and the AIC values of each model were compared to assess the best fit when there were significant differences between models. When no significant differences were detected, the simplest model was selected. These models specified the hierarchical structure of the data by including, as random factors, cells nested into animals. Therefore, the effects of multiple cells belonging to a single animal, as well as repeated measures being taken from each cell, were considered by the model. The possible effects of layer variability and using different arenas, rooms and trials were also considered when relevant for each model. The functions ‘joint_tests’ and ‘emmeans’ from the package ‘emmeans’ (<https://cran.r-project.org/web/packages/emmeans/emmeans.pdf>) were used to study main effects and for pairwise comparisons, respectively. Tukey corrections for multiple comparisons were used for pairwise comparisons. Statistical comparison between two different groups was performed with a student’s t-test, for normally distributed data, or Wilcoxon test, for non-normally distributed data.

The main effects obtained by the linear mixed effects models are reported with the F-statistic (F), with its associated degrees of freedom within brackets, and the p value (p). The results obtained with pairwise comparisons by the linear mixed effects models are reported with the fixed-effects estimate (β), the standard error (SE), the t-statistic (t) and the p value (p). The z-statistic (z) is reported, instead of t-statistic, when the function ‘glmer’ for generalised mixed effects models is used.

Percentages were compared in two different ways; through Fisher's exact test, when some of the expected frequencies are smaller than 5 (Kim, 2017) or when there were more than two possible outcomes, and through mixed models with a binomial distribution. Fisher's exact test was also used to compare the proportions of “increasing” and “decreasing” cells, as linear mixed effects models were found unsuitable due to the large n number in the simulated data in comparison to the observed data, leading to highly unbalanced data. The function ‘pairwiseNominalIndependence’ from the package ‘rcompanion’ (<https://cran.r-project.org/web/packages/rcompanion/rcompanion.pdf>) was used to perform the Fisher's exact test. Bonferroni corrections for multiple comparisons were used.

4.3. Results

4.3.1. J20 mice and WT mice spend similar time next to the borders of the arena

The tracking position for each trial was divided into time spent within 15 cm from the walls of the open arenas, referred to as time next to the borders of the arena and expressed as a percentage of the total recording time, and time spent in the middle of the arena (Fig. 4.1B). All mice spent a similar amount of time next to the borders of the arena independently of genotype ($F(1, 6.97) = 0.71, p = 0.43$, Fig. 4.1Ci) or context ($F(1, 37.33) = 1.04, p = 0.31$, Fig. 4.1Cii). These results contrast with the differences observed between both genotypes in the previous chapter. However, a key difference between both experiments is that mice were only food restricted and encouraged to explore the open arena with food rewards in the experiment described in this chapter, which may confound these results.

The time spent in each running speed bin averaged across animals in each group and trial can be seen in figure 4.1A. WT and J20 mice showed similar average running speeds ($F(1, 6.98) = 0.09, p = 0.77$, Fig. 4.1Di), which did not change significantly when exploring the novel context ($F(1, 36.80) = 1.24, p = 0.27$, Fig. 4.1Dii).

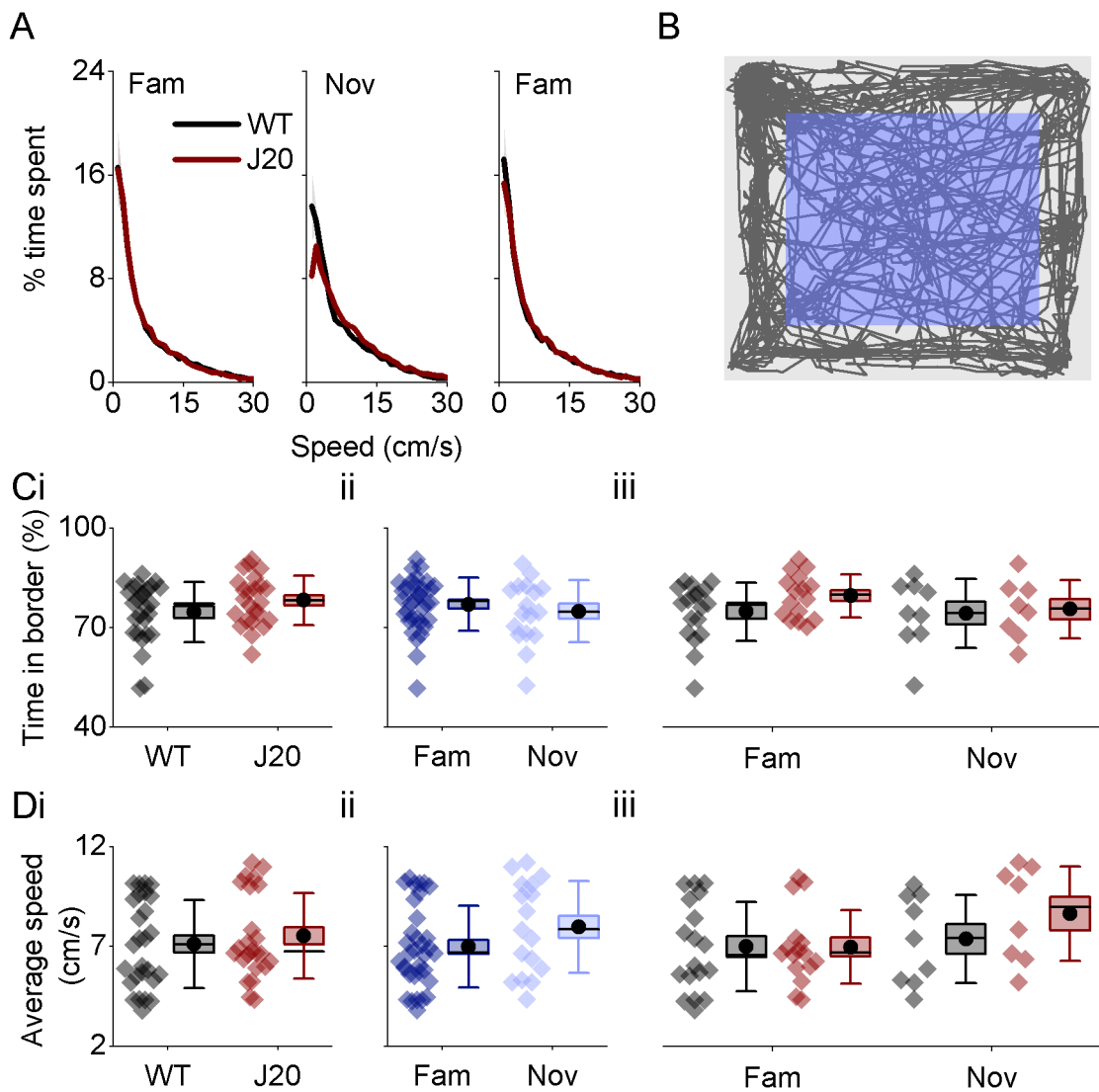


Figure 4.1 J20 mice and WT mice spend a similar amount time next to the borders of the arena. **A)** Mean time spent in each running speed bin, from 0 to 30 cm/s, expressed as a percentage. This is shown, from left to right, for the first exposure to the familiar arena, the exposure to the novel arena and the second exposure to the familiar arena for both WT and J20 mice. Error bars are included in this plot but are not visible due to their small values. **B)** Example of tracking data separated into the central (blue shade) and the border (grey shade) areas of the arena. Borders are defined as 15 cm from the wall. Arena size is 86.5 x 86.5 cm. **C)** Time spent next to the border of the arena for both genotypes **(i)**, between contexts **(ii)** and by context in WT (black) and J20 (red) mice **(iii)**. The data shown in **(i)**, **(ii)** and **(iii)** is the same data replotted separately. **D)** Average speed for both genotypes **(i)**, between contexts **(ii)** and between the two contexts in WT (black) and J20 mice (red). The data shown in **(i)**, **(ii)** and **(iii)** is the same data replotted separately. Line plots: line corresponds to the mean and error bars represent the \pm SEM. Box plots: box corresponds to the mean \pm SEM, the circle to the mean, the line to the median and the whiskers to the SD. (* $p \leq 0.05$, ** $p \leq 0.01$, *** $p \leq 0.001$)

4.3.2. Broadband spectral analysis shows no differences between both genotypes

All recordings were performed in the superficial layers of the dorsal MEC. However, the layer recording location was not always the same, with some shanks being in either layer II or III (Fig. 4.2A and B). Furthermore, although all recordings were performed within 900 μ m from the dorsal border of the MEC (Fig. 4.2C and D), the recording locations in J20 mice were more ventral than in WT mice when estimating the probe tip location ($t(24.9) = -2.41$, $p = 0.02$, independent t-test, Fig. 4.2C) and the position of each recorded cell ($W = 4217$, $p = 4.54E-10$, Wilcoxon test, Fig. 4.2D). Both cortical thickening and thinning have been described in certain brain regions in J20 mice. For example, cortical thickening has been observed in the EC of J20 mice at ~3 months of age (Hébert *et al.*, 2013). At ~6 months of age, cortical thickening has been seen in areas such as the LEC, the entorhinal cortex and the primary visual cortex in J20 mice (Badhwar *et al.*, 2013). On the other hand, J20 mice experience greater EC cortical thinning as they age relatively to their initial thickness at 3 months of age (Hébert *et al.*, 2013). Changes of thickness in the EC and nearby areas, such as the entorhinal cortex and the primary visual cortex, could lead to differences in the recording position along the dorsoventral axis in J20 mice. If the volume of these areas is increased, more dorsal recording positions should be expected in J20 mice. However, the results showed in figure 4.2 show that the recordings in J20 mice were performed more ventrally, which makes it unlikely that an increase of cortical thickness is the cause of this difference. On the other hand, the studies mentioned above did not specifically focus on the MEC and it may be possible that a slight decrease in its volume could lead to more ventral recording locations in J20 mice. However, the factors leading to more ventral recording locations in J20 mice cannot be established with certainty in this thesis.

The power spectrum averaged across animals in each group and trial can be seen in figure 4.3A. Spectral analysis was performed for theta and high gamma frequency oscillations. Total broadband power was used to normalise the power in the different frequency bands for comparison. The normalised theta power did not differ between both genotypes ($F(1, 6.99) = 0.24$, $p = 0.64$, Fig. 4.3Bi) nor

context ($F(1, 36.27) = 0.03$, $p = 0.87$, Fig. 4.3Bii). Although the normalised high gamma power was not different between WT and J20 mice ($F(1, Inf) = 0.14$, $p = 0.71$, Fig. 4.3Ci), an effect of context was observed ($F(1, Inf) = 4.57$, $p = 0.03$, Fig. 4.3Cii).

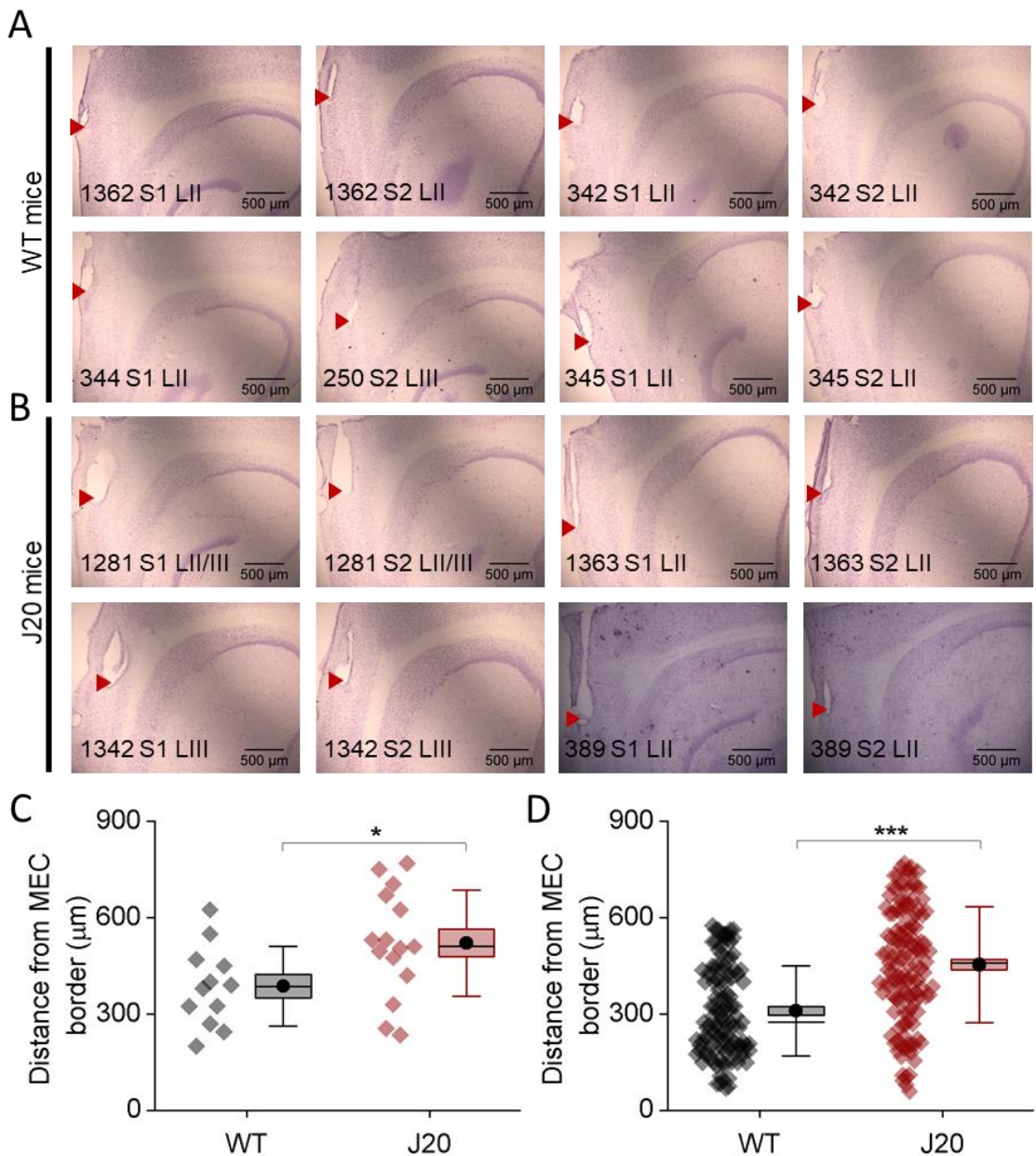


Figure 4.2 MEC recording sites. **A)** Recording sites for WT mice, with the numbers in the bottom left corner being the ID of each animal. S1 and S2 refer to shank 1 and shank 2, respectively. Animal 250 was implanted in layer III. **B)** Recording sites for J20 mice, with the numbers in the bottom left corner being the ID of each animal. S1 and S2 refer to shank 1 and shank 2, respectively. Animal 1342 was implanted in layer III. Animal 1281 was implanted between layers II and III. **C)** Estimated distance from the dorsal border of the MEC to the probe tip. **D)** Estimated distance, for every cell recorded, from the dorsal border of the MEC. Red arrows show the end of the last recording position for each animal. Box plots: box corresponds to the mean \pm SEM, the circle to the mean, the line to the median and the whiskers to the SD. (* $p \leq 0.05$, ** $p \leq 0.01$, *** $p \leq 0.001$)

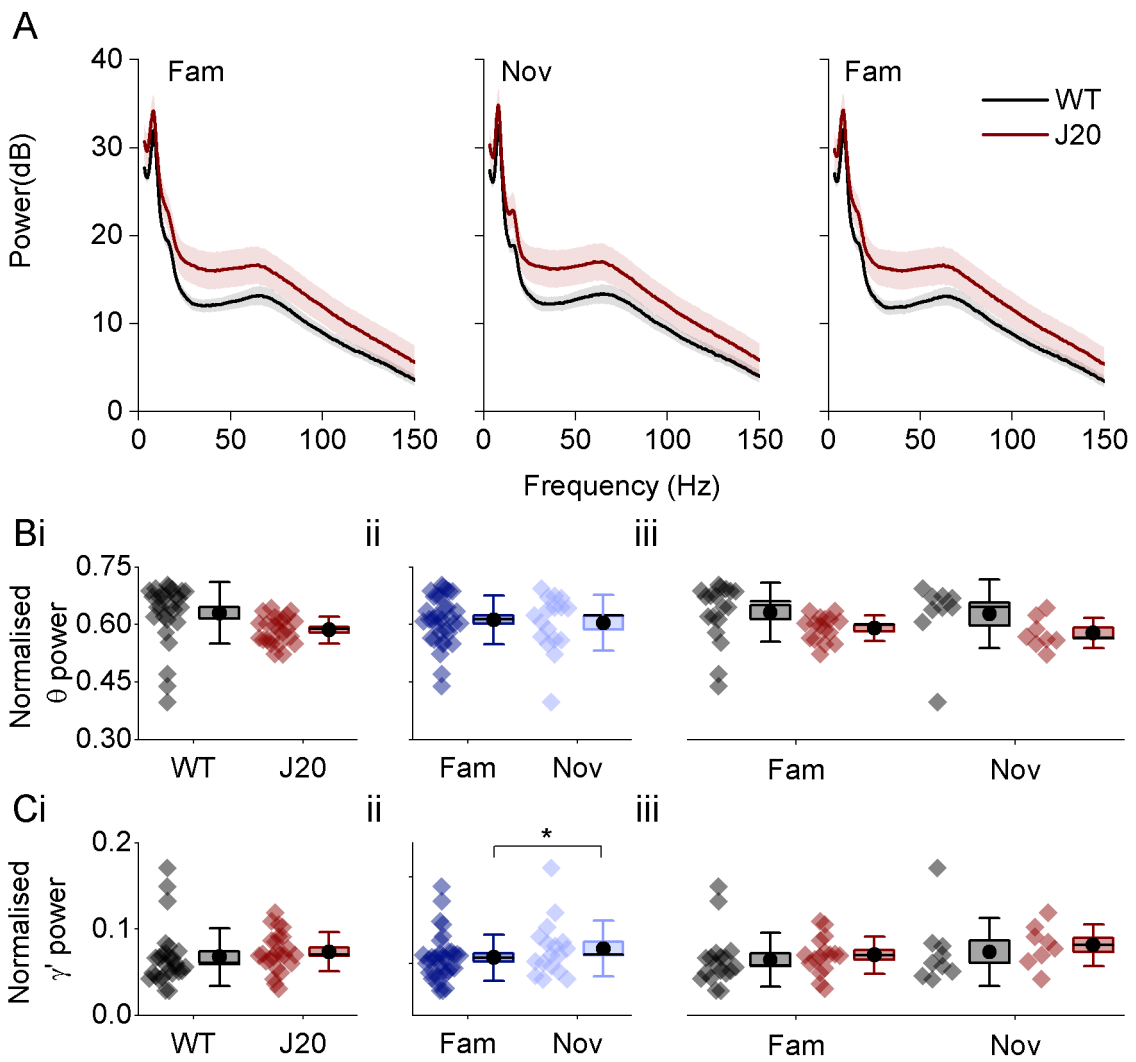


Figure 4.3 Power spectrum shows no deficits in J20 mice. **A)** Pooled power spectrum averaged across animals in each group for each trial. **B)** Pooled data showing no significant differences in the theta band (normalised using the broadband power) between both genotypes (**i**), between contexts (**ii**) and between contexts in WT (black) and J20 (red) mice (**iii**). The data shown in **(i)**, **(ii)** and **(iii)** is the same data replotted separately. **C)** Pooled data showing high gamma (γ') power (normalised using the broadband power) between both genotypes (**i**), by context (**ii**) and between contexts in WT (black) and J20 (red) mice (**iii**). The data shown in **(i)**, **(ii)** and **(iii)** is the same data replotted separately. Line plots: line corresponds to the mean and error bars represent the \pm SEM. Box plots: box corresponds to the mean \pm SEM, the circle to the mean, the line to the median and the whiskers to the SD. (* $p \leq 0.05$, ** $p \leq 0.01$, *** $p \leq 0.001$)

4.3.3. MEC network oscillations

In chapter 3, changes in the relationship of theta and high gamma frequency oscillations with running speed due to novelty and familiarity were studied. These changes were examined through the slopes resulting from the linear fits performed on this data. Previously presented results showed that the theta power slope was steeper in the familiar trial than in the second novel trial in both WT and J20 mice. Interestingly, it was also observed that the slope from the relationship between the frequency and power of high gamma oscillations and running speed became steeper in the most familiar trial when compared to the novel ones. However, this only occurred in WT animals, with J20 mice showing no changes. In this chapter, these relationships were again studied to confirm the deficits observed in J20 mice in the previous chapter.

Heat plots showing changes in theta power and frequency on the first familiar trial, overlapped with the running speed, can be observed in figures 4.4Ai and ii for a WT and a J20 mouse, respectively. Changes in theta power and frequency with running speed, averaged across animals in each group and trial, can be seen in figure 4.4Bi and ii. In agreement with the results of the previous chapter, the slope resulting from the relationship between the power of theta frequency oscillations and running speed was not different between WT and J20 mice ($F(1, 7.20) = 0.30, p = 0.60$, Fig. 4.4Ci). However, it significantly decreased in the novel environment in both WT and J20 mice ($F(1, 40.01) = 22.01, p < 0.0001$, Fig. 4.4Cii), which is consistent with the previous results. This was not true for the frequency slope of these oscillations ($F(1, 37) = 0.16, p = 0.69$, Fig. 4.4Dii). In addition, the frequency slope was similar between WT and J20 mice ($F(1, 6.98) = 0.22, p = 0.65$, Fig. 4.4Di). No changes related to the frequency intercept were observed between both genotypes ($F(1, Inf) = 3.72, p = 0.054$, Fig. 4.4Ei) nor context ($F(1, Inf) = 1.69, p = 0.19$, Fig. 4.4Eii).

Heat plots showing changes in high gamma power and frequency on the first familiar trial, overlapped with the running speed, can be observed in figures 4.5Ai and ii for a WT and a J20 mouse, respectively. Changes in high gamma power and frequency with running speed, averaged across animals in each group and trial, can be seen in figure 4.5Bi and ii. The analysis of the slope of high gamma

power versus running speed showed a significant interaction between genotype and context ($F(1, \text{Inf}) = 13.11, p = 0.0003$, Fig. 4.5C). However, contrasting with the results presented in the previous chapter, further pairwise comparisons showed that the slope of this relationship significantly decreased with novelty in J20 mice ($\beta = 0.32, \text{SE} = 0.10, z(51) = 3.23, p = 0.007$, Fig. 4.5Ciii) but not in WT mice ($\beta = -0.14, \text{SE} = 0.08, z(51) = -1.77, p = 0.29$, Fig. 4.5Ciii). The frequency slope and intercept of gamma oscillations did not differ between both genotypes (slope: $F(1, 7.21) = 2.51, p = 0.16$, Fig. 4.5Di; intercept: $F(1, \text{Inf}) = 0.13, p = 0.72$, Fig. 4.5Ei) and showed no changes due to novelty (slope: $F(1, 40.01) = 1.06, p = 0.31$, Fig. 4.5Dii; intercept: $F(1, \text{Inf}) = 1.22, p = 0.27$, Fig. 4.5Eii).

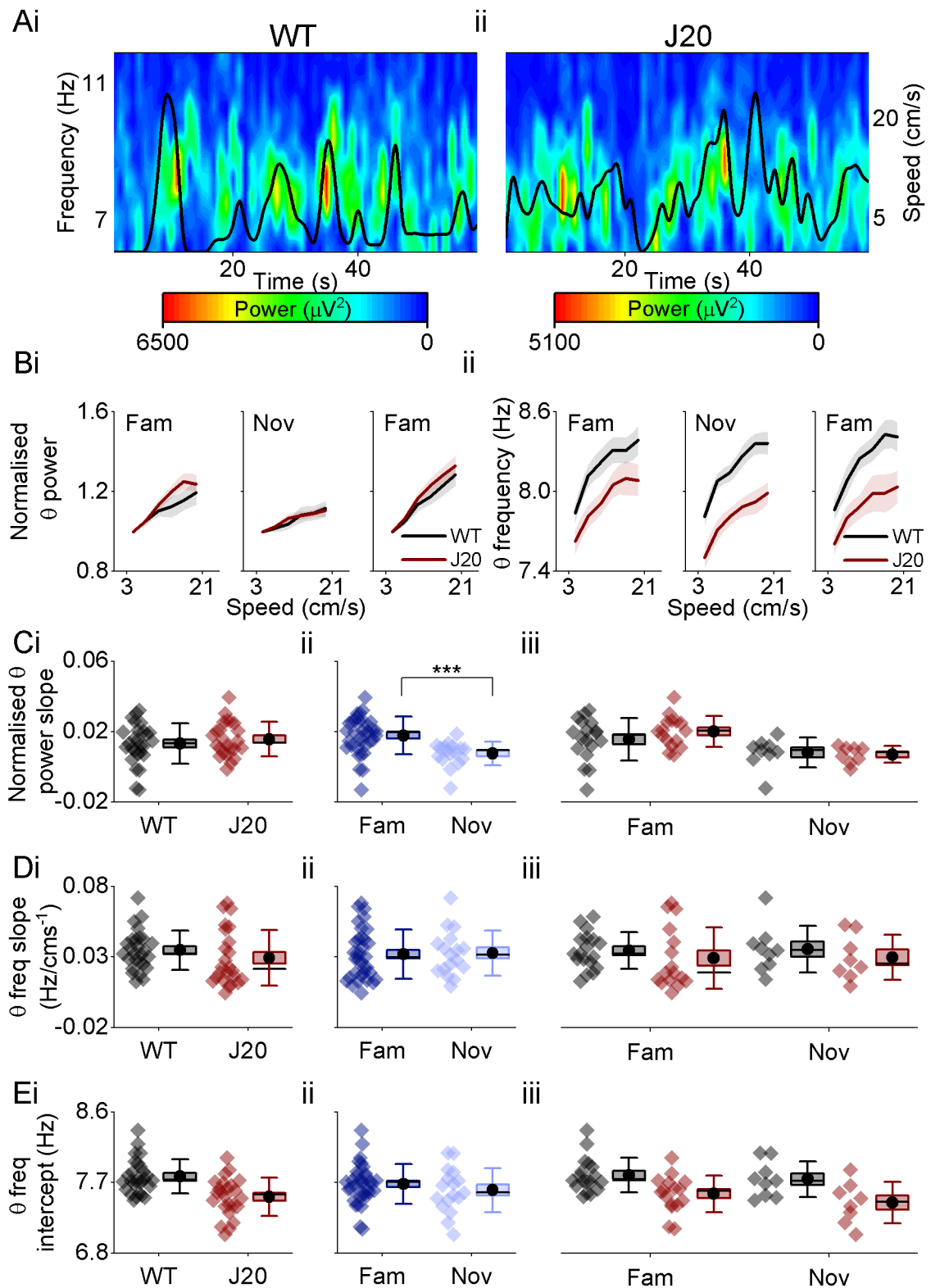


Figure 4.4 The power slope of theta oscillations is affected by novelty in both WT and J20 mice. **A)** Example heat plots showing changes in the frequency and power of theta oscillations with running speed for a WT (i) and a J20 (ii) mouse over a minute in a familiar trial. **B)** Pooled theta power (normalised using the first value) (i) and frequency (ii) versus running speed, averaged across animals in each group for each trial. **C)** Comparison of theta power – running speed slopes between both genotypes (i), between both contexts (ii) and between both contexts in WT (black) and J20 (red)

mice (**iii**). The data shown in **(i)**, **(ii)** and **(iii)** is the same data replotted separately. **D)** Comparison of theta frequency – running speed slopes between both genotypes **(i)**, by context **(ii)** and between both contexts in WT (black) and J20 (red) mice **(iii)**. The data shown in **(i)**, **(ii)** and **(iii)** is the same data replotted separately. **E)** Comparison of theta frequency intercepts between both genotypes **(i)**, between contexts **(ii)** and between contexts in WT (black) and J20 (red) mice **(iii)**. The data shown in **(i)**, **(ii)** and **(iii)** is the same data replotted separately. Line plots: line corresponds to the mean and error bars represent the \pm SEM. Box plots: box corresponds to the mean \pm SEM, the circle to the mean, the line to the median and the whiskers to the SD. (* $p \leq 0.05$, ** $p \leq 0.01$, *** $p \leq 0.001$)

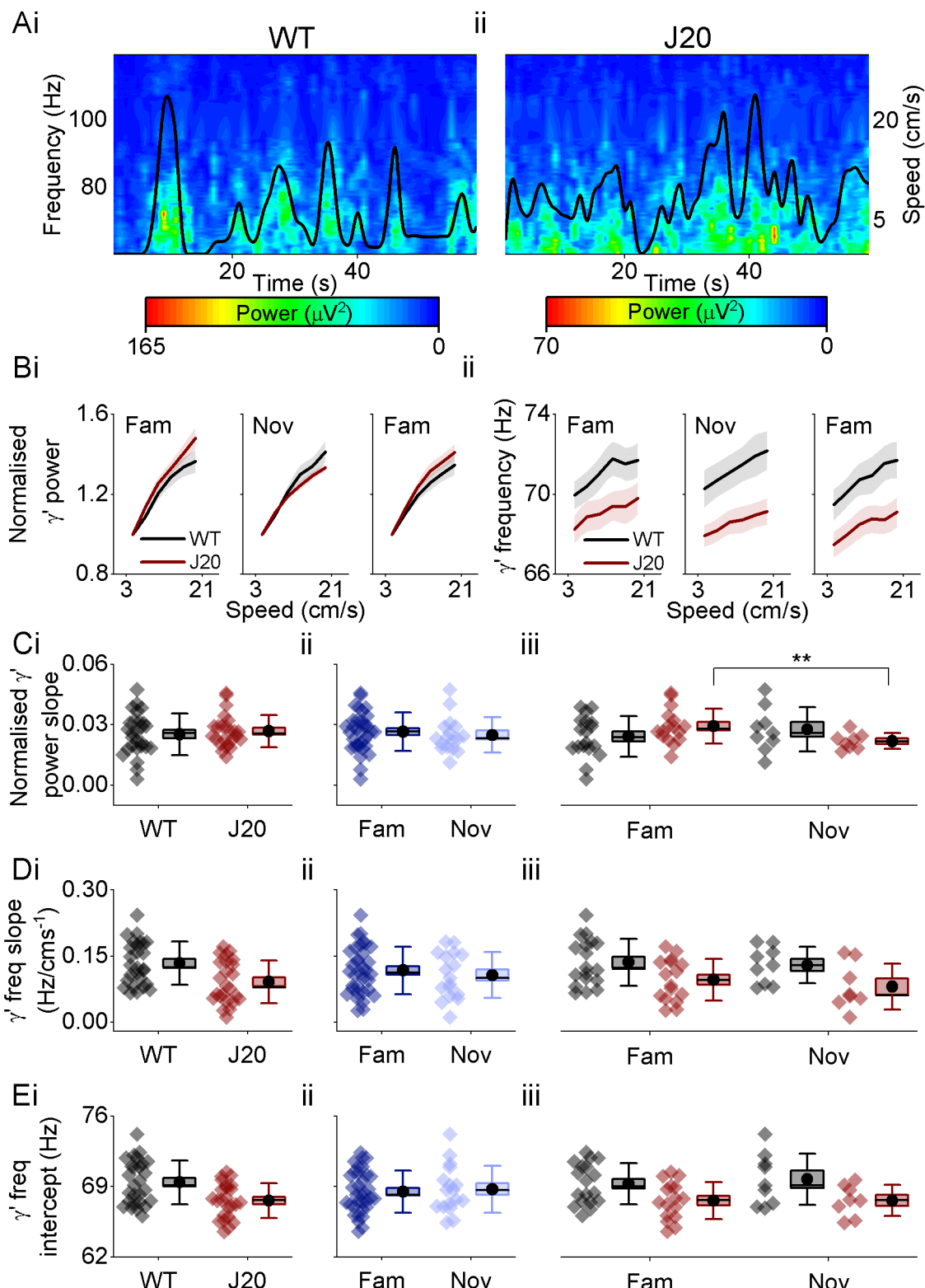


Figure 4.5 The power slope of high gamma oscillations is affected by novelty only in J20 mice. **A)** Example heat plots showing changes in the frequency and power of high gamma oscillations with running speed for a WT (i) and a J20 (ii) mouse over a minute in a familiar trial. **B)** Pooled high gamma power (normalised using the first value) (i) and frequency (ii) versus running speed, averaged across animals in each group for each trial. **C)** Comparison of high gamma power – running speed slopes between both genotypes (i), between contexts (ii) and between contexts in WT (black)

and J20 (red) mice (**iii**). The data shown in **(i)**, **(ii)** and **(iii)** is the same data replotted separately. **D**) Comparison of high gamma frequency – running speed slopes between both genotypes **(i)**, between contexts **(ii)** and between contexts in WT (black) and J20 (red) mice **(iii)**. The data shown in **(i)**, **(ii)** and **(iii)** is the same data replotted separately. **E**) Comparison of high gamma frequency intercepts between both genotypes **(i)**, between contexts **(ii)** and between contexts in WT (black) and J20 (red) mice **(iii)**. The data shown in **(i)**, **(ii)** and **(iii)** is the same data replotted separately. Line plots: line corresponds to the mean and error bars represent the \pm SEM. Box plots: box corresponds to the mean \pm SEM, the circle to the mean, the line to the median and the whiskers to the SD. (* $p \leq 0.05$, ** $p \leq 0.01$, *** $p \leq 0.001$)

Figure 4.6A shows PAC comodulograms averaged across animals in each group for representative speed bins in each trial. Figure 4.6B shows changes in the MI values versus running speed for each trial and genotype. The slope between running speed and the MI values between the phase of theta oscillations and the amplitude of high gamma oscillations was also studied in here. As observed in the previous chapter, MI slopes were not different between WT and J20 mice ($F(1, 8.18) = 0.59$, $p = 0.46$, Fig. 4.6Ci). Consistent with the results presented in the previous chapter, MI slopes significantly decreased with novelty ($F(1, 40.15) = 7.24$, $p = 0.01$, Fig. 4.6Cii) in both WT and J20 mice.

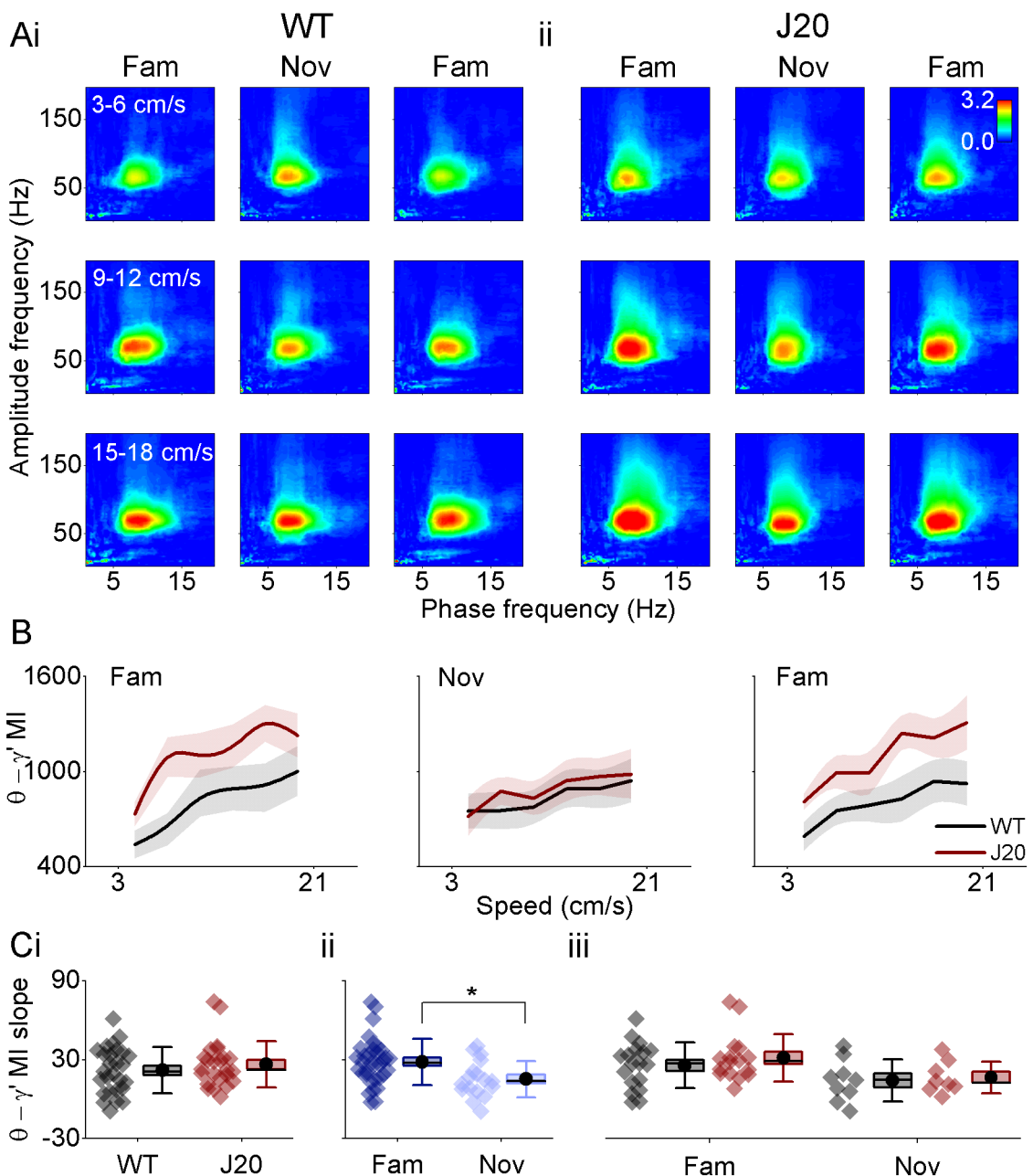


Figure 4.6 MI slopes decrease with novelty in the MEC of both WT and J20 mice. **A)** Averaged phase-amplitude comodulograms across animals for certain running speed examples in WT (**i**) and J20 (**ii**) mice, for each trial. **B)** Pooled MI values for high gamma versus running speed, averaged across animals in each group for each trial. **C)** Comparison of MI values – running speed slopes between both genotypes (**i**), between contexts (**ii**) and between contexts in WT (black) and J20 (red) mice (**iii**). The data shown in **(i)**, **(ii)** and **(iii)** is the same data replotted separately. Line plots: line corresponds to the mean and error bars represent the \pm SEM. Box plots: box corresponds to the mean \pm SEM, the circle to the mean, the line to the median and the whiskers to the SD. (* $p \leq 0.05$, ** $p \leq 0.01$, *** $p \leq 0.001$)

4.3.4. More cells are classified as theta modulated with the TMI criteria

Theta modulation was first studied with the TMI method (Langston *et al.*, 2010). Figure 4.7A shows examples of firing autocorrelations and Fourier transform of a theta modulated (Fig. 4.7Ai) and a non-modulated WT cell (Fig. 4.7Aii). Figure 4.7B shows examples of firing autocorrelations and Fourier transform of a theta modulated (Fig. 4.7Bi) and a non-modulated J20 cell (Fig. 4.7Bii). The proportion of cells classified as theta modulated was similar between both genotypes ($F(1, Inf) = 0.12$, $p = 0.73$, Fig. 4.7Ci). In addition, the proportion of theta modulated cells was not significantly different between the familiar and the novel context ($F(1, Inf) = 0.90$, $p = 0.34$, Fig. 4.7Cii) and this was consistent in both genotypes ($F(1, Inf) = 0.40$, $p = 0.53$, Fig. 4.7Cii). The proportion of theta modulated cells was equivalent between putative excitatory and putative interneurons ($F(1, Inf) = 0.76$, $p = 0.38$, Fig. 4.7Ciii) and these proportions were equal between genotypes ($F(1, Inf) = 0.57$, $p = 0.45$, Fig. 4.7Ciii). The proportions of WT layer II cells which were theta modulated were significantly higher than in layer III ($F(1, Inf) = 15.08$, $p = 0.0001$, Fig. 4.7Civ).

The preferred phase of the theta wave of each theta modulated cell was also analysed (Fig. 4.8A and B). No differences were found between both genotypes ($F(1, Inf) = 0.16$, $p = 0.69$, Fig. 4.8Ci). However, a greater percentage of theta modulated cells were coupled to the peak of the theta wave in layer III relative to layer II ($F(1, Inf) = 42.69$, $p < 0.0001$, Fig. 4.8Cii), which suggests that the apparent differences observed between WT and J20 (Fig. 4.8Ci) are due to a layer effect. The proportion of putative interneurons coupled to the trough of theta was similar to the proportion of putative excitatory cells ($F(1, Inf) = 1.41$, $p = 0.23$, Fig. 4.8Ciii).

The frequency at which the modulation occurred showed no significant changes due to genotype ($F(1, Inf) = 0.01$, $p = 0.91$, Fig. 4.9A) nor between putative interneurons and putative excitatory cells ($F(1, Inf) = 3.03$, $p = 0.08$, Fig. 4.9D). However, the frequency of the modulation was affected by context ($F(1, Inf) = 4.99$, $p = 0.025$, Fig. 4.9C). Furthermore, the analysis showed that layer III cells had a lower frequency of rhythmicity than layer II cells ($F(1, Inf) = 14.75$, $p = 0.0001$, Fig. 4.9B). The strength of the modulation was measured through both

the TMI and the resultant mean vector length. No differences were observed due to genotype in the TMI ($F(1, Inf) = 1.08$, $p = 0.30$, Fig. 4.10A) or in the vector length ($F(1, Inf) = 3.35$, $p = 0.07$, Fig. 4.11A). No effects of context was observed in either measure (TMI: $F(1, Inf) = 3.25$, $p = 0.07$, Fig. 4.10B; Vector length: $F(1, Inf) = 0.04$, $p = 0.84$, Fig. 4.11C). The strength of the modulation was greater in putative interneurons than in putative excitatory cells (TMI: $F(1, Inf) = 35.51$, $p < 0.0001$, Fig. 4.10C; Vector length: $F(1, Inf) = 5.95$, $p = 0.015$, Fig. 4.11D). Layer III cells had lower vector length values than layer II cells ($F(1, Inf) = 7.42$, $p = 0.006$, Fig. 4.11B), reflecting relatively little theta modulation in these cells.

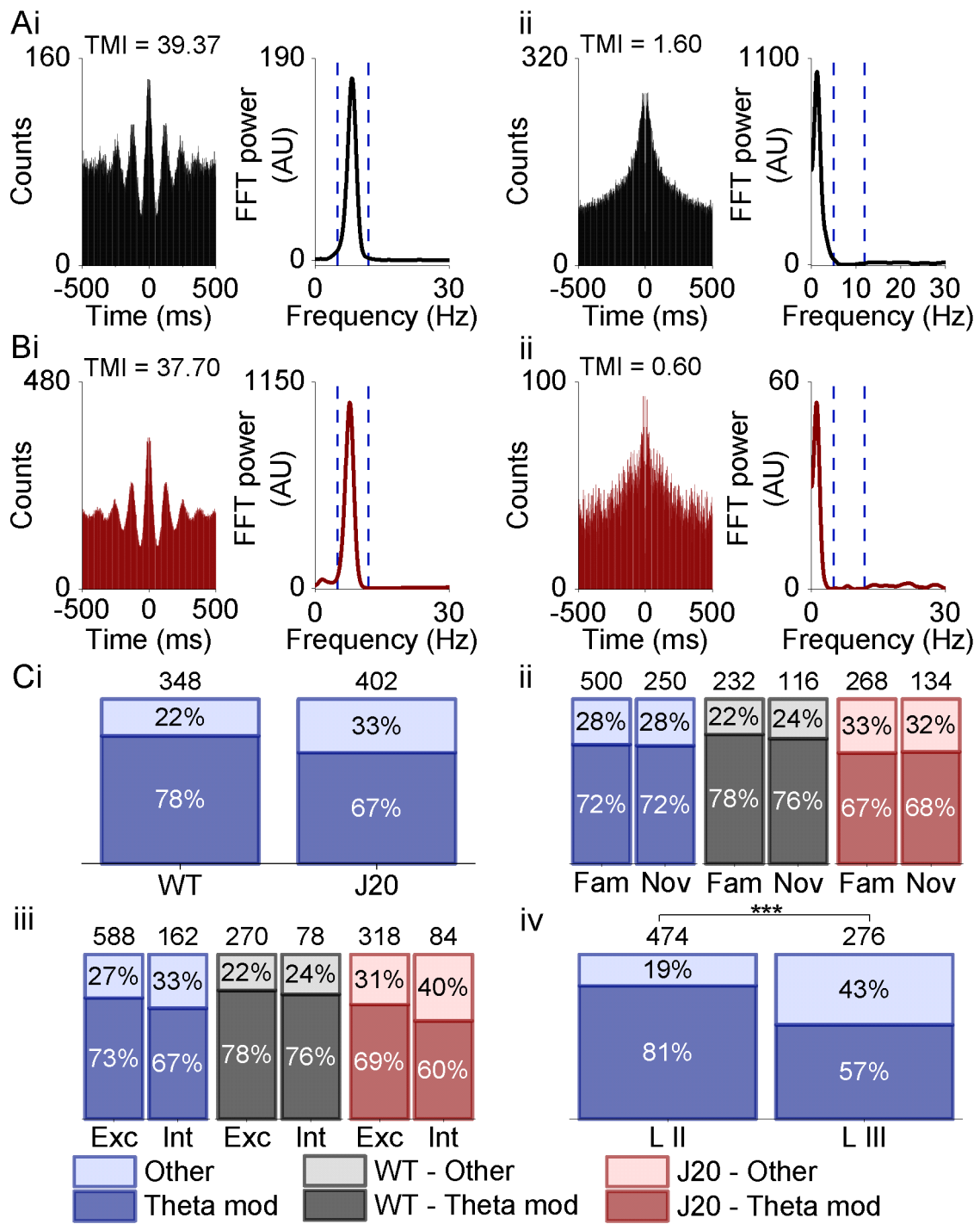


Figure 4.7 The proportion of theta modulated cells is lower in layer III of the MEC. **A)** Examples of firing autocorrelations and Fourier transform of these autocorrelations in a WT theta modulated cell (**i**) and a non-modulated cell (**ii**). **B)** Examples of firing autocorrelations and Fourier transform of these autocorrelations in a J20 theta modulated cell (**i**) and a non-modulated cell (**ii**). **C)** Proportions of theta modulated and other (non-theta modulated) cells between both genotypes (**i**), by context (**ii**), by cell type (putative excitatory versus putative interneurons) (**iii**) and by layer (**iv**). Numbers above bars represent the total n number. (* p ≤ 0.05, ** p ≤ 0.01, *** p ≤ 0.001)

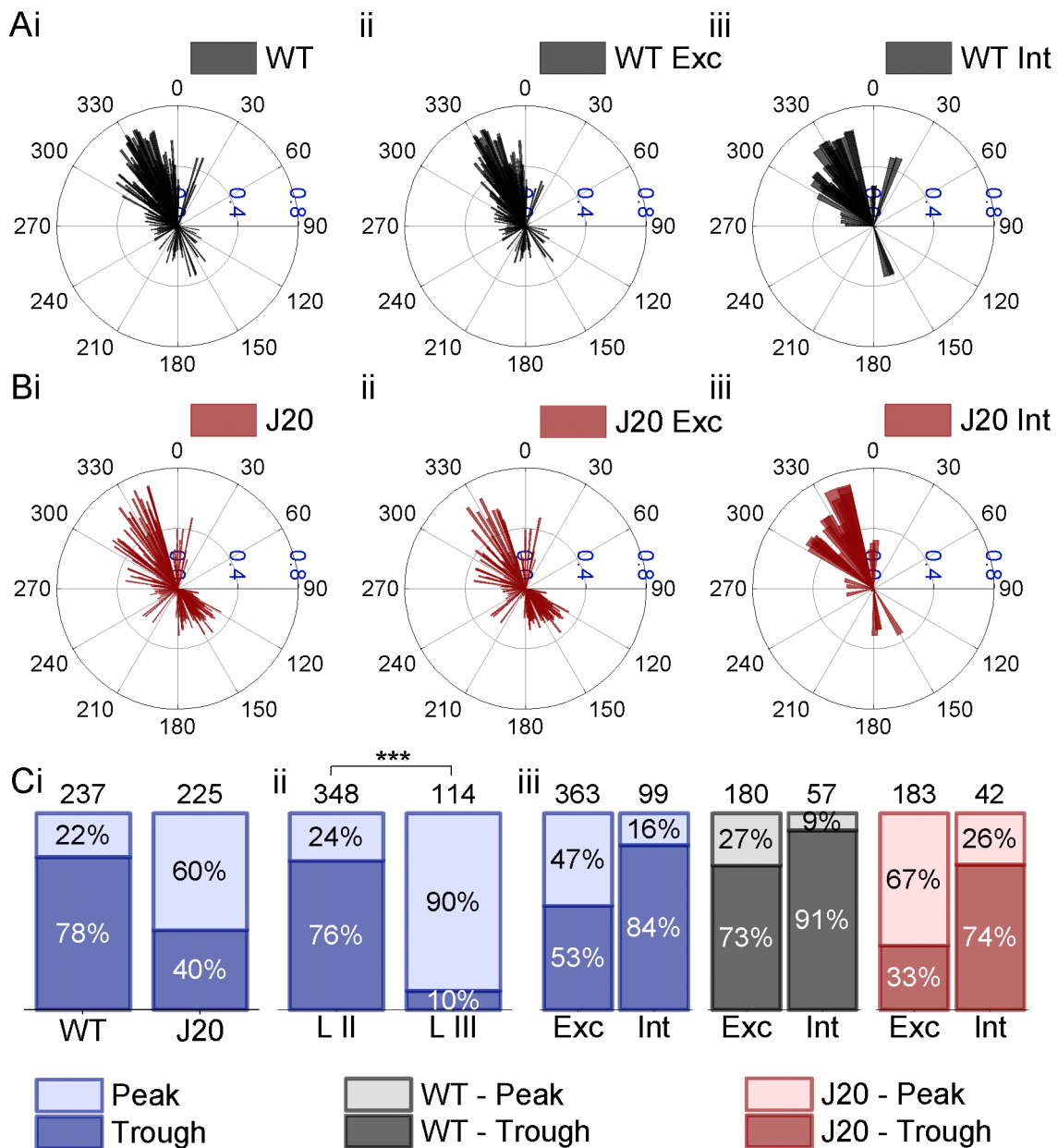


Figure 4.8 The firing of a higher proportion of layer III cells is locked to the peak of theta oscillations. A) Circular mean of the preferred firing phase of each cell plotted against its respective mean resultant vector length of WT cells in the first familiar trial (i) the novel trial (ii) and the second familiar trial (iii). **B)** Circular mean of the preferred firing phase of each cell plotted against its respective mean resultant vector length of J20 cells in the first familiar trial (i) the novel trial (ii) and the second familiar trial (iii). **C)** Proportions of cells with a circular mean of their preferred firing phase corresponding to the peak and the trough of theta oscillations by genotype (i), layer (ii) and cell type (putative excitatory versus putative interneurons) (iii). Numbers above bars represent the total n number. (* p ≤ 0.05, ** p ≤ 0.01, *** p ≤ 0.001)

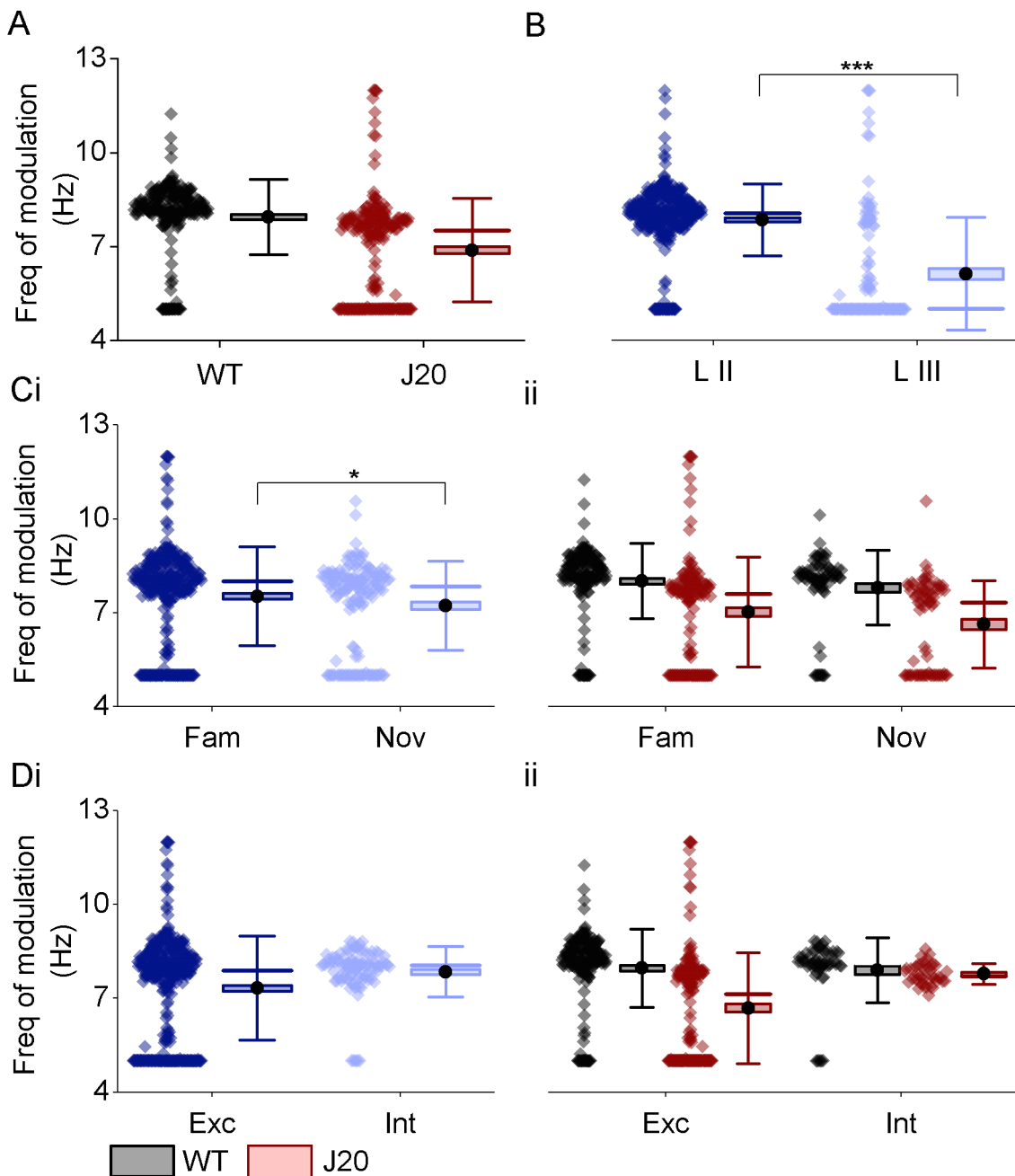


Figure 4.9 The frequency of the modulation is lower in cells of layer III of the MEC. **A)** Pooled frequency of the modulation data by each genotype and **B)** by layer. **C)** Pooled frequency of the modulation data between both contexts (**i**) and between contexts in WT (black) and J20 (red) mice (**ii**). **D)** Pooled frequency of the modulation data by cell type (putative excitatory versus putative interneurons) (**i**) and by cell type in WT (black) and J20 (red) mice (**ii**). The data shown in **A**, **B**, **C** and **D** is the same data replotted separately. Box plots: box corresponds to the mean \pm SEM, the circle to the mean, the line to the median and the whiskers to the SD. (* $p \leq 0.05$, ** $p \leq 0.01$, *** $p \leq 0.001$)

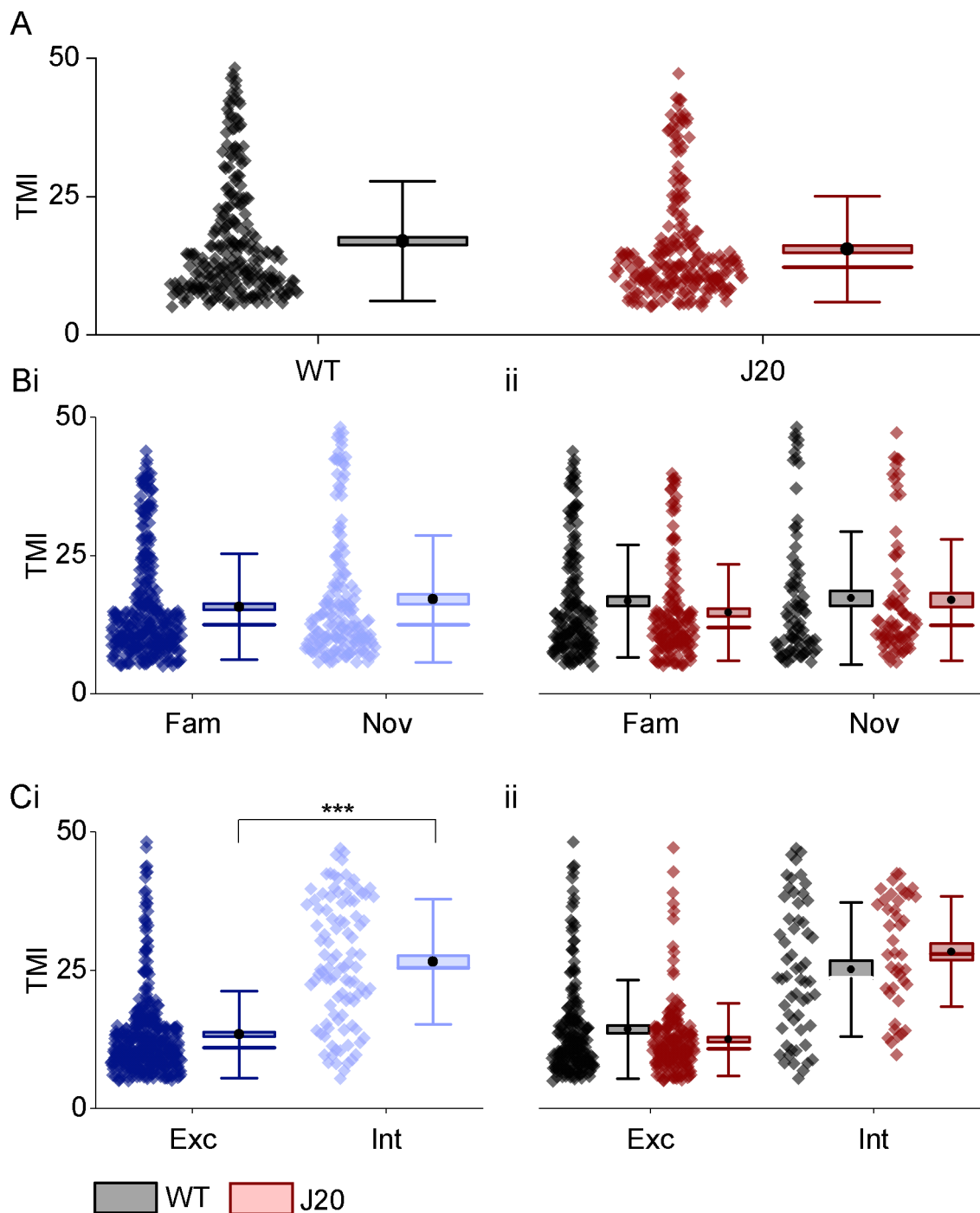


Figure 4.10 The TMI is lower in putative excitatory cells than in putative interneurons. **A)** Pooled TMI data by each genotype. **B)** Pooled TMI data between both contexts (**i**) and between contexts in WT (black) and J20 (red) mice (**ii**). **C)** Pooled TMI data by cell type (putative excitatory versus putative interneurons) (**i**) and by cell type in WT (black) and J20 (red) mice (**ii**). The data shown in **A**, **B** and **C** is the same data replotted separately. Box plots: box corresponds to the mean \pm SEM, the circle to the mean, the line to the median and the whiskers to the SD. (* $p \leq 0.05$, ** $p \leq 0.01$, *** $p \leq 0.001$)

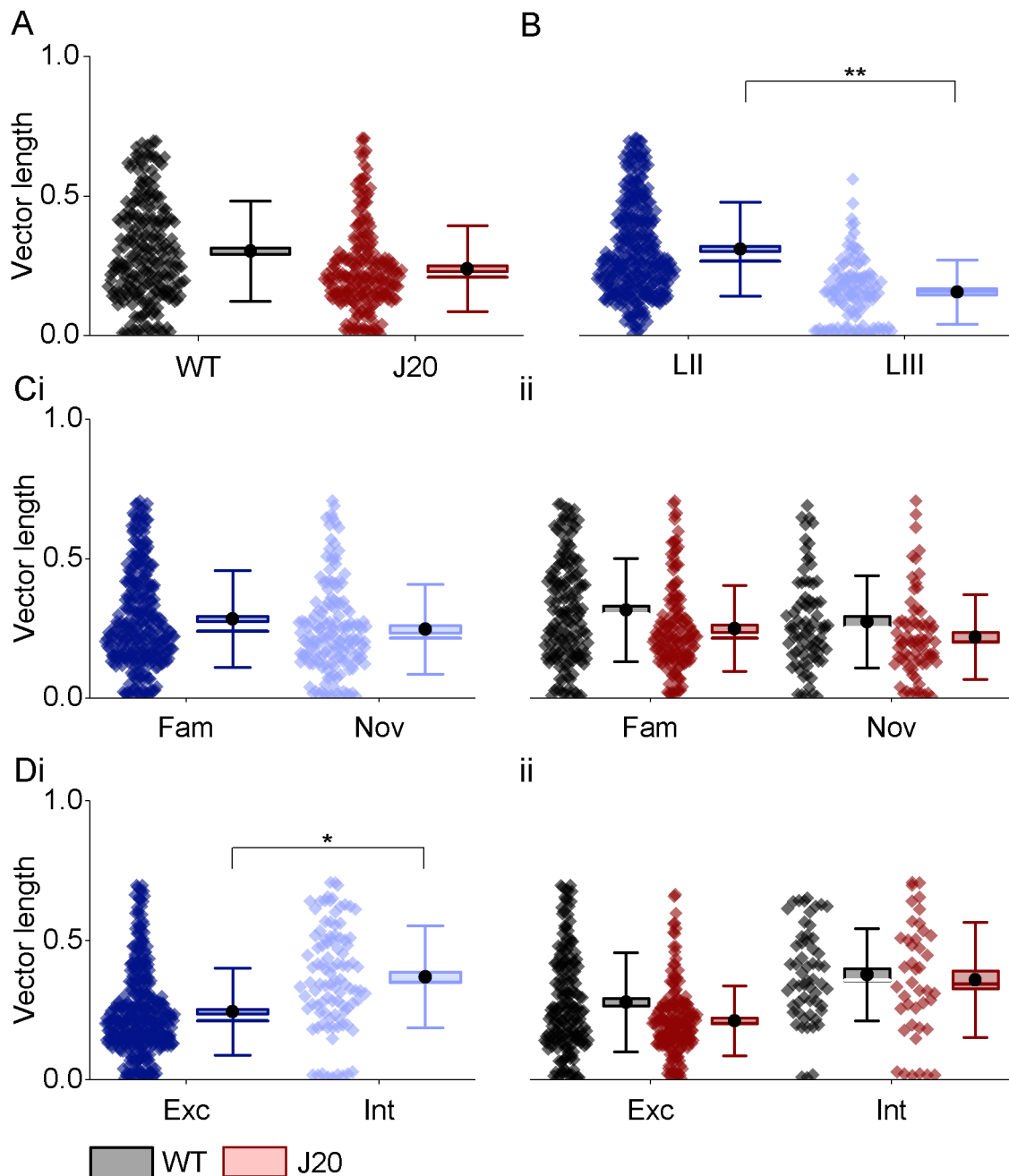


Figure 4.11 The mean vector length is lower in putative excitatory cells than in putative interneurons. A) Pooled mean vector length data by each genotype and **B)** by layer. **C)** Pooled mean vector length data between both contexts (**i**) and between contexts in WT (black) and J20 (red) mice (**ii**). **D)** Pooled mean vector length data by cell type (putative excitatory versus putative interneurons) (**i**) and by cell type in WT (black) and J20 (red) mice (**ii**). The data shown in **A**, **B**, **C** and **D** is the same data replotted separately. Box plots: box corresponds to the mean \pm SEM, the circle to the mean, the line to the median and the whiskers to the SD. (* $p \leq 0.05$, ** $p \leq 0.01$, *** $p \leq 0.001$)

4.3.5. The analysis with the MLE method for theta modulation shows differences in the frequency of modulation

Theta modulation was also analysed with a MLE method (Climer *et al.*, 2015; Hinman *et al.*, 2016), which assessed if a cell had significant rhythmic firing and the frequency of this rhythmicity. This method represented a more robust alternative to the TMI method, as it statistically assesses the rhythmicity of a cell rather than using an arbitrary threshold. Figure 4.12A shows examples of firing autocorrelations of a theta modulated (left) and a non-modulated WT cell (right). Figure 4.12B shows examples of firing autocorrelations of a theta modulated (left) and a non-modulated J20 cell (right). The MLE method for theta modulation showed a decrease in the proportion of theta modulated cells and this was more noticeable for J20 cells. However, no differences were found between genotypes ($F(1, \text{Inf}) = 0.05, p = 0.82$, Fig. 4.12Ci). These results suggest this was caused by differences in the recording sites in each animal, with layer III having a lower percentage of theta modulated cells than layer II ($F(1, \text{Inf}) = 82.72, p < 0.0001$, Fig. 4.12Cii). A reduction of theta modulated cells with novelty was observed ($F(1, \text{Inf}) = 6.59, p = 0.01$, Fig. 4.12Ciii). However, there was only a trend of a significant interaction between context and genotype ($F(1, \text{Inf}) = 3.74, p = 0.053$, Fig. 4.12Ciii). No differences were observed when comparing putative excitatory cells against putative interneurons ($F(1, \text{Inf}) = 0.45, p = 0.50$, Fig. 4.12Civ), and these proportions were equal between genotypes ($F(1, \text{Inf}) = 0.43, p = 0.51$, Fig. 4.12Civ).

Most of the cells that were coupled with the peak of the theta wave in section 4.3.4 did not pass the criteria for theta modulation with the MLE method. Therefore, this resulted in a decrease in the proportion of cells coupled to the peak of theta in both genotypes, and this reduction was more prominent for J20 cells (Fig. 4.13A and B). No differences between genotypes were observed in the proportion of cells coupled with the peak and the trough of theta ($F(1, \text{Inf}) = 0.44, p = 0.51$, Fig. 4.13Ci). The same was true when comparing putative excitatory cells with putative interneurons ($F(1, \text{Inf}) = 0.51, p = 0.47$, Fig. 4.13Cii).

Regarding the frequency of modulation, the results obtained with this method contrast with the ones presented in section 4.3.4. J20 cells displayed a lower

frequency of modulation than WT cells ($F(1, 5.21) = 9.79, p = 0.025$, Fig. 4.14A). Interestingly, a decrease in the frequency of the modulation was also observed in the novel context compared to the familiar context ($F(1, 176) = 9.74, p = 0.002$, Fig. 4.14Bi). This was also the case for putative interneurons when compared to putative excitatory cells ($F(1, 94) = 8.67, p = 0.004$, Fig. 4.14Ci). It has been shown that the frequency of subthreshold membrane potential oscillations and the resonance frequency of stellate cells decrease along the MEC dorsoventral axis (Giocomo *et al.*, 2007). Thus, it is possible that the differences observed between WT and J20 mice are due to the variations in the recording locations (Fig. 4.2). However, including in a second model the estimated position of each cell decreased its fit, suggesting that the differences in the recording locations did not have any effects. Model 1, which was specified as ‘Frequency of modulation ~ Genotype*Context*Cell type + (1 | Animal/Cell ID)’, had an AIC value of 193.3 whereas the AIC value of model 2, which was specified as ‘Frequency of modulation ~ Genotype*Context*Cell type + Distance from border + (1 | Animal/Cell ID)’, was of 194.3. In addition, both models were not significantly different for which the simpler model, model 1, was preferred. Furthermore, the results of model 2 yielded similar results, with J20 cells still exhibiting a significant lower frequency of modulation than WT cells ($F(1, 5.82) = 7.67, p = 0.033$). In addition, a decrease in the frequency of the modulation with novelty was also observed ($F(1, 176) = 9.74, p = 0.002$) and the frequency of the modulation was lower in putative interneurons ($F(1, 92.31) = 9.50, p = 0.003$). Importantly, the distance from the MEC border showed no effect on the frequency of the modulation ($F(1, 83.44) = 0.93, p = 0.34$). In agreement with these results, although a significant correlation between the frequency of the modulation and estimated the recording position for all cells was observed (slope = -9.77E-4, $r = -0.32, p = 5.53E-8$, Fig. 4.15A), no significant correlations were found when the data was segregated by genotype (WT: slope = 1.06E-4, $r = 0.04, p = 0.63$, Fig. 4.15B; J20: slope = -1.35E-4, $r = -0.04, p = 0.68$, Fig. 4.15C).

Results for the modulation strength, also measured through both the TMI and the mean resultant vector length, agreed with the results obtained in section 4.3.4. No changes were observed between genotypes (TMI: $F(1, 3.41) = 0.98, p = 0.39$, Fig. 4.16A, Vector length: $F(1, 3.47) = 0.79, p = 0.43$, Fig. 4.17A). While the TMI increased in the novel context for both WT and J20 mice ($F(1, 5.10) = 6.68, p =$

0.048, Fig. 4.16B), the vector length decreased with novelty ($F(1, 177.47) = 9.34$, $p = 0.003$, Fig. 4.17B). For both measures, putative interneurons exhibited a greater modulation strength than putative excitatory cells (TMI: $F(1, 84.06) = 34.38$, $p < 0.0001$, Fig. 4.16C, Vector length: $F(1, 85.71) = 11.30$, $p = 0.0012$, Fig. 4.17C).

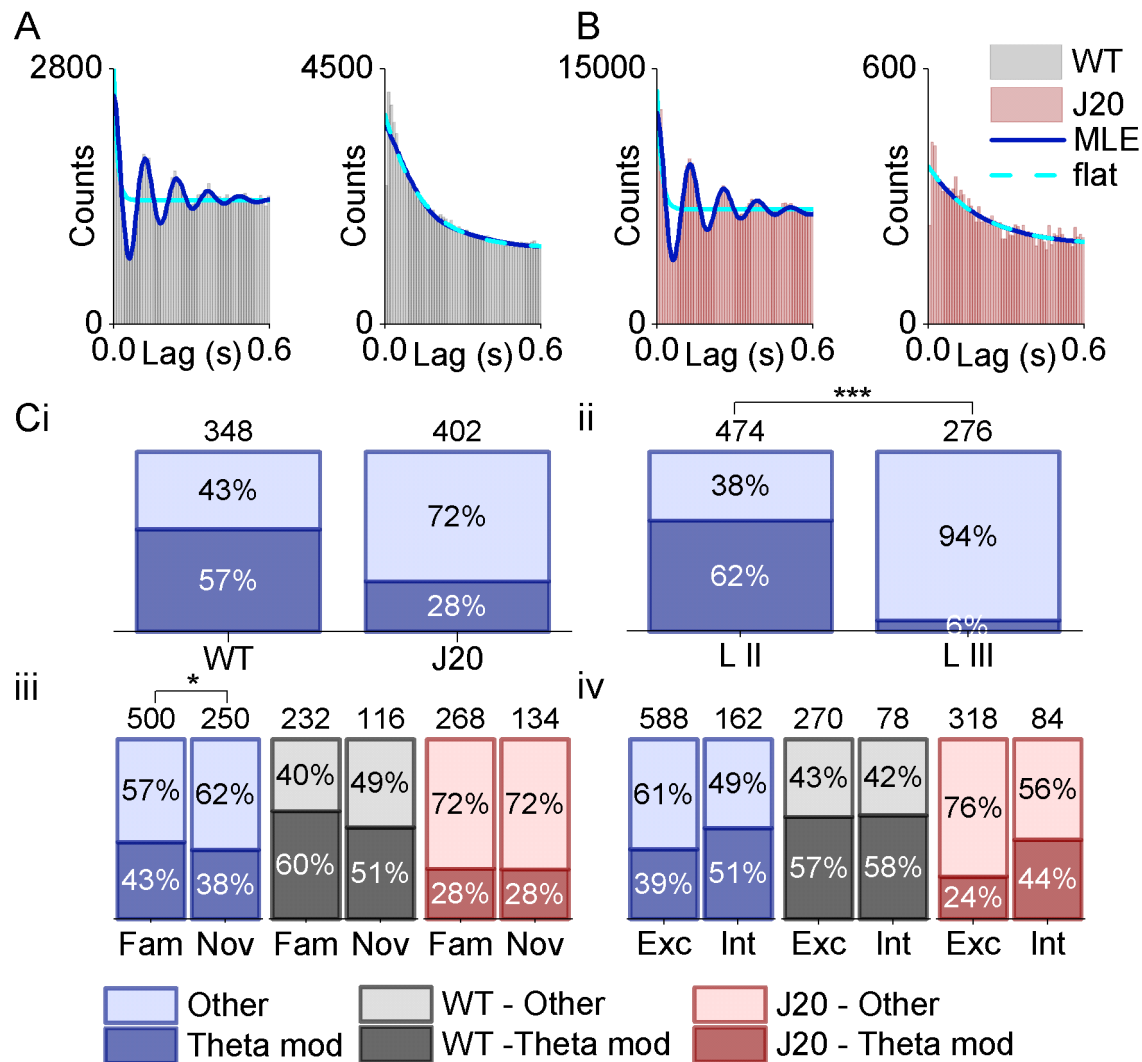


Figure 4.12 The proportion of theta modulated cells is lower in layer III of the MEC. **A)** Examples of firing autocorrelations in a WT theta modulated cell (left) and a non-modulated cell (right). **B)** Examples of firing autocorrelations in a J20 theta modulated cell (left) and a non-modulated cell (right). Dark blue lines show maximum likelihood estimates (MLE) and dashed light blue lines show a flat model (no rhythmicity). **C)** Proportions of theta modulated and other (non-theta modulated) cells between both genotypes **(i)**, by layer **(ii)**, by context **(iii)** and by cell type (putative excitatory versus putative interneurons) **(iv)**. Numbers above bars represent the total n number. (* $p \leq 0.05$, ** $p \leq 0.01$, *** $p \leq 0.001$)

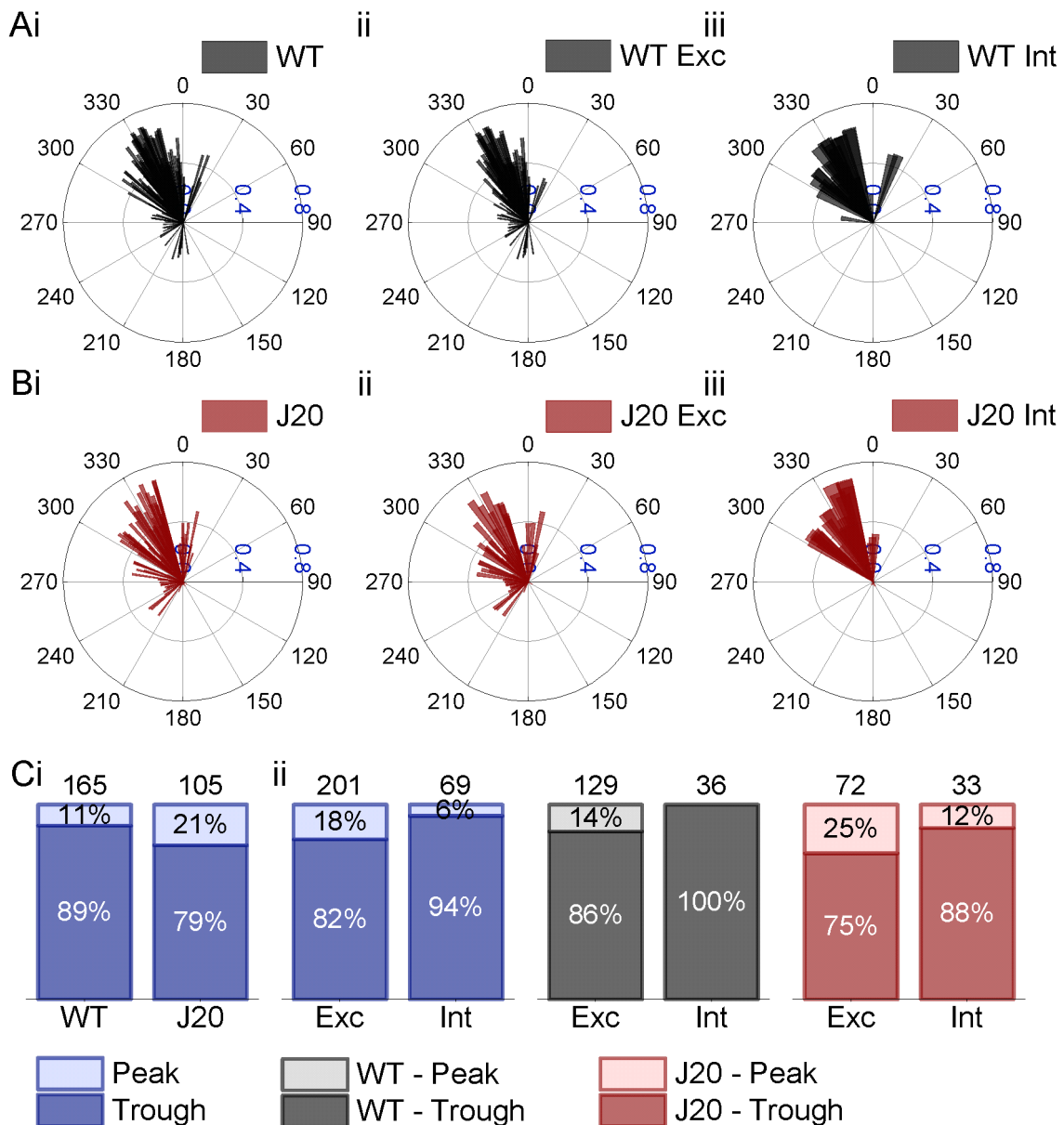


Figure 4.13 A similar proportion of cells have their firing locked to the trough of theta oscillations in both genotypes. A) Circular mean of the preferred firing phase of each cell plotted against its respective mean resultant vector length of WT cells in the first familiar trial (i) the novel trial (ii) and the second familiar trial (iii). **B)** Circular mean of the preferred firing phase of each cell plotted against its respective mean resultant vector length of J20 cells in the first familiar trial (i) the novel trial (ii) and the second familiar trial (iii). **C)** Proportions of cells with a circular mean of their preferred firing phase corresponding to the peak and the trough of theta oscillations by genotype (i), and cell type (putative excitatory versus putative interneurons) (ii). Numbers above bars represent the total n number. (* p ≤ 0.05, ** p ≤ 0.01, *** p ≤ 0.001)

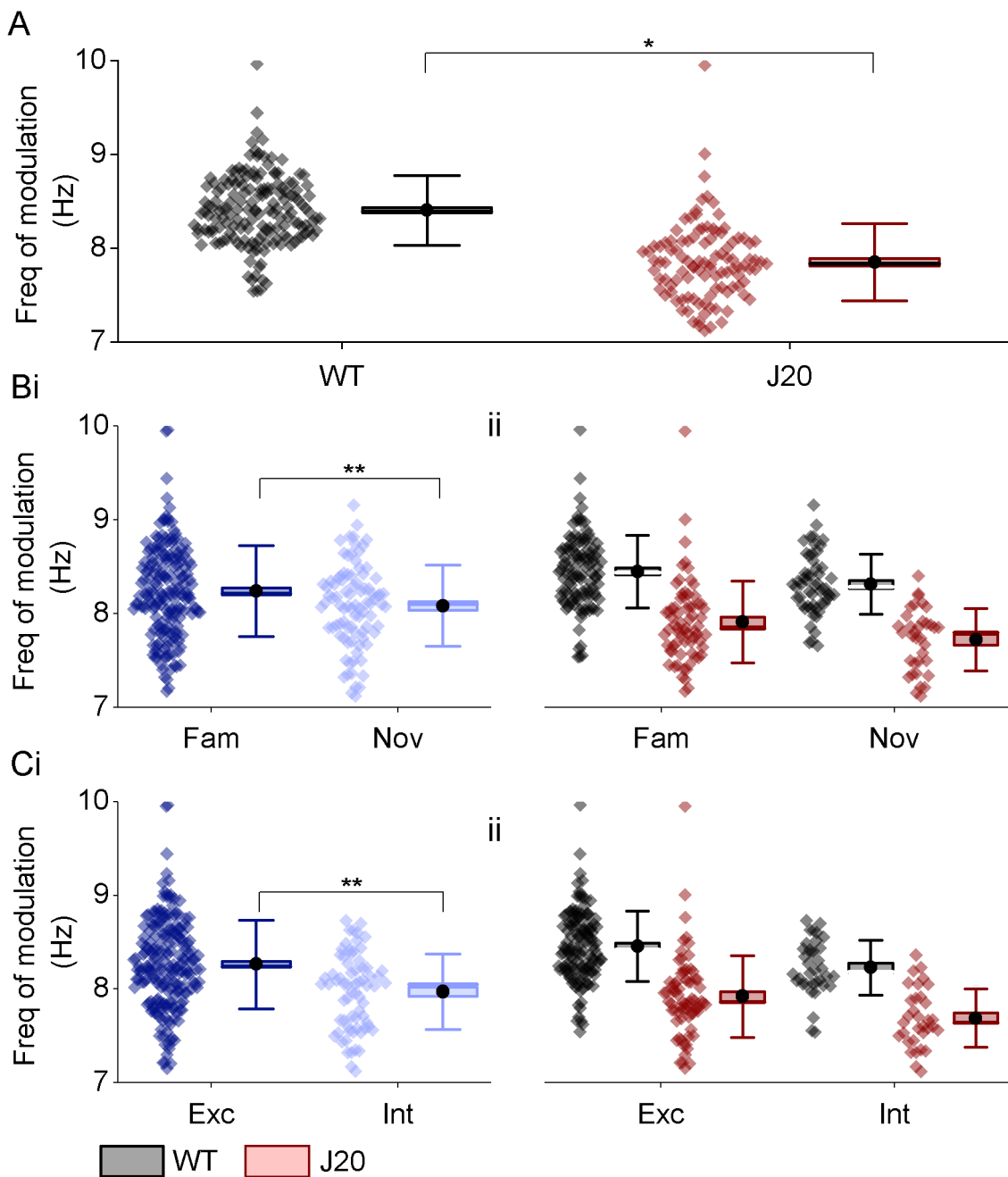


Figure 4.14 The frequency of the modulation is lower in J20 cells. A) Pooled frequency of the modulation data by each genotype, **B)** Pooled frequency of the modulation data between both contexts (**i**) and between contexts in WT (black) and J20 (red) mice (**ii**). **D)** Pooled frequency of the modulation data by cell type (putative excitatory versus putative interneurons) (**i**) and by cell type in WT (black) and J20 (red) mice (**ii**). The data shown in **A**, **B** and **C** is the same data replotted separately. Box plots: box corresponds to the mean \pm SEM, the circle to the mean, the line to the median and the whiskers to the SD. (* $p \leq 0.05$, ** $p \leq 0.01$, *** $p \leq 0.001$)

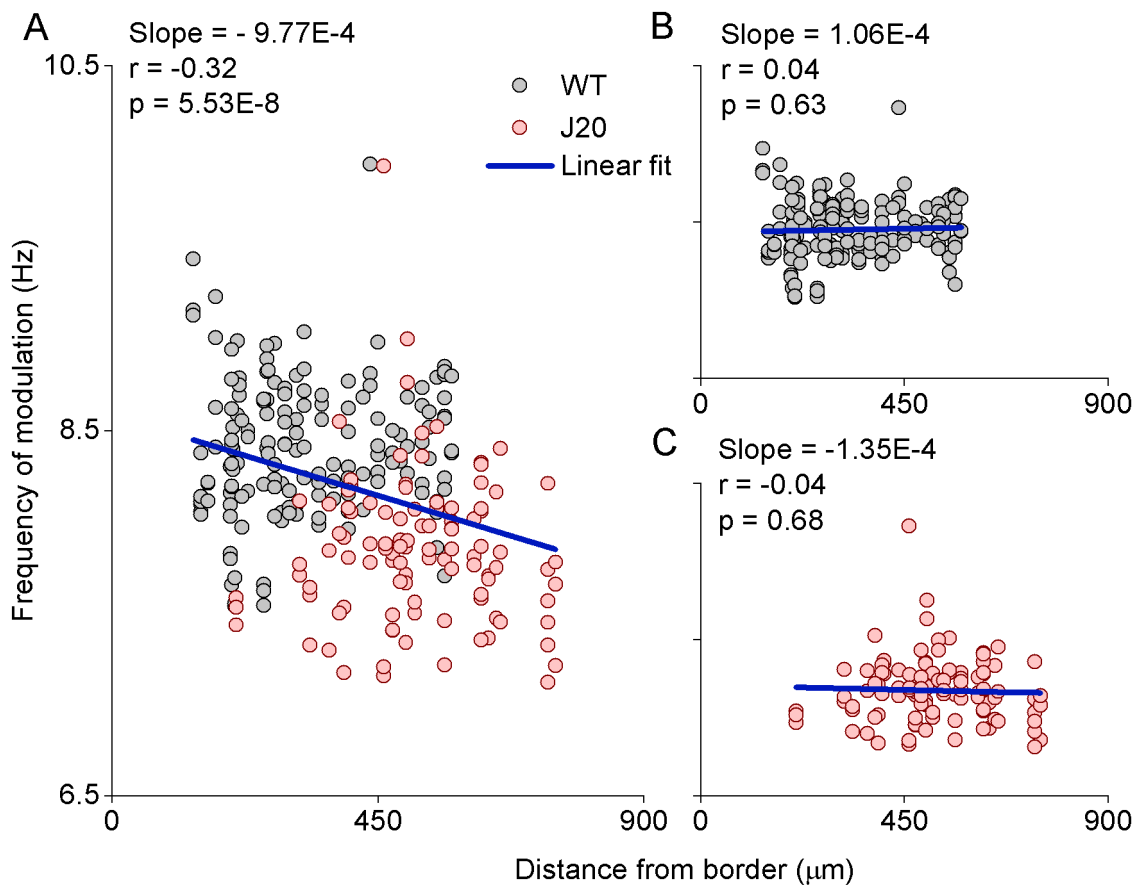


Figure 4.15 The frequency of modulation does not correlate with distance from MEC border. **A)** Linear fit of frequency of modulation plotted against the distance from the MEC border for all cells. **B)** Linear fit of frequency of modulation plotted against the distance from the MEC border for WT cells. **C)** Linear fit of frequency of modulation plotted against the distance from the MEC border for J20 cells. In each individual graph, the results of the linear fit are represented with the slope, Pearson's r (r) and the p value.

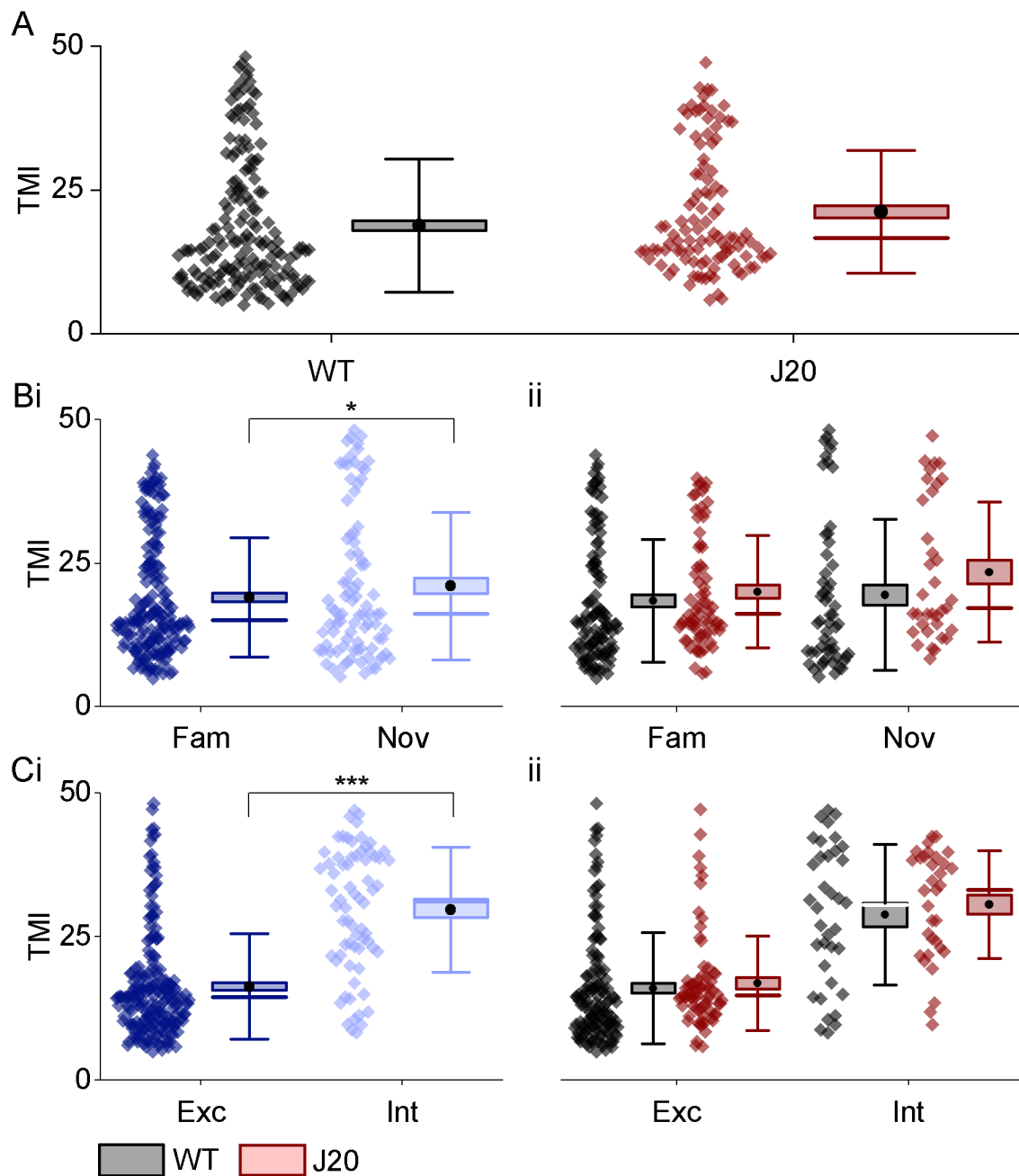


Figure 4.16 The TMI is lower in putative excitatory cells than in putative interneurons. A) Pooled TMI data by each genotype. **B)** Pooled TMI data between both contexts (i) and between contexts in WT (black) and J20 (red) mice (ii). **C)** Pooled TMI data by cell type (putative excitatory versus putative interneurons) (i) and by cell type in WT (black) and J20 (red) mice (ii). The data shown in **A**, **B** and **C** is the same data replotted separately. Box plots: box corresponds to the mean \pm SEM, the circle to the mean, the line to the median and the whiskers to the SD. (* $p \leq 0.05$, ** $p \leq 0.01$, *** $p \leq 0.001$)

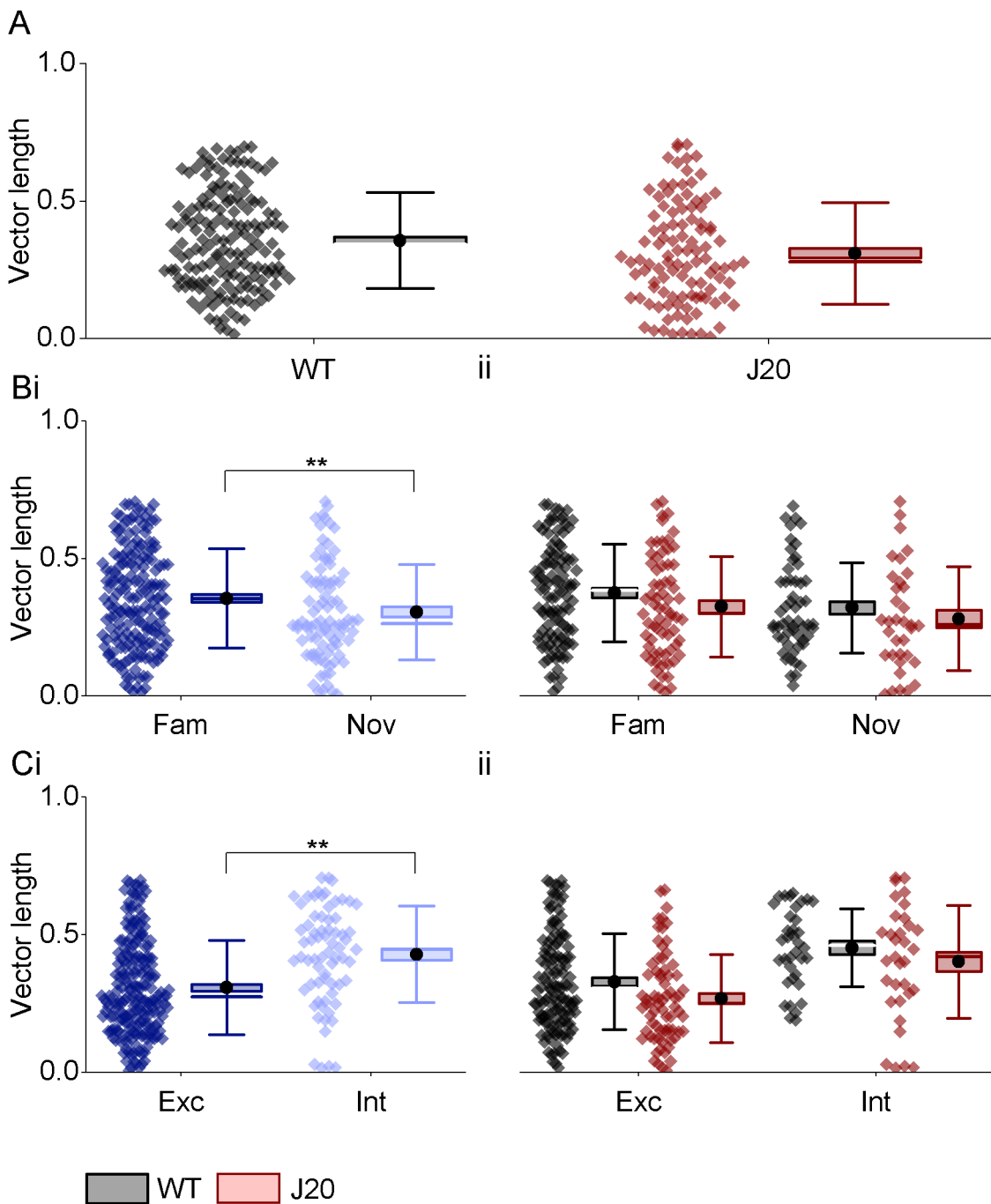


Figure 4.17 The mean vector length is lower in putative excitatory cells than in putative interneurons. **A)** Pooled mean vector length data by each genotype **B)** Pooled mean vector length data between both contexts (**i**) and between contexts in WT (black) and J20 (red) mice (**ii**). **C)** Pooled mean vector length data by cell type (putative excitatory versus putative interneurons) (**i**) and by cell type in WT (black) and J20 (red) mice (**ii**). The data shown in **A**, **B** and **C** is the same data replotted separately. Box plots: box corresponds to the mean \pm SEM, the circle to the mean, the line to the median and the whiskers to the SD. (* $p \leq 0.05$, ** $p \leq 0.01$, *** $p \leq 0.001$)

4.3.6. Speed sensitive cells show no deficits in J20 mice

Figure 4.18A shows the firing rate plotted against the running speed of a WT (Fig. 4.18Ai) and a J20 (Fig. 4.18Aii) speed sensitive cell. The distribution of observed speed scores and shuffle distributions for linear and saturating data can be observed in figure 4.18B for WT cells and in figure 4.18C for J20 cells. The proportion of speed sensitive cells was similar between both genotypes ($F(1, Inf) < 0.001, p = 0.99$, Fig. 4.18Di). This was also the case for putative interneurons, in which a similar percentage of them were speed sensitive when compared to putative excitatory cells ($F(1, Inf) = 2.85, p = 0.09$, Fig. 4.18Diii). However, the proportion of speed sensitive cells significantly decreased in the novel context ($F(1, Inf) = 9.21, p = 0.002$, Fig. 4.18Dii).

Examples of the firing rate plotted against the running speed for a linearly modulated and a saturating WT and J20 speed sensitive cell can be seen in figure 4.19A and B, respectively. The distribution of saturating and linearly modulated speed sensitive cells was similar between both genotypes ($F(1, Inf) = 0.14, p = 0.71$, Fig. 4.19Ci). This was also the case for putative interneurons and excitatory cells ($F(1, Inf) = 0.65, p = 0.42$, Fig. 4.19Ciii). A layer effect was observed in the proportions of saturating and linearly modulated cells, with a higher proportion of saturating cells in layer III when compared to layer II ($F(1, Inf) = 11.47, p = 0.0007$, Fig. 4.19Cii). Examples of the firing rate plotted against the running speed for a positive and a negative WT and J20 speed sensitive cell can be seen in figure 4.19D and E, respectively. The proportion of negatively modulated speed sensitive cells was similar between both genotypes ($F(1, Inf) = 0.39, p = 0.53$, Fig. 4.19Fi) and between putative excitatory cells and putative interneurons ($F(1, Inf) = 0.80, p = 0.37$, Fig. 4.19Fii).

Figures 4.20A and B show examples of decreasing, increasing and no changes WT and J20 cells. The proportion of speed sensitive cells that showed a decrease in their scores in the novel exposure (Fig. 4.20Ci), when compared to the two familiar exposures, was compared to the proportion of cells expected purely by chance. The proportions of cells decreasing their scores were significantly higher in both WT and J20 mice (WT: $p < 0.0001$, J20: $p < 0.0001$, Fisher's exact test, Fig. 4.20Cii). Furthermore, the proportion of decreasing cells was similar in both

genotypes ($p = 0.57$, Fisher's exact test, Fig. 4.20Cii). The proportion of speed sensitive cells that showed an increase in their scores (Fig. 4.20Di) was also compared to the proportion of cells expected by chance. The proportion of cells increasing their scores was not different in WT mice ($p = 0.17$, Fisher's exact test, Fig. 4.20Dii). However, J20 mice showed a lower proportion of increasing cells than what could be expected by chance ($p = 0.009$, Fisher's exact test, Fig. 4.20Dii) and than WT mice ($p = 0.002$, Fisher's exact test, Fig. 4.20Dii).

Speed sensitive cells recorded from WT and J20 mice had similar speed scores ($F(1, 13.10) = 3.96$, $p = 0.07$, Fig. 4.21A). Putative interneurons and excitatory cells differed in their mean speed scores ($F(1, 232.89) = 17.84$, $p < 0.0001$, Fig. 4.21Bi). In addition to this, speed sensitive cells were significantly affected by novelty ($F(1, 460) = 134.59$, $p < 0.0001$, Fig. 4.21Ci). The speed scores of both increasing and decreasing cells changed with context (Decreasing: $\beta = 0.07$, SE = 0.005, $t(702) = 14.84$, $p < 0.0001$, Fig. 4.21Di; Increasing: $\beta = -0.06$, SE = 0.007, $t(702) = -8.23$, $p < 0.0001$, Fig. 4.21Ei). Including the layer effect did not improve the mixed model and was therefore not included.

The firing rate of speed sensitive cells was also compared. No differences due to genotype were observed ($F(1, \text{Inf}) = 1.51$, $p = 0.22$, Fig. 4.22A). As expected, putative interneurons displayed higher firing rates than putative excitatory cells ($F(1, \text{Inf}) = 61.18$, $p < 0.0001$, Fig. 4.22Bi). The firing rate of speed cells was significantly affected by context ($F(1, \text{Inf}) = 10.91$, $p = 0.001$, Fig. 4.22Ci). Further analysis of changes in the firing rate of cells between the familiar and novel trials with the rate difference index was performed. None of the speed cells were found to have passed the threshold (Fig. 4.23A and B). This threshold corresponded to the 99th percentile of the distribution of rate difference indexes calculated between the two exposures to the familiar arena, and applied to the rate indexes calculated between the exposures to the familiar arena and the exposure to the novel arena.

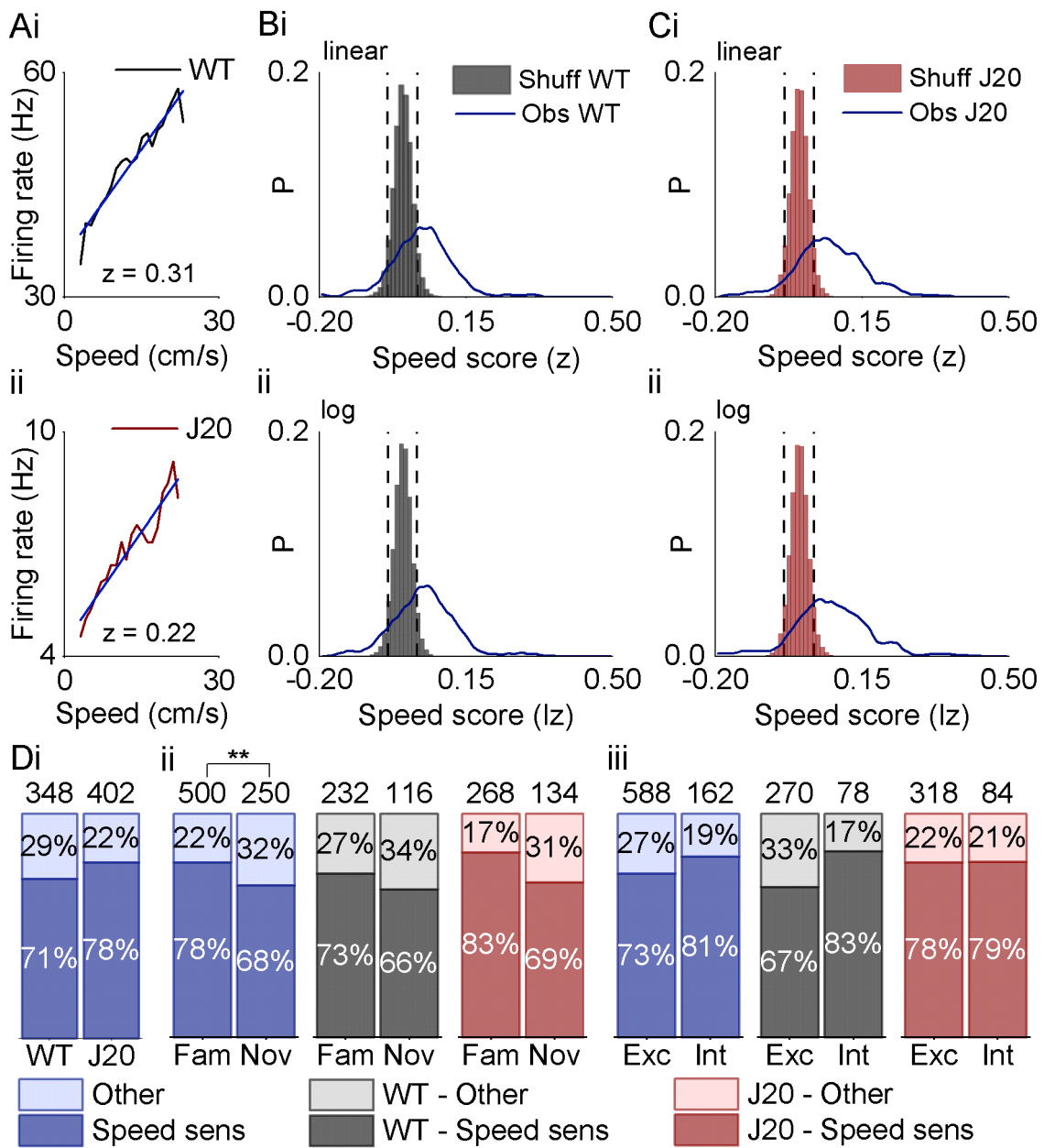


Figure 4.18 The proportion of speed sensitive cells decreases with novelty. **A)** Example of firing rate plotted against the running speed for a WT (**i**) and a J20 (**ii**) speed sensitive cell. **B)** Distribution of speed scores for non-transformed data (linear) (**i**) and log transformed data (saturating) (**ii**) with shuffled distribution in WT animals. **C)** Distribution of speed scores for non-transformed data (linear) (**i**) and log transformed data (saturating) (**ii**) with shuffled distribution in J20 animals. **D)** Proportions of speed sensitive cells by genotype (**i**), context (**ii**) and cell type (putative excitatory versus putative interneurons) (**iii**). Numbers above bars represent the total n number. (* $p \leq 0.05$, ** $p \leq 0.01$, *** $p \leq 0.001$)

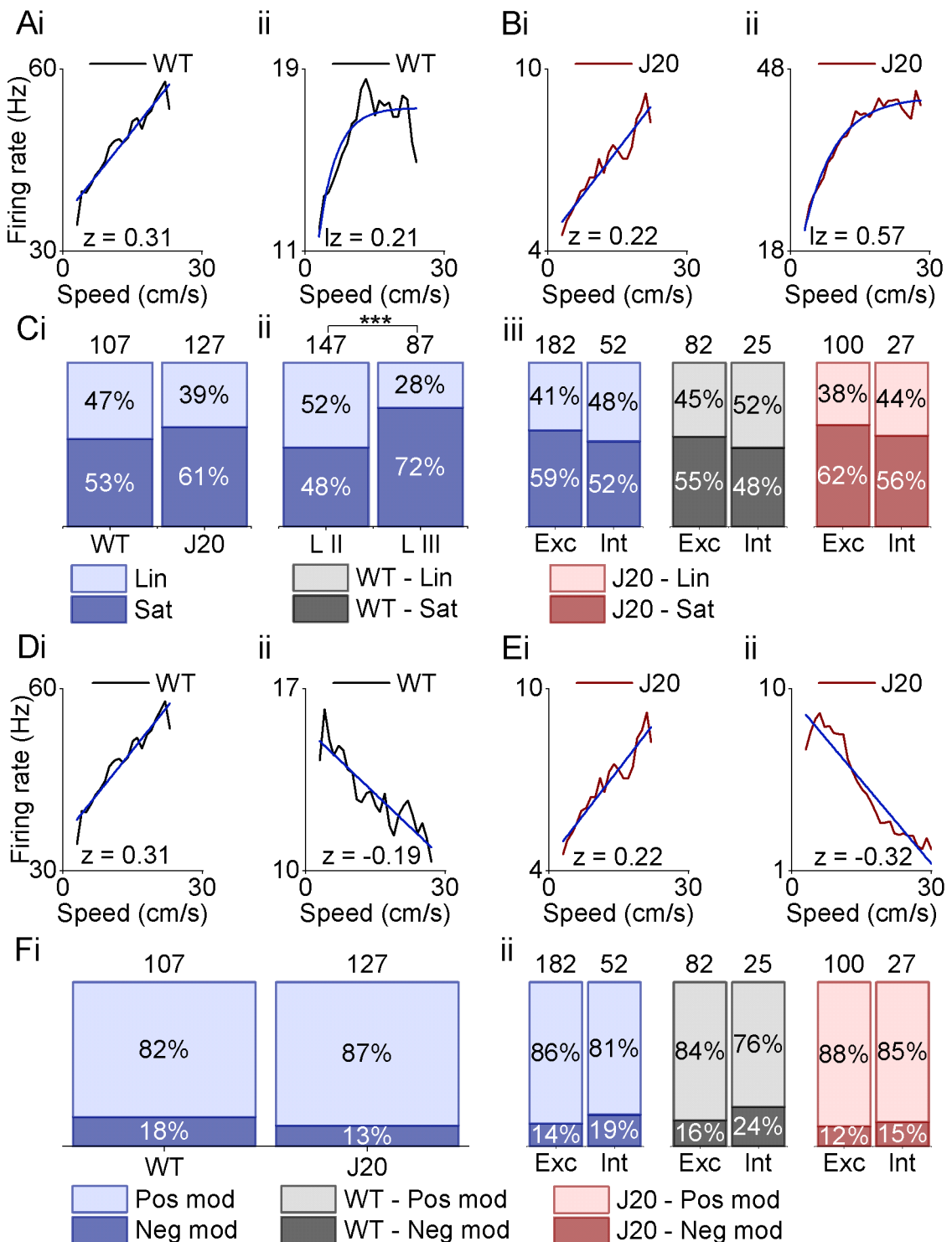


Figure 4.19 Layer III has a higher proportion of saturating speed sensitive cells than layer II. **A)** Example of firing rate plotted against the running speed for a WT linearly modulated (**i**) and a saturating speed sensitive cell (**ii**). **B)** Example of firing rate plotted against the running speed for a J20 linearly modulated (**i**) and a saturating speed sensitive cell (**ii**). **C)** Proportions of saturating and linearly modulated speed sensitive cells by genotype (**i**), layer (**ii**), and cell type (putative excitatory versus putative interneurons) (**iii**). **D)** Example of firing rate plotted against the running speed for a WT positive (**i**) and a negative speed sensitive cell (**ii**). **E)** Example of firing rate plotted against the running speed for a J20 positive

(i) and a negative speed sensitive cell **(ii)**. **F**) Proportions of positive and negative speed sensitive cells by genotype **(i)** and cell type (putative excitatory versus putative interneurons) **(ii)**. Numbers above bars represent the total n number. (* $p \leq 0.05$, ** $p \leq 0.01$, *** $p \leq 0.001$)

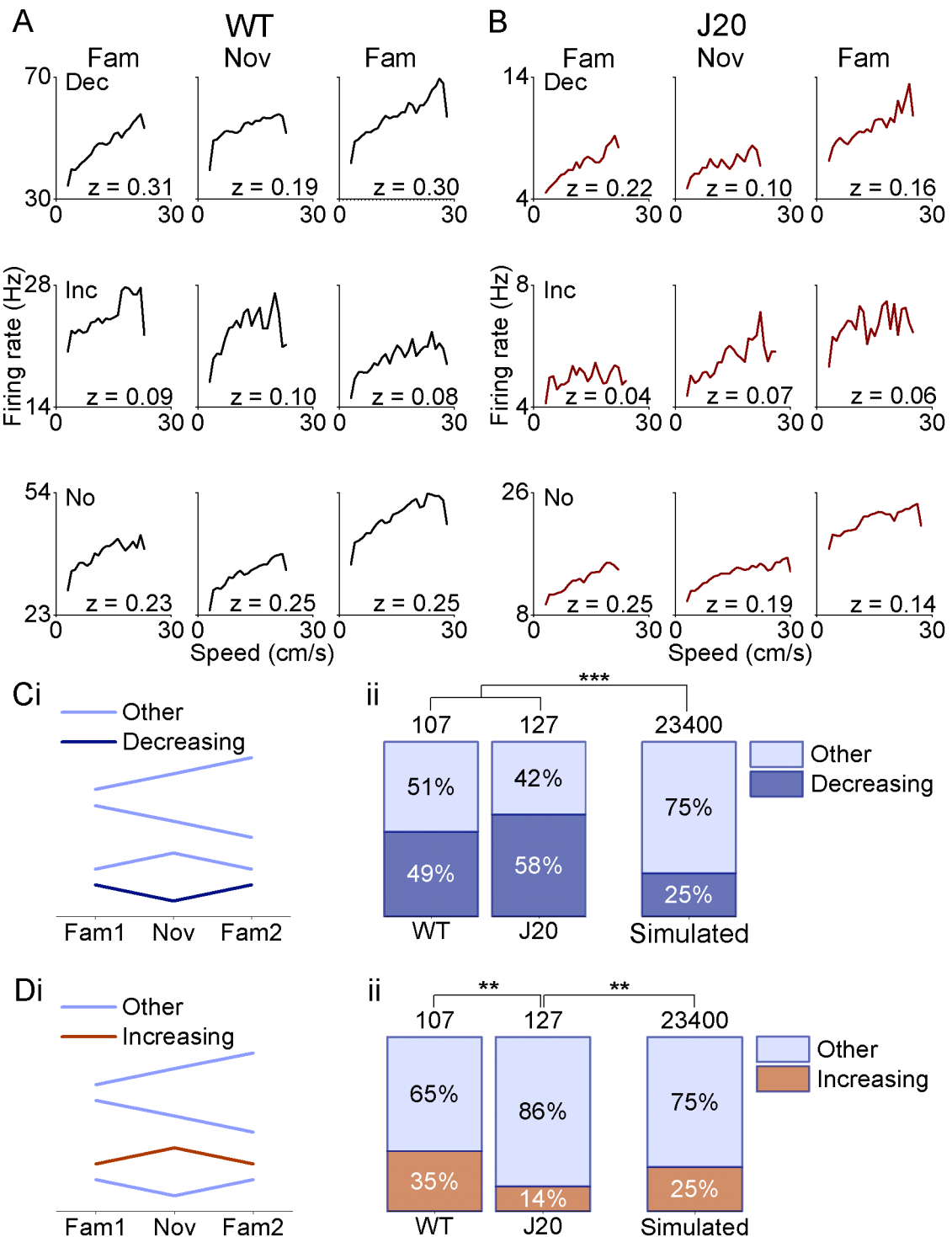


Figure 4.20 The proportion of decreasing speed sensitive cells is higher than the level expected by chance. **A)** Examples of firing rate plotted against the running speed for the three trials for a decreasing (i), an increasing (ii) and a speed sensitive cell showing no changes due to context in WT mice (iii). **B)** Examples of firing rate plotted against the running speed for the three trials for a decreasing (i), an increasing (ii) and a speed sensitive cell showing no changes due to context in J20 mice (iii). **C**) Example patterns of decreasing cells (dark blue) and other cells (light blue), which encompasses increasing and no-changes cells (i), proportions of decreasing and other cells in both genotypes compared to the simulated

proportions (ii). **D**) Example patterns of increasing cells (orange) and other cells (light blue), which encompasses increasing and no-changes cells (i), proportions of increasing and other cells in both genotypes compared to the simulated proportions (ii). Numbers above bars represent the total n number. (* $p \leq 0.05$, ** $p \leq 0.01$, *** $p \leq 0.001$)

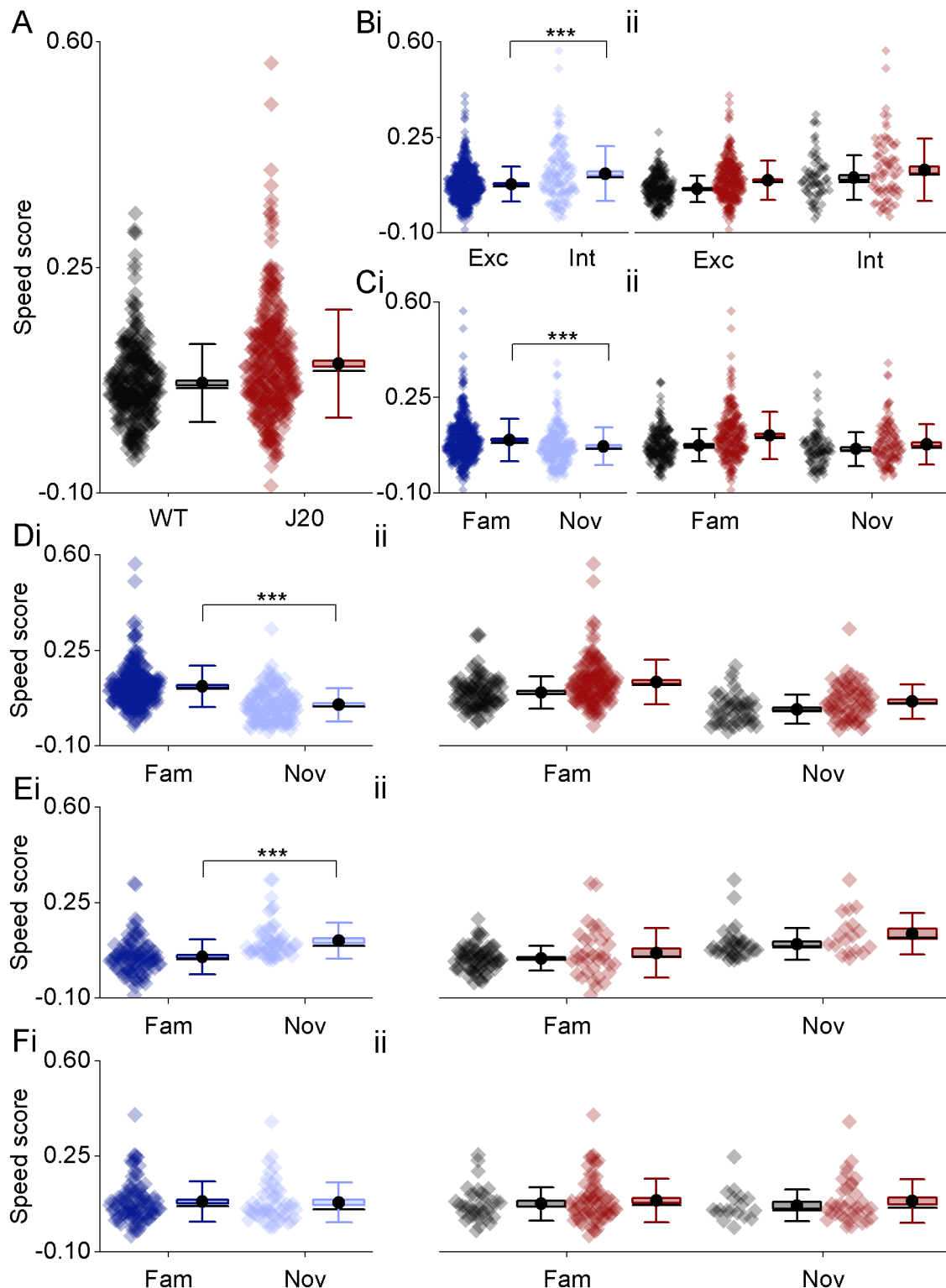


Figure 4.21 Speed scores are higher in speed sensitive putative interneurons. **A)** Pooled speed scores by genotype. **B)** Pooled speed scores by cell type (putative excitatory versus putative interneurons) **(i)** and by cell type in WT (black) and J20 (red) mice **(ii)**. **C)** Pooled speed scores of all speed sensitive cells by context **(i)** and by context in WT (black) and J20 (red) mice **(ii)**. **D)** Pooled speed scores of decreasing cells by context **(i)** and by context in WT (black) and J20 (red) mice **(ii)**. **E)** Pooled speed scores of increasing cells by context **(i)** and by context in WT (black) and

J20 (red) mice (**ii**). **F**) Pooled speed scores of cells showing no changes by context (**i**) and by context in WT (black) and J20 (red) mice (**ii**). The data shown in **A**, **B**, **C**, **D**, **E** and **F** is the same data replotted separately. Box plots: box corresponds to the mean \pm SEM, the circle to the mean, the line to the median and the whiskers to the SD. (* $p \leq 0.05$, ** $p \leq 0.01$, *** $p \leq 0.001$)

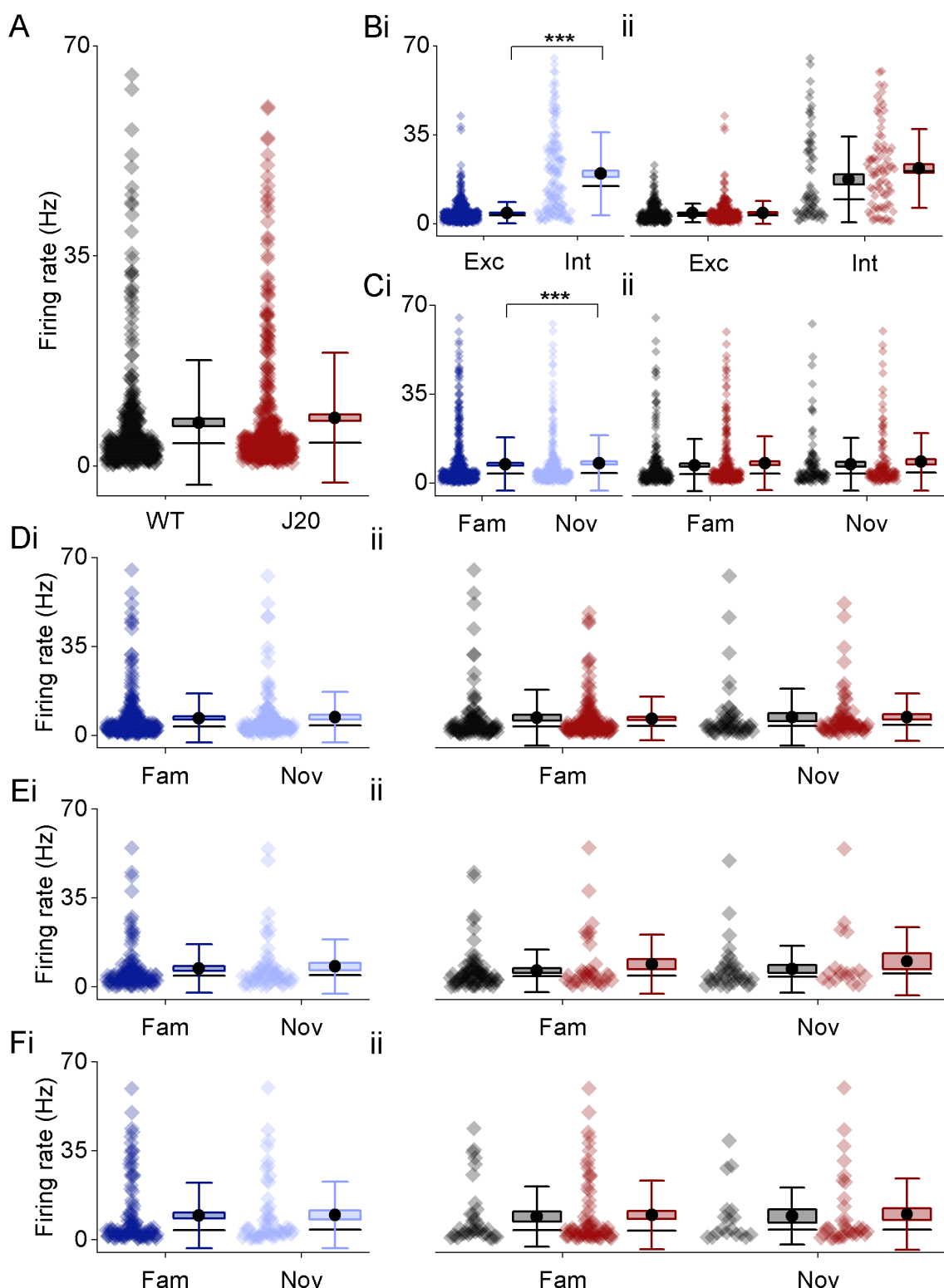


Figure 4.22 Firing rate is higher in speed sensitive putative interneurons. **A)** Pooled firing rate of speed sensitive cells by genotype. **B)** Pooled firing rate of speed sensitive cells by cell type (putative excitatory versus putative interneurons) (**i**) and by cell type in WT (black) and J20 (red) mice (**ii**). **C)** Pooled firing rate of all speed sensitive cells by context (**i**) and by context in WT (black) and J20 (red) mice (**ii**). **D)** Pooled firing rate of decreasing speed sensitive cells by context (**i**) and by context in WT (black) and J20 (red) mice (**ii**). **E)** Pooled firing rate of increasing speed sensitive

cells by context **(i)** and by context in WT (black) and J20 (red) mice **(ii)**. **F** Pooled firing rate of speed sensitive cells showing no changes by context **(i)** and by context in WT (black) and J20 (red) mice **(ii)**. The data shown in **A, B, C, D, E** and **F** is the same data replotted separately. Box plots: box corresponds to the mean \pm SEM, the circle to the mean, the line to the median and the whiskers to the SD. (* $p \leq 0.05$, ** $p \leq 0.01$, *** $p \leq 0.001$)

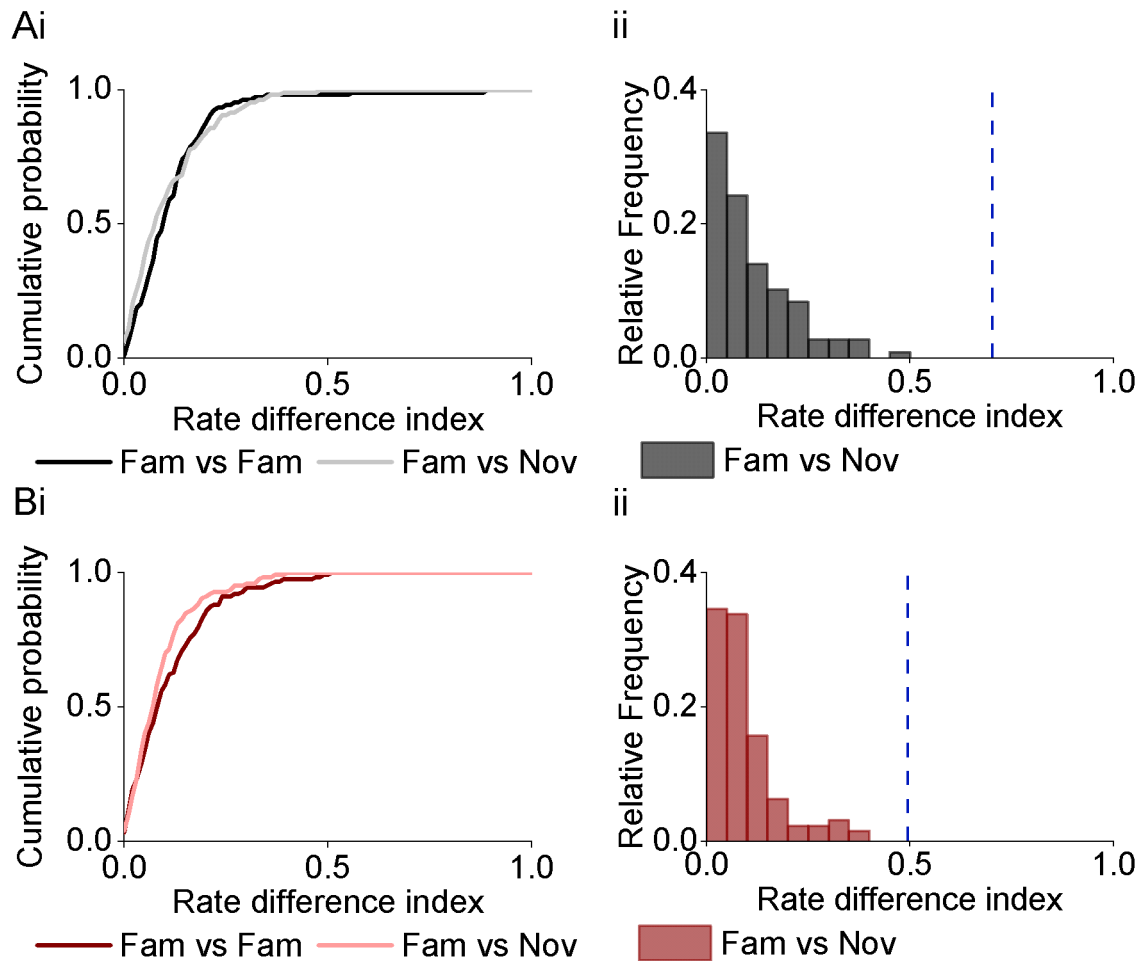


Figure 4.23 No cells pass the rate difference index threshold. A) Plot showing the cumulative probability of rate difference indexes for the WT distribution **(i)** and histogram showing the relative frequency of this distribution **(ii)**. **B)** Plot showing the cumulative probability of rate difference indexes for the J20 distribution **(i)** and histogram showing the relative frequency of this distribution **(ii)**.

4.3.7. HD sensitive cells show no differences between genotypes

Figure 4.24A shows polar plot examples of WT and J20 HD sensitive cells. The observed distributions of HD scores and shuffled distributions for WT and J20 cells can be seen in figure 4.24B. HD sensitive cells were found in the same proportion in WT and J20 cells ($F(1, \text{Inf}) = 1.84, p = 0.17$, Fig. 4.24Ci). In addition, no differences were found due to context ($F(1, \text{Inf}) = 0.19, p = 0.66$, Fig. 4.24Cii). A very low number of interneurons showed HD sensitivity ($n = 3$) and was deemed too low for analysis.

Figure 4.25A and B show polar plot examples for WT and J20 decreasing, increasing and no changes HD sensitive cells. The proportion of HD sensitive cells that showed a decrease in their scores in the novel exposure (Fig. 4.25Ci), when compared to the two familiar exposures, was compared to the proportion of cells expected purely by chance. The proportions of cells decreasing their scores were not significantly different to chance levels in both WT and J20 mice (WT: $p = 0.78$, J20: $p = 0.79$, Fisher's exact test, Fig. 4.25Cii). Furthermore, the proportion of decreasing cells was similar in both genotypes ($p = 1.00$, Fisher's exact test, Fig. 4.25Cii). The proportion of HD sensitive cells that showed an increase in their scores (Fig. 4.25Di) was also compared to the proportion of cells expected by chance. The proportion of cells increasing their scores was also not different to chance levels in both WT mice and J20 mice (WT: $p = 0.21$, J20: $p = 0.82$, Fisher's exact test, Fig. 4.25Dii). In addition, both J20 and WT mice showed a similar proportion of increasing cells ($p = 0.15$, Fisher's exact test, Fig. 4.25Dii). However, the n numbers (WT: $n = 27$, J20: $n = 17$) included here are relatively low and should be taken into consideration.

Figure 4.26A shows example polar plots of WT and J20 cells with small (0 to 60 degrees) and large (60 to 180 degrees) phase shifts. The phase shift of the preferred firing direction between the animals first and second exposures to the familiar arenas were compared. No differences were found between genotypes ($F(1, \text{Inf}) = 0.43, p = 0.51$, Fig. 4.26Ci), but two different populations were observed (Fig. 4.26Cii). These populations were divided into a small phase shift and a larger phase shift for analysis. The proportion of HD sensitive cells in both groups was not significantly different between genotypes ($p = 0.35$, Fisher's exact

test, Fig. 4.26B). However, a larger circular correlation for a given cell, between its firing rate as a function of HD in each familiar sessions, significantly predicted if a small or a large shift would occur between both familiar sessions ($\beta = 6.89$, $SE = 2.84$, $t(44) = 2.42$, $p = 0.02$, Fig. 4.26D).

Mean resultant vector lengths, which represent HD scores, were not different between WT and J20 cells ($F(1, 6.54) = 0.01$, $p = 0.91$, Fig. 4.27A). However, HD sensitive cells were affected by novelty ($F(2, 82) = 20.81$, $p < 0.0001$, Fig. 4.27), with a significant interaction between decreasing cells and context ($\beta = 0.17$, $SE = 0.03$, $t(132) = 6.10$, $p < 0.0001$, Fig. 4.27Ci). This interaction was also observed for increasing cells ($\beta = -0.13$, $SE = 0.04$, $t(132) = -3.33$, $p = 0.016$, Fig. 4.27Di) but not for cells showing no changes due to novelty ($\beta = 0.009$, $SE = 0.03$, $t(132) = 0.33$, $p = 1.00$, Fig. 4.27Ei). The firing rate of these cells was also studied. No changes were observed due to genotype ($F(1, Inf) = 0.20$, $p = 0.65$, Fig. 4.28A). However, a significant change in the firing rate with novelty was observed ($F(1, Inf) = 16.63$, $p < 0.0001$, Fig. 4.28Bi).

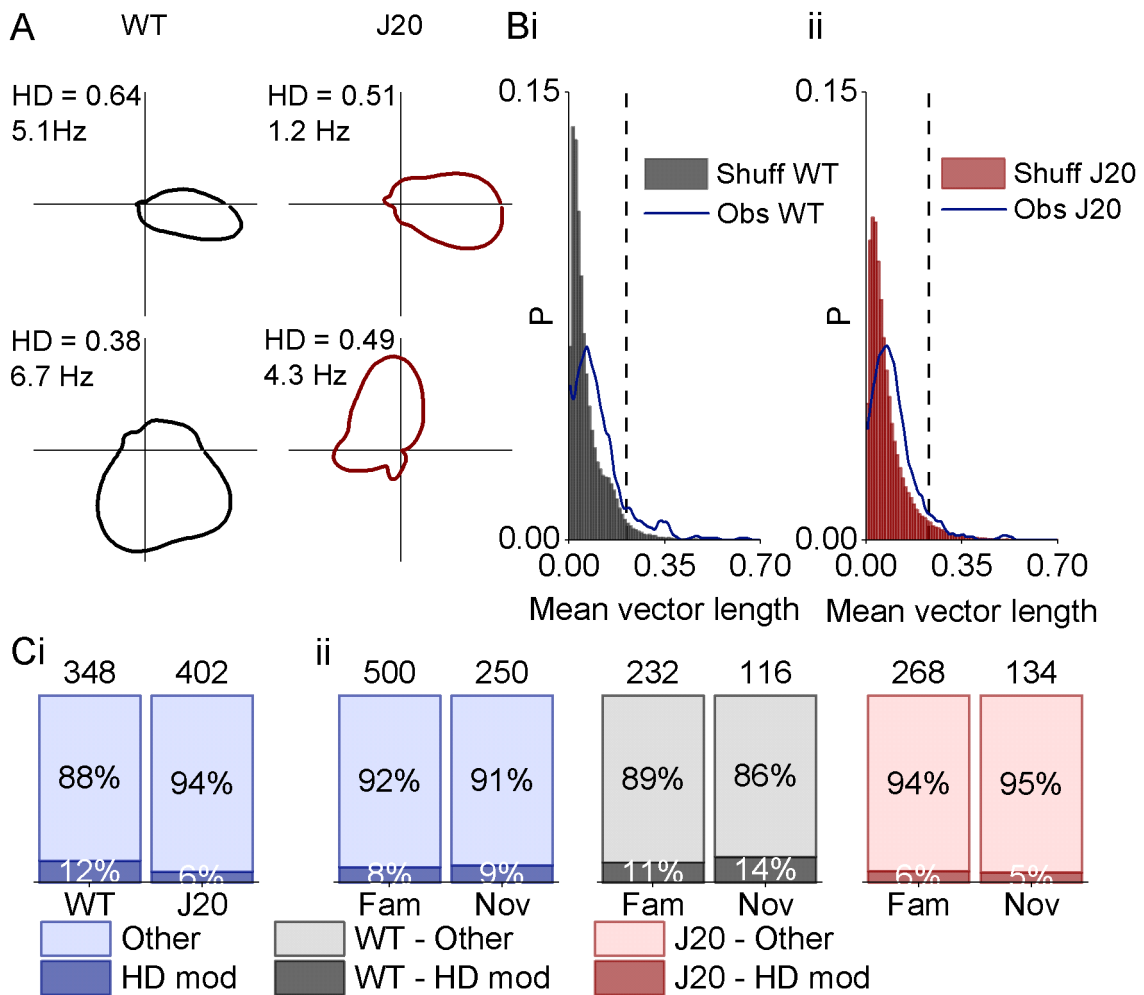


Figure 4.24 The proportion of HD sensitive cells is the same between both genotypes. **A)** Polar plots examples of HD sensitive cells in both WT and J20 mice. **B)** Distribution of HD scores with shuffled distribution in WT (i) and J20 mice (ii). **C)** Proportion of HD sensitive cells by genotype (i) and context (ii). Numbers above bars represent the total n number. (* p ≤ 0.05, ** p ≤ 0.01, *** p ≤ 0.001)

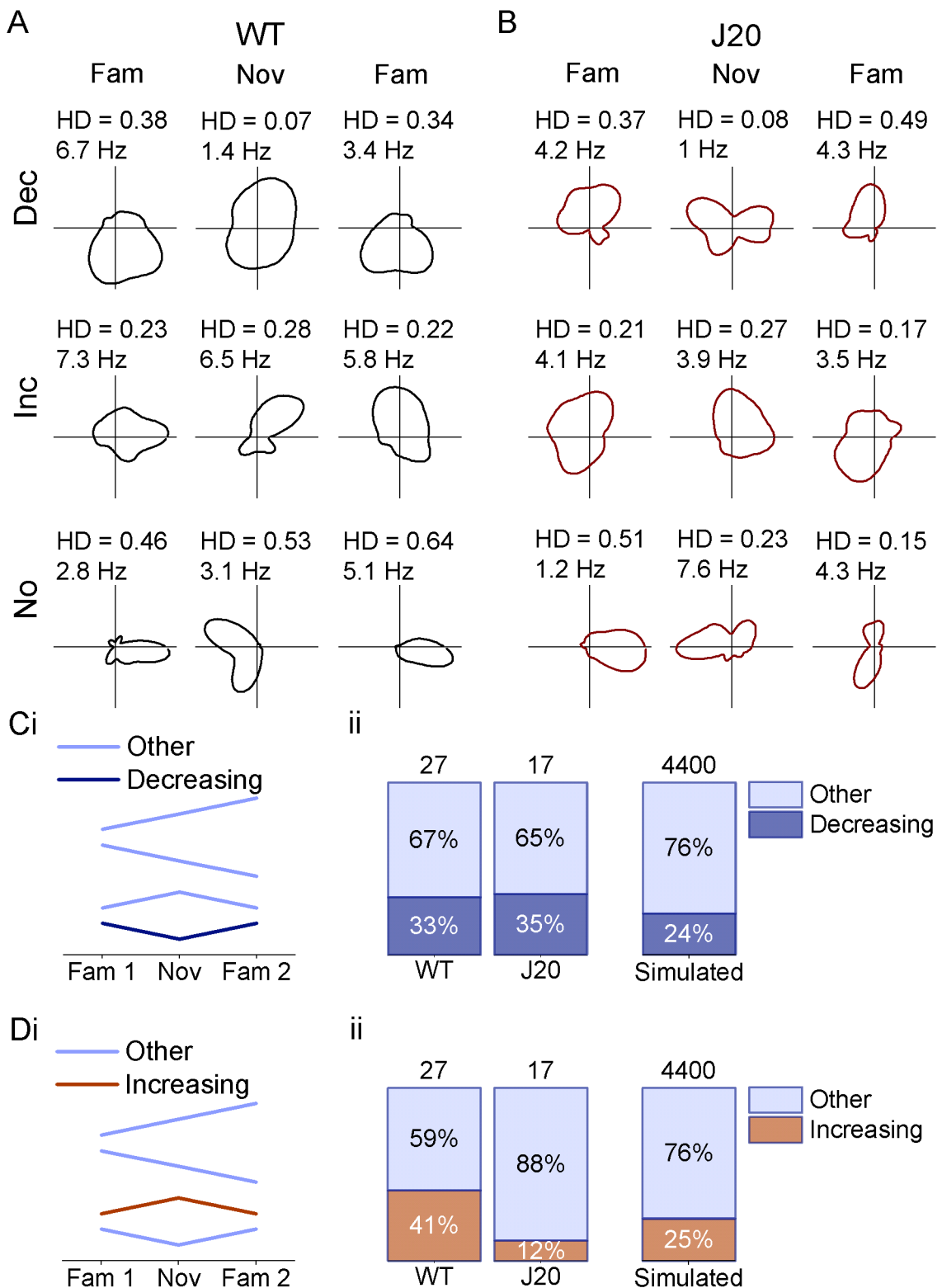


Figure 4.25 The proportions of decreasing and increasing HD sensitive cells are not different to the simulated data. **A)** Polar plots examples of HD sensitive cells for the three trials for a decreasing (i), an increasing (ii) and a HD sensitive cell showing no changes due to context in WT mice (iii). **B)** Polar plots examples of HD sensitive cells for the three trials for a decreasing (i), an increasing (ii) and a HD sensitive cell showing no changes due to context in J20 mice (iii). **C)** Example patterns of decreasing cells (dark blue) and other cells (light blue), which encompasses increasing

and no-changes cells (**i**), proportions of decreasing and other cells in both genotypes compared to the simulated proportions (**ii**). **D**) Example patterns of increasing cells (orange) and other cells (light blue), which encompasses increasing and no-changes cells (**i**), proportions of increasing and other cells in both genotypes compared to the simulated proportions (**ii**). Numbers above bars represent the total n number. (* p ≤ 0.05, ** p ≤ 0.01, *** p ≤ 0.001)

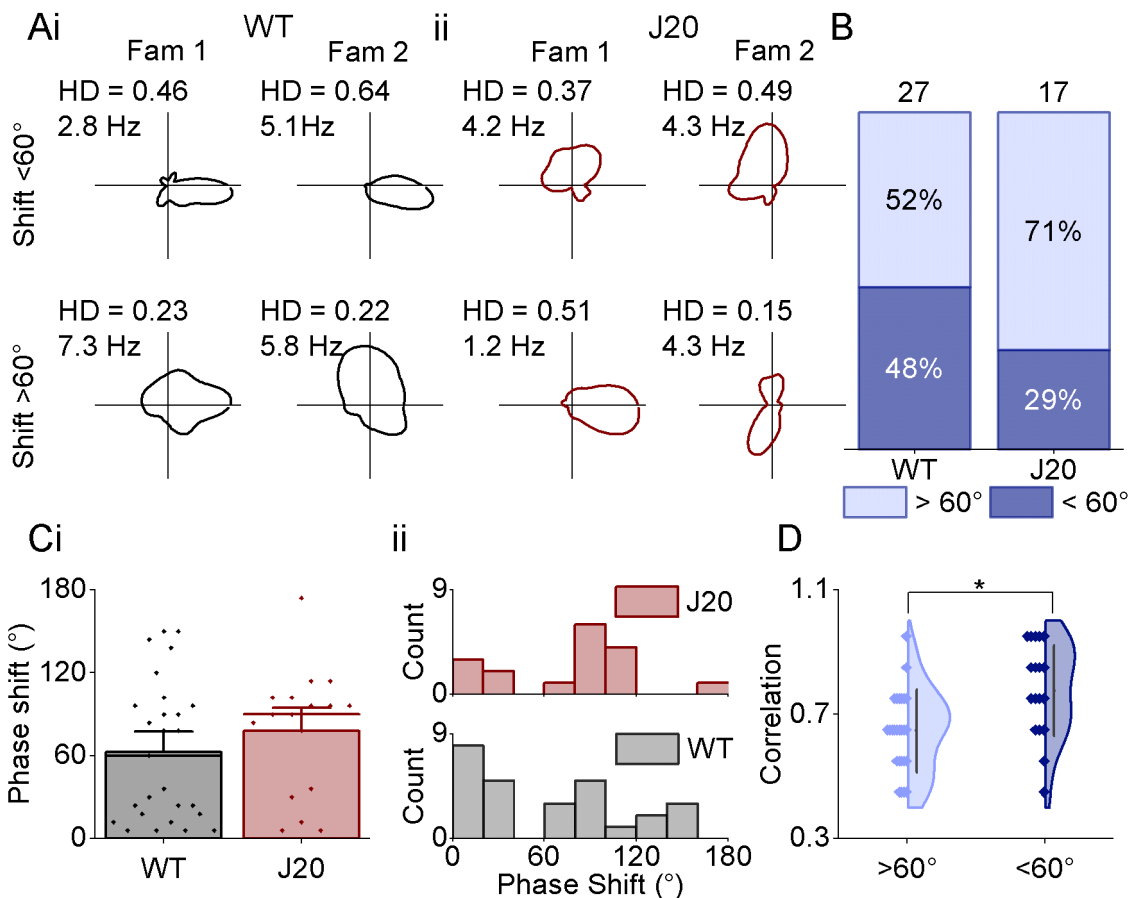


Figure 4.26 Head direction sensitive cells with small phase shifts (<60°) show a higher correlation in their polar plots between the two familiar trials. **A)** Polar plot examples of HD sensitive cells with small and large phase shifts for WT (**i**) and J20 (**ii**) mice. **B)** Proportion of cells with large and small phase shifts by genotype. **C)** Pooled phase shift data by genotype (**i**) and histograms showing the distribution of phase shifts for WT and J20 mice. **D)** Correlation between the data from the two familiar trials plotted against the phase shift size. Numbers above bars represent the total n number. (* p ≤ 0.05, ** p ≤ 0.01, *** p ≤ 0.001)

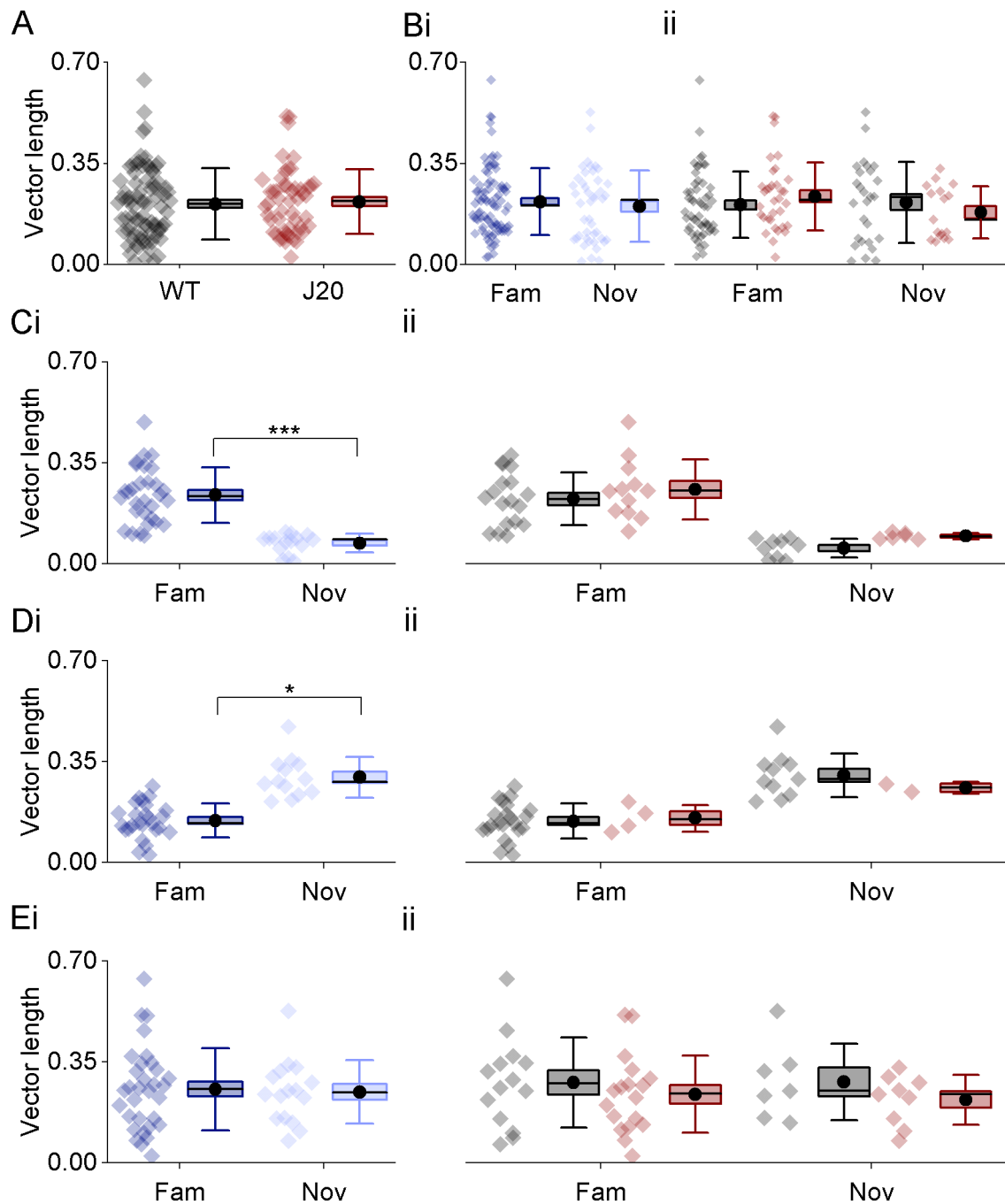


Figure 4.27 Mean resultant vector length (HD scores) of HD sensitive cells are similar between WT and J20 mice. A) Pooled mean resultant vector length values of all HD sensitive cells by genotype. **B)** Pooled mean resultant vector length values of all HD sensitive cells by context (i) and by context in WT (black) and J20 (red) mice (ii). **C)** Pooled mean resultant vector length values of decreasing cells by context (i) and by context in WT (black) and J20 (red) mice (ii). **D)** Pooled mean resultant vector length values of increasing by context (i) and by context in WT (black) and J20 (red) mice (ii). **E)** Pooled mean resultant vector length values of cells showing no changes by context (i) and by context in WT (black) and J20 (red) mice (ii). The data shown in **A**, **B**, **C**, **D** and **E** is the same data replotted separately. Box plots: box corresponds to the mean ± SEM, the circle to the

mean, the line to the median and the whiskers to the SD. (* $p \leq 0.05$, ** $p \leq 0.01$, *** $p \leq 0.001$)

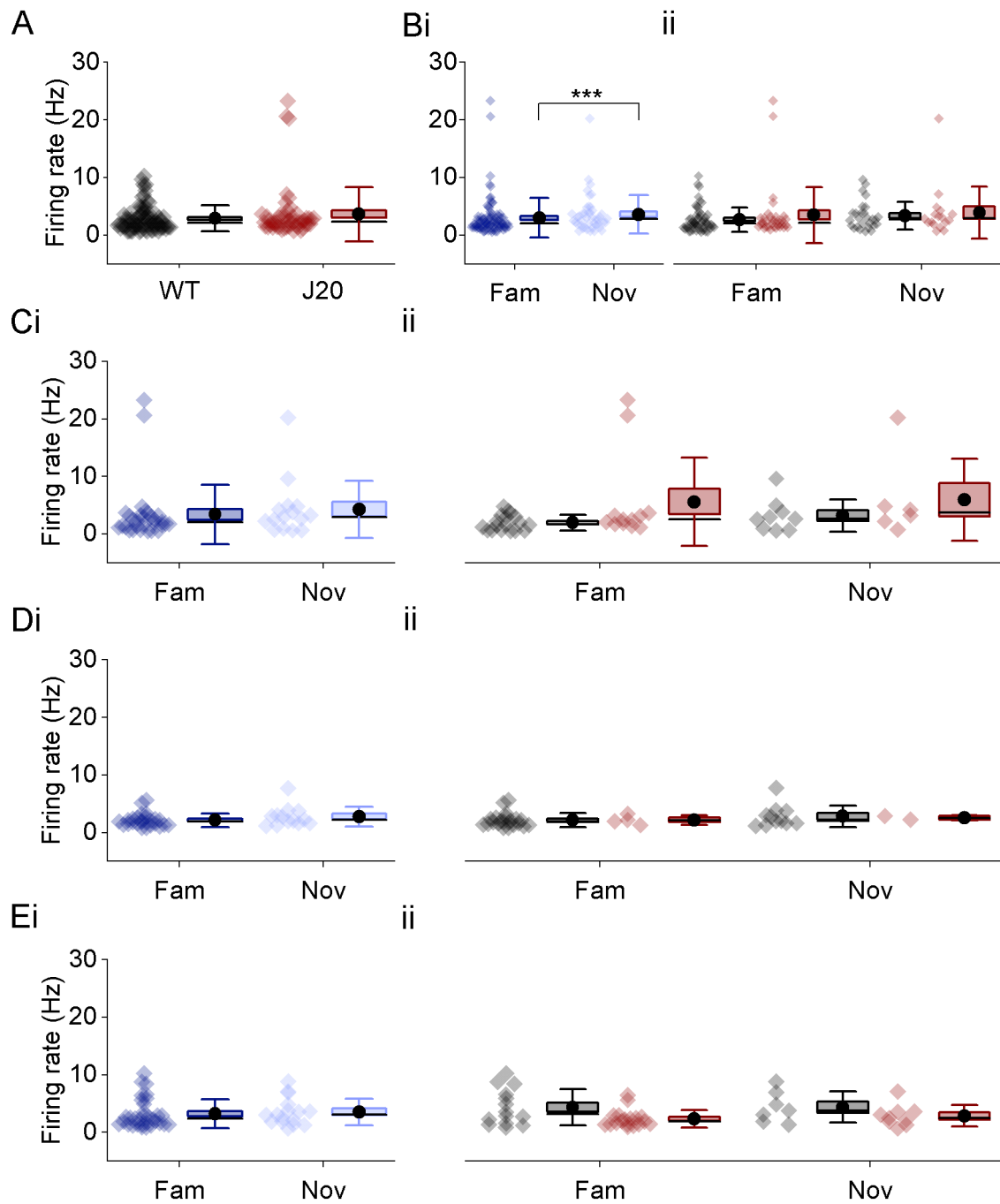


Figure 4.28 The firing rate of HD sensitive cells is similar between WT and J20 mice. A) Pooled firing rate data of HD sensitive cells by genotype. **B)** Pooled firing rate data of all HD sensitive cells by context (i) and by context in WT (black) and J20 (red) mice (ii). **C)** Pooled firing rate data of decreasing HD sensitive cells by context (i) and by context in WT (black) and J20 (red) mice (ii). **D)** Pooled firing rate data of increasing HD sensitive cells by context (i) and by context in WT (black) and J20 (red) mice (ii). **E)** Pooled firing rate data of HD sensitive cells showing no changes by context (i) and by context in WT (black) and J20 (red) mice (ii). The data shown in **A**, **B**, **C**, **D** and **E** is the same data replotted separately. Box plots: box corresponds to the mean \pm SEM, the circle to the mean, the line to the median and the whiskers to the SD. (* $p \leq 0.05$, ** $p \leq 0.01$, *** $p \leq 0.001$)

4.3.8. Cells with grid periodicity analysed with Langston's method

The observed proportions of cells with grid periodicity were not above 5% for either of the genotypes, which leads to the potential that the cells that exceeded the 95th percentile were solely due to chance. These results contrast with studies which have reported that 10-20% of MEC cells have significant grid periodicity (Giocomo *et al.*, 2011; Perez-Escobar *et al.*, 2016; Diehl *et al.*, 2017; Miao *et al.*, 2017; Munn *et al.*, 2020). In fact, figures 4.29Aii and 4.30B show that the cells observed in J20 mice do not show grid patterns. It is therefore likely that the cells included in the following analysis are not true grid cells, and thus the following analysis should be taken cautiously.

Figure 4.29A shows examples of the spatial firing patterns and spatial autocorrelograms of WT and J20 cells. The observed distribution of grid scores and the shuffled distribution of WT and J20 cells can be seen in figure 4.29B. The proportion of cells showing grid periodicity was the same between genotypes ($F(1, \text{Inf}) = 0.07, p = 0.78$, Fig. 4.29Ci), and this was also the case between familiar and novel contexts ($F(1, \text{Inf}) = 0.78, p = 0.38$, Fig. 4.29Cii). As it occurred with HD sensitive cells, the number of putative interneurons showing grid periodicity was deemed too low ($n = 1$) to be included in the analysis. In addition, introducing layer effect did not improve the mixed model and therefore was not considered.

Examples of the spatial firing pattern and autocorrelograms of WT and J20 decreasing and increasing cells can be seen in figure 4.30A and B. No cells were classified as no changes. The proportion of cells with grid periodicity that showed a decrease in their scores in the novel exposure (Fig. 4.30Ci), when compared to the two familiar exposures, was compared to the proportion of cells expected purely by chance. The proportions of cells decreasing their scores were not significantly different to chance levels in both WT and J20 mice (WT: $p = 0.47$, J20: $p = 1.00$, Fisher's exact test, Fig. 4.30Cii). Furthermore, the proportion of decreasing cells was similar in both genotypes ($p = 1.00$, Fisher's exact test, Fig. 4.30Cii). The proportion of cells with grid periodicity that showed an increase in their scores was also compared to the proportion of cells expected by chance (Fig. 4.30Di). The proportion of cells increasing their scores was also not different

to chance levels in both WT mice and J20 mice (WT: $p = 0.11$, J20: $p = 1.00$, Fisher's exact test, Fig. 4.30Cii). In addition, both J20 and WT mice showed a similar proportion of increasing cells ($p = 1.00$, Fisher's exact test, Fig. 4.30Cii). However, the low percentage of cells showing grid periodicity results in n numbers which are relatively low (WT: $n = 11$, J20: $n = 17$), and this should be taken into consideration.

Grid scores were compared between different groups. WT and J20 cells showed similar grid scores ($F(1, 5.97) = 1.77$, $p = 0.23$, Fig. 4.31A). Context was observed to affect grid scores ($F(2, 52) = 41.19$, $p < 0.0001$, Fig. 4.31) with decreasing cells significantly decreasing with novelty ($\beta = 0.38$, $SE = 0.06$, $t(84) = 6.40$, $p < 0.0001$, Fig. 4.31Ci) and increasing cells significantly increasing their grid score ($\beta = -0.35$, $SE = 0.06$, $t(84) = -6.22$, $p < 0.0001$, Fig. 4.31Di). No changes were found in the firing rate between genotypes ($F(1, 5.04) = 3.27$, $p = 0.13$, Fig. 4.32A) or due to context ($F(1, 52) = 2.71$, $p = 0.10$, Fig. 4.32B).

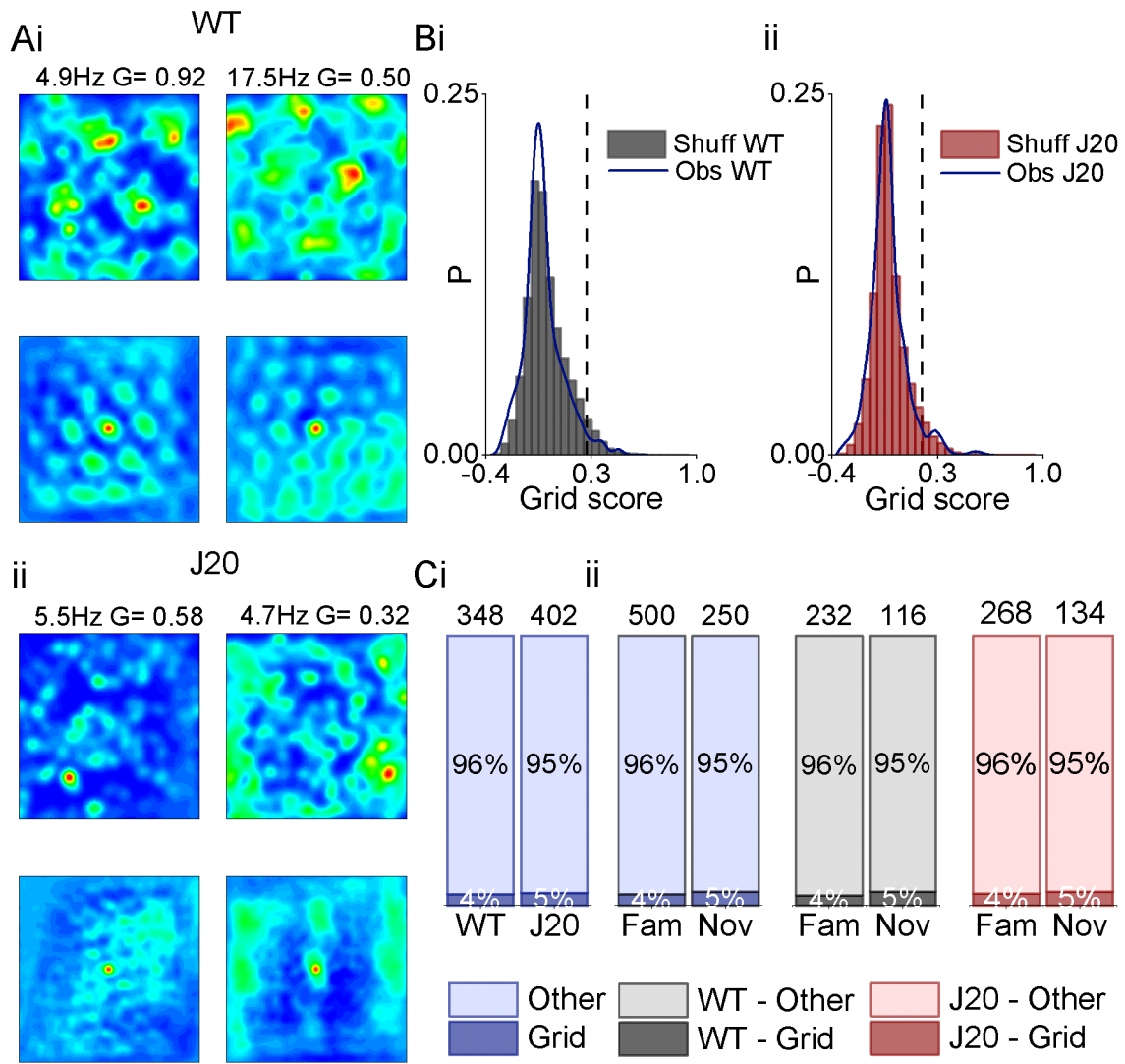


Figure 4.29 The proportion of cells with significant grid periodicity is not above chance levels. A) Examples of the spatial firing pattern (top) and spatial autocorrelograms (bottom) of cells with significant grid periodicity in WT mice (**i**) and J20 mice (**ii**), showing their peak firing rate and grid score (G) above the plot. **B)** Distribution of grid scores and shuffled scores for WT (**i**) and J20 (**ii**) mice. **C)** Proportion of cells with significant grid periodicity by genotype (**i**) and context (**ii**). Numbers above bars represent the total n number. (* p ≤ 0.05, ** p ≤ 0.01, *** p ≤ 0.001)

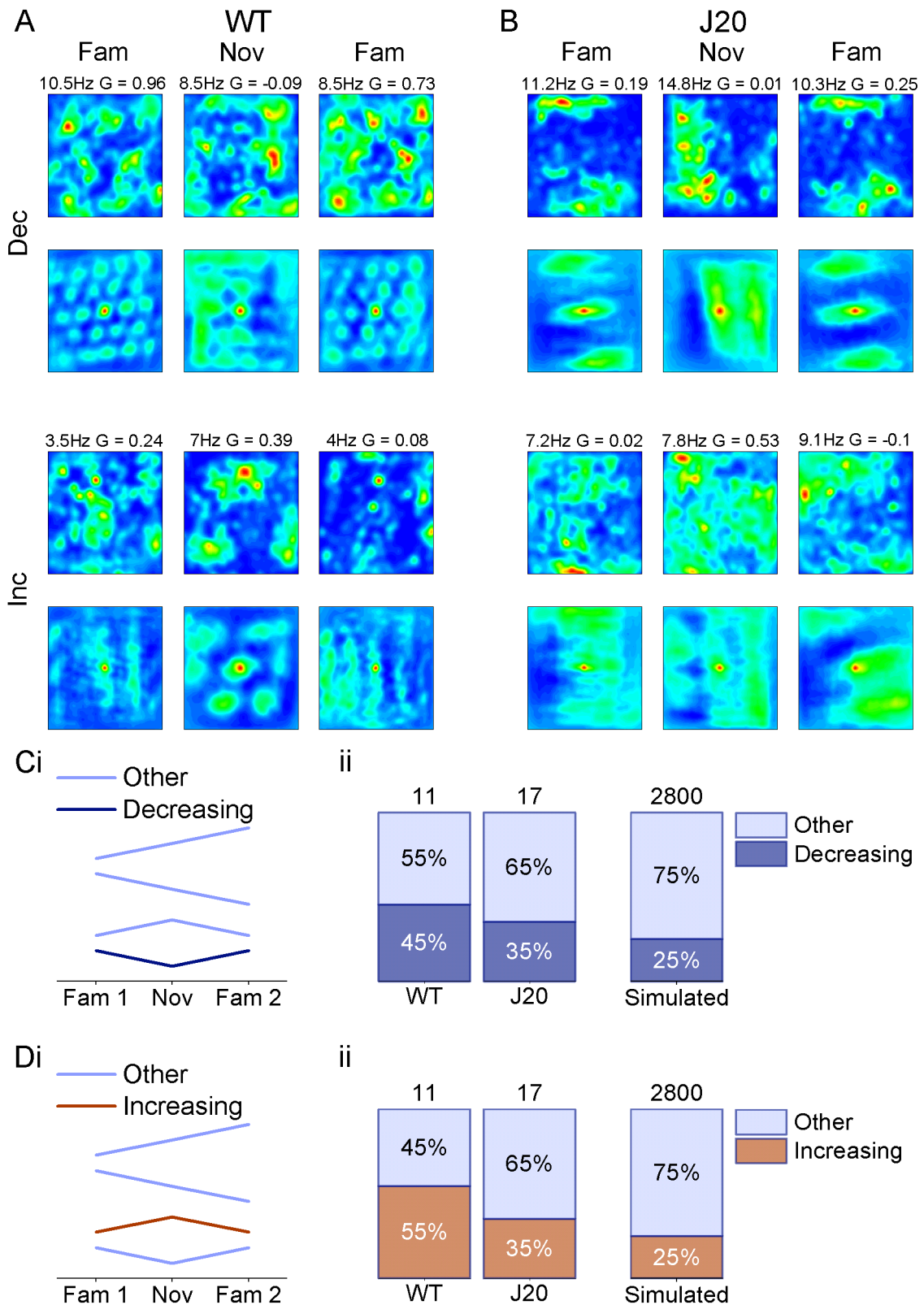


Figure 4.30 The proportion of decreasing and increasing cells with grid periodicity is similar to the simulated data. **A)** Examples of the spatial firing pattern (top) and spatial autocorrelograms (bottom) of cells with grid periodicity for the three trials for a decreasing cell (dec), and an increasing cell (inc) in WT mice. Peak firing rate and grid score (G) are shown above the plot. **B)** Examples of the spatial firing pattern (top) and spatial

autocorrelograms (bottom) of cells with grid periodicity for the three trials for a decreasing cell (dec), and an increasing cell (inc) in J20 mice. Peak firing rate and grid score (G) are shown above the plot. **C)** Example patterns of decreasing cells (dark blue) and other cells (light blue), which encompasses increasing and no-changes cells (**i**), proportions of decreasing and other cells in both genotypes compared to the simulated proportions (**ii**). **D)** Example patterns of increasing cells (orange) and other cells (light blue), which encompasses increasing and no-changes cells (**i**), proportions of increasing and other cells in both genotypes compared to the simulated proportions (**ii**). Numbers above bars represent the total n number. (* $p \leq 0.05$, ** $p \leq 0.01$, *** $p \leq 0.001$)

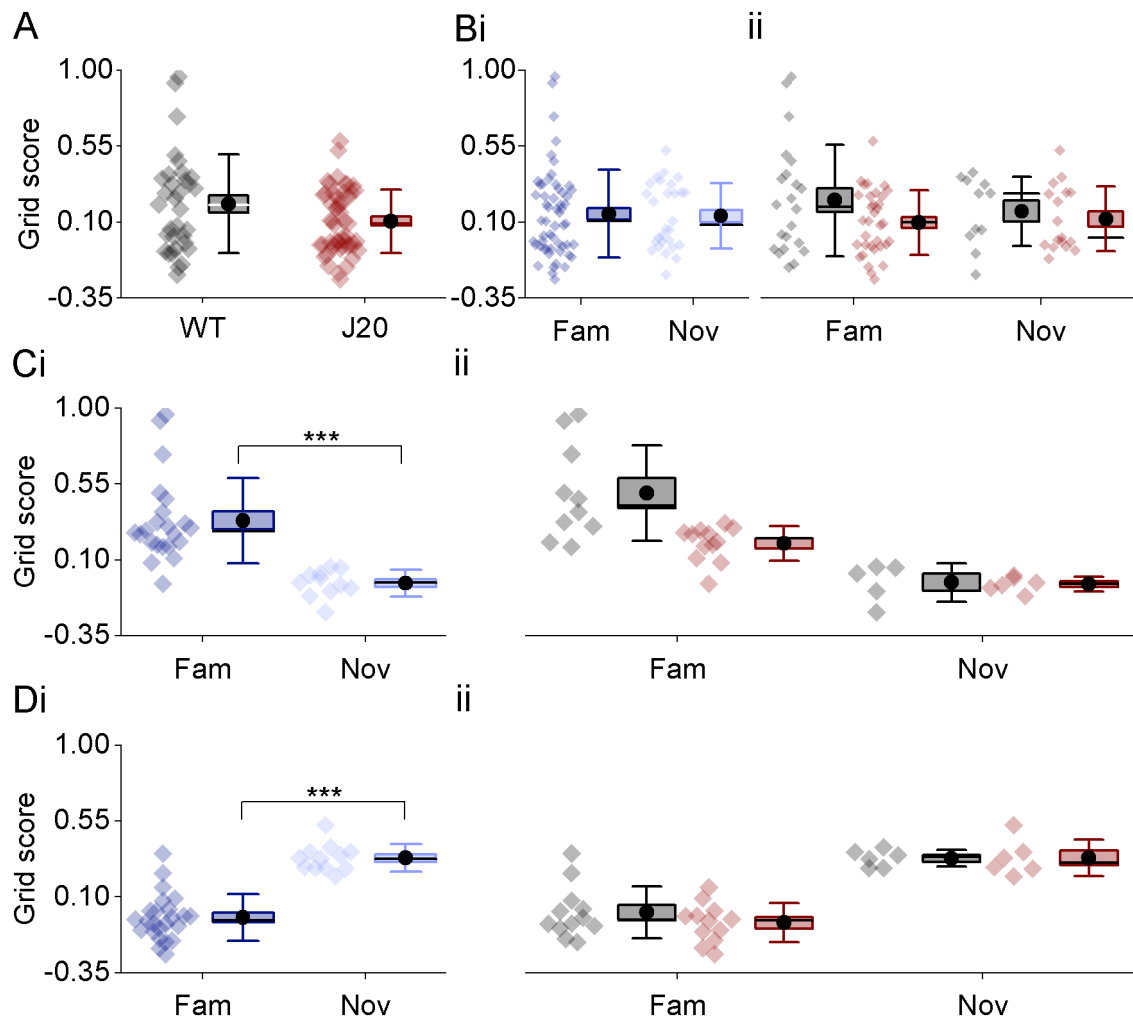


Figure 4.31 Grid scores are similar in J20 mice than in WT mice. A) Pooled grid scores data by genotype. **B)** Pooled grid scores of all cells with grid periodicity by context **(i)** and by context in WT (black) and J20 (red) mice **(ii)**. **C)** Pooled grid scores data of decreasing cells by context **(i)** and by context in WT (black) and J20 (red) mice **(ii)**. **D)** Pooled grid scores data of increasing cells by context **(i)** and by context in WT (black) and J20 (red) mice **(ii)**. The data shown in **A**, **B**, **C** and **D** is the same data replotted separately. Box plots: box corresponds to the mean \pm SEM, the circle to the mean, the line to the median and the whiskers to the SD. (* $p \leq 0.05$, ** $p \leq 0.01$, *** $p \leq 0.001$)

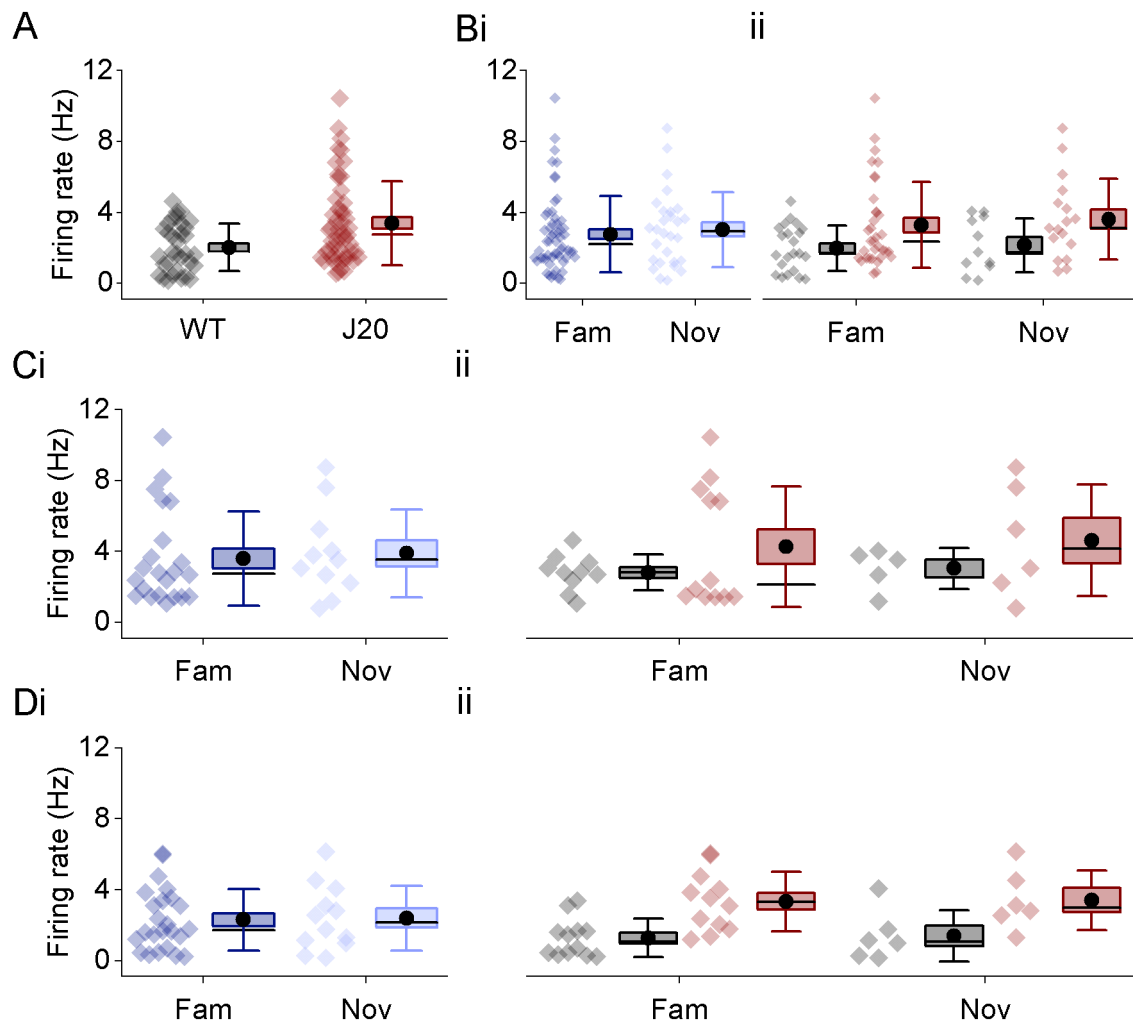


Figure 4.32 There are no changes in the firing rate of cells with grid periodicity between both genotypes. A) Pooled firing rate data by genotype, **B)** Pooled firing rate of all cells with grid periodicity by context (**i**) and by context in WT (black) and J20 (red) mice (**ii**). **C)** Pooled firing rate data of decreasing cells by context (**i**) and by context in WT (black) and J20 (red) mice (**ii**). **D)** Pooled firing rate data of increasing cells by context (**i**) and by context in WT (black) and J20 (red) mice (**ii**). The data shown in **A**, **B**, **C** and **D** is the same data replotted separately. Box plots: box corresponds to the mean \pm SEM, the circle to the mean, the line to the median and the whiskers to the SD. (* $p \leq 0.05$, ** $p \leq 0.01$, *** $p \leq 0.001$)

4.3.9. Cells with grid periodicity analysed with Sargolini's method

The analysis performed with the Sargolini's method highlighted higher proportions of cells with grid periodicity in WT mice (10%). However, the proportion of these cells in J20 mice were still not above 5%, which again leads to the potential that the J20 cells that exceeded the 95th percentile were solely due to chance. The proportion of cells with grid periodicity observed in WT mice are within the low range of the proportions observed in other studies, which reported that 10-20% of MEC cells have significant grid periodicity (Giocomo *et al.*, 2011; Perez-Escobar *et al.*, 2016; Diehl *et al.*, 2017; Miao *et al.*, 2017; Munn *et al.*, 2020).

Figure 4.33A shows examples of the spatial firing patterns and spatial autocorrelograms of WT and J20 cells. The observed distribution of grid scores and the shuffled distribution of WT and J20 cells can be seen in figure 4.33B. The proportion of cells showing grid periodicity was significantly different between both genotypes ($F(1, \text{Inf}) = 6.4, p = 0.01$, Fig. 4.33Ci). However, no differences were observed between familiar and novel contexts ($F(1, \text{Inf}) = 1.5, p = 0.21$, Fig. 4.33Cii). Introducing layer effect did not improve the mixed model and therefore was not considered.

Examples of the spatial firing pattern and autocorrelograms of WT and J20 decreasing and increasing cells can be seen in figure 4.34A and B. The proportion of cells with grid periodicity that showed a decrease in their scores in the novel exposure (Fig. 4.34Ci), when compared to the two familiar exposures, was compared to the proportion of cells expected purely by chance. The proportions of cells decreasing their scores were not significantly different to chance levels in both WT and J20 mice (WT: $p = 0.35$, J20: $p = 0.79$, Fisher's exact test, Fig. 4.34Cii). Furthermore, the proportion of decreasing cells was similar in both genotypes ($p = 1.00$, Fisher's exact test, Fig. 4.34Cii). The proportion of cells with grid periodicity that showed an increase in their scores was also compared to the proportion of cells expected by chance (Fig. 4.34Di). The proportion of cells increasing their scores was also not different to chance levels in both WT mice and J20 mice (WT: $p = 0.07$, J20: $p = 0.81$, Fisher's exact test, Fig. 4.34Cii). In addition, both J20 and WT mice showed a similar proportion

of increasing cells ($p = 0.13$, Fisher's exact test, Fig. 4.34Cii). However, the low percentage of cells showing grid periodicity results in n numbers which are relatively low (WT: $n = 27$, J20: $n = 17$), and this should be taken into consideration.

The grid field size was used to measure the grid scale. A significant interaction between context and genotype was observed ($F(1, \text{Inf}) = 4.28, p = 0.04$, Fig. 4.35A), which highlighted an increase of the grid field size in WT cells with novelty ($\beta = -0.14, \text{SE} = 0.03, z(132) = -4.71, p < 0.0001$, Fig. 4.35A) but not in J20 cells ($\beta = -0.039, \text{SE} = 0.04, z(132) = -0.93, p = 0.79$, Fig. 4.35A). In addition, the grid field size was not significantly different between WT and J20 cells in the familiar ($\beta = -0.22, \text{SE} = 0.14, z(132) = -1.49, p = 0.44$, Fig. 4.35A) nor the novel environment ($\beta = -0.11, \text{SE} = 0.15, z(132) = -0.73, p = 0.88$, Fig. 4.35A). The firing rate maps of both familiar trials were correlated for all cells with significant grid periodicity. This was also done for the familiar trials and the novel trial. No differences were observed between genotypes ($F(1, 5.74) = 0.99, p = 0.36$, Fig. 4.35B). However, the correlation values were higher when correlating the firing rate maps of both familiar trials than the familiar and novel trials for both WT ($\beta = 0.61, \text{SE} = 0.04, t(132) = 16.95, p < 0.0001$, Fig. 4.35B) and J20 cells ($\beta = 0.43, \text{SE} = 0.04, t(32) = 9.47, p < 0.0001$, Fig. 4.35B). Grid scores were compared between different groups. WT and J20 cells showed similar grid scores ($F(1, 8.27) = 1.16, p = 0.31$, Fig. 4.36A). Context was observed to not affect grid scores ($F(2, 82) = 24.3, p < 0.0001$, Fig. 4.36) with decreasing cells significantly decreasing with novelty ($\beta = 0.75, \text{SE} = 0.12, t(132) = 6.02, p < 0.0001$, Fig. 4.36Ci) and increasing cells significantly increasing their grid score ($\beta = -0.75, \text{SE} = 0.18, t(132) = -4.08, p = 0.001$, Fig. 4.36Di). No differences were seen due to context ($\beta = -0.02, \text{SE} = 0.13, t(132) = -4.08, p = 0.14$, Fig. 4.36Ei). No changes were found in the firing rate between both genotypes ($F(1, \text{Inf}) = 0.16, p = 0.69$, Fig. 4.37A). However, a significant increase in the firing rate was observed during the exploration of the novel arena was seen ($F(1, \text{Inf}) = 6.32, p = 0.012$, Fig. 4.37B).

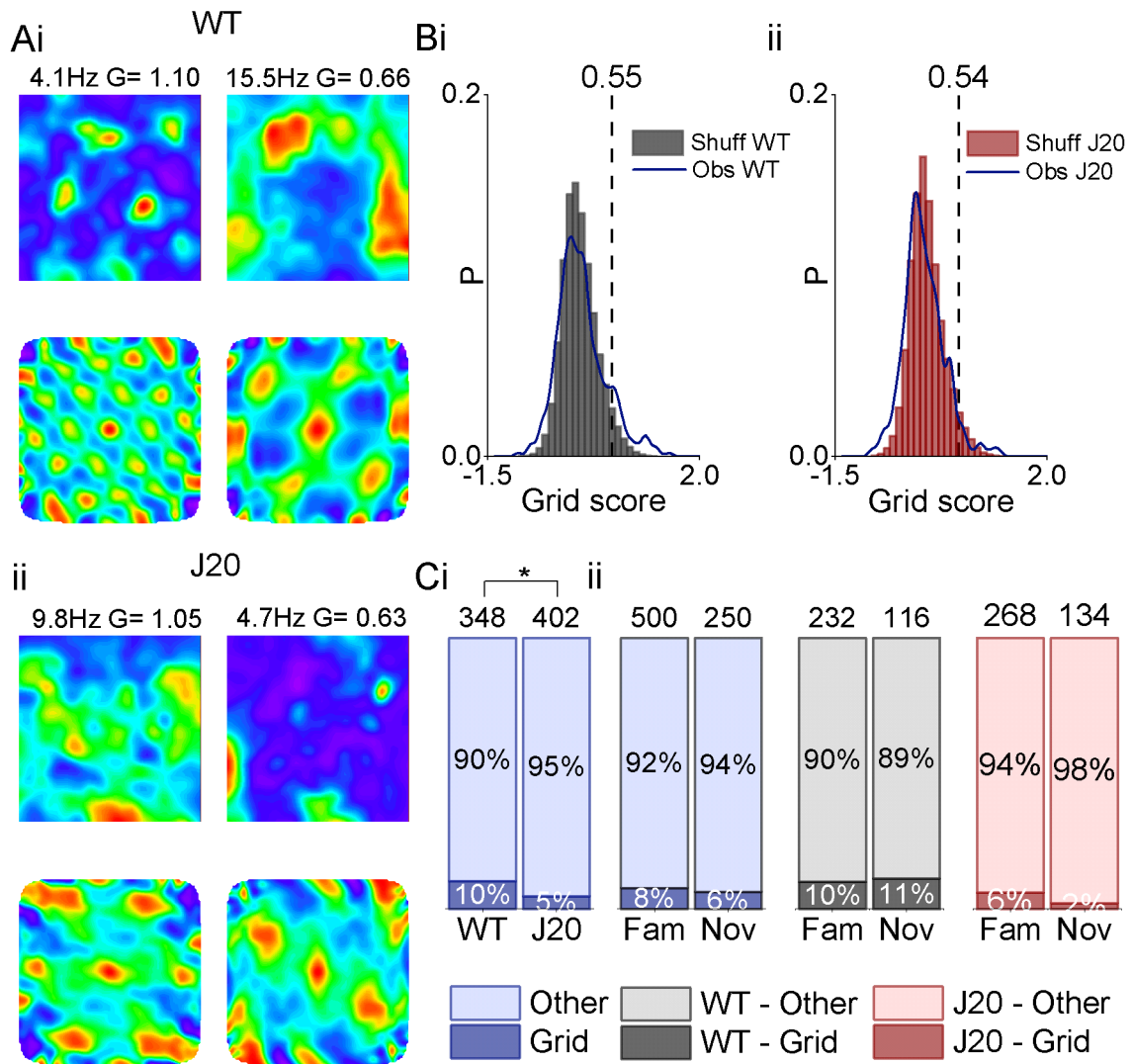


Figure 4.33 The proportion of cells with significant grid periodicity is higher in WT mice. A) Examples of the spatial firing pattern (top) and spatial autocorrelograms (bottom) of cells with significant grid periodicity in WT mice (**i**) and J20 mice (**ii**), showing their peak firing rate and grid score (G) above the plot. For firing rate maps, red is maximum and purple is zero. For autocorrelograms, red is maximum and purple is minimum. **B)** Distribution of grid scores and shuffled scores for WT (**i**) and J20 (**ii**) mice. **C)** Proportion of cells with significant grid periodicity by genotype (**i**) and context (**ii**). Numbers above bars represent the total n number. (* p < 0.05, ** p < 0.01, *** p < 0.001)

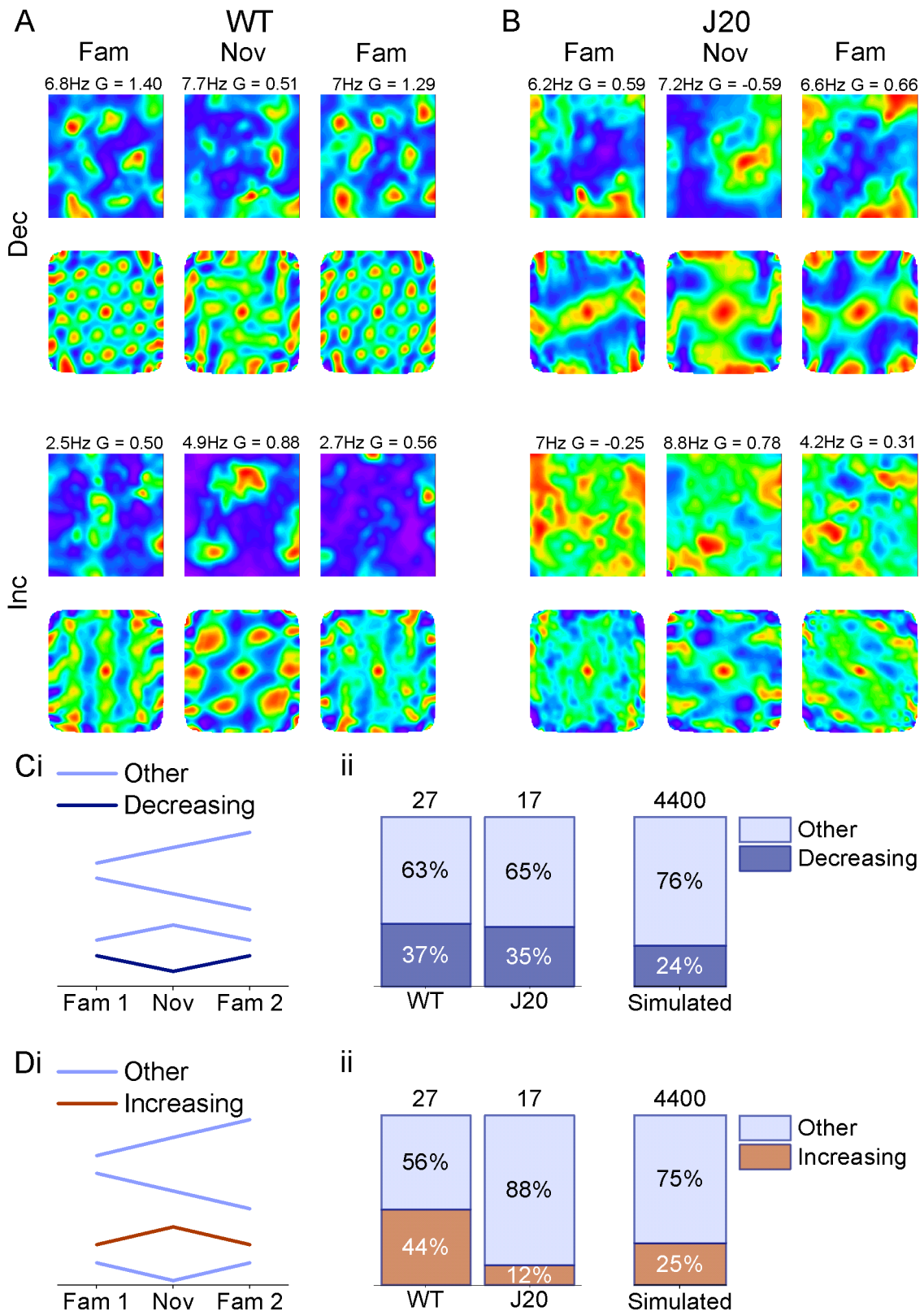


Figure 4.34 The proportion of decreasing and increasing cells with grid periodicity is similar to the simulated data. **A)** Examples of the spatial firing pattern (top) and spatial autocorrelograms (bottom) of cells with grid periodicity for the three trials for a decreasing cell (dec), and an increasing cell (inc) in WT mice. Peak firing rate and grid score (G) are shown above the plot. **B)** Examples of the spatial firing pattern (top) and spatial

autocorrelograms (bottom) of cells with grid periodicity for the three trials for a decreasing cell (dec), and an increasing cell (inc) in J20 mice. Peak firing rate and grid score (G) are shown above the plot. **C**) Example patterns of decreasing cells (dark blue) and other cells (light blue), which encompasses increasing and no-changes cells (**i**), proportions of decreasing and other cells in both genotypes compared to the simulated proportions (**ii**). **D**) Example patterns of increasing cells (orange) and other cells (light blue), which encompasses increasing and no-changes cells (**i**), proportions of increasing and other cells in both genotypes compared to the simulated proportions (**ii**). For firing rate maps, red is maximum and purple is zero. For autocorrelograms, red is maximum and purple is minimum. Numbers above bars represent the total n number. (* p ≤ 0.05, ** p ≤ 0.01, *** p ≤ 0.001)

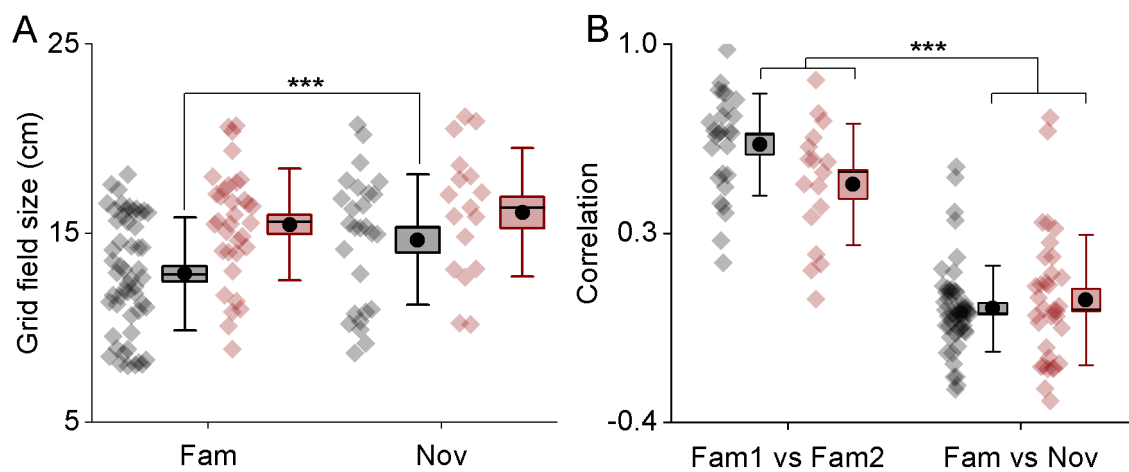


Figure 4.35 Cells with grid periodicity show stability between both familiar exposures. A) Pooled grid field size of all cells with grid periodicity by context in WT (black) and J20 (red) mice. **B)** Correlation between the firing rate map of the two familiar trials and of the familiar trials and the novel trial for WT (black) and J20 (red) cells. Box plots: box corresponds to the mean ± SEM, the circle to the mean, the line to the median and the whiskers to the SD. (* p ≤ 0.05, ** p ≤ 0.01, *** p ≤ 0.001)

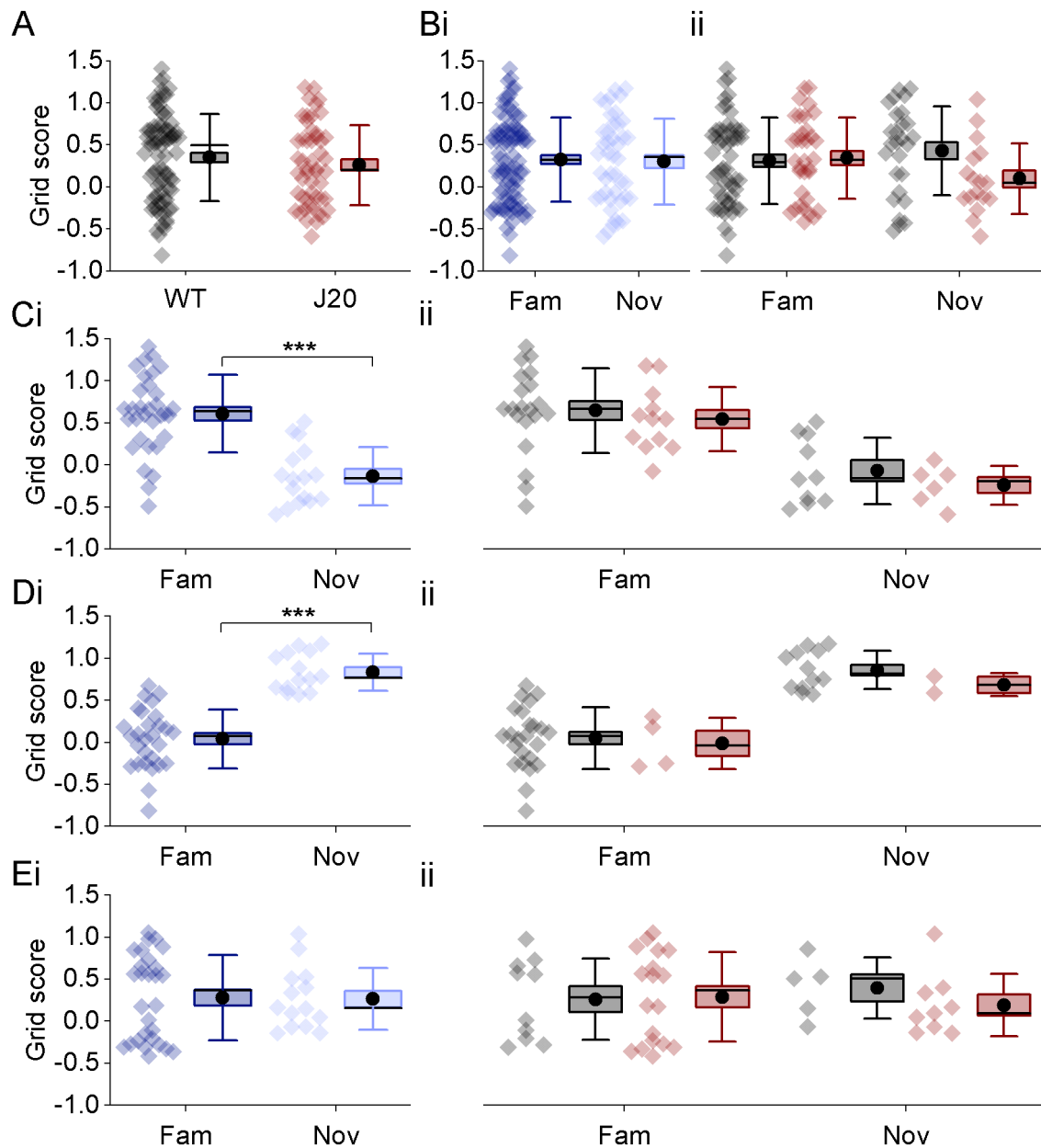


Figure 4.36 Grid scores are similar in WT mice and J20 mice. A) Pooled grid scores data by genotype. **B)** Pooled grid scores of all cells with grid periodicity by context **(i)** and by context in WT (black) and J20 (red) mice **(ii)**. **C)** Pooled grid scores data of decreasing cells by context **(i)** and by context in WT (black) and J20 (red) mice **(ii)**. **D)** Pooled grid scores data of increasing cells by context **(i)** and by context in WT (black) and J20 (red) mice **(ii)**. **E)** Pooled grid scores data of no changes cells by context **(i)** and by context in WT (black) and J20 (red) mice **(ii)**. The data shown in **A, B, C, D** and **E** is the same data replotted separately. Box plots: box corresponds to the mean \pm SEM, the circle to the mean, the line to the median and the whiskers to the SD. (* p \leq 0.05, ** p \leq 0.01, *** p \leq 0.001)

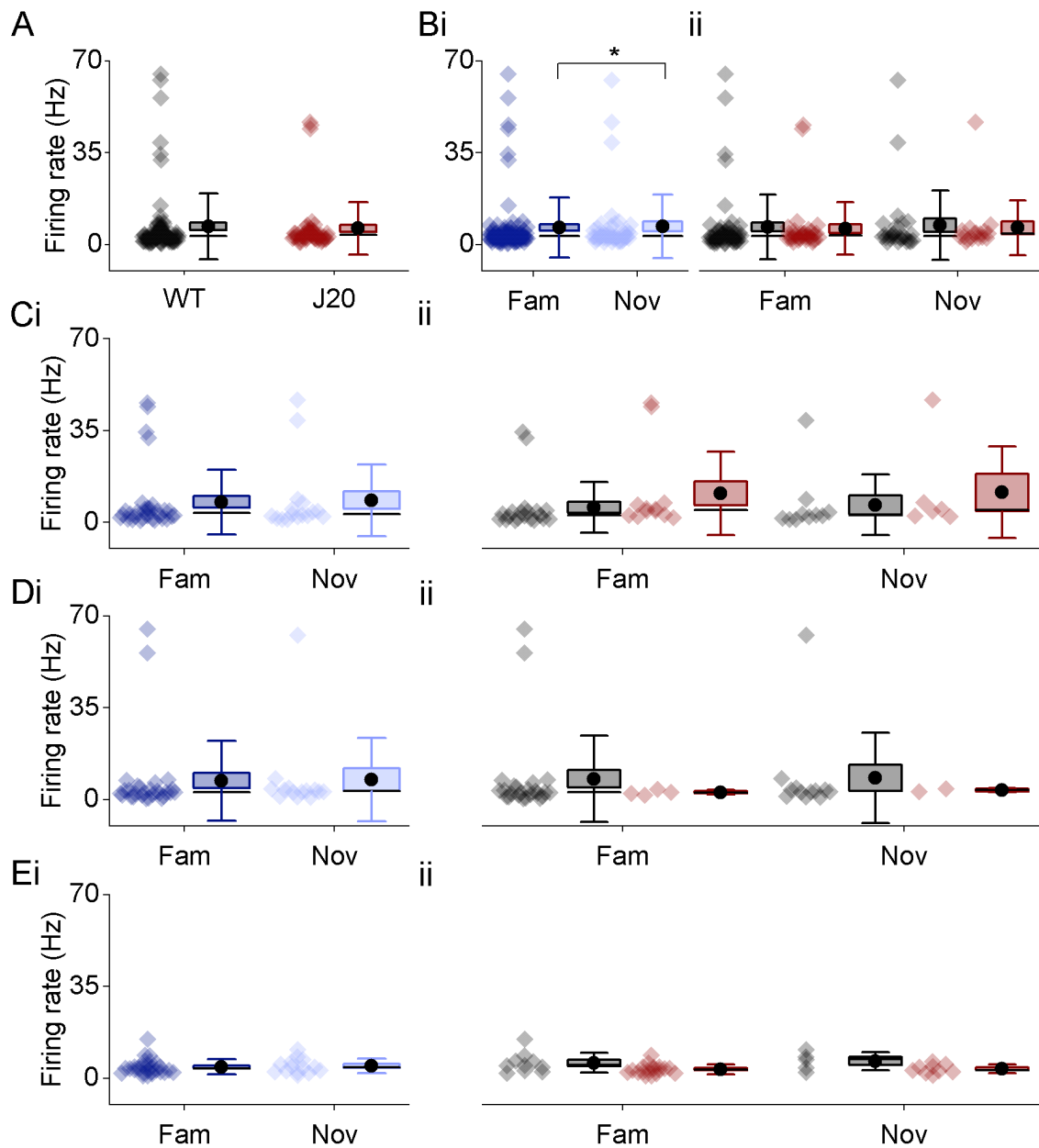


Figure 4.37 The firing rate of cells with grid periodicity increases during the exploration of the novel environment. A) Pooled firing rate data by genotype. **B)** Pooled firing rate of all cells with grid periodicity by context (i) and by context in WT (black) and J20 (red) mice (ii). **C)** Pooled firing rate data of decreasing cells by context (i) and by context in WT (black) and J20 (red) mice (ii). **D)** Pooled firing rate data of increasing cells by context (i) and by context in WT (black) and J20 (red) mice (ii). **E)** Pooled firing rate data of no changes cells by context (i) and by context in WT (black) and J20 (red) mice (ii). The data shown in **A**, **B**, **C**, **D** and **E** is the same data replotted separately. Box plots: box corresponds to the mean \pm SEM, the circle to the mean, the line to the median and the whiskers to the SD. (* $p \leq 0.05$, ** $p \leq 0.01$, *** $p \leq 0.001$)

4.3.10. Border sensitive cells show no differences between genotypes

Examples of the spatial firing pattern of WT and J20 border sensitive cells can be seen in figure 4.38A. The observed distribution and shuffled distribution of border scores of WT and J20 cells can be found in figure 4.38B. The number of cells considered border sensitive were equal between WT and J20 cells ($F(1, \text{Inf}) = 0.87, p = 0.35$, Fig. 4.38Ci). This was also the case for the proportion of border sensitive cells in familiar and novel contexts ($F(1, \text{Inf}) = 1.92, p = 0.17$, Fig. 4.38Cii) and when comparing the proportion of border sensitive cells of the total number of putative interneurons and putative excitatory cells ($F(1, \text{Inf}) = 0.75, p = 0.39$, Fig. 4.38Ciii).

Examples of the spatial firing pattern of WT and J20 decreasing, increasing and no changes border sensitive cells can be seen in figure 4.39A and B. The proportion of border sensitive cells that showed a decrease in their scores in the novel exposure (Fig. 4.39Ci), when compared to the two familiar exposures, was compared the proportion of cells expected purely by chance. The proportions of cells decreasing their scores were significantly higher than chance levels in both WT and J20 mice (WT: $p = 0.04$, J20: $p = 0.04$, Fisher's exact test, Fig. 4.39Cii). Furthermore, the proportion of decreasing cells was similar in both genotypes ($p = 1.00$, Fisher's exact test, Fig. 4.39Cii). The proportion of border sensitive cells that showed an increase in their scores (Fig. 4.39Di) was also compared to the proportion of cells expected by chance. In contrast, the proportion of cells increasing their scores was not different to chance levels in both WT mice and J20 mice (WT: $p = 1.00$, J20: $p = 1.00$, Fisher's exact test, Fig. 4.39Dii). In addition, both J20 and WT mice showed a similar proportion of increasing cells ($p = 1.00$, Fisher's exact test, Fig. 4.39Dii). However, due to the low percentage of border sensitive cells, the n numbers (WT: $n = 19$, J20: $n = 19$) included here are relatively low and should be taken into consideration.

Border scores were compared for each group. No changes were observed between WT and J20 cells ($F(1, 37.2) = 0.16, p = 0.69$, Fig. 4.40A) not between putative interneurons with putative excitatory cells ($F(1, 37.2) = 3.21, p = 0.08$, Fig. 4.40B). However, context had a significant effect ($F(2, 68) = 13.40, p < 0.0001$, Fig. 4.40) on decreasing ($\beta = 0.24, SE = 0.06, t(114) = 3.84, p = 0.004$,

Fig. 4.40Di) and increasing cells ($\beta = -0.33$, SE = 0.09, $t(114) = -3.55$, $p = 0.009$, Fig. 4.40Ei). The firing rate was not different when comparing genotypes ($F(1, 30.09) = 3.69$, $p = 0.06$, Fig. 4.41A), nor was affected by context ($F(1, 68) = 3.17$, $p = 0.08$, Fig. 4.41C). As expected, putative interneurons showed higher firing rates than putative excitatory cells ($F(1, 30.09) = 29.40$, $p < 0.0001$, Fig. 4.41Bi).

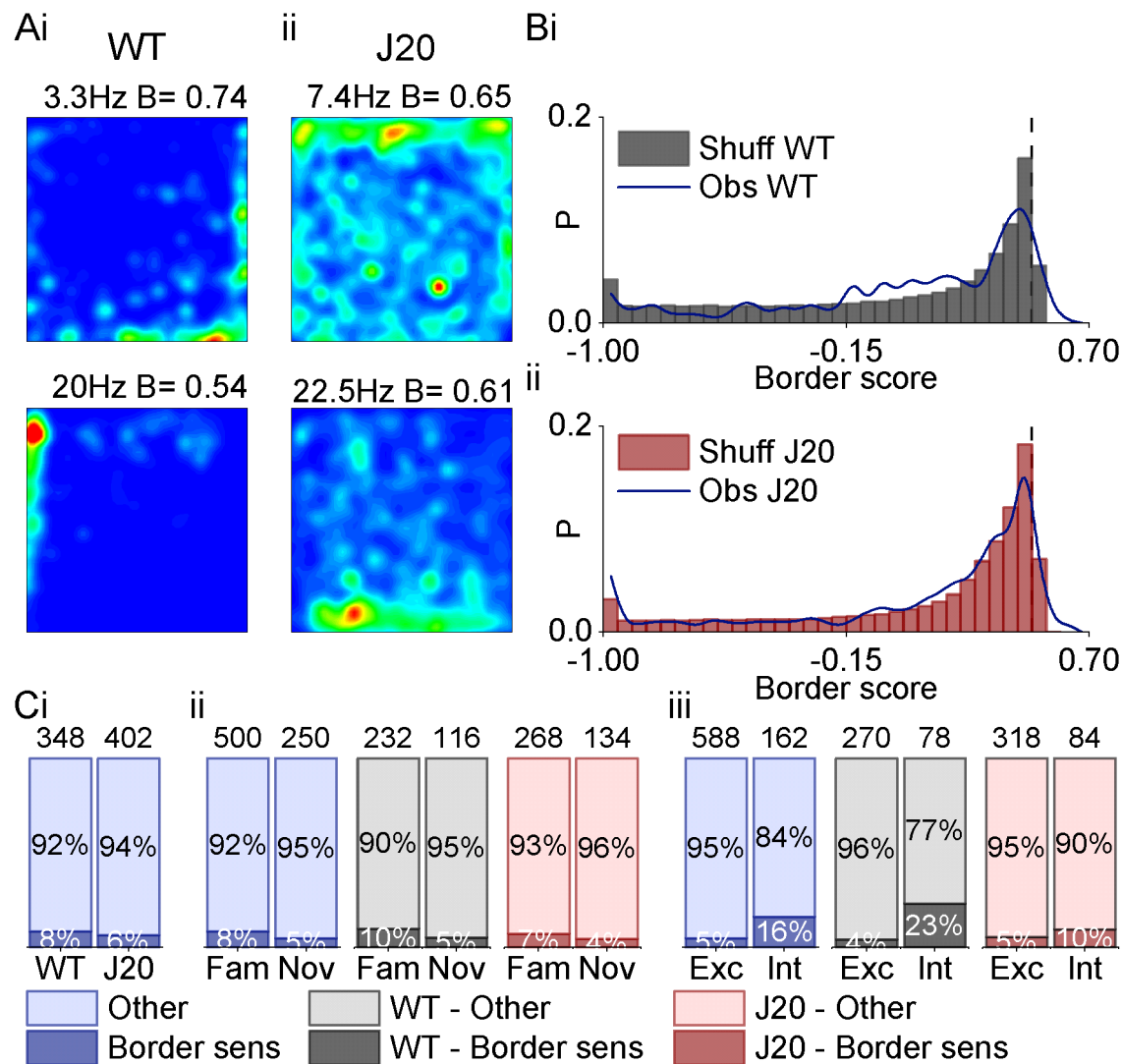


Figure 4.38 The proportion of border sensitive cells is the same between both genotypes. **A)** Examples of the spatial firing pattern of border sensitive cells in WT mice (**i**) and J20 mice (**ii**), showing their peak firing rate and border score (B) above the plot. **B)** Distribution of observed border scores and shuffled scores for WT (**i**) and J20 (**ii**) mice. **C)** Proportion of cells with significant grid periodicity by genotype (**i**), by context (**ii**) and by cell type (putative excitatory versus putative interneurons) (**iii**). Numbers above bars represent the total n number. (* $p \leq 0.05$, ** $p \leq 0.01$, *** $p \leq 0.001$)

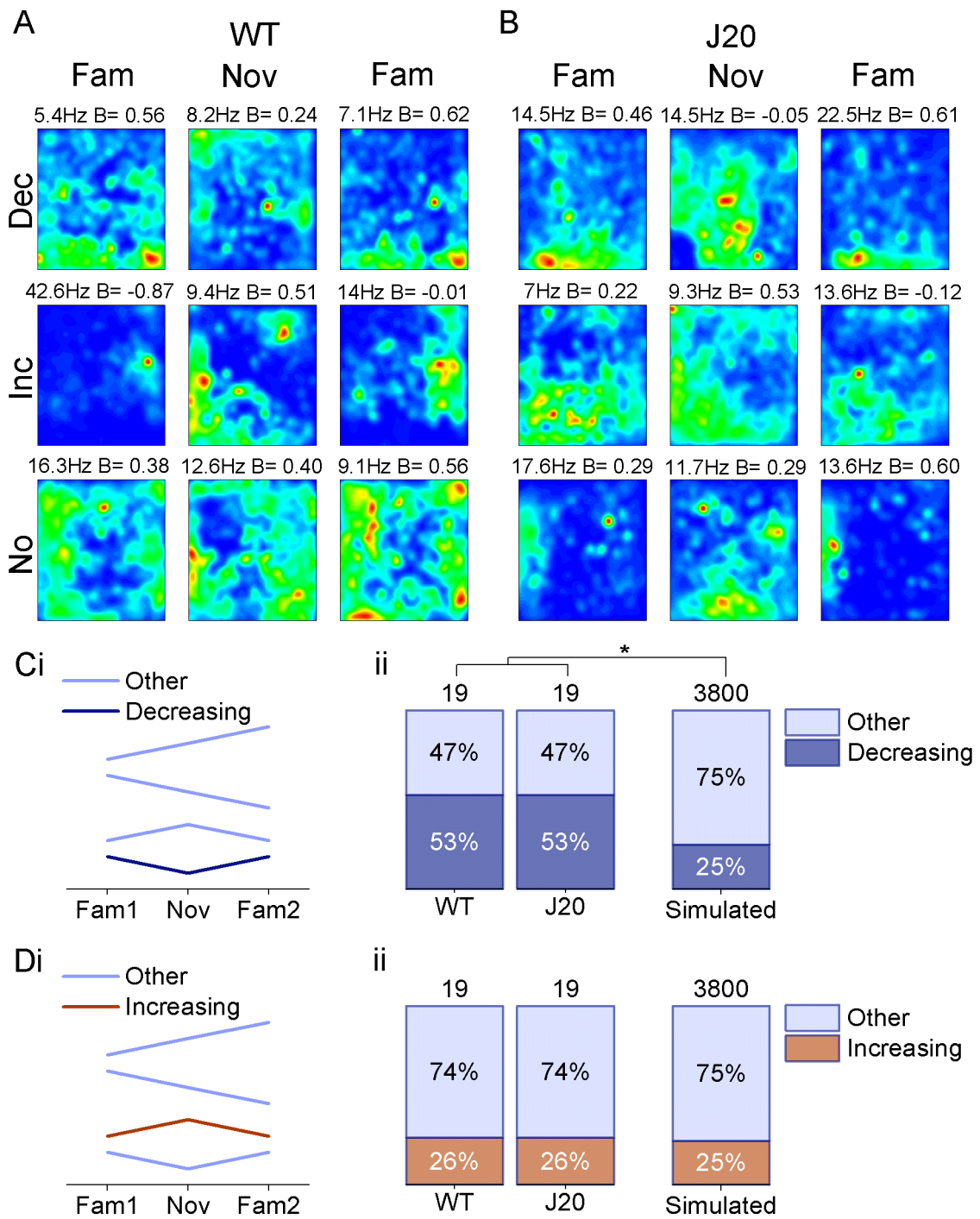


Figure 4.39 WT and J20 mice show a higher proportion of decreasing border sensitive cells than the simulated data. A) Examples of the spatial firing patterns of border sensitive cells for the three trials for a decreasing cell (dec), an increasing cell (inc) and a cell showing no differences due to context (no) in WT mice. Peak firing rate and border score (B) are shown above the plot. **B)** Examples of the spatial firing patterns of border sensitive cells for the three trials for a decreasing cell (dec), an increasing cell (inc) and a cell showing no differences due to context (no) in J20 mice. Peak firing rate and border score (B) are shown above the plot. **C)** Example patterns of decreasing cells (dark blue) and other cells (light blue), which encompasses increasing and no-changes cells (**i**), proportions of decreasing and other cells in both genotypes compared to the simulated

proportions (ii). **D**) Example patterns of increasing cells (orange) and other cells (light blue), which encompasses increasing and no-changes cells (i), proportions of increasing and other cells in both genotypes compared to the simulated proportions (ii). Numbers above bars represent the total n number. (* $p \leq 0.05$, ** $p \leq 0.01$, *** $p \leq 0.001$)

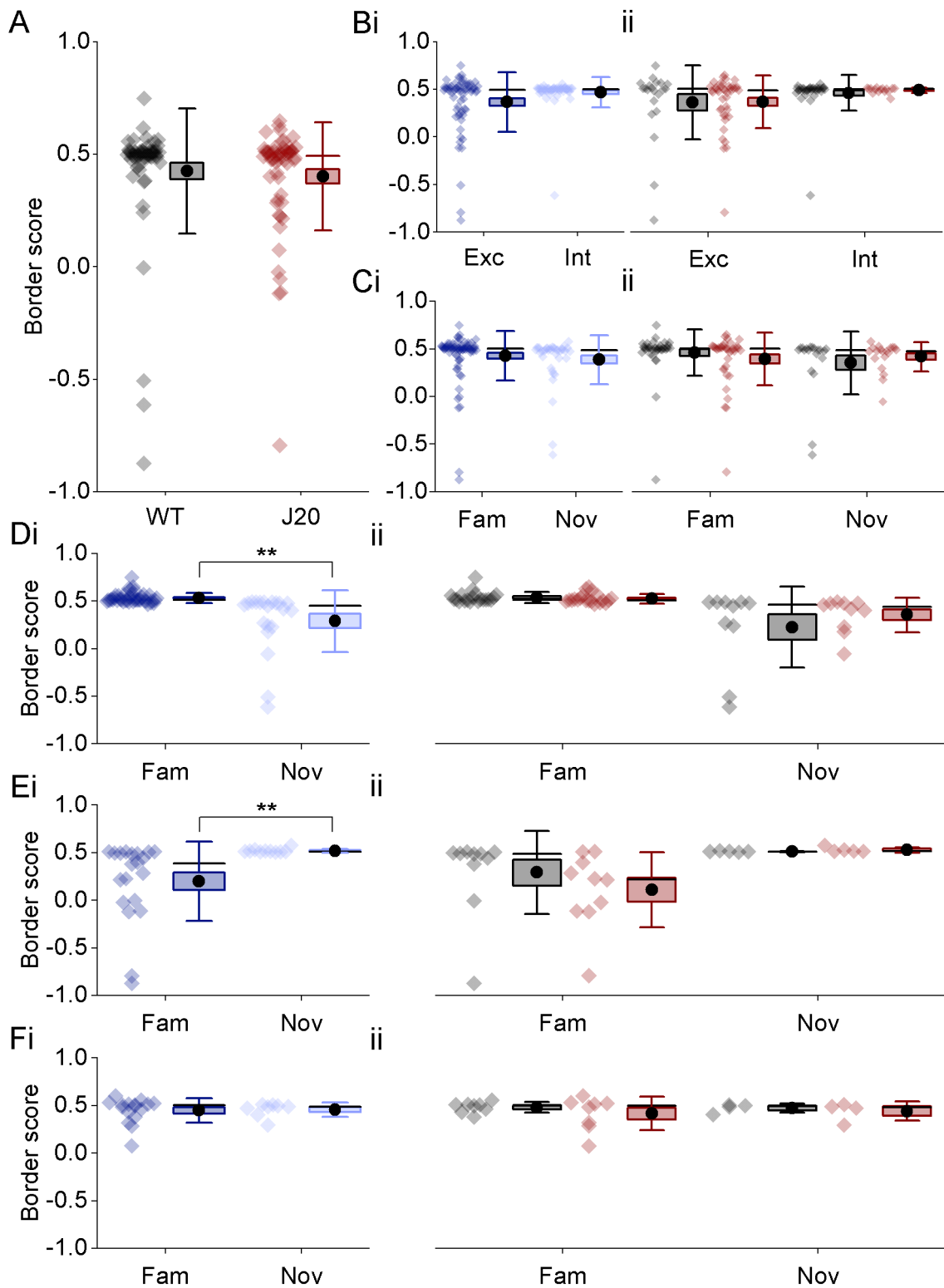


Figure 4.40 Border scores of WT and J20 mice are similar. A) Pooled border scores data by genotype. **B)** Pooled border scores by cell type (putative excitatory versus putative interneurons) **(i)** and by cell type in WT (black) and J20 (red) mice **(ii)**. **C)** Pooled border scores of all border sensitive cells by context **(i)** and by context in WT (black) and J20 (red) mice **(ii)**. **D)** Pooled border scores of decreasing cells by context **(i)** and by context in WT (black) and J20 (red) mice **(ii)**. **E)** Pooled border scores of increasing cells by context **(i)** and by context in WT (black) and J20 (red) mice **(ii)**.

mice **(ii)**. **F**) Pooled border scores of cells showing no changes by context **(i)** and by context in WT (black) and J20 (red) mice **(ii)**. The data shown in **A, B, C, D, E** and **F** is the same data replotted separately. Box plots: box corresponds to the mean \pm SEM, the circle to the mean, the line to the median and the whiskers to the SD. (* $p \leq 0.05$, ** $p \leq 0.01$, *** $p \leq 0.001$)

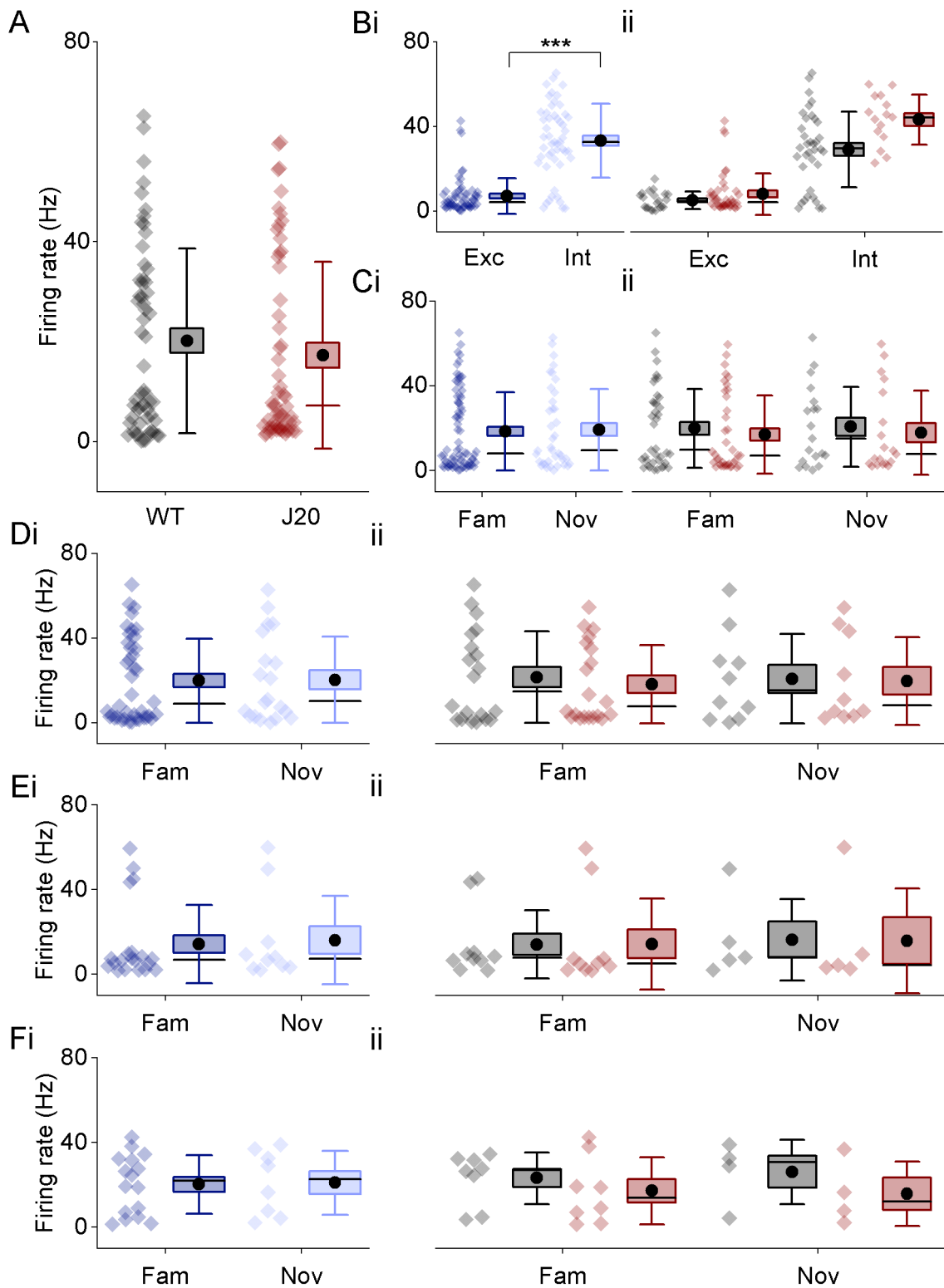


Figure 4.41 The firing rate of border sensitive cells is similar in WT and J20 mice. **A)** Pooled firing rate data by genotype. **B)** Pooled firing rate by cell type (putative excitatory versus putative interneurons) (**i**) and by cell type in WT (black) and J20 (red) mice (**ii**). **C)** Pooled firing rate of all border sensitive cells by context (**i**) and by context in WT (black) and J20 (red) mice (**ii**). **D)** Pooled firing rate of decreasing cells by context (**i**) and by context in WT (black) and J20 (red) mice (**ii**). **E)** Pooled firing rate of increasing cells by context (**i**) and by context in WT (black) and J20 (red) mice (**ii**). **F)** Pooled

firing rate of cells showing no changes by context (**i**) and by context in WT (black) and J20 (red) mice (**ii**). The data shown in **A**, **B**, **C**, **D**, **E** and **F** is the same data replotted separately. Box plots: box corresponds to the mean \pm SEM, the circle to the mean, the line to the median and the whiskers to the SD. (* $p \leq 0.05$, ** $p \leq 0.01$, *** $p \leq 0.001$)

4.3.11. Spatial information does not differ between genotypes

Examples of the spatial firing pattern of WT and J20 cells conveying spatial information can be seen in figure 4.42A. The observed distribution and shuffled distribution of spatial information scores of WT and J20 cells can be found in figure 4.42B. The percentage of cells conveying significant spatial information was the same among both genotypes ($F(1, Inf) = 0.05$, $p = 0.82$, Fig. 4.42Ci). In addition, the proportions were also the similar for familiar and novel contexts ($F(1, Inf) = 2.03$, $p = 0.15$, Fig. 4.42Cii). The inclusion of layer effect did not improve the model and was not included.

Examples of the spatial firing pattern of WT and J20 decreasing, increasing and no changes cells can be seen in figure 4.43A and B. The proportion of cells with significant spatial information that showed a decrease in their scores in the novel exposure (Fig. 4.43Ci), when compared to the two familiar exposures, was compared the proportion of cells expected purely by chance. The proportions of cells decreasing their scores were significantly higher than chance levels in both WT and J20 mice (WT: $p = 0.03$, J20: $p = 0.01$, Fisher's exact test, Fig. 4.43Cii). Furthermore, the proportion of decreasing cells was similar in both genotypes ($p = 1.00$, Fisher's exact test, Fig. 4.43Cii). The proportion of cells with significant spatial information that showed an increase in their scores (Fig. 4.43Di) was also compared to the proportion of cells expected by chance. In contrast, the proportion of cells increasing their scores was not different to chance levels in both WT mice and J20 mice (WT: $p = 1.00$, J20: $p = 1.00$, Fisher's exact test, Fig. 4.43Dii). In addition, both J20 and WT mice showed a similar proportion of increasing cells ($p = 1.00$, Fisher's exact test, Fig. 4.43Dii).

When comparing the spatial information, no main differences were observed due to genotype ($F(1, 6.33) = 2.68$, $p = 0.15$, Fig. 4.44A). Spatial information was affected by context ($F(2, 168) = 34.89$, $p < 0.0001$, Fig. 4.44), with decreasing

cells showing a reduction in the novel context ($\beta = 0.18$, SE = 0.02, $t(261) = 7.92$, $p < 0.0001$, Fig. 4.44Ci), and increasing cells showing a gain in the novel context ($\beta = -0.13$, SE = 0.03, $t(261) = -4.26$, $p = 0.0005$, Fig. 4.44Di). The firing rate of these cells did not differ when comparing between genotypes ($F(1, Inf) = 1.23$, $p = 0.27$, Fig. 4.45A). However, a context effect was observed ($F(1, Inf) = 11.34$, $p = 0.0008$, Fig. 4.45Bi).

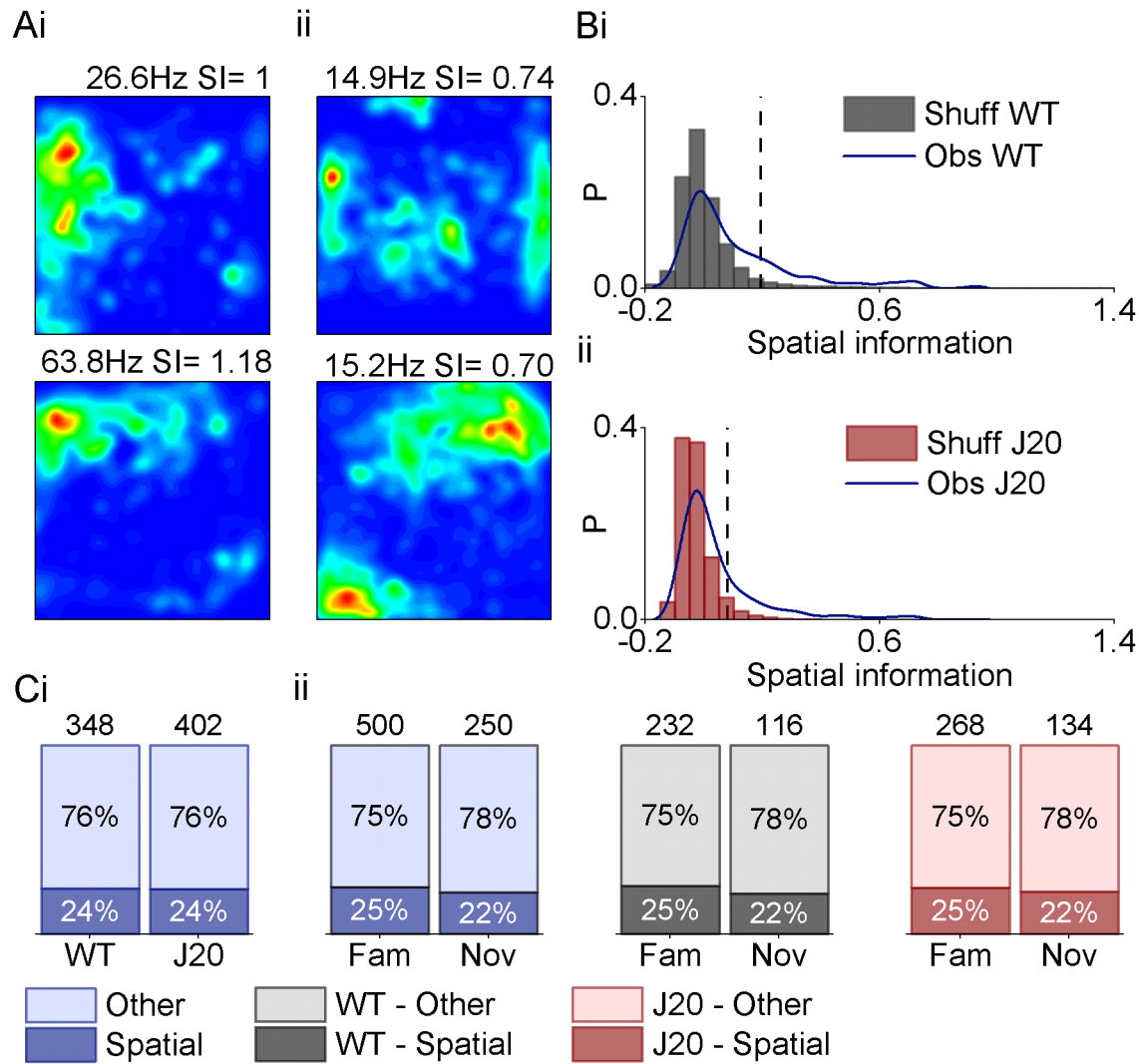


Figure 4.42 The proportion of cells conveying significant spatial information is similar in WT and J20 mice. A) Examples of the spatial firing pattern of cells conveying significant spatial information in WT mice (i) and J20 mice (ii), showing their peak firing rate and spatial information score (SI) above the plot. **B)** Distribution of observed spatial information scores and shuffled scores for WT (i) and J20 (ii) mice. **C)** Proportion of cells conveying significant spatial information by genotype (i) and by context (ii). Numbers above bars represent the total n number. (* $p \leq 0.05$, ** $p \leq 0.01$, *** $p \leq 0.001$)

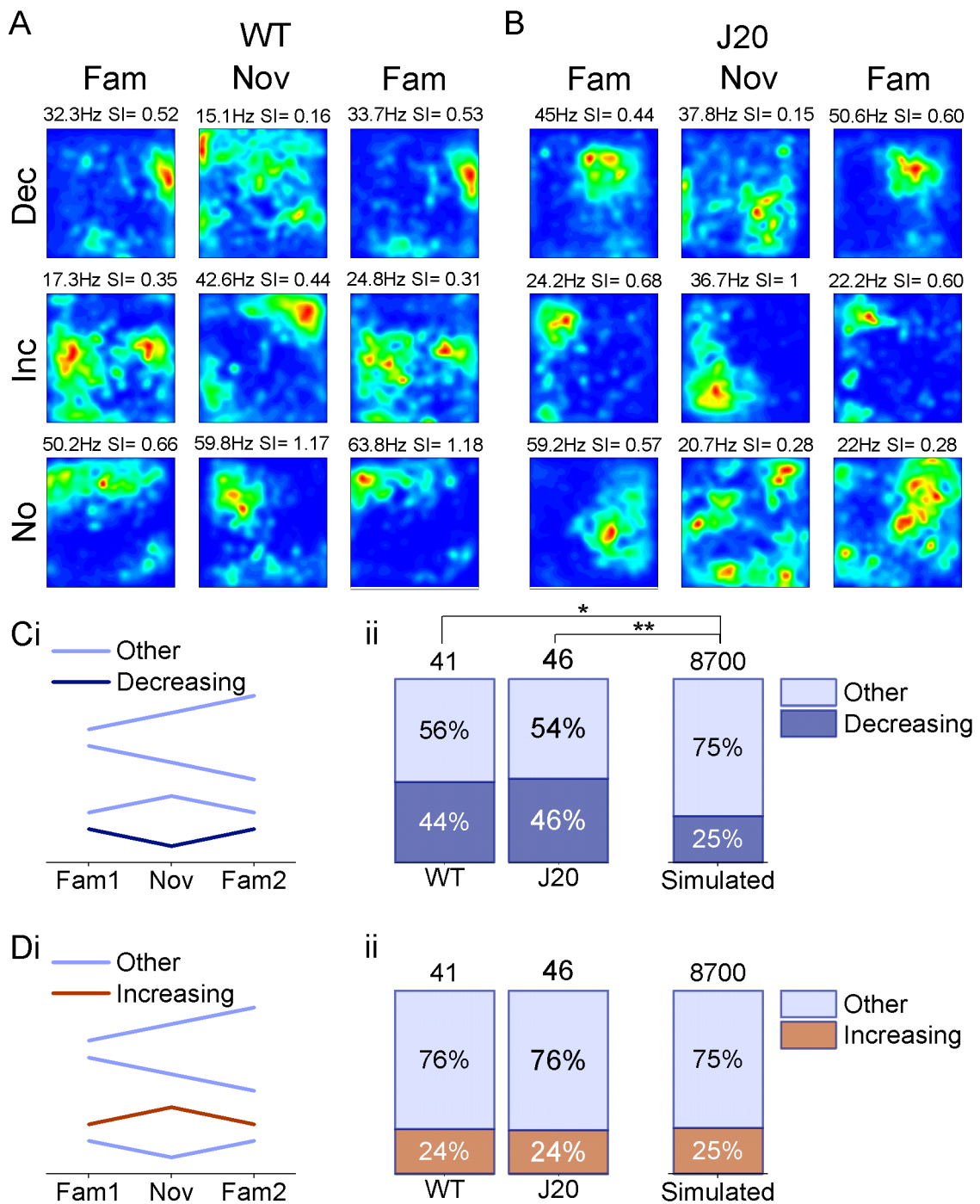


Figure 4.43 WT and J20 mice show a higher proportion of decreasing cells conveying significant spatial information than the simulated data. **A)** Examples of the spatial firing patterns of cells conveying significant spatial information for the three trials for a decreasing cell (dec), an increasing cell (inc) and a cell showing no differences due to context (no) in WT mice. Peak firing rate and spatial information (SI) are shown above the plot. **B)** Examples of the spatial firing patterns of cells conveying significant spatial information for the three trials for a decreasing cell (dec), an increasing cell (inc) and a cell showing no differences due to context (top) in J20 mice. Peak firing rate and spatial information (SI) are shown above the plot. **C)** Example patterns of decreasing cells (dark blue) and other cells (light blue), which encompasses increasing and no-changes cells **(i)**,

proportions of decreasing and other cells in both genotypes compared to the simulated proportions (ii). **D**) Example patterns of increasing cells (orange) and other cells (light blue), which encompasses increasing and no-changes cells (i), proportions of increasing and other cells in both genotypes compared to the simulated proportions (ii). Numbers above bars represent the total n number. (* $p \leq 0.05$, ** $p \leq 0.01$, *** $p \leq 0.001$)

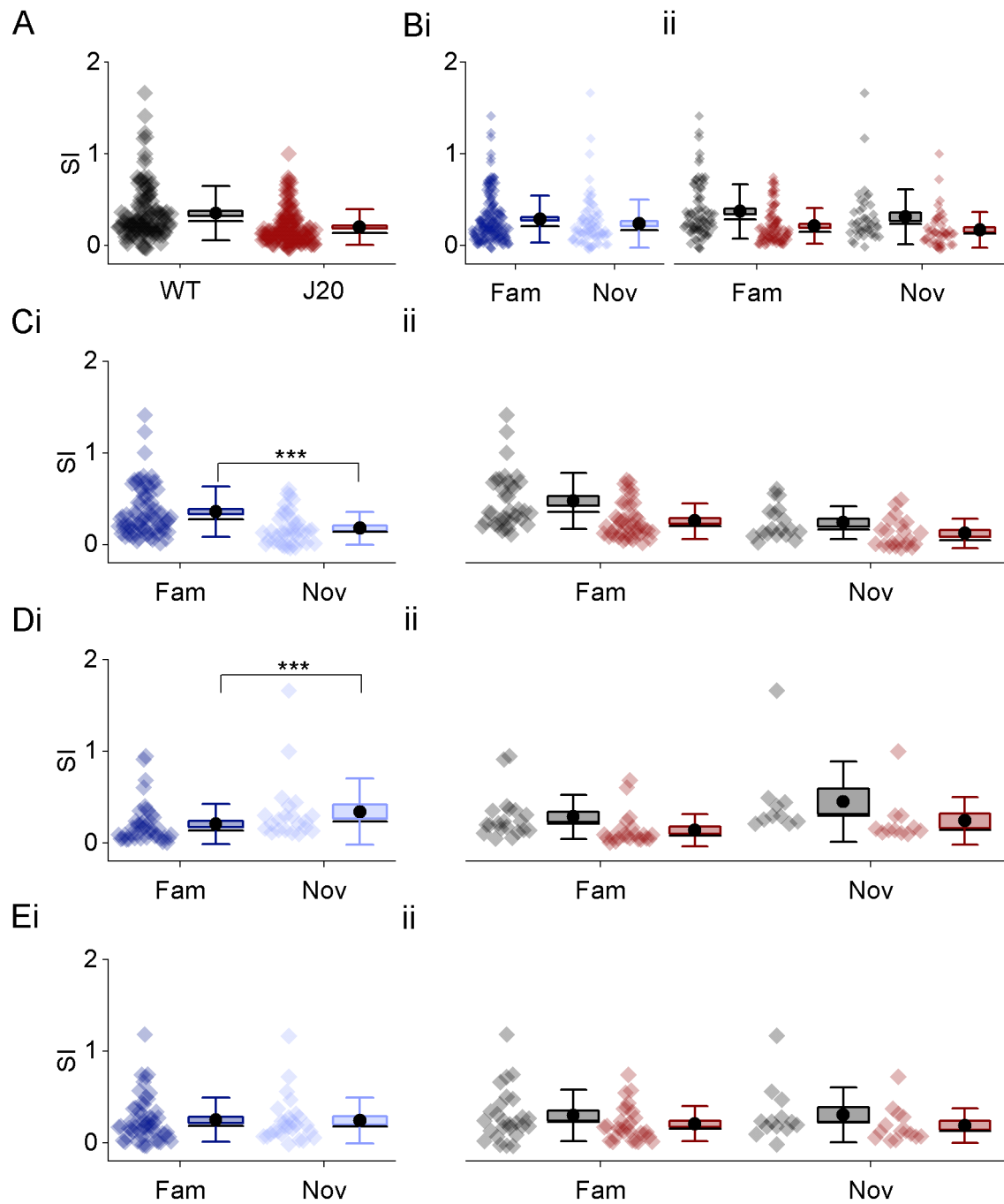


Figure 4.44 The spatial information score of cells conveying significant spatial information are similar between WT and J20 mice.

A) Pooled spatial information scores by genotype. **B)** Pooled spatial information scores of all cells by context (**i**) and by context in WT (black) and J20 (red) mice (**ii**). **C)** Pooled spatial information scores of decreasing cells by context (**i**) and by context in WT (black) and J20 (red) mice (**ii**). **D)** Pooled spatial information scores of increasing cells by context (**i**) and by context in WT (black) and J20 (red) mice (**ii**). **E)** Pooled spatial information scores of cells showing no changes by context (**i**) and by context in WT (black) and J20 (red) mice (**ii**). The data shown in **A**, **B**, **C**, **D** and **E** is the same data replotted separately. Box plots: box corresponds to the mean \pm

SEM, the circle to the mean, the line to the median and the whiskers to the SD. (* $p \leq 0.05$, ** $p \leq 0.01$, *** $p \leq 0.001$)

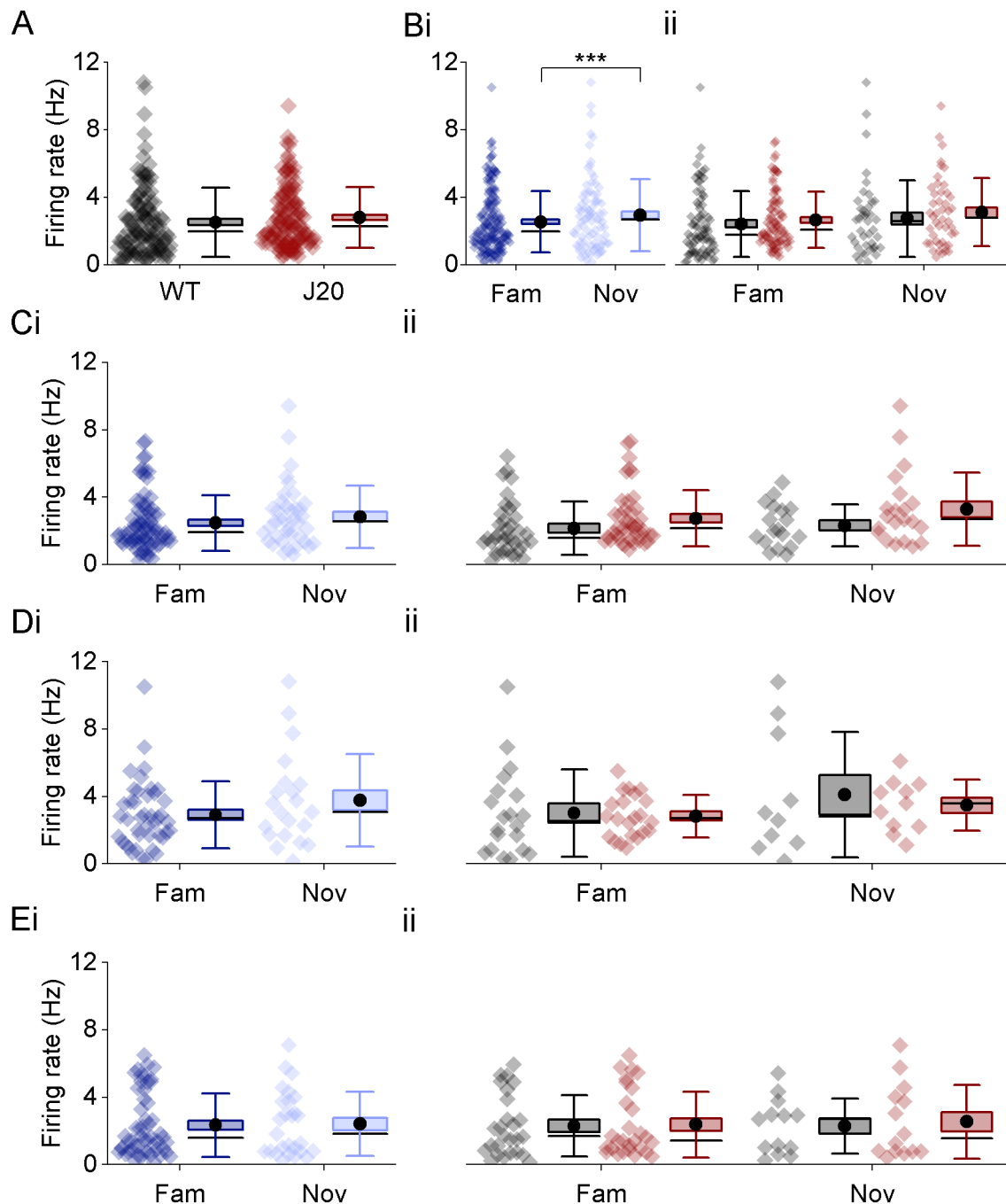


Figure 4.45 The firing rate of cells conveying significant spatial information show no changes between genotypes. **A)** Pooled firing rate by genotype, **B)** Pooled firing rate of all cells by context (**i**) and by context in WT (black) and J20 (red) mice (**ii**). **C)** Pooled firing rate of decreasing cells by context (**i**) and by context in WT (black) and J20 (red) mice (**ii**). **D)** Pooled firing rate of increasing cells by context (**i**) and by context in WT (black) and J20 (red) mice (**ii**). **E)** Pooled firing rate of cells showing no changes by context (**i**) and by context in WT (black) and J20 (red) mice (**ii**). The data shown in **A**, **B**, **C**, **D** and **E** is the same data replotted separately. Box plots: box corresponds to the mean \pm SEM, the circle to the mean, the line to the median and the whiskers to the SD. (* $p \leq 0.05$, ** $p \leq 0.01$, *** $p \leq 0.001$)

4.3.12. Number of MEC cells passing multiple criteria

Overall, WT and J20 mice exhibited a similar proportion of cells satisfying one criterion, single class cells, and those satisfying multiple criteria, conjunctive cells ($p = 0.90$, Fisher's exact test, Fig. 4.46A). Speed sensitive cells showed a different distribution of single class and conjunctive cells between both genotypes ($p = 0.04$, Fisher's exact test, Fig. 4.46B). In a similar manner, differences in the distribution of HD sensitive cells ($p = 0.015$, Fisher's exact test, Fig. 4.46C) were observed. On the other hand, cells showing grid periodicity ($p = 0.11$, Fisher's exact test, Fig. 4.46E) and border sensitive cells ($p = 0.39$, Fisher's exact test, Fig. 4.46D) displayed a similar distribution in WT and J20 mice.

However, a caveat to these results is that for all cell types beside speed cells, the n numbers are relatively low and so it should be taken into consideration.

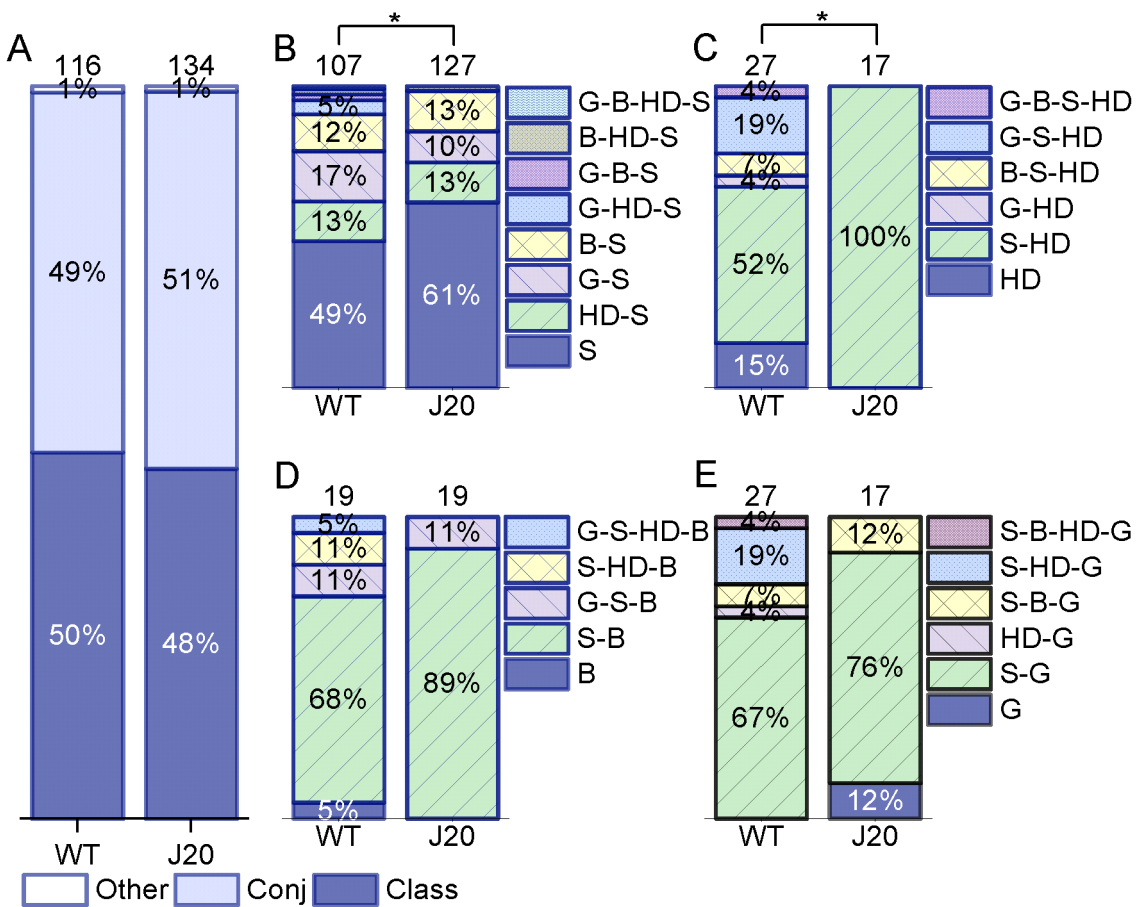


Figure 4.46 The proportion of single class and conjunctive cells is similar in WT mice and J20 mice. A) Proportions of cells classified as single class, conjunctive and other, B) Conjunctive and single class proportions of speed sensitive cells, C) of HD sensitive cells, D) of border sensitive cells and E) of cells with grid periodicity. Numbers above bars represent the total n number. (* p ≤ 0.05, ** p ≤ 0.01, * p ≤ 0.001)**

4.4. Discussion

4.4.1. Summary

This study aimed to provide an insight into the changes that may occur due to novelty in the properties of a variety of MEC subclasses of cells, which was further explored in J20 mice.

The results of this study are the first to show a reduction in the frequency of cell rhythmicity in J20 mice, which also affected putative interneurons, ultimately identifying potential mechanisms for memory and spatial navigation impairments in these mice.

Interestingly, speed sensitive cells, border sensitive cells and cells conveying spatial information were observed to respond to novelty significantly above what would be expected by chance which, to my knowledge, has not been described in literature.

4.4.2. Layer effects in MEC recordings

Although MEC layer II was targeted for these recordings, this was not always achieved. Histological images showed that two probes, one in each genotype, were clearly implanted in layer III (Fig. 4.2). Another probe was found to be potentially in layer III in a J20 mouse, with the uncertainty stemming from the size of the electrolytic lesion.

Studies often include combined data of both MEC layers II and III for analysis in mice (Fyhn *et al.*, 2008; Giocomo *et al.*, 2014; Gil *et al.*, 2018; Jun *et al.*, 2020). However, other studies have identified relevant differences between these two layers. A large proportion of cells exhibit strong phase-locking to the ongoing theta frequency oscillations in the MEC (Solstad *et al.*, 2008; Schmidt-Hieber and Häusser, 2013; Kropff *et al.*, 2015). While MEC layer II neurons display a strong preference for the trough of theta, neurons in layer III exhibit a greater variability in the phase preference (Quilichini, Sirota and Buzsáki, 2010). In addition,

neurons located in layer III exhibit less theta modulation than neurons in layer II (Quilichini, Sirota and Buzsáki, 2010; Burgalossi *et al.*, 2011). Consistently with these studies, these three animals showed a lower proportion of theta modulated cells, when compared to all other animals. Therefore, these probes were assumed to be in layer III when analysing the results presented in this chapter.

To account for layer variability, whenever possible, mixed models were used to analyse the data presented in this chapter. These models allow for the consideration of hierarchical structures in the data, cells within animals, as well as unobserved heterogeneity between different animals. In addition, layer was included as a fixed effect when this significantly improved the fit of the models.

4.4.3. Anxiety levels and hyperactivity in J20 mice

While some studies have reported reduced anxiety levels in J20 mice when exploring the open arms of an elevated plus maze (Chin *et al.*, 2005; Fujikawa *et al.*, 2017), others have reported normal anxiety levels (Wright *et al.*, 2013; Etter *et al.*, 2019). Although the behavioural experiment carried out in this chapter did not include specific anxiety testing, the time mice spent next to the walls of the open arena and in the centre can also be used as an indicator of anxiety (Simon, Dupuis and Costentin, 1994; Seibenhener and Wooten, 2015). The tendency to stay near the walls of the open arena, which is denominated thigmotaxis, was measured as the time spent within 15 cm from the walls. No differences were observed between both genotypes in this study. However, the results presented in chapter 3 showed reduced levels of anxiety in J20 mice. All mice were food restricted and trained to search for food pieces in the study presented in this chapter, whereas mice were not food restricted and explored freely the open arenas in the experiment described in chapter 3. This poses an important design difference, as in the experiment presented here mice were more encouraged to explore the centre of the arena, which could mask anxiety-induced thigmotaxis. Thus, it is not clear whether the J20 mice included in this study showed signs of abnormal anxiety levels.

Hyperactivity has also been reported in J20 mice (Cheng *et al.*, 2007; Wright *et al.*, 2013; Fujikawa *et al.*, 2017). Although the results presented in this chapter showed no differences in the running speed between both genotypes, all mice in this study were tethered during the exploration of the open arenas, which may affect running speed.

4.4.4. The slope of theta power is modulated by novelty

Theta frequency oscillations are associated with memory and spatial navigation. The increase in theta frequency in relation to running speed has been well studied in different areas of the brain such as the MS, the hippocampus and the MEC (Hinman *et al.*, 2011; Wells *et al.*, 2013; Chen *et al.*, 2016). The results presented in this chapter showed that the slope of theta frequency was not affected by novelty. This contrasts to what has been previously reported in the hippocampus and the MEC of rats, where there was an increase in the slope of theta frequency during the exploration of familiar environments (Newman *et al.*, 2013; Wells *et al.*, 2013).

In this chapter, a strong decrease in the slope of theta power with novelty was observed instead, which occurred equally in both genotypes. Literature has pointed towards an overall theta power increase during the exploration of novel environments in the hippocampus (Penley *et al.*, 2013). However, this increase has also been reported as not reliable (Wells *et al.*, 2013). In humans, theta power has been reported to increase during movement initiation in familiar environments when compared to novel ones in the MTL (Kaplan *et al.*, 2012). Furthermore, theta power is higher in goal-directed navigation than in aimless navigation in humans (Cornwell *et al.*, 2008). Theta power is also higher during decision making periods and before a correct choice in rats (Belchior *et al.*, 2014). Together, these studies may suggest a possible role of theta frequency oscillations in memory retrieval of spatial information, which is further supported by the data presented here. Furthermore, these results indicate that J20 mice display normal functioning of theta activity associated to memory retrieval.

4.4.5. The slope of high gamma power

In the previous chapter, a strong increase in the slope of high gamma power was observed in WT mice but not in J20 mice as the environment became more familiar. In contrast, the results presented here show the opposite, with high gamma power slopes showing a decrease with novelty in J20 mice but no changes in WT mice. High gamma frequency oscillations have been related to the encoding of new information in CA1 (Kemere *et al.*, 2013; Zheng *et al.*, 2016), and are likely driven by MEC inputs (Colgin, Denninger, Fyhn, Hafting, Bonnevie, Jensen, M.-B. Moser, *et al.*, 2009; Kemere *et al.*, 2013). It is therefore possible that the increase in the slope of high gamma power observed in the previous results was due to an increase of spatial information encoding rather than to increased familiarity. Furthermore, high gamma slopes have been reported to decrease with familiarity in the MEC, mirroring the same effect observed in CA1 (Kemere *et al.*, 2013). A key difference between the previous experimental design and the one presented in this chapter is the length of the experiment. While in the previous experiment mice were exposed a total of 6 times (2 trials x 3 days) to the familiar arena before the familiar trial, in this experiment all mice were exposed a minimum of 8 times over for a minimum of 8 days to the familiar arena before the experiment. Considering that this was the minimum number of trials, and that this experiment was performed twice, the level of familiarity reached in this study was likely to be significantly higher than in the previous study. From the data showed in this thesis, it is apparent that a delay in the increase of high gamma power slope is present in initial recordings. As high gamma power slopes decrease with familiarity in the MEC, it is possible that in the experiment presented here, the slope is considerably depleted due to the achieved level of familiarity. Therefore, the potential exists that little differences could be seen between a highly familiar exposure and the initial novel exposure.

As mentioned above, the slope of high gamma power decreased with novelty in J20 mice. These results could imply that while WT mice are capable of keeping a basal level of memory encoding in the initial exposure to the novel arena, J20 mice experience a decline. This could link back to the previous results chapter in

which the high gamma power slope did not increase during the familiar exposures in J20 mice, suggesting deficits in the encoding of new information.

4.4.6. Phase amplitude coupling between theta and high gamma frequency oscillations

It has been observed that PAC between theta and gamma frequency oscillations increases with running speed in the hippocampus (Chen *et al.*, 2011). Although a recent study showed that J20 mice exhibit normal theta-high gamma PAC in the hippocampus (Etter *et al.*, 2019), theta-gamma PAC has been related to memory processing (Tort *et al.*, 2008, 2009; Canolty and Knight, 2010) and it is possible that the slope resulting from its relationship with running speed is modulated by the novelty of the context. Supporting this, the data presented in the previous chapter showed an increase in the slope of theta-high gamma PAC in the most familiar trial when compared to the second novel trial. However, no differences were found between both genotypes. The data from theta and high gamma frequency oscillations, presented in the previous chapter and here, suggest that the experiment presented in this chapter achieved a higher level of familiarity. Therefore, this experiment studies the effects of context on the slope of theta-high gamma PAC in a more familiar set up. In agreement with the previous results, PAC slope decreased during the exploration of the novel context in both WT and J20 mice. It has been shown that theta power, but not high gamma power, influences the strength of theta-gamma PAC (Canolty *et al.*, 2006; Tort *et al.*, 2009), so that the decrease with novelty of the theta power slope could account for the decrease observed in theta-gamma PAC. Together, these results show a reduction on theta-high gamma PAC with novelty which occurs equally in WT and J20 mice, suggesting no alterations in theta-high gamma PAC in the MEC of J20 mice.

4.4.7. TMI analysis provides less restricted criteria to classify theta modulated cells

Consistent with literature (Quilichini, Sirota and Buzsáki, 2010; Burgalossi *et al.*, 2011), initial analysis of theta modulation with the TMI identified that layer III cells have a lower frequency of rhythmicity, are mainly coupled to the peak of the theta wave and are less strongly modulated by the ongoing theta oscillations. Theta modulation was additionally analysed with a more recent method, which applies an MLE to detect significant rhythmic cell firing and the frequency of this rhythmicity (Climer *et al.*, 2015; Hinman *et al.*, 2016). This MLE analysis provided several advantages over the TMI analysis. The MLE method allowed for a more sensitive detection of cell rhythmicity on cells with low firing rates. Furthermore, this method involved a statistical comparison between a flat and a rhythmic fit of the data to determine significant cell rhythmicity, which is more appropriate than the arbitrary threshold used with the TMI model (Langston *et al.*, 2010). The proportion of cells that passed the criteria of the MLE method was reduced. The MLE analysis highlighted that there was a lower proportion of theta modulated cells in layer III, suggesting that the majority of cells that did not pass the criteria were located in this layer. The MLE analysis provided stronger criteria when classifying theta modulated cells, thus it was preferred and will be used in the rest of this discussion.

Interestingly, including layer as a factor decreased the fit of the mixed model when analysing the frequency of the rhythmicity and the strength of the modulation, suggesting the irrelevance of this factor on these measurements. Therefore, it was concluded that layer had no effect on these measurements and further discussions of these results will be in the following section.

4.4.8. J20 cells exhibit lower frequency of the cell rhythmicity than WT cells

The results of this study showed that J20 cells had a lower frequency of rhythmicity than WT cells. However, it is important to consider that the recording locations of J20 cells were significantly more ventral than the ones of WT cells. It

has been shown that both the frequency of subthreshold membrane potential oscillations and the resonance frequency of stellate cells decrease at more ventral locations in the MEC dorsoventral axis (Giocomo *et al.*, 2007). Thus, the estimated distance from the MEC border for each cell was also considered. Adding the distance from the MEC border to the model did not improve its fit, suggesting that this variable has an irrelevant effect in the frequency of the modulation in this dataset. In addition, there was not a significant correlation between the frequency of the modulation and the distance from the border for neither WT nor J20 cells, further suggesting that these results are due to genotype. The results of this chapter suggest that J20 cells fire at a slower pace than WT cells at a baseline level.

In the results of this chapter, the modulation strength was greater in putative interneurons, supporting observations of GABAergic interneurons driving theta oscillations in the MEC and the hippocampus (Gonzalez-Sulser *et al.*, 2014; Amilhon *et al.*, 2015). In addition, no differences were observed between genotypes, suggesting that interneurons are equally modulated by theta oscillations in J20 mice. Putative principal cells showed a higher frequency of modulation than putative interneurons in both WT and J20 mice, which is consistent with what has been observed in the hippocampus (Geisler *et al.*, 2010). However, the general reduction in the frequency of the cell rhythmicity also applied to J20 putative interneurons, which may suggest impairments in these cells.

A recent study showed that cooling of the MS resulted in a decrease in the frequency and power of theta oscillations, along with a reduction of the frequency of pyramidal neurons and interneurons rhythmicity, in the hippocampus (Petersen and Buzsáki, 2020). In conjunction with these physiological effects, MS cooling also resulted in memory impairment. Reductions in the frequency of the cell rhythmicity have been observed in different studies; for example, during MS inactivation (Brandon *et al.*, 2011; Koenig *et al.*, 2011) and, interestingly, with novelty in MEC cells with significant grid periodicity (Barry *et al.*, 2012). In these studies, the decrease in the frequency of the rhythmicity concurred with a reduction in the grid score of cells with grid periodicity. In addition to the general reduction observed in J20 mice cells, the results presented here also show that

the frequency of the cell rhythmicity broadly decreases with novelty for all cells, independently of the genotype. On the other hand, no differences in grid scores were observed between WT and J20 mice. However, the analysis of cells with grid periodicity performed in this chapter highlighted a very low percentage of these cells, which did not exceed the proportions expected by chance in J20 mice. This raises concerns whether these are true grid cells. Thus, the data presented here does not allow for strong conclusions to be drawn on if changes in grid scores occur in J20 mice. In addition, no clear changes in grid scores were observed due to novelty, with some cells increasing their scores and others decreasing it. However, the effects of novelty were observed in the stability of the rate maps of cells with grid periodicity, which were stable between both familiar trials for both WT and J20 cells. In addition, an increase of the grid scale was observed in WT cells, which has been previously described in rats (Barry *et al.*, 2012). Interestingly, this grid scale increase was only detected in WT cells but not in J20 cells, suggesting impairments on these cells in J20 mice.

Both cholinergic and GABAergic inputs from the MS onto the MEC are likely to play a role in memory processing, working in coordination to ensure an appropriate balance between excitation and inhibition during the exploration of novel and familiar environments. GABA release has been shown to increase with familiarity in the cortex of rats, whereas acetylcholine release increases with novelty in both the cortex and the hippocampus of rats (Giovannini *et al.*, 2001). Furthermore, while activation of GABA_A receptors prevents taste memory encoding, inhibiting these receptors prevents the memory retrieval of a familiar taste (Rodríguez-García and Miranda, 2016). Interestingly, the inhibition of these receptors was accompanied by an increase of acetylcholine levels. Furthermore, something similar has been observed in the hippocampus, where the activity of FS putative interneurons increase with familiarity (Frank, Stanley and Brown, 2004).

Acetylcholine has been shown to decrease the resonance frequency of MEC stellate cells (Heys, Giocomo and Hasselmo, 2010), which could lead to the reduction in the frequency of rhythmicity found in this chapter. Furthermore, it has been shown that the frequency of the rhythmicity of theta modulated non-spatial MEC cells decreases with the modulation of the MS cholinergic neurons

excitability, without affecting the strength of theta modulation (Carpenter, Burgess and Barry, 2017). Increases in acetylcholine release during the exploration of the novel arena may explain the decrease in the frequency of the modulation with novelty in all cells. However, it may not explain the general reduction in the frequency of the modulation observed in J20 cells. No evidence has been found of a decrease in the number of cholinergic neurons, or changes in their normal activity, in the MS of ~5 mo J20 mice (Brown *et al.*, 2018). In agreement with this study, a loss of hippocampal cholinergic innervation and a reduction of MS cholinergic activity has been reported at ~13 months but not at 6 months in J20 mice (Aucoin *et al.*, 2005).

On the other hand, a reduction of MS GABAergic projections onto the hippocampal neurons and in the number of synaptic boutons has been observed in 8 mo J20 mice (Rubio *et al.*, 2012). Considering that the MS sends GABAergic projections to both the hippocampus and the MEC (Gonzalez-Sulser *et al.*, 2014; Justus *et al.*, 2017), this reduction could also be true for the MEC. In addition, the theta modulation data presented here shows a reduction in the frequency of putative interneurons rhythmicity in J20 mice, further supporting GABAergic deficits. Furthermore, a recent study showed that spatial memory performance of J20 mice improves when low gamma oscillations are increased in the hippocampus, by stimulating FS interneurons in the MS (Etter *et al.*, 2019). These studies suggest a link between GABAergic deficits and the spatial memory impairments observed in these mice and could potentially explain the reduction in the frequency of rhythmicity of J20 cells observed in this study.

Alternatively, changes in the theta frequency intercept have been linked to anxiety, with systemic administration of anxiolytic drugs reducing it in the hippocampus (Wells *et al.*, 2013) and the MEC (Monaghan, Chapman and Hasselmo, 2017). Furthermore, anxiolytic drugs also seem to reduce the frequency of the modulation of cells with grid periodicity in the MEC, without affecting the strength of this modulation (Monaghan, Chapman and Hasselmo, 2017). In this chapter, a trend towards a lower intercept in the relationship between the frequency of theta oscillations and running speed was observed in J20 mice. Furthermore, although the mice included in this study appeared to not exhibit signs of either lower or higher anxiety levels, the results in chapter 3

supported reduced anxiety in J20 mice. However, this reduction in anxiety was not accompanied by a significant reduction, nor a trend, in the theta frequency intercept of J20 mice. On the other hand, although reductions in the theta frequency slope have been related to novelty (Newman *et al.*, 2013; Wells *et al.*, 2013), some anxiolytic drugs also seem to reduce the theta frequency slope in the MEC (Monaghan, Chapman and Hasselmo, 2017) but not in the hippocampus (Wells *et al.*, 2013). In the results presented in this thesis, theta frequency slopes were not lower in J20 mice. Furthermore, the theta frequency slope was not affected by novelty and a decrease in the theta power slope was observed instead. Together, these results may suggest a higher complexity on the effects of anxiety and novelty on theta frequency oscillations than previously hypothesised, whose mechanisms still need to be elucidated.

Both anxiety and novelty are able to affect the frequency of the modulation of MEC cells (Barry *et al.*, 2012; Monaghan, Chapman and Hasselmo, 2017), but only novelty appears to affect the scale of grid fields. In addition, both anxiolytic drugs and cholinergic modulation seem to affect the theta frequency intercept in the MEC. It has been shown that cholinergic blockade increases the theta frequency intercept (Newman *et al.*, 2013) and that MS cholinergic modulation reduces peak theta frequency in the MEC, which also increases anxiety-like behaviour (Carpenter, Burgess and Barry, 2017). Relevantly, anxiolytic drugs have been reported to impair spatial memory in different studies (Zanotti *et al.*, 1994; Hogan *et al.*, 2005). These deficits could be related to their effects reducing the theta frequency intercept and the frequency of modulation. In support of this, reduced theta frequency, along with a reduction of the frequency of cell rhythmicity, has been linked to memory impairments (Petersen and Buzsáki, 2020). Ultimately, the reduction in the frequency of modulation observed in J20 mice could be linked to the spatial memory impairments reported in these mice.

4.4.9. J20 mice cells show normal speed modulation

Around 70-80% (Hinman *et al.*, 2016) of cells in the MEC show significant speed sensitivity, which matches with the results observed in this chapter. The results

in this chapter indicate that the proportion of speed sensitive cells and their speed scores are similar in WT and J20 mice. Speed scores have been reported to increase when the MS is inactivated (Hinman *et al.*, 2016), but this was not replicated in a later study (Dannenberg *et al.*, 2019). However, both studies suggest that MEC speed sensitive cells encode speed information independently from MS inputs. It is therefore possible that the decrease in the frequency of modulation, observed in theta modulated cells in J20 mice, does not affect speed sensitive cells in the MEC. These results suggest that the speed encoding of speed sensitive cells is not affected in J20 mice.

4.4.10. HD sensitive cells show no differences between genotypes

Studies report a variable number of HD sensitive cells in the superficial layers of the MEC, varying between 11% to 40% (Giocomo *et al.*, 2014; Chen *et al.*, 2018; Ye *et al.*, 2018). HD sensitive cells seem to be mainly confined to layer III (Miao *et al.*, 2017) but they can also be found in layer II (Giocomo *et al.*, 2014). The proportions of HD sensitive cells that were recorded in this study are within the proportions reported in other studies and were similar between both genotypes. In addition, adding layer effect to the model did not improve the fit, which suggests that layer has an irrelevant effect in the proportion of HD sensitive cells in this dataset.

The results presented in this chapter suggest that the normal function of HD sensitive cells is not altered in J20 mice; as they displayed a similar proportion of HD sensitive cells, comparable mean resultant vector lengths and firing rates to what was observed in WT mice. As observed in speed sensitive cells, during MS inactivation, HD sensitive cells retain their selectivity but there is a significant reduction in the spatial periodicity of grid cells (Brandon *et al.*, 2011; Koenig *et al.*, 2011). However, inactivation of HD cell activity in the anterior thalamic nuclei results in the decrease of grid and HD scores in the MEC cells, without alterations in theta frequency oscillations (Winter, Clark and Taube, 2015). Together, this suggests that, while MS inputs and theta frequency oscillations are necessary to keep the spatial periodicity of grid cells, HD sensitive cells seem to be able to

function normally without these inputs. It is therefore possible that the impairments described in the frequency of modulation, observed in theta modulated cells, do not affect HD activity.

Previous studies reported that HD sensitive cells display stable directional tuning curves between trials in the MEC and the anterior thalamic nuclei of rats (Taube, 1995; Sargolini *et al.*, 2006). However, HD sensitive cells in the anterior thalamic nuclei of mice seem to display lower stability than what has been seen in rats between trials (Yoder and Taube, 2009). In addition, stable and unstable HD sensitive cells within the same trial have been described in the MEC of mice (Chen *et al.*, 2016). HD stability was analysed between both familiar trials, by looking at the phase shift of the preferred direction and the correlation between the directional tuning curves of both trials. No differences were found when comparing between genotypes. However, the phase shift data seemed to follow a bimodal distribution, suggesting that there were two different populations of HD sensitive cells. One population with relatively small phase shifts and higher correlation between trials, therefore more stable, and another less stable with large phase shifts and lower correlation. In both genotypes, the proportion of more and less stable cells was the same. These results are consistent with what has been previously observed in mice, and it is likely that the two populations correspond to the within-trial stable and unstable HD sensitive cells reported in previous studies (Chen *et al.*, 2016).

In summary, as there were no significant changes in the normal functioning of HD sensitive cells between genotypes, it can be concluded that the impairments to theta modulated cells does not influence the activity of HD sensitive cells. However, as the n number of HD sensitive cells are relatively low, it is recommended that further studies are performed to add further evidence and increase confidence in this conclusion.

4.4.11. The number of cells with grid periodicity is lower than expected

The results in this chapter showed a very low proportion of MEC cells with significant grid periodicity (WT: 4%, J20: 5%, Fig. 4.29Ci), when analysed with

the Langston method. On the other hand, the Sargolini method showed a higher proportion of these cells in WT mice but not in J20 mice (WT: 10%, J20: 5%, Fig. 4.33Ci), with J20 mice exhibiting a significantly lower number than WT mice. Specifically in J20 mice, these results contrast with studies in which approximately 10-20% of cells show grid periodicity (Giocomo *et al.*, 2011; Perez-Escobar *et al.*, 2016; Diehl *et al.*, 2017; Miao *et al.*, 2017; Munn *et al.*, 2020). Grid cells can be recorded in both layer II and layer III in mice (Fyhn *et al.*, 2008; Giocomo *et al.*, 2011; Miao *et al.*, 2017), thus recording positions are unlikely to be the source of this discrepancy. In addition, most of the WT recordings were done in layer II. Therefore, the reason behind the low numbers of these cells observed in the results is currently unclear. However, in some studies it can be seen that while a large number of cells with grid periodicity are recorded from certain animals, little to none are recorded from others (Giocomo *et al.*, 2011; Carpenter, Burgess and Barry, 2017). There is the potential that the lack of grid cells recorded in this experiment is purely due to chance. It is also possible that the spacing of some recorded grid cells was too large for the size of the open arenas used (86.5cm x 86.5cm), as cells with a single or two firing fields have been observed in the data presented (Fig. 4.42 and Fig. 4.43) (Fyhn *et al.*, 2008).

4.4.12. Border sensitive cells and cells conveying significant spatial information show no differences between genotypes

About 5-10% of cells in the MEC are classified as border sensitive cells (Solstad *et al.*, 2008; Diehl *et al.*, 2017; Ye *et al.*, 2018; Høydal *et al.*, 2019), which matches with the proportions observed in this study. Spatial non-grid cells, which include border sensitive cells and other spatially modulated cells, appear to not be as affected as cells with grid periodicity by the inactivation of the MS (Koenig *et al.*, 2011), which suggests that these cell functional subtypes should not be affected by abnormal MS GABAergic activity. In agreement with this, no effects of genotype were observed in border sensitive cells and cells conveying spatial information in this study, suggesting that these functional subtypes are not affected in J20 mice.

4.4.13. A proportion of some MEC cell subtypes is affected by novelty

A comparison of the different scores between the familiar and novel trials, highlighted that not all cells behaved in the same way. Some cells would increase their score in the novel context, others would decrease, and some would not show any type of change related to this new context. There is a potential that these variations in scores occurred at random. The approach taken in this study was to simulate randomly changing scores for the novel trial and the second familiar trial. Although no limitations were imposed on this simulation, 4 outcomes were statistically probable: (1) the score is lower in the novel trial than in both familiar trials, (2) the score is higher in the novel trial than in both familiar trials, (3) the score would increase in the novel trial and further increase in the second familiar trial, and (4) the score would decrease in the novel trial and further decrease in the second familiar trial. Therefore, each option matched the statistically expected proportions of approximately 25% each. To study if the proportion of decreasing cells was above what could be expected purely by chance, the proportion of observed decreasing cells were compared to the simulated one (outcome 1). The same process was followed to compare the proportion of increasing cells (outcome 2).

It was confirmed that the proportions of decreasing cells were above chance for the speed sensitive cells, border sensitive cells and cells conveying spatial information. In contrast, the proportions of increasing cells were not above chance in any of the cell types studied. HD sensitive cells were the only functional subtype which did not show a significant proportion of decreasing cells. Literature has shown that the activity of speed sensitive cells, border sensitive cells, HD sensitive cells and cells conveying spatial information is linked to allocentric cues and is affected by context changes (Sargolini *et al.*, 2006; Solstad *et al.*, 2008; Perez-Escobar *et al.*, 2016; Diehl *et al.*, 2017; Campbell *et al.*, 2018; Munn *et al.*, 2020). In the study presented here, all animals were brought inside their home cage to the novel recording room, making likely that a disorientation occurred. It has been shown that when animals navigate themselves from one environment to a new one, path integration skills are able to sustain similar preferred directions of HD sensitive cells in the new environment (Yoder *et al.*, 2011). However, when

animals are taken from one environment to another, HD sensitive cells experience random shifts in their preferred direction (Yoder *et al.*, 2011). When both environments are familiar, fast reorganization of the activity of these functional cell subtypes should be expected, as neural connections are pre-established. However, the establishment of new neuronal connections, which likely involves a disorganization and reorganization of these signals, is expected when animals are taken to a non-recognised environment, as seen in HD sensitive cells (Yoder *et al.*, 2011). This process may be associated to the effects of novelty observed on cells with grid periodicity (Barry *et al.*, 2012). It is possible that this process is also associated to effects on border sensitive cells and cells conveying spatial information. Potentially, this could lead to the decrease of border scores and spatial information with novelty observed in the results presented here. On the other hand, HD sensitivity was not affected by novelty. It has been shown that the preferred direction of HD sensitive cells is associated to allothetic cues (Taube, 1995; Sargolini *et al.*, 2006) and these associations appear to develop rapidly in novel environments (Goodridge *et al.*, 1998), suggesting a fast reorganization of these signals.

Speed cells were initially suggested to provide an invariant speed signal (Kropff *et al.*, 2015). However, the results of several studies suggest that the response of cells with grid periodicity to context changes is coupled to the response of speed sensitive cells (Chen *et al.*, 2016; Perez-Escobar *et al.*, 2016; Campbell *et al.*, 2018; Munn *et al.*, 2020). For example, the disruption of grid periodicity during total darkness (Chen *et al.*, 2016; Perez-Escobar *et al.*, 2016) is accompanied with a decrease in the speed score and firing rate of speed sensitive cells (Perez-Escobar *et al.*, 2016). In virtual reality navigation, mismatches between the real distance travelled and the virtual distance travelled produces an asymmetrical response in both cells with grid periodicity and speed sensitive cells. When the virtual distance travelled exceeds the real distance travelled, a phase shift in the grid patterns of cells with grid periodicity and an increase in the slope from the firing rate – running speed relationship of speed sensitive cells is observed. Conversely, when the real distance travelled exceeds the virtual distance travelled, grid fields rescale and the firing rate slope of speed sensitive cells is not affected (Campbell *et al.*, 2018). Furthermore, a recent study has shown that environmental perturbations result in the rescale of both cells with grid periodicity

and speed sensitive cells. In more detail, compressing the environment results in an asymmetrical rescale of grid patterns, which decreases the spacing only in the compression axis. Matching this asymmetry, it also results in an increase in the slope and intercept of the firing rate vs running speed relationship of speed sensitive cells, which is greater in the compression axis. In the same manner, expanding the environment results in a symmetrical rescale of grid patterns together with a symmetrical decrease in the slope and intercept of the firing rate relationship with running speed of speed sensitive cells (Munn *et al.*, 2020).

The mechanisms leading to the decrease in the speed scores of a proportion of speed sensitive cells with novelty, observed here, remains unclear. It has been shown that cells with grid periodicity respond to the novelty of the environment by expanding their grid fields, which also decrease their stability and become more irregular (Barry *et al.*, 2012). The expansion of grid fields has been related to a loss of resolution on the spatial representation of a given environment (Fiete, Burak and Brookings, 2008; Barry *et al.*, 2012). With the hypothesis that the response of speed sensitive cells and cells with grid periodicity to contextual changes is coupled, it is plausible to also observe an effect of novelty also in the activity of speed sensitive cells. The results presented in this chapter further support a coupled response of cells with grid periodicity and speed sensitive cells.

An interesting aspect of these results is that only part of these cells showed a decrease in their scores during the exploration of the novel context. It has been shown that Ocean MEC cells in layer II participate in context discrimination through their projections into the DG and CA3 (Kitamura *et al.*, 2015). Therefore, it is also necessary to consider that the MEC cell subtypes studied here could show context-specificity and that different combinations of them could be active in distinctive contexts. This is a potential explanation for the decreasing cells observed in the results presented here, as this could be due to context-specificity rather than novelty, or a combination of both. Context-specificity manifests as distinct Ca^{2+} activity depending on the context in Ocean MEC cells in layer II, in around 36% of cells, although a majority show the same level of activity through different environments (Kitamura *et al.*, 2015). Similarly, another study has also shown changes in the firing rate of MEC cell subtypes with context non-metric changes (Perez-Escobar *et al.*, 2016), in which about 35% showed significant

differences. HD sensitive cells have also been reported to change their firing rate when visual landmarks are altered (Kornienko *et al.*, 2018). In contrast, other studies have pointed towards no firing rate changes in HD sensitive cells (Kornienko *et al.*, 2018) and cells with grid periodicity with environmental non-metric changes (Marozzi *et al.*, 2015).

However, the results of this chapter showed no firing rate changes in decreasing cells between the familiar and novel contexts. Furthermore, when a similar approach to the one taken in previous studies (Kitamura *et al.*, 2015; Perez-Escobar *et al.*, 2016) was applied to classify context-specific cells, it was found that none of the speed sensitive cells were classified as context-specific through this method. Interestingly, the proportion of context-specific cells observed in previous studies (Kitamura *et al.*, 2015) was much lower when the two contexts were similar, with only about 9% of cells being context-specific. It is possible that the arenas used in this experiment were perceived as more similar by the mice than the contexts used in the previously mentioned studies, leading to a lower context-specificity. The results presented in this chapter show that the observed decreases in the different scores are not caused by changes in the firing rate of these cells.

It is also possible that context-specificity could manifest as a stronger modulation to different spatial variables in distinctive combinations of cells depending on the environment, which could explain why only a percentage of cells experienced a decrease in their scores with novelty. However, a corresponding proportion of increasing cells would be expected, which was not observed here. It would still be possible that the results observed in this chapter are a combination of novelty and context-specificity effects, in which novelty could explain the low numbers of increasing cells observed. Unexpectedly, the proportion of increasing cells in J20 mice was lower than the one observed in WT mice and in the simulated proportions. These results could hint deficits in the establishment of context-specificity in novel contexts in J20 mice, which further studies could clarify. The experimental design of the study presented in this chapter could have benefited from several exposures to the novel arena, instead of only one, which would have allowed to discriminate between the effects of novelty and context-specificity. If the decrease in the scores of decreasing cells is due to novelty, a progressive

increase should be observed with repeated exposures. On the other hand, if these results are due to context-specificity, the proportion of decreasing cells should remain stable and the proportion of increasing cells would be expected to grow.

In conclusion, the responses towards the novel context observed in this study are likely to be induced by novelty rather than contest-specificity, or a combination of both effects. These results support a growing body of evidence suggesting that speed sensitive cells do not provide an invariant speed signal. Furthermore, these results may indicate that the activity of speed sensitive cells, border sensitive cells and cells conveying spatial information reflect the novelty of the environment. However, both genotypes showed a similar proportion of decreasing cells, which suggest no impairments in J20 mice.

4.5. Conclusions

The primary conclusion of this experiment is that speed sensitive cells, border sensitive cells and cells conveying spatial information are significantly impacted by novelty in the MEC, and this occurs in a similar manner in both WT and J20 mice.

A strong reduction in the slope of theta power with running speed was observed during the exploration of the novel context in both WT and J20 mice. However, a reduced frequency of the modulation of theta modulated cells was observed in J20 mice, which has been linked to both memory impairments and lower levels of anxiety.

Together, these results suggest that J20 mice show no deficits in memory retrieval in this study. However, the reduction in the frequency of the modulation in theta modulated cells could provide mechanisms for the deficits in spatial memory observed in J20 mice.

Chapter 5. General discussion

5.1. Summary of key findings

Chapter 3 investigated the effects of contextual novelty and familiarity on the MEC neuronal networks. Specifically, these effects were studied in theta and high gamma frequency oscillations and their relationship with running speed. It was hypothesised that the theta frequency-running speed slope would become steeper as the familiarization to the context increased in WT mice but not in J20 mice. It was further hypothesised that the high gamma power-running speed slope would decrease, as the familiarity to the context increased, in WT mice but not in J20 mice. Although it was not a specific aim of chapter 4, these effects were also studied to confirm the results obtained in chapter 3. The key findings of these chapters showed the following:

- Both chapters 3 and 4 were consistent in showing that the theta frequency – running speed slope is not affected by the familiarity of the context in the MEC of the mice included in these studies.
- While chapter 3 showed a small reduction in the slope resulting from the relationship between theta power and running speed in the second novel context, chapter 4 showed a more robust reduction of this slope in both WT and J20 mice as they explored the novel context.
- Chapter 3 showed that the slope of high gamma power and frequency vs running speed was reduced in both novel contexts only in WT mice. Contrasting with these results, chapter 4 showed a decrease in the slope of high gamma power during the exploration of the novel environment only in J20 mice, whereas no effects of context were seen in the slope of high gamma frequency.

Chapter 4 further studied the effects of environmental novel and familiar stimuli on the MEC functional cell subtypes involved in these networks in WT and J20

mice. It was hypothesised that the activity of MEC functional cell subtypes reflects the effects of novelty and familiarity observed at the level of neuronal networks in both literature and in this thesis. It was further hypothesised that the deficits observed in high gamma oscillations in the MEC of J20 mice translate into deficits in the activity of these MEC functional cell subtypes. The results obtained in chapter 4 highlighted the following:

- The frequency of the modulation of theta modulated cells was lower in J20 mice than in WT mice.
- The activity of the MEC functional cell subtypes studied here showed no deficits in J20 mice.
- Effects of novelty were observed in a proportion of almost all MEC functional cell subtypes. However, these effects were not seen in HD sensitive cells.

5.2. Deficits in memory processing in J20 mice

The three experiments presented in this thesis are likely to have reached different levels of familiarity to the context, which may have yielded the differences observed in the results. However, high gamma oscillations appeared to be affected in the MEC of J20 mice in the three of them. Although only a trend was observed, the triangular track experiment may have hinted lower slopes of high gamma power in the MEC of J20 mice. The higher number of exposures of the two open arenas experiment boosted the familiarity to the environment, and highlighted that the slope of both the power and frequency of high gamma oscillations increased with repeated exposures in the MEC of WT mice but not of J20 mice. As discussed in chapter 3, these results were initially associated to increased familiarity and thus related to memory retrieval deficits. However, the results presented in chapter 4 contradicted this interpretation. Unexpectedly, these results showed that the slope of high gamma power was higher in the

familiar context in the MEC of J20 mice but not of WT mice. As discussed in chapter 4, this experiment is likely to have reached higher levels of familiarity than the two open arenas experiment presented in chapter 3. A decrease in the high gamma power-running speed slopes with increased familiarity has been previously described in both the hippocampus and the MEC (Kemere *et al.*, 2013), associating greater slopes of high gamma power with memory encoding. If high gamma power slopes decrease as the environment becomes more familiar, it is possible that the two open arenas experiment of chapter 3 was not long enough to observe this process. Furthermore, it is possible that the length of the experiment presented in chapter 4 allowed for a significant depletion of the high gamma power slope associated with memory encoding. The joint consideration of the results presented in this thesis suggests that the slope of high gamma power increases as a result of memory encoding in the MEC, in agreement with literature (Kemere *et al.*, 2013; Zheng *et al.*, 2016), and further suggests memory encoding deficits in J20 mice.

The higher level of familiarity achieved in chapter 4 may also be reflected in the activity of theta oscillations, with the results of this thesis suggesting that the power slope of these oscillations, and not their frequency, is increased in familiar environments in these mice. Furthermore, the modulation of speed sensitive cells, border sensitive cells and cells conveying spatial information was higher in a proportion of MEC cells while animals explored the familiar context. These effects are likely related to memory retrieval rather than encoding, as they were consistent between both explorations of the familiar arena. In addition, a more subtle effect was observed in the slope of theta power in the experiments presented in chapter 3, where the context was likely less familiar to the mice. Furthermore, a role of the power of theta oscillations in memory retrieval has been supported by several studies (Cornwell *et al.*, 2008; Kaplan *et al.*, 2012; Belchior *et al.*, 2014; Bush *et al.*, 2017). The effects of novelty and familiarity on the MEC network oscillations and at the level of single units occurred equally in both WT and J20 mice, which may suggest no impairments related to memory retrieval in the MEC of J20 mice. However, memory retrieval deficits have been observed in these mice (Etter *et al.*, 2019). Interestingly, it has been reported that J20 mice only exhibit memory impairments in the MWM task when the probe trial is performed after 2 days, but show no deficiencies when it is performed after 5

days (Harris *et al.*, 2010). Thus, it is possible that a large number of repeated exposures to the same environment, as performed in chapter 4, could mask memory retrieval deficits.

While MEC and hippocampal high gamma power has been primarily associated to memory encoding, hippocampal low gamma power has been linked to memory retrieval (Kemere *et al.*, 2013; Zheng *et al.*, 2016). A reduction of slow gamma power has previously been reported in the hippocampus (Iaccarino *et al.*, 2016) and the dentate gyrus (Gillespie *et al.*, 2016) of different AD models. Furthermore, reduced hippocampal high gamma power and impairments in high gamma coupling between the MEC and the CA1 region have also been described in an amyloid mouse model (Jun *et al.*, 2020). In J20 mice, both high and low gamma power appears to be reduced in the hippocampus and the parietal cortex (Verret *et al.*, 2012; Etter *et al.*, 2019). These studies, together with the results presented in this thesis, suggest that both memory encoding and retrieval are affected in J20 mice. Abnormalities in gamma frequency oscillations have also been found in AD patients (Stam *et al.*, 2002, 2009; Koenig *et al.*, 2005; Guillon *et al.*, 2017). In the same manner, deficits in both memory encoding and retrieval have been described in AD (Backman, Small and Fratiglioni, 2001; Golby *et al.*, 2005; Lim *et al.*, 2020). Restoring gamma activity through the stimulation of MS FS interneurons at low gamma frequency or by increasing Nav1.1 levels in FS interneurons recues memory impairments in J20 mice (Verret *et al.*, 2012; Magdalena Martinez-Losa *et al.*, 2018; Etter *et al.*, 2019), suggesting that treatments aiming to enhance gamma activity may have the potential to improve memory deficits in AD patients.

5.3. Implications of a lower frequency of the modulation in theta modulated cells

In chapter 4, a reduction in the frequency of modulation of theta modulated cells was observed in the MEC of J20 mice. As discussed in chapter 4, this reduction may have different implications. The scale of grid fields has been associated to the intrinsic frequency of these cells, with lower frequencies of modulation

correlating with larger scales (Giocomo *et al.*, 2007; Barry *et al.*, 2012). However, anxiolytic compounds have been shown to reduce the frequency of the modulation without affecting the scale of grid fields (Monaghan, Chapman and Hasselmo, 2017). Thus, it is possible that cells with grid periodicity are not affected by this reduction. Yet, it is also possible that the reduction of the frequency of the modulation affects the scale of grid fields. In this regard, increases in the size of grid fields and lower grid scores have been reported in cells with grid periodicity in an APP knockin mouse model (Jun *et al.*, 2020), whereas in humans, grid-like activity appears to be reduced in AD genetic carriers (Kunz *et al.*, 2015). Here, although no differences in the scale of grid fields were observed between WT and J20 cells, only WT cells experienced an increase of scale with novelty. This effect has been previously reported in WT animals (Barry *et al.*, 2012) and may highlight deficits in the activity of cells with grid periodicity in J20 mice. Cells with grid periodicity play a key role in spatial navigation, by integrating idiothetic information (Burgess, Barry and O'Keefe, 2007; Burak and Fiete, 2009; Gil *et al.*, 2018) and sensory cues (Fyhn *et al.*, 2007; Perez-Escobar *et al.*, 2016; Diehl *et al.*, 2017). Furthermore, these cells contribute to the formation of hippocampal place fields, and appear to be particularly important for the formation of place fields located far from the borders of the environment (Moser, Kropff and Moser, 2008; Langston *et al.*, 2010; Mallory *et al.*, 2018). Impairments in the normal activity of these cells may contribute the spatial memory deficits observed in AD.

5.4. Limitations and directions for future research

5.4.1. Mouse models of Alzheimer's disease

Mouse models of AD have allowed the investigation of aspects of this disease that otherwise would not be possible, providing an invaluable source of information (Ashe and Zahs, 2010; Webster *et al.*, 2014). However, they are not exempt from limitations. In the last two decades, many therapeutical treatments, which were successful at the preclinical stage, have failed on clinical trials (Mehta

et al., 2017). Although many different factors may be leading to this outcome, the use of mouse models may be one of them (Drummond and Wisniewski, 2017; Mehta *et al.*, 2017; Oxford, Stewart and Rohn, 2020). These models exhibit certain aspects of the disease but do not develop AD (Ashe and Zahs, 2010; Webster *et al.*, 2014). For instance, amyloid mouse models do not develop neurofibrillary tangles (Ashe and Zahs, 2010; Elder, Sosa and Gasper, 2010), one of the main hallmarks observed in AD (Serrano-Pozo *et al.*, 2011; Drummond and Wisniewski, 2017). In addition, the vast majority of AD mouse models are based on AD familial mutations (Elder, Sosa and Gasper, 2010; Drummond and Wisniewski, 2017). This contrasts with the majority of AD cases being sporadic, with only less than 1% of the cases being caused by known familial mutations in the *APP*, *PSEN1* and *PSEN2* genes (Castellani, Rolston and Smith, 2010; Van Cauwenbergh, Van Broeckhoven and Sleegers, 2016; Lanoiselée *et al.*, 2017).

5.4.2. Future directions

One of the main limitations of this study is the low number of cells with grid periodicity, which has not allowed for the clear assessment of potential impacts caused by the deficits in the MEC of J20 mice observed in this thesis. Studying the activity of these cells is key to understand the spatial memory deficits observed in these mice and to further elucidate whether the reduced frequency of the modulation may affect their activity. It would be relevant to study the activity of a larger number of cells with grid periodicity along the dorsoventral axis of the MEC to more precisely distinguish the effects of genotype and distance from the border of the MEC.

The two open arenas experiment presented in chapter 3 and the experiment presented in chapter 4 are likely to have achieved different levels of familiarity to the environment. Considering that the results presented in this thesis point towards memory encoding deficits in the MEC network oscillations of J20 mice, studying the activity of MEC functional cell subtypes as mice become familiar to the environment may highlight deficits in their activity. Thus, it would be relevant to study these signals as mice repeatedly explore and get familiar to a novel

context. Furthermore, this would allow for the determination of whether the changes occurring during the exploration of the familiar and novel contexts, on some MEC functional cell subtypes, are due to novelty or a combination of novelty and context-specificity.

5.5. Conclusions

This thesis has contributed to the understanding of the mechanisms underlying spatial memory deficits in amyloidopathy, by highlighting novel impairments in the MEC neuronal networks of J20 mice. Furthermore, it has cast light on the processes that normally occur in the activity of different MEC functional cell subtypes with contextual novelty and familiarity, providing of a novel insight into these mechanisms, which are likely associated to spatial memory. Improving our knowledge about the mechanisms behind spatial memory and the deficits on its neuronal substrates is key to identify potential biomarkers and drug targets for AD.

References

- Ahmed, O. J. (2012) 'Running speed alters the frequency of hippocampal gamma oscillations', *J Neurosci*, 32, pp. 7373–7383.
- Akaike, H. (1974) 'A New Look at the Statistical Model Identification', *IEEE Transact Autom Contr*, 19, pp. 716–723.
- Albert, M. S. et al. (2011) 'The Diagnosis of Mild Cognitive Impairment due to Alzheimer's Disease: Recommendations from the National Institute on Aging-Alzheimer's Association Workgroups on Diagnostic Guidelines for Alzheimer's Disease', *Alzheimers Dement*, 7, pp. 270–279.
- Allison, S. L. et al. (2016) 'Spatial Navigation in Preclinical Alzheimer's Disease', *J Alzheimers Dis*, 52, pp. 77–90.
- Alme, C. B. et al. (2014) 'Place cells in the hippocampus: Eleven maps for eleven rooms', *Proc. Natl. Acad. Sci.*, 111, pp. 18428–18435.
- Alonso, A. and Llinás, R. R. (1989) 'Subthreshold Na⁺-dependent theta-like rhythmicity in stellate cells of entorhinal cortex layer II', *Nature*, 342, pp. 175–177.
- Alzheimer's Association (2019) 'Alzheimer's Disease Facts and Figures', *Alzheimers Dement*, 5, pp. 321–87.
- Amaral, D. G. and Witter, M. P. (1989) 'The three-dimensional organization of the hippocampal formation: A review of anatomical data', *Neuroscience*, 31, pp. 571–591.
- Ameen-Ali, K. E. et al. (2019) 'The Time Course of Recognition Memory Impairment and Glial Pathology in the hAPP-J20 Mouse Model of Alzheimer's Disease', *Journal of Alzheimer's Disease*, 68, pp. 609–624.
- Amilhon, B. et al. (2015) 'Parvalbumin Interneurons of Hippocampus Tune Population Activity at Theta Frequency', *Neuron*, 86, pp. 1277–1289.
- Armstrong, C. et al. (2016) 'Target-selectivity of parvalbumin-positive interneurons in layer II of medial entorhinal cortex in normal and epileptic animals', *Hippocampus*, 26, pp. 779–793.

- Armstrong, C. and Soltesz, I. (2012) 'Basket cell dichotomy in microcircuit function', *J Physiol*, 590, pp. 683–94.
- Ashe, K. H. and Zahs, K. R. (2010) 'Probing the biology of Alzheimer's disease in mice', *Neuron*, 66, pp. 631–645.
- Atri, A. (2019) 'Current and Future Treatments in Alzheimer's Disease', *Semin Neurol*, 39, pp. 227–240.
- Aucoin, J. S. et al. (2005) 'Selective cholinergic denervation, independent from oxidative stress, in a mouse model of Alzheimer's disease', *Neuroscience*, 132, pp. 73–86.
- Axmacher, N. et al. (2010) 'Cross-frequency coupling supports multi-item working memory in the human hippocampus', *Proc. Natl. Acad. Sci.*, 107, pp. 3228–3233.
- Babiloni, C. et al. (2020) 'What electrophysiology tells us about Alzheimer's disease: a window into the synchronization and connectivity of brain neurons', *Neurobiol Aging*, 85, pp. 58–73.
- Backman, L., Small, B. J. and Fratiglioni, L. (2001) 'Stability of the preclinical episodic memory deficit in Alzheimer's disease', *Brain*, 124, pp. 96–102.
- Badhwar, A. et al. (2013) 'Impaired structural correlates of memory in Alzheimer's disease mice', *NeuroImage: Clinical*, 3, pp. 290–300.
- Balkan, S. et al. (2003) 'Effect of donepezil on EEG spectral analysis in Alzheimer's disease', *Acta Neurol Belg*, 103, pp. 164–169.
- Barry, C. et al. (2007) 'Experience-dependent rescaling of entorhinal grids', *Nat Neurosci*, 10, pp. 682–684.
- Barry, C. et al. (2012) 'Grid cell firing patterns signal environmental novelty by expansion', *Proc Natl Acad Sci*, 109, pp. 17687–17692.
- Barry, C., Heys, J. G. and Hasselmo, M. E. (2012) 'Possible role of acetylcholine in regulating spatial novelty effects on theta rhythm and grid cells', *Front Neural Circuits*, 6, p. 5.
- Bartus, R. T. et al. (1982) 'The Cholinergic Hypothesis of Geriatric Memory Dysfunction', *Science*, 217, pp. 408–417.

- Bayer, T. A. (2015) 'Proteinopathies, a core concept for understanding and ultimately treating degenerative disorders?', *Eur Neuropsychopharmacol*, 25, pp. 713–724.
- Belchior, H. et al. (2014) 'Increase in hippocampal theta oscillations during spatial decision making', *Hippocampus*, 24, pp. 693–702.
- Bellgowan, P. S. F. et al. (2006) 'Lateralized spatial and object memory encoding in entorhinal and perirhinal cortices', *Learn Mem*, 16, pp. 433–438.
- Bender, F. et al. (2015) 'Theta oscillations regulate the speed of locomotion via a hippocampus to lateral septum pathway', *Nat Commun*, 6, p. 8521.
- Berens, P. (2009) 'CircStat: A MATLAB Toolbox for Circular Statistics', *J Stat Softw*, 31, pp. 1–21.
- Bergland, G. D. (1969) 'A guided tour of the fast Fourier transform', *IEEE Spectrum*, 6, pp. 41–52.
- Berlyne, D. E. (1950) 'Novelty and curiosity as determinants of exploratory behaviour', *Br J Psychol*, 41, pp. 68–80.
- Bernardi, G. et al. (2019) 'Regional delta waves in human rapid eye movement sleep', *J Neurosci*, 39, pp. 2686–2697.
- Betterton, R. T. et al. (2017) 'Acetylcholine modulates gamma frequency oscillations in the hippocampus by activation of muscarinic M1 receptors', *Eur J Neurosci*, 45, pp. 1570–1585.
- Bierbrauer, A. et al. (2020) 'Unmasking selective path integration deficits in Alzheimer's disease risk carriers', *Sci Adv*, 6, p. eaba1394.
- Bland, S. K. and Bland, B. H. (1986) 'Medial septal modulation of hippocampal theta cell discharges', *Brain Res*, 375, pp. 102–116.
- Blennow, K. et al. (2015) 'Amyloid biomarkers in Alzheimer's disease', *Trends Pharmacol Sci*, 36, pp. 297–309.
- Boccara, C. N. et al. (2010) 'Grid cells in pre- and parasubiculum', *Nat Neurosci*, 13, pp. 987–994.

- Bohbot, V. D. et al. (2017) 'Low-frequency theta oscillations in the human hippocampus during real-world and virtual navigation', *Nat Commun*, 8, p. 14415.
- Bonnevie, T. et al. (2013) 'Grid cells require excitatory drive from the hippocampus.', *Nat Neurosci*, 16, pp. 309–17.
- Borchelt, D. R. et al. (1996) 'Familial Alzheimer's Disease-Linked Presenilin 1 Variants Elevate A β 1–42/1–40 Ratio In Vitro and In Vivo', *Neuron*, 17, pp. 1005–1013.
- Bostock, E., Muller, R. U. and Kubie, J. L. (1991) 'Experience-dependent modifications of hippocampal place cell firing', *Hippocampus*, 1, pp. 193–206.
- Braak, H. and Braak, E. (1991) 'Neuropathological stageing of Alzheimer-related changes', *Acta Neuropathol*, 82, pp. 239–259.
- Braak, H. and Braak, E. (1997) 'Frequency of stages of Alzheimer-related lesions in different age categories', *Neurobiol Aging*, 18, pp. 351–357.
- Brandner, C. (2009) 'Spatial Memory', in Binder, M. D., Hirokawa, N., and Windhorst, U. (eds) *Encyclopedia of Neuroscience*. Berlin, Heidelberg: Springer Berlin Heidelberg, pp. 3804–3806.
- Brandon, M. P. et al. (2011) 'Reduction of Theta Rhythm Dissociates Grid Cell Spatial Periodicity from Directional Tuning', *Science*, 332, pp. 595–599.
- Brandon, M. P. et al. (2014) 'New and distinct hippocampal place codes are generated in a new environment during septal inactivation', *Neuron*, pp. 789–96.
- Brereton, R. G. (2015) 'The t-distribution and its relationship to the normal distribution', *Journal of Chemometrics*, 29, pp. 481–483.
- Breydo, L. and Uversky, V. N. (2015) 'Structural, morphological, and functional diversity of amyloid oligomers', *FEBS Letters*, 589, pp. 2640–2648.
- Briggs, A. R., Kennelly, S. P. and Neill, D. O. (2016) 'Drug treatments in Alzheimer's disease', *Clin Med*, 16, pp. 247–253.
- Brown, R. et al. (2018) 'Circadian and brain state modulation of network hyperexcitability in Alzheimer's disease', *eNeuro*, 5, pp. e0426-17.2018.

- Burak, Y. and Fiete, I. R. (2009) 'Accurate Path Integration in Continuous Attractor Network Models of Grid Cells', *PLoS Comput Biol*, 5, p. e1000291.
- Burgalossi, A. et al. (2011) 'Microcircuits of Functionally Identified Neurons in the Rat Medial Entorhinal Cortex', *Neuron*, 70, pp. 773–786.
- Burgess, N. (2008) 'Grid cells and theta as oscillatory interference: Theory and predictions', *Hippocampus*, 18, pp. 1157–1174.
- Burgess, N., Barry, C. and O'Keefe, J. (2007) 'An oscillatory interference model of grid cell firing', *Hippocampus*, 17, pp. 801–812.
- Burggren, A. C. et al. (2011) 'Thickness in entorhinal and subiculum cortex predicts episodic memory decline in mild cognitive impairment', *Int J Alzheimers Dis.*, 2011, p. 956053.
- Busche, M. A. and Konnerth, A. (2016) 'Impairments of neural circuit function in Alzheimer's disease', *Philos Trans R Soc Lond B Biol Sci*, 371, p. 20150429.
- Bush, D. et al. (2017) 'Human hippocampal theta power indicates movement onset and distance travelled', *Proc Natl Acad Sci*, 114, pp. 12297–12302.
- Bush, D. and Burgess, N. (2014) 'A hybrid oscillatory interference/continuous attractor network model of grid cell firing', *The Journal of Neuroscience*, 34, pp. 5065–5079.
- Bush, D. and Schmidt-hieber, C. (2018) 'Computational Models of Grid Cell Firing', in V., C. et al. (eds) *Hippocampal Microcircuits*. Cham: Springer Series in Computational Neuroscience, pp. 585–613.
- Buzsáki, G. (2002) 'Theta oscillations in the hippocampus', *Neuron*, 33, pp. 325–340.
- Buzsáki, G. (2005) 'Theta rhythm of navigation: Link between path integration and landmark navigation, episodic and semantic memory', *Hippocampus*, 15, pp. 827–840.
- Buzsáki, G. (2006) *Rhythms of the brain*. New York: Oxford University Press.

- Buzsáki, G., Anastassiou, C. A. and Koch, C. (2012) 'The origin of extracellular fields and currents — EEG, ECoG, LFP and spikes', *Nat Rev Neurosci*, 13, pp. 407–420.
- Buzsáki, G. and Draguhn, A. (2004) 'Neuronal oscillations in cortical networks', *Science*, 304, pp. 1926–1929.
- Buzsáki, G. and Wang, X.-J. (2012) 'Mechanisms of gamma oscillations', *Annu Rev Neurosci*, 35, pp. 203–225.
- Cacucci, F. *et al.* (2008) 'Place cell firing correlates with memory deficits and amyloid plaque burden in Tg2576 Alzheimer mouse model', *Proc. Natl. Acad. Sci.*, 105, pp. 7863–7868.
- Campbell, M. G. *et al.* (2018) 'Principles governing the integration of landmark and self-motion cues in entorhinal cortical codes for navigation', *Nat Neurosci*, 21, pp. 1096–1106.
- Cannon, J. *et al.* (2014) 'Neurosystems: Brain rhythms and cognitive processing', *Eur J Neurosci*, 39, pp. 705–719.
- Canolty, R. T. *et al.* (2006) 'High Gamma Power Is Phase-Locked to Theta Oscillations in Human Neocortex', *Science*, 313, pp. 1626–1628.
- Canolty, R. T. and Knight, R. T. (2010) 'The functional role of cross-frequency coupling', *Trends Cogn Sci*, 14, pp. 506–515.
- Canto, C. B., Wouterlood, F. G. and Witter, M. P. (2008) 'What Does the Anatomical Organization of the Entorhinal Cortex Tell Us?', *Neural Plast*, 2008, p. 381243.
- Cardin, J. A. *et al.* (2009) 'Driving fast-spiking cells induces gamma rhythm and controls sensory responses', *Nature*, 459, pp. 663–667.
- Carpenter, F., Burgess, N. and Barry, C. (2017) 'Modulating medial septal cholinergic activity reduces medial entorhinal theta frequency without affecting speed or grid coding', *Sci Rep*, 7, p. 14573.
- Carvalho, M. M. *et al.* (2020) 'A Brainstem Locomotor Circuit Drives the Activity of Speed Cells in the Medial Entorhinal Cortex', *Cell Rep*, 32, p. 108123.

- Castanho, I. *et al.* (2020) 'Transcriptional Signatures of Tau and Amyloid Neuropathology', *Cell Reports*, 30, pp. 2040–2054.
- Castellani, R. J., Rolston, R. K. and Smith, M. A. (2010) 'Alzheimer Disease', *Dis Mon*, 56, pp. 484–546.
- Van Cauwenbergh, C., Van Broeckhoven, C. and Sleegers, K. (2016) 'The genetic landscape of Alzheimer disease: Clinical implications and perspectives', *Genet Med*, 18, pp. 421–430.
- Chen, G. *et al.* (2016) 'Absence of Visual Input Results in the Disruption of Grid Cell Firing in the Mouse', *Curr Biol*, 26, pp. 2335–2342.
- Chen, G. *et al.* (2018) 'Spatial cell firing during virtual navigation of open arenas by head-restrained mice', *eLife*, 7, pp. 1–20.
- Chen, Z. *et al.* (2011) 'Speed controls the amplitude and timing of the Hippocampal Gamma rhythm', *PLoS ONE*, 6, p. e21408.
- Cheng, I. H. *et al.* (2007) 'Accelerating amyloid- β fibrillization reduces oligomer levels and functional deficits in Alzheimer disease mouse models', *J Biol Chem*, 282, pp. 23818–23828.
- Chin, J. *et al.* (2005) 'Fyn kinase induces synaptic and cognitive impairments in a transgenic mouse model of Alzheimer's disease', *J Neurosci*, 25, pp. 9694–9703.
- Cho, J. and Sharp, P. E. (2001) 'Head direction, place, and movement correlates for cells in the rat retrosplenial cortex', *Behav Neurosci*, 115, pp. 3–25.
- Citron, M. *et al.* (1992) 'Mutation of the beta-amyloid precursor protein in familial Alzheimer's disease increases beta-protein production', *Nature*, 360, pp. 672–674.
- Citron, M. *et al.* (1997) 'Mutant presenilins of Alzheimer's disease increase production of 42-residue amyloid β -protein in both transfected cells and transgenic mice', *Nat Med*, 3, pp. 67–72.
- Climer, J. R. *et al.* (2015) 'Examination of rhythmicity of extracellularly recorded neurons in the entorhinal cortex', *Hippocampus*, 25, pp. 460–473.

Cline, E. N. *et al.* (2018) 'The Amyloid- β Oligomer Hypothesis: Beginning of the Third Decade', *J Alzheimers Dis.*, 64, pp. S567–S610.

Cohen, R. M. *et al.* (2013) 'A transgenic alzheimer rat with plaques, tau pathology, behavioral impairment, oligomeric A β , and frank neuronal loss', *J Neurosci*, 33, pp. 6245–6256.

Colgin, L. L., Denninger, T., Fyhn, M., Hafting, T., Bonnevie, T., Jensen, O., Moser, M. B., *et al.* (2009) 'Frequency of gamma oscillations routes flow of information in the hippocampus', *Nature*, 462, pp. 353–357.

Colgin, L. L., Denninger, T., Fyhn, M., Hafting, T., Bonnevie, T., Jensen, O., Moser, M.-B., *et al.* (2009) 'Frequency of gamma oscillations routes flow of information in the hippocampus', *Nature*, 462, pp. 353–357.

Colom, L. V. *et al.* (2005) 'Characterization of medial septal glutamatergic neurons and their projection to the hippocampus', *Synapse*, 58, pp. 151–164.

Cornwell, B. R. *et al.* (2008) 'Human Hippocampal and Parahippocampal Theta during Goal-Directed Spatial Navigation Predicts Performance on a Virtual Morris Water Maze', *J Neurosci*, 28, pp. 5983–5990.

Costall, B. *et al.* (1989) 'Exploration of mice in a black and white test box: Validation as a model of anxiety', *Pharmacology, Biochemistry and Behavior*, 32, pp. 777–785.

Couey, J. J. *et al.* (2013) 'Recurrent inhibitory circuitry as a mechanism for grid formation', *Nat Neurosci*, 16, pp. 318–24.

Dannenberg, H. *et al.* (2019) 'The firing rate speed code of entorhinal speed cells differs across behaviorally relevant time scales and does not depend on medial septum inputs', *J Neurosci*, 39, pp. 3434–3453.

Delpolyi, A. R. *et al.* (2007) 'Spatial cognition and the human navigation network in AD and MCI', *Neurology*, 69, pp. 986–997.

Deshmukh, S. S. *et al.* (2010) 'Theta modulation in the medial and the lateral entorhinal cortices', *J Neurophysiol*, 104, pp. 994–1006.

- Deshmukh, S. S., Johnson, J. L. and Knierim, J. J. (2012) 'Perirhinal cortex represents nonspatial, but not spatial, information in rats foraging in the presence of objects: Comparison with lateral entorhinal cortex', *Hippocampus*, 22, pp. 2045–2058.
- Diehl, G. W. et al. (2017) 'Grid and non-grid cells in medial entorhinal cortex represent spatial location and environmental features with complementary coding schemes', *Neuron*, 94, pp. 83–92.
- Doan, T. P. et al. (2019) 'Convergent Projections from Perirhinal and Postrhinal Cortices Suggest a Multisensory Nature of Lateral, but Not Medial, Entorhinal Cortex', *Cell Rep*, 29, pp. 617–627.
- Doeller, C. F., Barry, C. and Burgess, N. (2010) 'Evidence for grid cells in a human memory network', *Nature*, 463, pp. 657–661.
- Drummond, E. and Wisniewski, T. (2017) 'Alzheimer's Disease: Experimental Models and Reality', *Acta Neuropathol*, 133, pp. 155–175.
- Dubois, B. et al. (2016) 'Preclinical Alzheimer's disease: Definition, natural history, and diagnostic criteria', *Alzheimers Dement*, 12, pp. 292–323.
- Ekstrom, A. D., Arnold, A. E. G. F. and Iaria, G. (2014) 'A critical review of the allocentric spatial representation and its neural underpinnings : toward a network-based perspective', *Front Hum Neurosci*, 8, p. 803.
- Elder, G. A., Sosa, M. A. G. and Gasper, R. De (2010) 'Transgenic Mouse Models of Alzheimer's Disease', *Mt Sinai J Med*, 77, pp. 69–81.
- Engel, A. K., Fries, P. and Singer, W. (2001) 'Dynamic predictions: Oscillations and synchrony in top-down processing', *Nat Rev Neurosci*, 2, pp. 704–716.
- Etter, G. et al. (2019) 'Optogenetic gamma stimulation rescues memory impairments in an Alzheimer's disease mouse model', *Nat Commun*, 10, p. 5322.
- Fantini, J., Chahinian, H. and Yahi, N. (2020) 'Progress toward Alzheimer's disease treatment: Leveraging the Achilles' heel of A β oligomers?', *Protein Sci*, 29, pp. 1748–1759.
- Fiete, I. R., Burak, Y. and Brookings, T. (2008) 'What grid cells convey about rat location', *J Neurosci*, 28, pp. 6858–6871.

- Foxe, J. J. and Snyder, A. C. (2011) 'The role of alpha-band brain oscillations as a sensory suppression mechanism during selective attention', *Front Psychol*, 2, p. 154.
- Francis, B. M. et al. (2012) 'Object recognition memory and BDNF expression are reduced in young TgCRND8 mice', *Neurobiol Aging*, 33, pp. 555–563.
- Francis, P. T. et al. (1999) 'The cholinergic hypothesis of Alzheimer's disease: a review of progress', *J Neurol Neurosurg Psychiatry*, 66, pp. 137–147.
- Frank, L. M. et al. (2001) 'A Comparison of the Firing Properties of Putative Excitatory and Inhibitory Neurons From CA1 and the Entorhinal Cortex', *J Neurophysiol*, 86, pp. 2029–2040.
- Frank, L. M., Stanley, G. B. and Brown, E. N. (2004) 'Hippocampal plasticity across multiple days of exposure to novel environments', *J Neurosci*, 24, pp. 7681–7689.
- Frisoni, G. B. et al. (2010) 'The clinical use of structural MRI in Alzheimer disease', *Nat Rev Neurosci*, 6, pp. 67–77.
- Fuchs, E. C. et al. (2007) 'Recruitment of Parvalbumin-Positive Interneurons Determines Hippocampal Function and Associated Behavior', *Neuron*, 53, pp. 591–604.
- Fuchs, E. C. et al. (2016) 'Local and Distant Input Controlling Excitation in Layer II of the Medial Entorhinal Cortex', *Neuron*, 89, pp. 194–208.
- Fuhs, M. C. and Touretzky, D. S. (2006) 'A Spin Glass Model of Path Integration in Rat Medial Entorhinal Cortex', *J Neurosci*, 26, pp. 4266–4276.
- Fujikawa, R. et al. (2017) 'Deficiency in EP4 Receptor–Associated Protein Ameliorates Abnormal Anxiety-Like Behavior and Brain Inflammation in a Mouse Model of Alzheimer Disease', *Am J Pathol*, 187, pp. 1848–1854.
- Furtak, S. C., Ahmed, O. J. and Burwell, R. D. (2012) 'Single Neuron Activity and Theta Modulation in Postrhinal Cortex during Visual Object Discrimination', *Neuron*, 76, pp. 976–988.
- Fyhn, M. et al. (2004) 'Spatial representation in the entorhinal cortex', *Science*, 305, pp. 1258–1264.

- Fyhn, M. et al. (2007) 'Hippocampal remapping and grid realignment in entorhinal cortex', *Nature*, 446, pp. 190–194.
- Fyhn, M. et al. (2008) 'Grid cells in mice', *Hippocampus*, 18, pp. 1230–1238.
- Gale, S. A., Acar, D. and Daffner, K. R. (2018) 'Dementia', *Am J Med*, 131, pp. 1161–1169.
- Galimberti, D. and Scarpini, E. (2011) 'Disease-modifying treatments for Alzheimer's disease', *Ther Adv Neurol Disord*, 4, pp. 203–216.
- Gallistel, C. R. (2008) 'Dead Reckoning, Cognitive Maps, Animal Navigation and the Representation of Space: An Introduction', in Jeffries, M. E. and Yeap, W. K. (eds) *Springer Tracts in Advanced Robotics*. Robotics a. Springer, Berlin, Heidelberg, pp. 137–143.
- Galvin, J. E. and Balasubramaniam, M. (2013) 'Lewy Body Dementia: The Under-Recognized but Common FOE.', *Cerebrum*, 2013, p. 13.
- Games, D. et al. (1995) 'Alzheimer-type neuropathology in transgenic mice overexpressing V717F β-amyloid precursor protein', *Nature*, 373, pp. 523–527.
- Geisler, C. et al. (2010) 'Temporal delays among place cells determine the frequency of population theta oscillations in the hippocampus', *Proc. Natl. Acad. Sci.*, 107, pp. 7957–7962.
- Germroth, P., Schwerdtfeger, W. K. and Buhl, E. H. (1989) 'GABAergic neurons in the entorhinal cortex project to the hippocampus', *Brain Res*, 494, pp. 187–192.
- Gianotti, L. R. R. et al. (2008) 'Rivastigmine effects on EEG spectra and three-dimensional LORETA functional imaging in Alzheimer's disease', *Psychopharmacology*, 198, pp. 323–332.
- Giesers, N. K. and Wirths, O. (2020) 'Loss of Hippocampal Calretinin and Parvalbumin Interneurons in the 5XFAD Mouse Model of Alzheimer's Disease', *ASN Neuro*, 12, pp. 1–12.
- Gil, M. et al. (2018) 'Impaired path integration in mice with disrupted grid cell firing', *Nat Neurosci*, 21, pp. 81–91.

- Gillespie, A. K. *et al.* (2016) ‘Apolipoprotein E4 Causes Age-Dependent Disruption of Slow Gamma Oscillations during Hippocampal Sharp-Wave Ripples’, *Neuron*, 90, pp. 740–751.
- Giocomo, L. M. *et al.* (2007) ‘Temporal frequency of subthreshold oscillations scales with entorhinal grid cell field spacing’, *Science*, 315, pp. 1719–1722.
- Giocomo, L. M. *et al.* (2011) ‘Grid cells use HCN1 channels for spatial scaling’, *Cell*, 147, pp. 1159–1170.
- Giocomo, L. M. *et al.* (2014) ‘Topography of head direction cells in medial entorhinal cortex’, *Curr Biol*, 24, pp. 252–262.
- Giocomo, L. M., Moser, M. B. and Moser, E. I. (2011) ‘Computational models of grid cells’, *Neuron*, 71, pp. 589–603.
- Giovannini, M. G. *et al.* (2001) ‘Effects of novelty and habituation on acetylcholine, GABA, and glutamate release from the frontal cortex and hippocampus of freely moving rats’, *Neuroscience*, 106, pp. 43–53.
- Girardeau, G. *et al.* (2009) ‘Selective suppression of hippocampal ripples impairs spatial memory’, *Nat Neurosci*, 12, pp. 1222–1223.
- Glenner, G. G. and Wong, C. W. (1984) ‘Alzheimer’s disease: Initial report of the purification and characterization of a novel cerebrovascular amyloid protein’, *Biochem Biophys Res Commun*, 120, pp. 885–890.
- Golby, A. *et al.* (2005) ‘Memory encoding in Alzheimer’s disease: an fMRI study of explicit and implicit memory’, *Brain*, 128, pp. 773–787.
- Gómez-Isla, T. *et al.* (1996) ‘Profound loss of layer II entorhinal cortex neurons occurs in very mild Alzheimer’s disease’, *J Neurosci*, 16, pp. 4491–4500.
- Gonzalez-Sulser, A. *et al.* (2014) ‘GABAergic projections from the medial septum selectively inhibit interneurons in the medial entorhinal cortex.’, *J Neurosci*, 34, pp. 16739–43.
- Goodman, M. S. *et al.* (2018) ‘Theta-Gamma coupling and working memory in Alzheimer’s dementia and mild cognitive impairment’, *Front Aging Neurosci*, 10, p. 101.

- Goodridge, J. P. *et al.* (1998) 'Cue control and head direction cells', *Behav Neurosci*, 112, pp. 749–761.
- Götz, J., Bodea, L. G. and Goedert, M. (2018) 'Rodent models for Alzheimer disease', *Nat Rev Neurosci*, 19, pp. 583–598.
- Goyal, A. *et al.* (2018) 'Electrical Stimulation in Hippocampus and Entorhinal Cortex Impairs Spatial and Temporal Memory', *J Neurosci*, 38, pp. 4471–4481.
- Goyal, A. *et al.* (2020) 'Functionally distinct high and low theta oscillations in the human hippocampus', *Nat Commun*, 11, p. 2469.
- Grieves, R. M. and Jeffery, K. J. (2017) 'The representation of space in the brain', *Behav Processes*, 135, pp. 113–131.
- Groen, T. van (2001) 'Entorhinal cortex of the mouse: cytoarchitectonic organization.', *Hippocampus*, 11, pp. 397–407.
- Grundke-Iqbali, I. *et al.* (1986) 'Abnormal phosphorylation of the microtubule-associated protein τ (tau) in Alzheimer cytoskeletal pathology', *Proc. Natl. Acad. Sci.*, 83, pp. 44913–44917.
- Gu, Z. *et al.* (2017) 'Hippocampus and Entorhinal Cortex Recruit Cholinergic and NMDA Receptors Separately to Generate Hippocampal Theta Oscillations', *Cell Reports*, 21, pp. 3585–3595.
- Guillon, J. *et al.* (2017) 'Loss of brain inter-frequency hubs in Alzheimer's disease', *Sci Rep*, 7, p. 10879.
- Hafting, T. *et al.* (2005) 'Microstructure of a spatial map in the entorhinal cortex.', *Nature*, 436, pp. 801–806.
- Hafting, T. *et al.* (2008) 'Hippocampus-independent phase precession in entorhinal grid cells', *Nature*, 453, pp. 1248–1252.
- Hales, J. B. *et al.* (2014) 'Medial entorhinal cortex lesions only partially disrupt hippocampal place cells and hippocampus-dependent place memory', *Cell Rep*, 9, pp. 893–901.
- Hales, J. B. *et al.* (2018) 'Recent and remote retrograde memory deficit in rats with medial entorhinal cortex lesions', *Neurobiol Learn Mem*, 155, pp. 157–163.

Hampel, H. *et al.* (2019) ‘Revisiting the Cholinergic Hypothesis in Alzheimer’s Disease: Emerging Evidence from Translational and Clinical Research’, *J Prev Alzheimers Dis*, pp. 2–15.

Hangya, B. *et al.* (2009) ‘GABAergic Neurons of the Medial Septum Lead the Hippocampal Network during Theta Activity’, *J Neurosci*, 29, pp. 8094–8102.

Hardcastle, K. *et al.* (2017) ‘A Multiplexed, Heterogeneous, and Adaptive Code for Navigation in Medial Entorhinal Cortex’, *Neuron*, 94, pp. 375–387.e7.

Hardy, J. A. and Higgins, G. A. (1992) ‘Alzheimer’s disease: The amyloid cascade hypothesis’, *Science*, 256, pp. 184–185.

Hardy, J. and Selkoe, D. J. (2002) ‘The amyloid hypothesis of Alzheimer’s disease: Progress and problems on the road to therapeutics’, *Science*, 297, pp. 353–356.

Harris, J. A. *et al.* (2010) ‘Many neuronal and behavioral impairments in transgenic mouse models of Alzheimer’s disease are independent of caspase cleavage of the amyloid precursor protein’, *J Neurosci*, 30, pp. 372–381.

Hayden, E. Y. and Teplow, D. B. (2013) ‘Amyloid β -protein oligomers and Alzheimer’s disease’, *Alzheimers Res Ther*, 5, p. 60.

Hébert, F. *et al.* (2013) ‘Cortical atrophy and hypoperfusion in a transgenic mouse model of Alzheimer’s disease’, *Neurobiology of Aging*, 34, pp. 1644–1652.

Henderson, V. W., Mack, W. and Williams, B. W. (1989) ‘Spatial disorientation in Alzheimer’s’, *Arch Neurol*, 46, pp. 391–1498.

Heys, J. G., Giocomo, L. M. and Hasselmo, M. E. (2010) ‘Cholinergic modulation of the resonance properties of stellate cells in layer II of medial entorhinal cortex’, *J Neurophysiol*, 104, pp. 258–270.

Hijazi, S. *et al.* (2019) ‘Early restoration of parvalbumin interneuron activity prevents memory loss and network hyperexcitability in a mouse model of Alzheimer’s disease’, *Mol Psychiatry*.

Hinman, J. R. *et al.* (2011) ‘Septotemporal variation in dynamics of theta: speed and habituation’, *J Neurophysiol*, 105, pp. 2675–2686.

- Hinman, J. R. et al. (2016) 'Multiple Running Speed Signals in Medial Entorhinal Cortex', *Neuron*, 91, pp. 666–679.
- Hogan, J. B. et al. (2005) 'Effects of CRF1 receptor antagonists and benzodiazepines in the Morris water maze and delayed non-matching to position tests', *Psychopharmacology*, 178, pp. 410–419.
- Hong, S. et al. (2016) 'Complement and Microglia Mediate Early Synapse Loss in Alzheimer Mouse Models', *Science*, 352, pp. 712–6.
- Howett, D. et al. (2019) 'Differentiation of mild cognitive impairment using an entorhinal cortex-based test of virtual reality navigation', *Brain*, 142, pp. 1751–1766.
- Høydal, Ø. A. et al. (2019) 'Object-vector coding in the medial entorhinal cortex', *Nature*, 568, pp. 400–404.
- Hunsaker, M. R. et al. (2013) 'The medial and lateral entorhinal cortex both contribute to contextual and item recognition memory: A test of the binding of items and context model', *Hippocampus*, 23, pp. 380–391.
- Hunt, L. A., Brown, A. E. and Gilman, I. P. (2010) 'Drivers With Dementia and Outcomes of Becoming Lost While Driving', *Am J Occup Ther*, 64, pp. 225–232.
- Iaccarino, H. F. et al. (2016) 'Gamma frequency entrainment attenuates amyloid load and modifies microglia', *Nature*, 540, pp. 230–235.
- Insausti, R. and Amaral, D. G. (2012) 'Hippocampal Formation', in Mai, J. K. and Paxinos, G. (eds) *The Human Nervous System*. Third. Amsterdam: Academic Press, pp. 896–942.
- Ishizuka, N., Weber, J. and Amaral, D. G. (1990) 'Organization of intrahippocampal projections originating from CA3 pyramidal cells in the rat', *J Comp Neurol*, 295, pp. 580–623.
- Jack, C. R. et al. (2010) 'Hypothetical model of dynamic biomarkers of the Alzheimer's pathological cascade', *Lancet Neurol*, 9, p. 119.
- Jacob, P. Y., Casali, G., et al. (2017) 'An independent, landmark-dominated head-direction signal in dysgranular retrosplenial cortex', *Nature Neuroscience*, 20, pp. 173–175.

- Jacob, P. Y., Gordillo-Salas, M., *et al.* (2017) 'Medial entorhinal cortex and medial septum contribute to self-motion-based linear distance estimation', *Brain Struct Funct*, 222, pp. 2727–2742.
- Jacobs, J. *et al.* (2013) 'Direct recordings of grid-like neuronal activity in human spatial navigation', *Nat Neurosci*, 16, pp. 1188–1190.
- Jacobs, J. (2014) 'Hippocampal theta oscillations are slower in humans than in rodents: implications for models of spatial navigation and memory', *Phil Trans, R Soc Lond B Biol Sci*, 369, p. 20130304.
- Jacobs, J. *et al.* (2016) 'Direct Electrical Stimulation of the Human Entorhinal Region and Hippocampus Impairs Memory', *Neuron*, 92, pp. 983–990.
- Jakes, R. *et al.* (1991) 'Identification of 3- and 4-repeat tau isoforms within the PHF in Alzheimer's disease', *The EMBO journal*, 10, pp. 2725–2729.
- Jankowsky, J. L. and Zheng, H. (2017) 'Practical considerations for choosing a mouse model of Alzheimer's disease', *Mol Neurodegener*, 12, p. 89.
- Jensen, O. and Colgin, L. L. (2007) 'Cross-frequency coupling between neuronal oscillations', *Trends Cogn Sci*, 11, pp. 267–269.
- Jeong, J. (2004) 'EEG dynamics in patients with Alzheimer's disease', *Clin Neurophysiol*, 115, pp. 1490–1505.
- Johnson-Wood, K. *et al.* (1997) 'Amyloid precursor protein processing and A β 42 deposition in a transgenic mouse model of Alzheimer disease', *Proc. Natl. Acad. Sci.*, 94, pp. 1550–1555.
- Jun, H. *et al.* (2020) 'Disrupted Place Cell Remapping and Impaired Grid Cells in a Knockin Model of Alzheimer's Disease', *Neuron*, 107, pp. 1–18.
- Justus, D. *et al.* (2017) 'Glutamatergic synaptic integration of locomotion speed via septoentorhinal projections', *Nat Neurosci*, 20, pp. 16–19.
- Kane, N. *et al.* (2017) 'A revised glossary of terms most commonly used by clinical electroencephalographers and updated proposal for the report format of the EEG findings. Revision 2017', *Clin Neurophysiol Pract*, 2, pp. 170–185.

- van der Kant, R. and Goldstein, L. S. B. (2015) 'Cellular Functions of the Amyloid Precursor Protein from Development to Dementia', *Dev Cell*, 32, pp. 502–515.
- Kaplan, R. et al. (2012) 'Movement-Related Theta Rhythm in Humans: Coordinating Self-Directed Hippocampal Learning', *PLoS Biology*, 10, p. e1001267.
- Kemere, C. et al. (2013) 'Rapid and Continuous Modulation of Hippocampal Network State during Exploration of New Places', *PLoS ONE*, 8, p. e73114.
- Kerbler, G. M. et al. (2015) 'Basal forebrain atrophy correlates with amyloid β burden in Alzheimer's disease', *Neuroimage Clin*, 7, pp. 105–113.
- Khan, U. A. et al. (2014) 'Molecular drivers and cortical spread of lateral entorhinal cortex dysfunction in preclinical Alzheimer's disease', *Nat Neurosci*, 17, pp. 304–311.
- Kim, H.-Y. (2017) 'Statistical notes for clinical researchers: Chi-squared test and Fisher's exact test', *Restor Dent Endod*, 42, pp. 152–155.
- Kim, H. J. et al. (2003) 'Selective neuronal degeneration induced by soluble oligomeric amyloid beta-protein', *The FASEB journal*, 17, pp. 118–120.
- Kirwan, C. B. and Stark, C. E. L. (2004) 'Medial Temporal Lobe Activation During Encoding and Retrieval of Novel Face-Name Pairs', *Hipp*, 14, pp. 919–930.
- Kitamura, T. et al. (2014) 'Island Cells Control Temporal Association Memory', *Science*, 343, pp. 896–901.
- Kitamura, T. et al. (2015) 'Entorhinal Cortical Ocean Cells Encode Specific Contexts and Drive Context-Specific Fear Memory', *Neuron*, 87, pp. 1317–1331.
- Kivipelto, M. et al. (2001) 'Midlife vascular risk factors and Alzheimer's disease in later life: longitudinal, population based study', *BMJ*, 322, pp. 1447–1451.
- Klatzky, R. L. (1998) 'Allocentric and Egocentric Spatial Representations : Definitions, Distinctions, and Interconnections', in Freksa, C., Habel, A. C., and Wender, K. F. (eds) *Spatial Cognition: An Interdisciplinary Approach to Representing and Processing Spatial Knowledge*. Berlin, Heidelberg: Springer-Verlag, pp. 1–17.

- Klimesch, W. (2012) 'Alpha-band oscillations, attention, and controlled access to stored information', *Trends Cogn Sci*, 16, pp. 606–617.
- Kloosterman, F., Witter, M. P. and Van Haeften, T. (2003) 'Topographical and laminar organization of subicular projections to the parahippocampal region of the rat', *J Comp Neurol*, 455, pp. 156–171.
- Knierim, J. J. et al. (2014) 'Functional correlates of the lateral and medial entorhinal cortex: objects , path integration and local – global reference frames', *Phil Trans*, 369, p. 20130369.
- Kobro-Flatmoen, A., Nagelhus, A. and Witter, M. P. (2016) 'Reelin-immunoreactive neurons in entorhinal cortex layer II selectively express intracellular amyloid in early Alzheimer's disease', *Neurobiol Dis*, 93, pp. 172–183.
- Koenig, J. et al. (2011) 'The Spatial Periodicity of Grid Cells Is Not Sustained During Reduced Theta Oscillations', *Science*, 332, pp. 592–595.
- Koenig, T. et al. (2005) 'Decreased EEG synchronization in Alzheimer's disease and mild cognitive impairment', *Neurobiol Aging*, 26, pp. 165–171.
- Koganezawa, N. et al. (2015) 'Excitatory postrhinal projections to principal cells in the medial entorhinal cortex', *J Neurosci*, 35, pp. 15860–15874.
- Kornienko, O. et al. (2018) 'Non-rhythmic head-direction cells in the parahippocampal region are not constrained by attractor network dynamics', *eLife*, 7, pp. 1–25.
- Kosik, K. S., Joachim, C. L. and Selkoe, D. J. (1986) 'Microtubule-associated protein tau (τ) is a major antigenic component of paired helical filaments in Alzheimer disease', *Proc. Natl. Acad. Sci.*, 83, pp. 4044–4048.
- Kramis, R., Vanderwolf, C. H. and Bland, B. H. (1975) 'Two types of hippocampal rhythmical slow activity in both the rabbit and the rat: Relations to behavior and effects of atropine, diethyl ether, urethane, and pentobarbital', *Exp Neurol*, 49, pp. 58–85.
- Kravitz, D. J. et al. (2011) 'A new neural framework for visuospatial processing', *Nat Rev Neurosci*, 12, pp. 217–230.

- Kravitz, D. J. *et al.* (2013) 'The ventral visual pathway: An expanded neural framework for the processing of object quality', *Trends Cogn Sci*, 17, pp. 26–49.
- Kropff, E. *et al.* (2015) 'Speed cells in the medial entorhinal cortex', *Nature*, 523, pp. 419–424.
- Krumm, S. *et al.* (2016) 'Cortical thinning of parahippocampal subregions in very early Alzheimer's disease', *Neurobiol Aging*, 38, pp. 188–196.
- Kucewicz, M. T. *et al.* (2014) 'High frequency oscillations are associated with cognitive processing in human recognition memory', *Brain*, 137, pp. 2231–2244.
- Kunz, L. *et al.* (2015) 'Reduced grid-cell-like representations in adults at genetic risk for Alzheimer's disease', *Science*, 350, pp. 430–433.
- Langston, R. F. *et al.* (2010) 'Development of the Spatial Representation System in the Rat', *Science*, 328, pp. 1576–1581.
- Lanoiselée, H. M. *et al.* (2017) 'APP, PSEN1, and PSEN2 mutations in early-onset Alzheimer disease: A genetic screening study of familial and sporadic cases', *PLoS Medicine*, 14, pp. 1–16.
- Latuske, P. *et al.* (2018) 'Hippocampal remapping and its entorhinal origin', *Frontiers in Behavioral Neuroscience*, 11, p. Article 253.
- Lavenex, P. and Amaral, D. G. (2000) 'Hippocampal-neocortical interaction: a hierarchy of associativity.', *Hippocampus*, 10, pp. 420–430.
- Lee, S. *et al.* (2010) 'The Largest Group of Superficial Neocortical GABAergic Interneurons Expresses Ionotropic Serotonin Receptors', *J Neurosci*, 30, pp. 16796–16808.
- Leger, M. *et al.* (2013) 'Object recognition test in mice', *Nat Protoc*, 8, pp. 2531–2537.
- Leitner, F. C. *et al.* (2016) 'Spatially segregated feedforward and feedback neurons support differential odor processing in the lateral entorhinal cortex', *Nat Neurosci*, 19, pp. 935–944.
- LeRoux, J. P. *et al.* (2005) 'Focal decline of cortical thickness in Alzheimer's disease identified by computational neuroanatomy', *Cereb Cortex*, 15, pp. 995–1001.

- Leutgeb, S. *et al.* (2005) 'Neuroscience: Independent codes for spatial and episodic memory in hippocampal neuronal ensembles', *Science*, 309, pp. 619–623.
- Leutgeb, S., Ragozzino, K. E. and Mizumori, S. J. Y. (2000) 'Convergence of head direction and place information in the CA1 region of hippocampus', *Neuroscience*, 100, pp. 11–19.
- Lever, C. *et al.* (2009) 'Boundary Vector Cells in the Subiculum of the Hippocampal Formation', *J Neurosci*, 29, pp. 9771–9777.
- Lewis, J. *et al.* (2001) 'Enhanced neurofibrillary degeneration in transgenic mice expressing mutant tau and APP', *Science*, 293, pp. 1487–1491.
- Li, S. *et al.* (2009) 'Soluble Oligomers of Amyloid β Protein Facilitate Hippocampal Long-Term Depression by Disrupting Neuronal Glutamate Uptake', *Neuron*, 62, pp. 788–801.
- Li, S. *et al.* (2011) 'Soluble A β oligomers inhibit long-term potentiation through a mechanism involving excessive activation of extrasynaptic NR2B-containing NMDA receptors', *J Neurosci*, 31, pp. 6627–6638.
- Li, S. *et al.* (2018) 'Decoding the synaptic dysfunction of bioactive human AD brain soluble A β to inspire novel therapeutic avenues for Alzheimer's disease', *Acta Neuropathol Commun*, 6, p. 121.
- Lim, Y. Y. *et al.* (2020) 'Association of deficits in short-term learning and A β and hippocampal volume in cognitively normal adults', *Neurology*, p. 10.1212/WNL.00000000000010728.
- Lisman, J. E. and Idiart, M. A. P. (1995) 'Storage of 7 ± 2 short-term memories in oscillatory subcycles', *Science*, 267, pp. 1512–1515.
- Liu, C.-C. *et al.* (2013) 'Apolipoprotein E and Alzheimer disease: risk, mechanisms, and therapy', *Nat Rev Neurol*, 9, pp. 106–118.
- Lue, L. *et al.* (1999) 'Soluble Amyloid β Peptide Concentration as a Predictor of Synaptic Change in Alzheimer's Disease', *Am J Pathol*, 155, pp. 853–862.

- Lyketsos, C. G. et al. (2006) 'Position statement of the American Association for geriatric psychiatry regarding principles of care for patients with dementia resulting from Alzheimer disease', *Am J Geriatr Psychiatry*, 14, pp. 561–573.
- M. Aghajan, Z. et al. (2017) 'Theta Oscillations in the Human Medial Temporal Lobe during Real-World Ambulatory Movement', *Curr Biol*, 27, pp. 3743–3751.
- Maass, A. et al. (2015) 'Functional subregions of the human entorhinal cortex', *eLife*, 4, p. e06426.
- Mably, A. J. et al. (2015) 'Anti-A β antibodies incapable of reducing cerebral A β oligomers fail to attenuate spatial reference memory deficits in J20 mice', *Neurobiol Dis*, 82, pp. 372–384.
- Macêdo, P. T. et al. (2018) 'Subtle alterations in spatial memory induced by amyloid peptides infusion in rats', *Front Aging Neurosci*, 10, p. 18.
- Magdalena Martinez-Losa et al. (2018) 'Nav1.1-Overexpressing Interneuron Transplants Restore Brain Rhythms and Cognition in a Mouse Model of Alzheimer's Disease', *Neuron*, 98, pp. 75–89.
- Mallory, C. S. et al. (2018) 'Grid scale drives the scale and long-term stability of place maps', *Nat Neurosci*, 21, pp. 270–282.
- Manns, I. D., Mainville, L. and Jones, B. E. (2001) 'Evidence for glutamate, in addition to acetylcholine and GABA, neurotransmitter synthesis in basal forebrain neurons projecting to the entorhinal cortex', *Neuroscience*, 107, pp. 249–263.
- Marozzi, E. et al. (2015) 'Purely translational realignment in grid cell firing patterns following nonmetric context change', *Cereb Cortex*, 25, pp. 4619–4627.
- Martinez-Losa, M. et al. (2018) 'Nav1.1-Overexpressing Interneuron Transplants Restore Brain Rhythms and Cognition in a Mouse Model of Alzheimer's Disease', *Neuron*, 98, pp. 75-89.e5.
- Masters, C. L. et al. (2015) 'Alzheimer's disease', *Nat Rev Dis Primers*, 1, p. 15056.
- Mayo, M. C. and Bordelon, Y. (2014) 'Dementia with Lewy bodies', *Semin Neurol*, 34, pp. 182–188.

- McLean, C. A. et al. (1999) 'Soluble pool of A β amyloid as a determinant of severity of neurodegeneration in Alzheimer's disease', *Ann Neurol*, 46, pp. 860–866.
- McNaughton, B. L. et al. (2006) 'Path integration and the neural basis of the "cognitive map"', *Nat Rev Neurosci*, 7, pp. 663–678.
- Mehta, D. et al. (2017) 'Why do trials for Alzheimer's disease drugs keep failing? A discontinued drug perspective for 2010–2015', *Expert Opin Investig Drugs*, 26, pp. 735–739.
- Meilandt, W. J. et al. (2009) 'Neprilysin overexpression inhibits plaque formation but fails to reduce pathogenic A β oligomers and associated cognitive deficits in human amyloid precursor protein transgenic mice', *J Neurosci*, 29, pp. 1977–1986.
- Melzer, S. et al. (2012) 'Long-Range – Projecting GABAergic Neurons Modulate Inhibition in Hippocampus and Entorhinal Cortex', *Science*, 335, pp. 1506–1510.
- Miao, C. et al. (2017) 'Parvalbumin and Somatostatin Interneurons Control Different Space-Coding Networks in the Medial Entorhinal Cortex', *Cell*, 171, pp. 507-521.e17.
- Millett, D. (2001) 'Hans Berger: From psychic energy to the EEG', *Perspect Biol Med*, 44, pp. 522–542.
- Mitchell, A. J. and Shiri-Feshki, M. (2009) 'Rate of progression of mild cognitive impairment to dementia - meta-analysis of 41 robust inception cohort studies', *Acta Psychiatr Scand*, 119, pp. 252–265.
- Mitchell, S. J. et al. (1982) 'Medial septal area lesions disrupt theta rhythm and cholinergic staining in medial entorhinal cortex and produce impaired radial arm maze behavior in rats', *J Neurosci*, 2, pp. 292–302.
- Mitchell, S. J. and Ranck, J. B. (1980) 'Generation of theta rhythm in medial entorhinal cortex of freely moving rats', *Brain Res*, 189, pp. 49–66.
- Mizuseki, K. et al. (2009) 'Theta oscillations provide temporal windows for local circuit computation in the entorhinal-hippocampal loop', *Neuron*, 64, pp. 267–280.

- Mokrisova, I. *et al.* (2016) 'Real-space path integration is impaired in Alzheimer's disease and mild cognitive impairment', *Behav Brain Res*, 307, pp. 150–158.
- Monacelli, A. M. *et al.* (2003) 'Spatial disorientation in Alzheimer's disease: the remembrance of things passed', *Neurology*, 61, pp. 1491–1497.
- Monaghan, C. K., Chapman, G. W. and Hasselmo, M. E. (2017) 'Systemic administration of two different anxiolytic drugs decreases local field potential theta frequency in the medial entorhinal cortex without affecting grid cell firing fields', *Neuroscience*, 364, pp. 60–70.
- Moreno, H. *et al.* (2007) 'Imaging the A β -Related Neurotoxicity of Alzheimer Disease', *Arch Neurol*, 64, pp. 1467–1477.
- Mormann, F. *et al.* (2005) 'Phase/amplitude reset and theta-gamma interaction in the human medial temporal lobe during a continuous word recognition memory task', *Hippocampus*, 15, pp. 890–900.
- Morris, M. *et al.* (2011) 'Review The Many Faces of Tau', *Neuron*, 70, pp. 410–426.
- Morzelle, M. C. *et al.* (2016) 'Neuroprotective effects of pomegranate peel extract after chronic infusion with amyloid- β peptide in mice', *PLoS ONE*, 11, pp. 1–20.
- Moser, E. I., Kropff, E. and Moser, M.-B. (2008) 'Place cells, grid cells, and the brain's spatial representation system.', *Annu Rev Neurosci*, 31, pp. 69–89.
- Moser, E. I. and Moser, M. B. (2008) 'A metric for space', *Hippocampus*, 18, pp. 1142–1156.
- Mucke, L. *et al.* (2000) 'High-level neuronal expression of A β 1-42 in wild-type human amyloid protein precursor transgenic mice: synaptotoxicity without plaque formation', *J Neurosci*, 20, pp. 4050–4058.
- Mucke, L. and Selkoe, D. J. (2012) 'Neurotoxicity of amyloid β -protein: Synaptic and network dysfunction', *Cold Spring Harb Perspect Med*, 2, p. a006338.
- Muessig, L. *et al.* (2015) 'A Developmental Switch in Place Cell Accuracy Coincides with Grid Cell Maturation', *Neuron*, 86, pp. 1167–1173.

- Mullan, M. *et al.* (1992) 'A pathogenic mutation for probable Alzheimer's disease in the APP gene at the N-terminus of beta-amyloid', *Nat Genet*, 1, pp. 345–347.
- Munn, R. G. K. *et al.* (2020) 'Entorhinal velocity signals reflect environmental geometry', *Nat Neurosci*, 23, pp. 239–251.
- Murrell, J. *et al.* (1991) 'A mutation in the amyloid precursor protein associated with hereditary Alzheimer's disease', *Science*, 254, pp. 97–99.
- Nakazono, T. *et al.* (2017) 'Impaired In Vivo Gamma Oscillations in the Medial Entorhinal Cortex of Knock-in Alzheimer Model', *Front Syst Neurosci*, 11, p. 48.
- Naumann, R. K. *et al.* (2016) 'Conserved size and periodicity of pyramidal patches in layer 2 of medial/caudal entorhinal cortex', *J Comp Neurol*, 524, pp. 783–806.
- Navarro Schroder, T. *et al.* (2015) 'Functional topography of the human entorhinal cortex', *eLife*, 4, p. e06738.
- Neve, R. L. *et al.* (1986) 'Identification of cDNA clones for the human microtubule-associated protein tau and chromosomal localization of the genes for tau and microtubule-associated protein 2', *Mol Brain Res*, 1, pp. 271–280.
- Neves, G., Cooke, S. F. and Bliss, T. V. P. (2008) 'Synaptic plasticity, memory and the hippocampus: a neural network approach to causality', *Nat Rev Neurosci*, 9, pp. 65–75.
- Newman, E. L. *et al.* (2013) 'Cholinergic blockade reduces theta-gamma phase amplitude coupling and speed modulation of theta frequency consistent with behavioral effects on encoding', *J Neurosci*, 33, pp. 19635–19646.
- Nilssen, E. S. *et al.* (2018) 'Inhibitory connectivity dominates the fan cell network in layer II of lateral entorhinal cortex', *J Neurosci*, 38, pp. 9712–9727.
- Nyberg, L. *et al.* (1996) 'General and specific brain regions involved in encoding and retrieval of events: What, where, and when', *Proceedings of the National Academy of Sciences of the United States of America*, 93, pp. 11280–11285.
- O'Keefe, J. (1976) 'Place units in the hippocampus of the freely moving rat', *Exp Neurol*, 51, pp. 78–109.

O'Keefe, J. (2006) 'Hippocampal Neurophysiology in the Behaving Animal', in Andersen, P. et al. (eds) *The hippocampus book*. Oxford University Press, pp. 475–548.

O'Keefe, J. and Dostrovsky, J. (1971) 'The hippocampus as a spatial map. Preliminary evidence from unit activity in the freely-moving rat', *Brain Res*, 34, pp. 171–175.

O'Keefe, J. and Nadel, L. (1978) *The Hippocampus as a Cognitive Map*. Oxford University Press.

Ohara, S. et al. (2018) 'Intrinsic Projections of Layer Vb Neurons to Layers Va, III, and II in the Lateral and Medial Entorhinal Cortex of the Rat', *Cell Rep*, 24, pp. 107–116.

Okada, K. et al. (2015) 'Distinct roles of basal forebrain cholinergic neurons in spatial and object recognition memory', *Sci Rep*, 5, p. 13158.

Okada, K., Vilberg, K. L. and Rugg, M. D. (2012) 'Comparison of the Neural Correlates of Retrieval Success in Tests of Cued Recall and Recognition Memory', *Hum Brain Mapp*, 33, pp. 523–533.

Onslow, A. C. E., Bogacz, R. and Jones, M. W. (2011) 'Quantifying phase - amplitude coupling in neuronal network oscillations', *Prog Biophys Mol Biol*, 105, pp. 49–57.

Ormond, J. and Mcnaughton, B. L. (2015) 'Place field expansion after focal MEC inactivations is consistent with loss of Fourier components and path integrator gain reduction', *Proc Natl Acad Sci*, 112, pp. 4116–4121.

Oxford, A. E., Stewart, E. S. and Rohn, T. T. (2020) 'Clinical Trials in Alzheimer's Disease: A Hurdle in the Path of Remedy', *Int J Alzheimers Dis.*, 2020, p. 5380346.

Parron, C. and Save, E. (2004) 'Evidence for entorhinal and parietal cortices involvement in path integration in the rat', *Exp Brain Res*, 159, pp. 349–359.

Pastoll, H. et al. (2013) 'Feedback Inhibition Enables Theta-Nested Gamma Oscillations and Grid Firing Fields', *Neuron*, 77, pp. 141–154.

- Paxinos, G. and Franklin, K. B. J. (2001) *The mouse brain in stereotaxic coordinates*. Second edi. San Diego: Academic Press.
- Penley, S. C. *et al.* (2013) ‘Novel space alters theta and gamma synchrony across the longitudinal axis of the hippocampus’, *Front Syst Neurosci*, 7, p. 20.
- Perez-Escobar, J. A. *et al.* (2016) ‘Visual landmarks sharpen grid cell metric and confer context specificity to neurons of the medial entorhinal cortex’, *eLife*, 5, p. e16937.
- Petersen, P. C. and Buzsáki, G. (2020) ‘Cooling of medial septum reveals theta phase lag coordination of hippocampal cell assemblies’, *Neuron*, 107, pp. 1–14.
- Philipson, O. *et al.* (2010) ‘Animal models of amyloid- β -related pathologies in Alzheimer’s disease’, *FEBS Journal*, 277, pp. 1389–1409.
- Popovi, M. *et al.* (2008) ‘Subfield and layer-specific depletion in calbindin-D28K, calretinin and parvalbumin immunoreactivity in the dentate gyrus of APP/PS1 transgenic mice’, *Neuroscience*, 155, pp. 182–191.
- Prince, M. *et al.* (2014) ‘World Alzheimer Report 2014 Dementia and Risk Reduction an Analysis of Protective and Modifiable Factors Supported’, *Alzheimer’s Disease International*.
- Pusil, S. *et al.* (2019) ‘Hypersynchronization in mild cognitive impairment: The “X” model’, *Brain*, 142, pp. 3936–3950.
- Puzzo, D. *et al.* (2008) ‘Picomolar Amyloid- β Positively Modulates Synaptic Plasticity and Memory in Hippocampus’, *J Neurosci*, 28, pp. 14537–14545.
- Qasim, S. E. *et al.* (2019) ‘Memory retrieval modulates spatial tuning of single neurons in the human entorhinal cortex’, *Nat Neurosci*, 22, pp. 2078–2086.
- Quilichini, P., Sirota, A. and Buzsáki, G. (2010) ‘Intrinsic circuit organization and theta-gamma oscillation dynamics in the entorhinal cortex of the rat’, *J Neurosci*, 30, pp. 11128–11142.
- Rademakers, R., Cruts, M. and Van Broeckhoven, C. (2004) ‘The role of tau (MAPT) in frontotemporal dementia and related tauopathies’, *Hum Mutat*, 24, pp. 277–295.

Raina, P. et al. (2008) 'Effectiveness of cholinesterase inhibitors and memantine for treating dementia: Evidence review for a clinical practice guideline', *Ann Intern Med*, 148, pp. 379–397.

Ranasinghe, K. G. et al. (2020) 'Neurophysiological signatures in Alzheimer's disease are distinctly associated with TAU, amyloid- β accumulation, and cognitive decline', *Sci Transl Med*, 12, p. eaaz4069.

Ray, S. et al. (2014) 'Grid-Layout and Theta-Modulation of Layer 2 Pyramidal Neurons in Medial Entorhinal Cortex', *Science*, 13, pp. 987–94.

Reiserer, R. S. et al. (2007) 'Impaired spatial learning in the APPSwe + PSEN1 Δ E9 bigenic mouse model of Alzheimer's disease', *Genes Brain Behav*, 6, pp. 54–65.

Ren, S. Q. et al. (2018) 'Amyloid β causes excitation/inhibition imbalance through dopamine receptor 1-dependent disruption of fast-spiking GABAergic input in anterior cingulate cortex', *Sci Rep*, 8, p. 302.

Resende, R. et al. (2008) 'Neurotoxic effect of oligomeric and fibrillar species of amyloid-beta peptide 1-42: Involvement of endoplasmic reticulum calcium release in oligomer-induced cell death', *Neuroscience*, 155, pp. 725–737.

Ripoli, C. et al. (2014) 'Intracellular accumulation of amyloid- β (A β) protein plays a major role in A β -induced alterations of glutamatergic synaptic transmission and plasticity', *J Neurosci*, 34, pp. 12893–12903.

Rodríguez-García, G. and Miranda, M. I. (2016) 'Opposing roles of cholinergic and GABAergic activity in the insular cortex and nucleus basalis magnocellularis during novel recognition and familiar taste memory retrieval', *J Neurosci*, 36, pp. 1879–1889.

Rossant, C. et al. (2016) 'Spike sorting for large, dense electrode arrays', *Nat Neurosci*, 19, pp. 634–641.

Rowe, M. A. et al. (2011) 'Persons with dementia missing in the community : Is it wandering or something unique?', *BMC Geriatrics*, 11, p. 28.

- Rubio, S. E. *et al.* (2012) 'Accelerated aging of the GABAergic septohippocampal pathway and decreased hippocampal rhythms in a mouse model of Alzheimer's disease', *FASEB Journal*, 26, pp. 4458–4467.
- Saganich, M. J. *et al.* (2006) 'Deficits in synaptic transmission and learning in amyloid precursor protein (APP) transgenic mice require C-terminal cleavage of APP', *J Neurosci*, 26, pp. 13428–13436.
- Salinas, E. and Sejnowski, T. J. (2001) 'Correlated neuronal activity and the flow of neural information', *Nat Rev Neurosci*, 2, pp. 539–550.
- Sargolini, F. *et al.* (2006) 'Conjunctive Representation of Position, Direction, and Velocity in Entorhinal Cortex', *Science*, 312, pp. 758–762.
- Sasahara, M. *et al.* (1991) 'PDGF B-chain in neurons of the central nervous system, posterior pituitary, and in a transgenic model', *Cell*, 64, pp. 217–227.
- Savelli, F. and Knierim, J. J. (2019) 'Origin and role of path integration in the cognitive representations of the hippocampus: Computational insights into open questions', *J Exp Biol*, 222, p. jeb188912.
- Scheff, S. W. *et al.* (2006) 'Hippocampal synaptic loss in early Alzheimer's disease and mild cognitive impairment', *Neurobiol Aging*, 27, pp. 1372–1384.
- Schmidt-Hieber, C. and Häusser, M. (2013) 'Cellular mechanisms of spatial navigation in the medial entorhinal cortex', *Nat Neurosci*, 16, pp. 325–331.
- Sederberg, P. B. *et al.* (2007) 'Gamma Oscillations Distinguish True From False Memories', *Psychol Sci*, 18, pp. 927–932.
- Seelaar, H. *et al.* (2008) 'Distinct genetic forms of frontotemporal dementia', *Neurology*, 71, pp. 1220–1226.
- Seibenhener, M. L. and Wooten, M. C. (2015) 'Use of the open field maze to measure locomotor and anxiety-like behavior in mice', *J Vis Exp*, p. e52434.
- Serpell, L. C. (2000) 'Alzheimer's amyloid fibrils: Structure and assembly', *Biochim Biophys Acta*, 1502, pp. 16–30.
- Serrano-Pozo, A. *et al.* (2011) 'Neuropathological alterations in Alzheimer disease', *Cold Spring Harb Perspect Med*, 1, p. a006189.

- Simon, P., Dupuis, R. and Costentin, J. (1994) 'Thigmotaxis as an index of anxiety in mice. Influence of dopaminergic transmissions', *Behav Brain Res*, 61, pp. 59–64.
- Sirota, A. *et al.* (2008) 'Entrainment of Neocortical Neurons and Gamma Oscillations by the Hippocampal Theta Rhythm', *Neuron*, 60, pp. 683–697.
- Skaggs, W. E. and McNaughton, B. L. (1998) 'Spatial firing properties of hippocampal CA1 populations in an environment containing two visually identical regions', *Journal of Neuroscience*, 18, pp. 8455–8466.
- Skaggs, W. E., McNaughton, B. L. and Gothard, K. M. (1993) 'An information-theoretic approach to deciphering the hippocampal code', *Neural Inf Process Syst*, pp. 1030–1037.
- Sohal, V. S. *et al.* (2009) 'Parvalbumin neurons and gamma rhythms enhance cortical circuit performance', *Nature*, 459, pp. 698–702.
- Solstad, T. *et al.* (2008) 'Representation of geometric borders in the entorhinal cortex', *Science*, 322, pp. 1865–1867.
- Spires-jones, T. and Knafo, S. (2012) 'Spines, Plasticity, and Cognition in Alzheimer's Model Mice', *Neural Plast*, 2012, p. 319836.
- Spitzer, B. and Haegens, S. (2017) 'Beyond the Status Quo : A Role for Beta Oscillations in Endogenous Content (Re) Activation', *eNeuro*, 4, pp. e0170-17.2017.
- Stam, C. J. *et al.* (2002) 'Generalized synchronization of MEG recordings in Alzheimer's disease: Evidence for involvement of the gamma band', *Clin Neurophysiol*, 19, pp. 562–574.
- Stam, C. J. *et al.* (2009) 'Graph theoretical analysis of magnetoencephalographic functional connectivity in Alzheimer's disease', *Brain*, 132, pp. 213–224.
- Staresina, B. P. *et al.* (2019) 'Recollection in the human hippocampal-entorhinal cell circuitry', *Nat Commun*, 10, p. 1503.
- Steffenach, H. A. *et al.* (2005) 'Spatial memory in the rat requires the dorsolateral band of the entorhinal cortex', *Neuron*, 45, pp. 301–313.

- Stelzma, R. A., Schnitzlein, H. N. and Murllagh, F. R. (1995) ‘An english translation of alzheimer’s 1907 paper, “über eine eigenartige erkankung der hirnrinde”, *Clinical Anatomy*, 8, pp. 429–431.
- Stensola, H. et al. (2012) ‘The entorhinal grid map is discretized.’, *Nature*, 492, pp. 72–8.
- Stoub, T. R. et al. (2006) ‘Hippocampal disconnection contributes to memory dysfunction in individuals at risk for Alzheimer’s disease’, *Proc Natl Acad Sci*, 103, pp. 10041–10045.
- Stranahan, A. M. and Mattson, M. P. (2010) ‘Selective vulnerability of neurons in layer II of the entorhinal cortex during aging and Alzheimer’s disease’, *Neural Plast*, 2010, p. 108190.
- Sun, X., Chen, W. D. and Wang, Y. D. (2015) ‘ β -Amyloid: The key peptide in the pathogenesis of Alzheimer’s disease’, *Frontiers in Pharmacology*, 6, pp. 1–9.
- Suthana, N. et al. (2012) ‘Memory Enhancement and Deep-Brain Stimulation of the Entorhinal Area’, *N Engl J Med*, 366, pp. 502–510.
- Tahvildari, B. and Alonso, A. (2005) ‘Morphological and electrophysiological properties of lateral entorhinal cortex layers II and III principal neurons’, *J Comp Neurol*, 491, pp. 123–140.
- Taube, J. S. (1995) ‘Head direction cells recorded in the anterior thalamic nuclei of freely moving rats’, *J Neurosci*, 15, pp. 70–86.
- Taube, J. S. (2007) ‘The Head Direction Signal: Origins and Sensory-Motor Integration’, *Annu Rev Neurosci*, 30, pp. 181–207.
- Taube, J. S. and Burton, H. L. (1995) ‘Head Direction Cell Activity Monitored in a Novel Environment and During a Cue Conflict Situation’, *J Neurophysiol*, 74, pp. 1953–1971.
- Taube, J. S., Muller, R. U. and Ranck, J. B. (1990a) ‘Head-direction cells recorded from the postsubiculum in freely moving rats. I. Description and quantitative analysis’, *J Neurosci*, 10, pp. 420–435.

- Taube, J. S., Muller, R. U. and Ranck, J. B. (1990b) 'Head-direction cells recorded from the postsubiculum in freely moving rats. II. Effects of environmental manipulations', *The Journal of Neuroscience*, 10, pp. 436–447.
- Thal, D. R. et al. (2002) 'Phases of A β -deposition in the human brain and its relevance for the development of AD', *Neurology*, 58, pp. 1791–1800.
- Titiz, A. S. et al. (2017) 'Theta-burst microstimulation in the human entorhinal area improves memory specificity', *eLife*, 6, p. e29515.
- Tolman, E. C. (1948) 'Cognitive maps in rats and men', *Psychol Rev*, 55, pp. 189–208.
- Tomiyama, T. et al. (2010) 'A Mouse Model of Amyloid β Oligomers: Their Contribution to Synaptic Alteration, Abnormal Tau Phosphorylation, Glial Activation, and Neuronal Loss In Vivo', *J Neurosci*, 30, pp. 4845–4856.
- Tort, A. B. L. et al. (2008) 'Dynamic cross-frequency couplings of local field potential oscillations in rat striatum and hippocampus during performance of a T-maze task', *Proc. Natl. Acad. Sci.*, 105, pp. 20517–20522.
- Tort, A. B. L. et al. (2009) 'Theta-gamma coupling increases during the learning of item-context associations', *Proc. Natl. Acad. Sci.*, 106, pp. 20942–20947.
- Trimper, J. B., Stefanescu, R. A. and Manns, J. R. (2014) 'Recognition memory and theta-gamma interactions in the hippocampus', *Hippocampus*, 24, pp. 341–353.
- Unal, G. et al. (2015) 'Synaptic Targets of Medial Septal Projections in the Hippocampus and Extrahippocampal Cortices of the Mouse', *J Neurosci*, 35, pp. 15812–15826.
- VandeVrede, L., Boxer, A. L. and Polydoro, M. (2020) 'Targeting tau: Clinical trials and novel therapeutic approaches', *Neurosci Lett*, 731, p. 134919.
- Vanssay-maigne, A. De et al. (2011) 'Modulation of encoding and retrieval by recollection and familiarity: Mapping the medial temporal lobe networks', *NeuroImage*, 58, pp. 1131–1138.
- Varela, F. et al. (2001) 'The brainweb: Phase synchronization and large-scale integration', *Nat Rev Neurosci*, 2, pp. 229–239.

- Velayudhan, L. et al. (2013) 'Entorhinal cortex thickness predicts cognitive decline in Alzheimer's disease', *J Alzheimers Dis.*, 33, pp. 755–766.
- Verret, L. et al. (2012) 'Inhibitory Interneuron Deficit Links Altered Network Activity and Cognitive Dysfunction in Alzheimer Model', *Cell*, 149, pp. 708–721.
- Veugelen, S. et al. (2016) 'Familial Alzheimer's Disease Mutations in Presenilin Generate Amyloidogenic Ab Peptide Seeds', *Neuron*, 90, pp. 410–416.
- Vugt, M. K. Van et al. (2010) 'Hippocampal gamma oscillations increase with memory load', *J Neurosci*, 30, pp. 2694–2699.
- Walker, J. M. et al. (2011) 'Spatial learning and memory impairment and increased locomotion in a transgenic amyloid precursor protein mouse model of Alzheimer's disease', *Behav Brain Res*, 222, pp. 169–175.
- Wang, H. W. et al. (2002) 'Soluble oligomers of β amyloid (1-42) inhibit long-term potentiation but not long-term depression in rat dentate gyrus', *Brain Res*, 924, pp. 133–140.
- Wang, Q. et al. (2004) 'Block of long-term potentiation by naturally secreted and synthetic amyloid β -peptide in hippocampal slices is mediated via activation of the kinases c-Jun N-terminal kinase, cyclin-dependent kinase 5, and p38 mitogen-activated protein kinase as well as m', *J Neurosci*, 24, pp. 3370–3378.
- Wang, Y. et al. (2015) 'Theta sequences are essential for internally generated hippocampal firing fields', *Nat Neurosci*, 18, pp. 282–288.
- Wang, Y. and Mandelkow, E. (2016) 'Tau in physiology and pathology', *Nat Rev Neurosci*, 17, pp. 5–21.
- Ward, L. M. (2003) 'Synchronous neural oscillations and cognitive processes', *Trends Cogn Sci*, 7, pp. 553–559.
- Webster, S. J. et al. (2014) 'Using mice to model Alzheimer's dementia: an overview of the clinical disease and the preclinical behavioral changes in 10 mouse models', *Front Genet*, 5, p. 88.
- Wells, C. E. et al. (2013) 'Novelty and Anxiolytic Drugs Dissociate Two Components of Hippocampal Theta in Behaving Rats', *J Neurosci*, 33, pp. 8650–8667.

- Whishaw, I. Q. and Brooks, B. L. (1999) 'Calibrating space: Exploration is important for allocentric and idiothetic navigation', *Hippocampus*, 9, pp. 659–667.
- Winson, J. (1978) 'Loss of hippocampal theta rhythm results in spatial memory deficit in the rat', *Science*, 201, pp. 160–163.
- Winter, S. S. et al. (2015) 'Passive Transport Disrupts Grid Signals in the Parahippocampal Cortex', *Curr Biol.*, 25, pp. 2493–2502.
- Winter, S. S., Clark, B. J. and Taube, J. S. (2015) 'Disruption of the head direction cell network impairs the parahippocampal grid cell signal', *Science*, 347, pp. 870–874.
- Wittenberg, R. et al. (2019) *Projections of Older People with Dementia and Costs of Dementia Care in the United Kingdom, 2019-2040, Care Policy and Evaluation Centre*.
- Witter, M. P. et al. (2017) 'Architecture of the entorhinal cortex a review of entorhinal anatomy in rodents with some comparative notes', *Front Syst Neurosci*, 11, p. 46.
- Wright, A. L. et al. (2013) 'Neuroinflammation and Neuronal Loss Precede A β Plaque Deposition in the hAPP-J20 Mouse Model of Alzheimer's Disease', *PLoS ONE*, 8, p. e59586.
- Xu, X. (2009) 'γ-Secretase catalyzes sequential cleavages of the A β PP transmembrane domain', *J Alzheimers Dis.*, 16, pp. 211–224.
- Yamamoto, J. et al. (2014) 'Successful execution of working memory linked to synchronized high-frequency gamma oscillations', *Cell*, 157, pp. 845–857.
- Ye, J. et al. (2018) 'Entorhinal fast-spiking speed cells project to the hippocampus', *Proc. Natl. Acad. Sci.*, 115, pp. E1627–E1636.
- Yoder, R. M. et al. (2011) 'Both visual and idiothetic cues contribute to head direction cell stability during navigation along complex routes', *J Neurophysiol*, 105, pp. 2989–3001.
- Yoder, R. M. and Pang, K. C. H. (2005) 'Involvement of GABAergic and cholinergic medial septal neurons in hippocampal theta rhythm', *Hippocampus*, 15, pp. 381–392.

Yoder, R. M. and Taube, J. S. (2009) 'Head direction cell activity in mice: Robust directional signal depends on intact otolith organs', *J Neurosci*, 29, pp. 1061–1076.

Zallo, F. *et al.* (2018) 'Loss of calretinin and parvalbumin positive interneurones in the hippocampal CA1 of aged Alzheimer's disease mice', *Neurosci Lett*, 681, pp. 19–25.

Zanotti, A. *et al.* (1994) 'Diazepam impairs place learning in naive but not in maze-experienced rats in the Morris water maze', *Psychopharmacology*, 115, pp. 73–78.

Zheng, C. *et al.* (2016) 'Fast gamma rhythms in the hippocampus promote encoding of novel object-place pairings', *eNeuro*, 3, pp. 3089–3096.